Thèse n° 9615

3D printing of elastomeric mechanical sensors designed for human motion monitoring

Présentée le 12 août 2022

Faculté des sciences et techniques de l'ingénieur
Laboratoire des Microsystèmes Souples
Programme doctoral en microsystèmes et microélectronique

pour l'obtention du grade de Docteur ès Sciences

par

Ryan Mitchell VAN DOMMELEN

Acceptée sur proposition du jury

Prof. L. G. Villanueva Torrijo, président du jury
Dr D. Briand, directeur de thèse
Dr G. Nyström, rapporteur
Prof. C. Boutry, rapporteuse
Prof. J. Brugger, rapporteur

École
polytechnique
fédérale
de Lausanne

2022

Just because something does not have an ending
doesn't mean it doesn't have a conclusion.
— Ian. M. Banks

Acknowledgements

First and foremost, I would like to thank Dr. Danick Briand for giving me the opportunity to join his research group in Neuchâtel and introduce me to the world of printed electronics. I am grateful for his guidance, critical eye, ideas, and his endless enthusiasm and motivation to see me succeed in producing this thesis.

I would like to express my appreciation to Prof. Clémentine Boutry, Prof. Jürgen Brugger, and Dr. G. Nyström, who agreed to review this thesis and Prof. Guillermo Villanueva for being the jury president.

I would like to give special thanks Marco Binelli, Yannick Nagel, and Gilberto Siqueira who I worked closely with on the D-Sense project. It was a pleasure working with you, and your drive to make this project succeed motivated me too to deliver the best result possible.

The support of the whole LMTS lab has been invaluable to me and I would like to thank everyone who I had the pleasure to work or share an apéro with. I would like to extend an especially warm thanks to my little group of printing enthusiasts: Alessio, Alexis, Giulio, James, Jaemin, Morgan, Nicolas, Sam, and Silvia for supporting me with your friendship and advice throughout the short or long time we've been together. A special thanks to Myriam Poliero for being the best secretary that a lab could have, and for always being available for a chat.

Furthermore, I would like to thank all the other Microcity people who have this place and Neuchâtel a great home for the last four years: Aymeric, Pieter, Peter, Ruben, Gözden, Jakub, and Olivier, for either sharing beers at MBC, barbecues by the lake, or random adventures in Switzerland. I would like to give special thanks to the eminent Dr. Peter van der Wal for his awesome knowledge of chemistry, beer, and all things dutch.

To all the friends I made in Neuchâtel over the last four years I would like to say, thank you all for making Switzerland feel like a second home. Thanks to Giada, Sammy, Esra, Luciana, Sabrina, Lisa, Alex, Maialen, Mirari, and Kopta for sharing great moments and helping me take my mind away from all the engineering from time to time. Lastly, I would like to give a thanks to my parents, Arthur and Cathy, for supporting me unconditionally during the years and for never stopping to believe in me.

Neuchâtel, 26th of April 2022 Ryan Mitchell van Dommelen

Abstract

In this thesis several advances are made to the emerging field of 3D printed mechanical sensors. Techniques and processes were developed to enable the integration of highly conductive, and capacitive and piezoresistive sensing features embedded within 3D printed elastomeric materials. With these technologies we enabled the fabrication of fully 3D printed piezoresistive and capacitive sensors for normal force, shear forces and angular bending sensing.

Integrating highly electrically conductive flexible silver films (<125 μΩ cm), printed by Direct Ink Writing (DIW), into a flexible thermoplastic polyurethane (TPU) printed by Fused Deposition Modelling (FDM) for low-power mechanical sensors was not possible due to thermal constraint. Using a cost-effective LED laser, we developed an in-situ laser sintering technique and studied the influences of laser power and scanning speed on the electrical conductivity of the printed silver films after sintering. In this fashion, we achieved sub 100 μm thickness line and plate features with resistivity values as lows as 58.2±7.7 μΩ cm. This technique was exploited to create fully 3D printed flexible capacitive normal pressure sensors (4.47±0.12 fF/N), conductors with low resistance (<2Ω), and a piezoresistive bending sensor. In this way we enabled the fabrication of fully 3D printed flexible electronic devices, with a significant conductivity increase in comparison with FDM printed devices found in the state of the art.

As FDM is limited in what types of materials can be produced, due to printed materials needing to be thermoplastic, we investigated the DIW printing of thermally stable silicone material systems. A structurally self-supporting material system composed of Crystalline Nanocellulose (CNC) reinforced silicone (CNC-PDMS) was realised that has ideal shear thinning behaviour required for DIW printing. By integrating printed strain gauges into the CNC-PDMS, from a piezoresistive carbon black (CB) silicone ink (CB-PDMS), piezoresistive normal force sensors were DIW printed with a normal force sensitivity of 14.9±0.4Ω/kPa (0.22±0.07%/kPa), and a linear response up to a normal load of 1000 kPa. Dynamic normal force sensing was shown to be possible for these pressures up to a frequency of at least 2 Hz. Exploiting the digital nature of 3D printing, a shear force sensor was printed with two strain gauges with directional compliancy that resulted in differential sensor able to sense shear forces and their direction up to 15 N. By integrating several of the normal and shear force sensors into a fully 3D printed wearable device, we demonstrated the capture of normal plantar pressures and shear forces of a foot during a range of day-to-day and sports activities. This technology enables the fabrication of fully 3D printable personalised wearables due to the digital nature of 3D printing.

For creating sensor with 3D topology, we developed a DIW printable UV curable silicone ink. By stacking multiple layers of this material, a novel capacitive bending sensor design was conceptualised with inclined slopes. These angular faces allow for a sensor with an asymmetric sensing behaviour. To fully 3D print this sensor, a fumed silica reinforced UV curable silicone ink was developed to be able to print stacks that could be cured in-situ using a UV LED. By stacking the layers strategically, angular faces were generated with an angle up to 41.2±2.3° on which conductive silver plates were printed. Through this method, the bending sensor was realised with slanted plates which increased in capacitance when bend towards each other and decreased when bending away from each other, making the direction of bending distinguishable. With a sensitivity of 2.50±0.04 fF/° (0.11±0.00 %F/°), the sensor was able to accurately track dynamic movements including the bending of a limb. Using this developed sensing mechanism, and printing approach, we demonstrated the fabrication of a novel human motion monitoring sensor.

The results presented in this PhD thesis could be seen as a stepping stone towards the development of fully 3D printed personalised wearables with integrated sensing. By exploiting the digital nature of 3D printing it was shown that novel and custom tailorable devices can be enabled.

Key words:
3D printing, Direct Ink Writing (DIW), elastomeric mechanical sensors, piezoresistive sensing, capacitive sensing, laser sintering, wearable sensors, human motion monitoring

Résumé

Dans cette thèse, plusieurs avancées sont réalisées dans le domaine émergent des capteurs mécaniques imprimés en 3D. Des techniques et des processus ont été développés pour permettre l'intégration de matériaux hautement conducteurs, incluant des propriétés capacitives et piézorésistives intégrées dans des élastomères imprimés en 3D. Grâce à ces technologies, nous avons pu fabriquer des capteurs piézorésistifs et capacitifs entièrement imprimés en 3D, pour la détection de la force normale, des forces de cisaillement et de la flexion angulaire. L'intégration de films d'argent flexibles de haute conductivité électriques (<125 μΩ cm), imprimés par Direct Ink Writing (DIW), incorporé un polyuréthane thermoplastique (PUT) flexible imprimé par Fused Deposition Modeling (FDM) afin de créer des capteurs mécaniques de faible puissance qui jusqu'alors n'étaient pas réalisable en raison des contraintes thermiques. En utilisant un laser LED, économique, nous avons développé une technique de frittage laser in-situ et étudié les influences de la puissance du laser et de sa vitesse de balayage sur la conductivité électrique des films d'argent imprimés après frittage. De cette manière, nous avons obtenu des lignes et des plaques d'une épaisseur inférieure à 100 μm avec des valeurs de résistivité aussi basses que 58,2±7,7 μΩ cm. Cette technique a été exploitée pour créer des capteurs de pression normale capacitifs flexibles entièrement imprimés en 3D (4.47±0.12 fF/N), des conducteurs à faible résistance (<2Ω) et un capteur de flexion piézorésistif. De cette façon, nous avons permis la fabrication de dispositifs électroniques flexibles entièrement imprimés en 3D, avec une augmentation significative de la conductivité par rapport aux dispositifs imprimés par FDM que l'on trouve dans l'état de l'art.

L'impression FDM étant limitée par le fait que les matériaux imprimés doivent être thermoplastiques, nous avons étudié l'impression DIW de composites en silicone thermiquement stables. Nous avons réalisé un système de matériau structurellement autoportant composé de silicone renforcé par de la nanocellulose cristalline (NCC) (NCC-PDMS) qui présente la propreté idéale de rhéofluidification requis pour l'impression DIW. En intégrant des jauges de contrainte imprimées dans le NCC-PDMS, à partir d'une encre silicone piézorésistive au Carbon Black (CB) (CB-PDMS), des capteurs de force normale piézorésistifs ont été imprimés par DIW avec une sensibilité à la force normale de 14.9±0.4Ω/kPa (0.22±0.07%/kPa), et une réponse linéaire jusqu'à une charge normale de 1000 kPa. La détection dynamique de la force normale s'est avérée possible pour ces pressions jusqu'à une fréquence d'au moins 2 Hz. En exploitant la nature numérique de l'impression 3D, un capteur de force de cisaillement a été imprimé avec deux jauges de contrainte ayant une conformité directionnelle qui a abouti à un capteur différentiel capable de détecter les forces de cisaillement et leur direction jusqu'à 15 N. En intégrant plusieurs des capteurs de force normale et de cisaillement dans un dispositif portable entièrement imprimé en 3D, nous avons démontré l'acquisition de la pression plantaire normale, et des forces de cisaillement d'un pied durant des activités quotidiennes et sportives. Cette technologie permet la fabrication de vêtements personnalisés entièrement imprimables en 3D grâce à la nature numérique de l'impression 3D.

Pour créer un capteur à topologie 3D, nous avons mis au point une encre silicone réticulable par UV et imprimable par DIW. En empilant plusieurs couches de ce matériau, nous avons conçu un nouveau capteur capacitif de flexion avec des pentes inclinées. Ces faces angulaires permettent d'obtenir un capteur avec un comportement de détection asymétrique. Pour imprimer entièrement ce capteur en 3D, une encre silicone renforcée de silice pyrogénée et durcissable aux UV a été mise au point afin de pouvoir imprimer des piles pouvant être durcies in-situ à l'aide d'une LED UV. En empilant les couches de manière stratégique, des faces angulaires ont été générées avec un angle allant jusqu'à $41.2\pm2.3°$ sur lesquelles des plaques d'argent conductrices ont été imprimées. Grâce à cette méthode, le capteur de flexion a été réalisé avec des plaques inclinées dont la capacité augmente lorsqu'elles se rapprochent les unes des autres et diminue lorsqu'elles s'éloignent, ce qui permet de distinguer la direction de la flexion. Avec une sensibilité de 2.50 ± 0.04 fF/° (0.11 ± 0.00 %F/°), le capteur a pu suivre avec précision des mouvements dynamiques, notamment la flexion d'un membre. En utilisant ce mécanisme de détection et cette approche d'impression, nous avons démontré la fabrication d'un nouveau capteur de suivi des mouvements humains.

Les résultats présentés dans cette thèse peuvent être considérés comme un premier pas vers le développement de dispositifs portables personnalisés entièrement imprimés en 3D et dotés de capteurs intégrés. En exploitant la nature numérique de l'impression 3D, il a été démontré que des systèmes nouveaux et personnalisés peuvent être créés.

Mots clés :

Impression 3D, Direct Ink Writing (DIW), capteurs mécaniques élastomères, capteurs piézo-résistifs, capteurs capacitifs, frittage laser, capteurs portables, surveillance des mouvements humains.

Contents

List of Figures

List of Tables

1 Introduction

1.1 Background and motivation

The ultimate smart wearable system is a device, with all functional parts seamlessly integrated, which provides a personalised approach towards monitoring health metrics. One way to achieve this is through fabrication by additive manufacturing, a methodology more commonly known as, 3D printing. By 3D printing the devices they are build bottom up in a layer by layer fashion, which allows for the seamless integration of different materials per layer[1]. Furthermore, by exploiting the digital nature in which 3D printers build objects from a 3D model, it becomes easy to make on the fly adjustments which allows for rapid customisation[2], [3]. This last part is especially of interest for the fabrication of custom tailored medical devices and sportswear[4], [5]. These types of devices often have to be made on specification, and are thus very laborious to create. By integrating flexible electronic elements directly into a printed body through 3D printing, smart features such as motion and biometric data collection can easily be introduced into a completely custom tailored wearable[6]–[8].

The process of Digital Manufacturing, in which a 3D model is converted into instructions for 3D printing infrastructure, offers a solution here as it allows for adaptability and easy customisation[3], [9]. By creating a 3D model using Computer Aided Design (CAD) programs, a digital design is easily converted into instructions using specialised software.

In comparison to devices constructed in a planar fashion, by either conventional or printing techniques, 3D printing allows for complex three dimensional features to be fabricated more flexibly and easily than by conventional processes[10]. Structures with three dimensional geometry and integrated electronics allow for a significant increase in the feature density[10], [11]. Smart systems with discrete electrical components and integrated sensors have been developed, but which were only partially 3D printed[12], are limited to rigid polymers[13], or created in combination with conventional microfabrication techniques[14].

Processes to create soft, complex, and wearable 3D printed objects are, however, still not fully explored. The main problem remains that many 3D printing machines are limited in the types of material that can be printed and that they are often not suited for multimaterial printing. The ideal 3D printing platform would have the capabilities to print multiple types of materials, and be able to integrate complex electrical components, within a single platform. While advances are being made, as additive manufacturing is a hot research topic[15], [16], this type of fabrication is still in its infancy and much research is still required. As such, fully 3D printed wearable devices with complex sensors suitable for human motion tracking have not been developed. Figure 1.1 illustrates how digital manufacturing process is structured in order to produce fully printed wearable smart systems for capturing health metrics such as gait monitoring.

The main focus of this thesis is on the development of 3D printed soft sensors using mechanical transduction principles which are suitable for human motion monitoring activities. These types of sensors are the ideal choice for motion monitoring wearables as they have either very low power consumption[17] or can be made autonomous by being self-powered through triboelectricity[18]. By integrating multiple sensors with other electric components into soft 3D printed bodies a way towards completely 3D printed wearable devices can be opened.

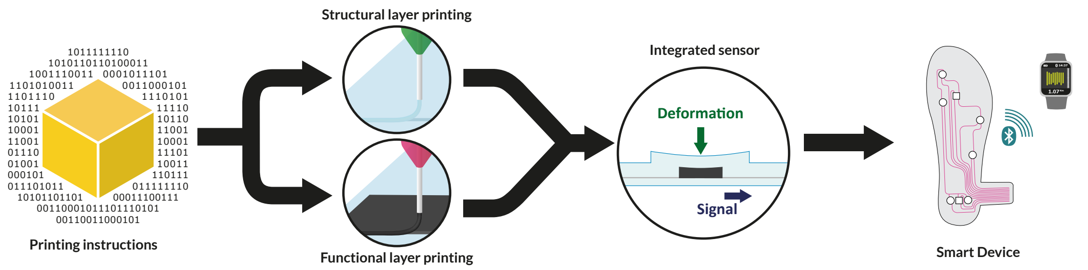

Figure 1.1 – Digital Manufacturing: by means of a set of 3D printing instructions integrated sensors can be constructed from a combination of structural and functional materials. These can be further integrated into a smart device that can be used to read out health metrics.

1.2 Thesis objectives and contributions

As stated in the previous section, 3D printed smart devices have a lot of potential for wearable motion monitoring applications. However, at this time there has been little research presented on truly 3D printed devices. In order to move towards autonomous and low-power 3D printed devices, the research in this is thesis focused on their development and testing.

In brief, the main objective of this thesis is to establish printing and processing methodologies to 3D print polymer based materials, use these to design and fabricate completely 3D printed multimaterial mechanical sensors and evaluate their performance.

A further goal was to realise these processes such that fully 3D printed sensors could be produced in a single tool. To realise this goal, several sub-objectives have been explored. The sub-objectives are provided in a summarised fashion along with the contributions that have been made which are presented in this thesis. These are divided in a material processing and a sensor development category.

Material and process development for the integration of sensing features into 3D printed materials

- Embedding highly conductive and piezoresistive sensing features into 3D printed structural materials to allow for rapid fabrication of 3D printed sensors with three dimensional geometry

I developed a method to locally laser sinter a DIW printed silver flexible ink to sinter the ink without damaging thermosensitive substrates (HDT = 60°C). By avoiding external processing in high temperature environments (oven or hotplate) the structural integrity of the substrate is retained while the ink is instantly heated above 100 °C, evaporating the solvent and solidifying the ink. Optimum printing and sintering conditions were determined to enable the fabrication of features with conductivity values between 50-125 $\mu\Omega$ cm. This enabled the stacking of multiple 3D printed conductive and structural layers using a hybrid combination of DIW printed paste and FDM printed TPU. Using this process I fabricated fully 3D printed flexible conductors which had less than 2 Ω of resistance and could be strained up to 6% without significant resistance change. Furthermore, I produced a linearly performing capacitive sensor with a sensitivity of 4.47 fF/N and capability to follow dynamic signals up to 4 Hz. We further demonstrated the ability to cure a piezoresistive silicone ink for the fabrication of a bending sensor with the ability to dynamically measure bending angles up to 90° with little noise. We further optimised this material to give it the shear thinning properties required for DIW printing. By reinforcing it with fumed silica and studying the influence of the solvent and carbon black (CB) loading, we arrived at a pentanol based ink with 4 wt% CB loading that could be thermally cured and used for piezoresistive sensors.

- Create a printable silicone based material systems and methodology for the printing of complex three-dimensional geometries with highly conductive features

Thermoset and UV curable DIW printable silicone inks were developed by reinforcing them with fumed silica and crystalline nanocellulose (CNC) to achieve the required shear thinning behaviour. Using silicone reinforced with varying levels of CNC we enabled stable multilayer prints to allow for the embedding of conductive silver traces and piezoresistive features. For the UV curable silicon ink reinforced with fumed silica, the influence on the printed dimensions of multi-line features I investigated by means of a Design of Experiments (DoE) approach. Printing parameters including, speed, pressure, spacing, and printing tip distance were evaluated to achieve consistent dimensions. Using settings to be able to consistently print sub 100-um layers, I developed a methodology to stack multiple layers with 3D structured geometry that could be cured in one shot by UV exposure directly after printing. This allowed me to DIW print features with slanted edges of up to 45°, and by printing conductive silver paste on top of these the fabrication of angled conductive features was enabled.

Development of fully 3D printed mechanical sensing devices

- Design, print, and characterise fully 3D printed soft piezoresistive normal and shear force sensors and compare them to those produced by conventional techniques

We designed, 3D printed, and characterised soft sensors in a collaborative effort from the developed CNC-silicone materials system which allows for three dimensional self supporting structures. Piezoresistive gauges, printed from our CB reinforced inks, showed the capability to measure both high and low impact normal forces with a linear response and a sensitivity of 14.9±0.4 Ω/kPa. With a gauge factor of 34.0±0.1, we achieved a response of the same magnitude as silicone based sensors created using conventional fabrication processes for soft materials. Using digital manufacturing to 3D print a compliant three-dimensionally structured strain gauge we created shear sensors capable of registering shear forces up to 15 N including the direction of the force.

- Model, design, and fabricate truly 3D printed soft sensors with three-dimensionally structured and non-planar features

I proposed a capacitive bending sensor design that which, due to its non-planar geometry, resulted in a bending sensor which can indicate the direction of bending from the change in capacitance. I derived an analytical model for this sensor which allows its behaviour to be simulated and which was verified by means of a Finite Element Model (FEM). The models were verified by physical copies created using FDM printed moulding casts, allowing for the fabrication of 3D structures which hard to attain through layer by layer processing. This design allowed for a capacitance change ($\Delta C/C_0$) of 9.3 ± 1.8% when its body was bend either 30° positive or negatively. By transferring this novel transduction mechanism to my developed 3D printing process a thin design was realised with a sensitivity of 7.55 fF/°cm^2. In this fashion I demonstrate a completely 3D printed soft mechanical sensor with a novel sensing mechanism and three-dimensional structuring.

- Integrate 3D printed sensors into a monolithic and personalisable wearable for the recording of human gait

We integrated several of our developed piezoresistive sensors into a insole demonstrator and use it to record data which was processed to demonstrate distinct normal and shear forces during a variety of activities, such as walking and going up and down the stairs. With this developed technology we enable the 3D printing of smart footwear, with integrated gait sensing, that can be easily personalised.

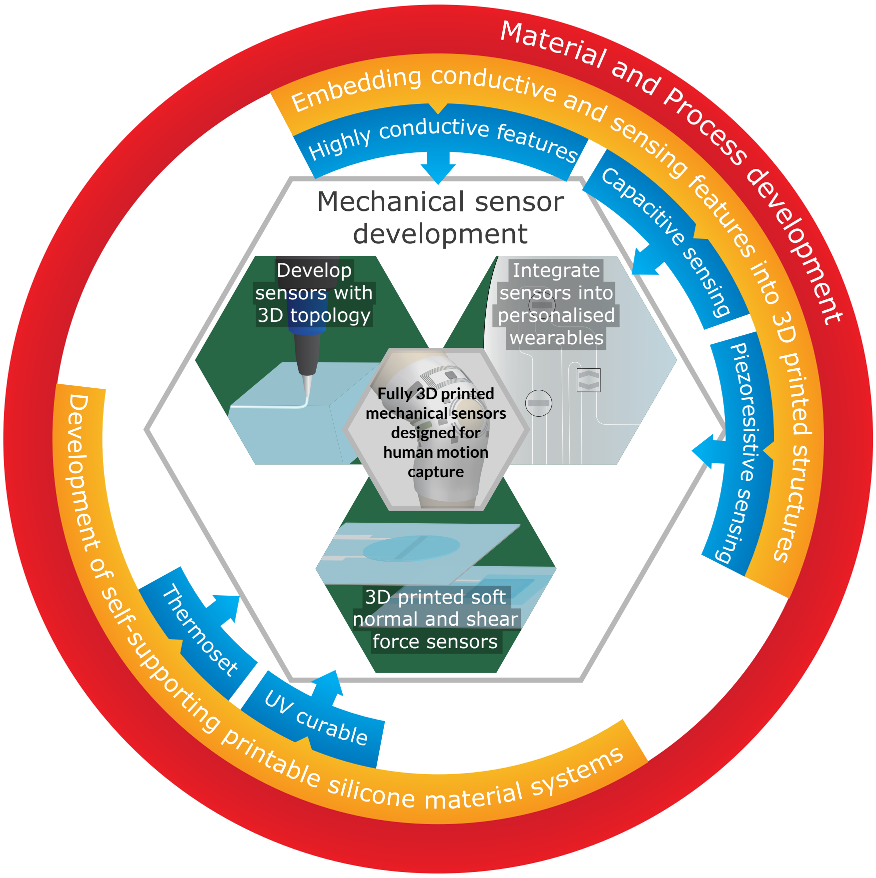

Figure 1.2 – Scope of the thesis topics explored and the resulting advances made.

1.3 Thesis outline

The work presented in this thesis concerns the development, design, and fabrication of 3D printed mechanical sensors which are suitable for human motion monitoring. Part of this work was performed within the frame of a project called D-Sense, funded by the Strategic

Focus Area Advanced Manufacturing (SFA-AM), which was performed in collaboration with the Complex Materials and the Cellulose and Wood Materials Laboratories at ETHZ and EMPA, respectively. The fabricated sensing devices included capacitive sensors made out of FDM and DIW materials, cellulose-silicone composite based piezoresistive normal and shear sensors produced by DIW printing, and an entirely DIW printed novel capacitive bending sensor.

As per the contributions outlined in the previous section, the structure of the thesis is as follows

Chapter 2 discusses the State of the Art (SotA) of 3D printing techniques that can be used to print soft devices. An overview of the working principles, strengths and limitations is given per techniques. An overview of 3D printed mechanical sensors which can be used for motion monitoring including their performance. Lastly, an overview is provided of the remaining challenges uncovered by my investigation and an approach is presented as how I planned to address these.

Chapter 3 presents the investigation into local sintering of silver pastes for embedding highly conductive features within thermosensitive FDM printed material without external processing. A study is presented to investigate the influences of laser power and scanning speed to determine optimal sintering conditions. The technique is extended for the curing of a carbon black silicone composites. Using the sintering method, three devices were fabricated including a capacitive pressure sensor, a flexible electrical conductor, and a piezoresistive bending sensor. To compare these to fully FDM printed devices, complementary piezoresistive strain and capacitive pressure sensors were developed by FDM printing only. This last work was performed by a master student under my supervision.

Chapter 4 presents the work performed on the development of piezoresistive and capacitive sensors out of DIW printable shear thinning crystalline nanocellulose (CNC) and fumed silica (FS) reinforced silicones. Several sensors were designed in order to evaluate the most suitable sensing mechanisms for human gait motions. Inks based on preexisting Carbon Black (CB) silicone composites were developed in cooperation with ETHZ, in order to create a DIW printable soft conductive material for piezoresistive sensing. Using the developed fabrication process, piezoresistive normal and shear force sensors were produced from the 3D printable silicone inks. The normal sensors were evaluated in terms of static, hysteresis, and dynamic response using human mimicking load cases. Results were used to improve the sensor designs and a comparison was made to the capacitive sensors to evaluate their performance and limitations. The shear sensors were evaluated in terms of their sensitivity, and a compliant strain gauge design was introduced that shows the capability to detect the direction of shear forces. Both piezoresistive normal and shear sensors were integrated into a fully 3D printed shoe insole demonstrator to be tested by human test subjects.

Chapter 5 presents the development of a DIW printable UV curable silicone ink to create 3D structured features for the development of a novel capacitive sensor for monitoring angular motions. A design parameter study of a capacitive bending sensor design was performed analytically and by Finite Element Modelling (FEM), and validated by a casting process using FDM printed moulds. To enable the 3D printing of such a sensor, a UV curable silicone ink suited for multilayer printing was developed and characterised. Using an extensive Design of Experiments (DoE) analysis, the influences of the printing parameters during DIW printing were determined. Processes and strategies were realised to be able to DIW print sub 100 um layers and stack these into 3D structures with angular features. By printing silver ink on top of these features, conductive non-planar capacitive plates were realised. A fully DIW printed capacitive bending sensor was produced by exploiting this technique which, through its design, showed directionality with respect to the direction of bending.

Chapter 6 discusses the results of gait motions captured through a fully 3D printed insole demonstrator. The design considerations and insole layout are discussed in this chapter, as well as the influences of sensor encapsulation. An electronic sensor readout system, developed for this demonstrator specifically, was used to capture gait data from several real-life motion scenarios presented in this chapter.

Chapter 7 is conclusion of this thesis and provides a summary of the work and an outlook on what potential new research this thesis enables.

1.4 Impact of this Thesis

In this thesis several aspects for the fabrication of 3D printed elastomeric mechanical sensors designed for human motion monitoring are advanced. Printing and processing methods for soft and flexible structural and conductive materials are introduced or improved upon from the state of the art. Furthermore, novel sensor designs are introduced and evaluated on their performance.

An in-situ curing process was developed to integrate highly conductive films into thermosensitive materials towards manufacturing sensors within a single 3D printing platform. This hybrid printing technique was exploited to create flexible electronic demonstrators.

Formulations for self-supporting thermoset and UV curable silicone inks suitable for 3D printing were realised or improved upon including those with piezoresisitive properties. These materials can be used to produce unique 3D structured geometries that are difficult to obtain using conventional microfabrication techniques. By exploiting these capabilities, fully DIW printed normal and shear force sensors were fabricated that are suitable for recording both impact and shear forces during dynamic activities. Due to their digital manufacturing nature, they can easily be integrated into a personalisable insole for the evaluation of human gait.

Furthermore, 3D structuring was exploited to create a sensor with a novel asymmetric capacitive transduction mechanism. This sensor was able to measure bending in two directions due to the asymmetric sensing behaviour enabled by the 3D structuring.

2 State of the art in 3D printing research of wearables for motion monitoring

3D printing is often used as a catch all term for additive fabrication processes in which objects are constructed that are not limited to planar geometries. A number of different 3D printing techniques exist, each with their advantages and disadvantages linked to either the available materials or their processing. In this chapter an overview is given of the state of the art of 3D printed electromechanical sensors and integrated devices which can be used for human motion monitoring.

First 3D printing techniques are discussed which are suitable for printing of soft materials. In this section Fused Deposition Modelling (FDM), Direct Ink Writing (DIW), and Photopolymerisation (SLA/DLP) techniques are discussed. The techniques are explored in terms of their operating principle and what materials they are capable of printing. Advantages, limitations and drawbacks of the printable materials are discussed separately per method to provide an overview of the capabilities of the 3D printing techniques. Of especial interest is the printing of conductive materials, as these are a central requirement for the fabrication of sensors, and their makeup is inherently different per printing techniques.

Following this, an overview is provided of electromechanical sensors which are either enabled by means of 3D printing or, ideally, are completely 3D printed. Sensors are categorised and presented by the types of motion they can detect, the transduction principles used, and their characteristics and performance. Furthermore, an overview is provided of one of the main issues for soft 3D printed systems for motion monitoring. Among these are the stretchability and conformability of 3D printed systems.

Finally the challenges are highlighted that were encountered during the literature survey on the fabrication of soft electromechanical sensors for human wear. To conclude this chapter, the open scientific challenges are discussed and the research approaches which have been explored in this thesis are addressed.

2.1 Overview of 3D printing techniques

For soft wearables it is important that the used materials are flexible, stretchable, and conformable such that they can be comfortably worn for extended periods of time[19]. Therefore, this chapter focuses on techniques which are able to 3D print soft polymers or polymer precursors. Techniques which are suitable for printing these kinds of materials are often limited to either resins, inks, or thermoplastics. Furthermore, in order to introduce smart features into 3D printed wearables, materials are required which are either inherently conductive or become so after processing[20]–[22], and which need to be compatible with the structural material that they are meant to be integrated within. Using multiple materials within a 3D printing process is commonly referred to as multimaterial printing[23]. Schematic overviews of the techniques discussed in this chapter are shown in Figure 2.1.

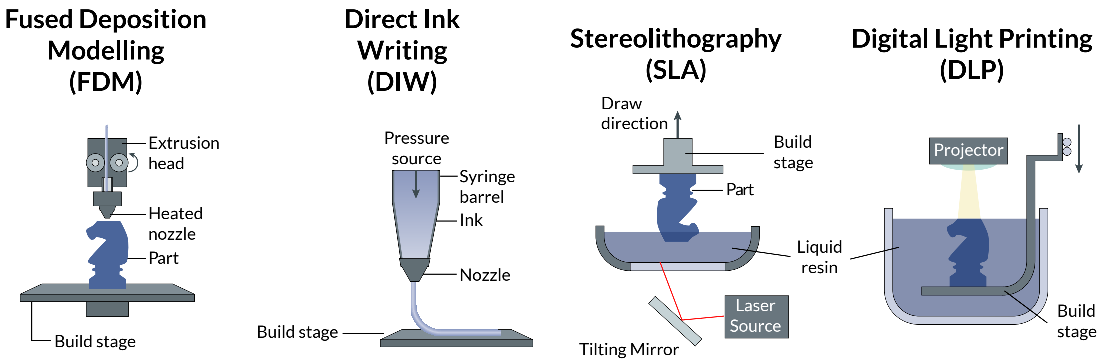

Figure 2.1 – An overview of the most common 3D printing techniques for the printing of soft materials. Adapted from [1]

2.1.1 Fused Deposition Modelling

One of the most popular polymer based 3D printing technique is Fused Deposition Modelling (FDM) mostly due to its low cost, which makes it very accessible[2]. Due to ease of access and the flexibility in printing any object from a 3D file it has proven especially popular within creative communities in schools and on the internet. All FDM printers rely on the translation of a 3D model into printing instructions that the machine can understand through a programming language called G-code. The conversion of a 3D model to G-code is called slicing and is performed by programs called slicers.

In FDM printing a semi-flexible thermoplastic filament is fed to an extrusion head by a set of gears where it is heated up far above the material glass transition temperature. While the exact temperature is tuned to the material, temperatures above 200°C are common. Once fully heated, the filament is extruded through a heated nozzle and deposited on a heated bed to prevent the effects of thermal shock[24]. Individual lines are printed to form a single individually patterned layers which are stacked on top of each other to form the final monolithic 3D geometry. Most materials have self-supporting properties but in order to create overhangs and freestanding structures a secondary support structure is usually printed.

Most FDM printable materials are rigid and printers are generally not build to handle flexible filaments. As such, these rigid material have limited applicability for wearables designed around being able to move along with the body. Even so, these materials could still see use within strategically designed rigid wearables for parts of the body that see little movement[25].

Even so, an advantage of FDM printing is that it is easy to print designs with a negative poison ratio (Figure 2.2 a) to be able to introduce the ability for FDM materials to deform more without the material itself having to be very stretchable[26]. Alternatively, flexible materials can also be added in strategic locations of a rigid FDM printed body created from a rigid material to introduce more flexibility[27].

A second limitation for device fabrication by FDM is that most materials are structural only. Several conductive Polylactic Acid (PLA) and Thermoplastic Polyurethane (TPU) filaments do exist. The filaments have been loaded with conductive sub-micron carbon particles and only exhibit low conductivity, often with multiple kilo-ohms of resistance. As they are generally quite stiff, they are unsuitable for creating stretchable conductors and, as such, they have mainly been used to create strain and capacitive sensors[28], [29]. However, due to way FDM structures are build, conductive features can be easily embedded inside of a FDM printed structural material (Figure 2.2 b).

While flexible conductive filaments are more suitable for wearables they are not without their issues, as jamming of the filament in the nozzle is common. A workaround is to create filaments on demand by extruding pellets through a heated nozzle[30]. However, as this requires specialised equipment, creating carbon analogue reinforced flexible filaments has been preferred by researchers.

They key strength of FDM printing remains that it is a powerful option for multimaterial printing as materials are "glued" together by their shared thermoplasticity[31], even if compounding them with conductive particles makes this adhesion weaker. This can be partially circumvented by using multiple filaments created from the same base polymer. By using conductive and non-conductive filaments, multi-material flexible stacks have been printed which were exploited for capacitive and [32] and strain[33]–[35] sensing.

A last key challenge towards producing FDM printed electronics is that FDM printed materials are difficult to combine with other 3D printing techniques due to the high surface roughness of FDM printed parts. The main difficulty lies in printing features with smaller geometries

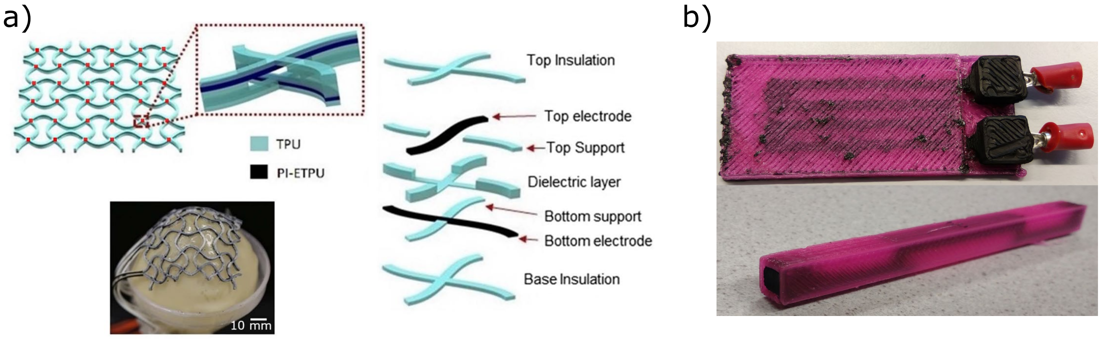

Figure 2.2 – An overview of materials and devices printed using Fused Deposition Modelling (FDM). **a**) Fully FDM printed multimaterial stack with TPU dielectric and conductive TPU material[26]. **b**) Incorporation of a carbon-black TPU based filament inside of a FDM printed TPU body[28].

on top of FDM printed surfaces. To tackle this, methods have been explored to reduce the roughness trough chemical polishing with acetone vapour[36], or by surface remelting[37], [38]. Further planarisation techniques such as milling, plasma etching, hot pressing, or spray coating[39], [40] have also been investigated. The latter can also be used to introduce thin functional layers.

2.1.2 Direct Ink Writing

A more flexible 3D printing technique towards depositing a large range of materials is called Direct Ink Writing (DIW). In this technique inks and pastes are pushed through a small orifice, often called the nozzle, by means of one of several types of extrusion mechanism. The extrusion can take place either through a hydraulic or pneumatic pressure difference, or by means of a screwing mechanism[1]. The material is deposited on top of either a previously printed material or a substrate by means of a conical tip or a needle, often referred to as the dispensing tip. By choice of this tip, the printing parameters, printing distance or material composition, and the dimensions of the printed material can be finely controlled. The complexity of what can be printed is further controlled by the degrees of freedom of the printer. Using a 5 axis printer, complex features such as the fully 3D printed soft heart valve shown in Figure 2.3 a can be produced[41].

Unlike FDM printing, in which only thermoplastics can be printed, a much larger range of materials can be be printed using DIW. Polymer precursors have been developed to DIW print different types of polymers including silicones[42], [43], acrylates[44], polyurethanes[45], vinyls[46], hydrogels[47], [48], or a composite of these[49], [50]. Depending on the ink formulation, the processed materials can be also be tailored to allow for specific material properties.

However, one key requirement for DIW printable inks is that they need to be shear thinning[51]. This behaviour leads materials to only deform under a shear stress, allowing the material to retain its shape for some time after deposition. Ideal DIW materials should have a quick recovery phase where they return to a solid form soon after deposition[52], which is commonly referred to as viscoelastic behaviour. To achieve this, the materials need an elastic or storage modulus ($G^{'}$) which The is larger than its loss modulus ($G^{''}$) when not sheared ($G^{'} > G^{''}$). The material will then start to flow at a sufficiently high shear stress where $G^{'}$ and $G^{''}$ cross over which is known as the yield point[53]. The relation between the two is the loss factor and is expressed as

$$\tan\delta = \frac{G^{''}}{G^{'}}, \tag{2.1}$$

where values of $\delta = 0°$ and $\delta = 90°$ equate ideally elastic and viscous behaviours, respectively[54].

As such, rheological modification by means of additives is a standard step in DIW ink development and can be used to finely tune the material behaviour. Inks are commonly reinforced using silica or other metal oxides to achieve the necessary viscoelastic behaviour[51], [55]. However, reinforcement by renewable materials is also possible, with natural fibers such as nanocellulose[56]. Furthermore, due to shearing action during printing, reinforcing particles with a high length-to-diameter ratio (aspect ratio) such as nanocellulose will be aligned and introduce anisotropic material properties[57]. However, precise tuning is not always necessary. A way to circumvent excessive materials engineering is to solidify the inks as rapidly as possible after deposition such as by UV[46] or laser[58].

To create complex, soft, and completely 3D printed wearables a combination of both structural and conductive materials are needed. Silicone is the material of choice for soft structural components as it is stable, non-toxic, and biocompatible[59]. Furthermore, its stiffness can easily be tuned to make it more or less stretchable[42]. Silicone inks have already been demonstrated for the use in free-standing structures 3D printed structures by fine-tuning their material composition[60]. An additional benefit of this material is that both bulk silicone and its surface can be chemically modified[61] and even reinforced with conductive particles to create DIW printable inks that can be used to print stretchable electronics (Figure 2.3 b)[43], [62]. Off the shelve DIW printable silicones, which contain all necessary components and which can easily be tuned rheologically, are rare but are slowly becoming more available[63].

However, complex multimaterial devices can only be created if both conductive and structural DIW printable materials are readily available. Often these materials are specifically synthesised based on the requirements and are not universally deployable. While much focus has been put on creating structural inks, a key challenge in creating entirely printed systems remains the development of highly stretchable composites with low electrical resistance[43]. Materials systems have, so far, been developed with high stretchability but low electrical conductivity, or vice versa.

The most popular materials for creating conductive features are carbon based due to carbon being relatively inexpensive and having many analogues with different properties[64]. Amongst these are carbon black, graphene, and carbon nanotubes[65]–[67]. Each type of particles results in different material behaviour depending on the loading and aspect ratio of the reinforcing material within composite materials[68]. While conductive, their resistance values are relatively high comparatively to metals[69], making them a poor choice for conductors. Highly stretchable carbon based electronics have been previously demonstrated for strain sensing without using printing techniques[70]. However, so far no DIW printable inks with similar performance have been developed. A lot of research has gone into the development of carbon based DIW printable ink suitable for the printing of static structures[71]. While some might exhibit some stretchability, carbon compounding introduces stiffness and, depending on the polymer matrix, the resulting composites can break easily under low amounts of strain (<2%) [72]. The most effective usage for DIW printable carbon based inks remains the printing of stretchable strain sensors[73] or contact pads[74].

Alternatively, silver has been a popular material for conductive DIW ink development as it has many advantages. Among these are its higher conductivity compared to other metals, insensitivity to moisture, and corrosion resistance[69]. Silver comes in many shapes and inks have been formulated with either silver nanoparticles, flakes, nanowires, or combinations of these[69], [75]. These inks are commonly designed for other printing techniques, such as screen printing, but if the viscosity is sufficiently high they can also be DIW printed[76]. Figure 2.3 c shows an example of a silver feature being printed by DIW using an ink for screen printing.

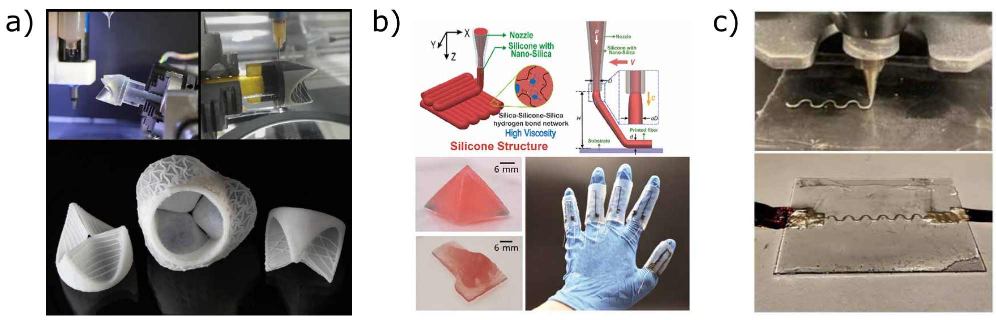

Figure 2.3 – An overview of devices and electronics printed using Direct Ink Writing (DIW). **a**) DIW printed heart valve printed through a 5-axis printer[41]. **b**) 3D printing of silicones and their integration into a simple glove[43]. **c**) DIW printing of a silver feature[76].

The main drawbacks of using silver based inks, however, are the high material cost, difficulty in synthesis, and the possibility for it to oxidize[20], [69]. Due to the latter, some form of protection is required to prevent a reduction in conductivity over time. Furthermore, silver is quite stiff in nature which means that it also easily cracks under deformation, which limits to what extent silver based inks can be applied in stretchable electronics. While this can also be exploited to some degree by strategic cracking[77], the best solution to achieve highly conductive stretchable films by DIW printing is by compounding it into a polymer matrix. Even so, high amounts of silver are needed to achieve percolation and the maximum material strain is significantly lowered by compounding[78].

In order to create stable DIW printable inks, they require the addition of binders and cross-linking agents which are non-conductive and affect the material properties of any conductive ink further[55]. Final ink formulation thus become a well controlled mixture of varying and balanced components. However, material compatibility problems do not only originate from within the ink formulation itself. Joining multiple DIW inks with mismatching materials properties into a printed device can result in a lack of adhesion which can lead to mechanical failure[79]. To address this issue, chemical modification to link multiple DIW printable materials that are normally not compatible, such as elastomers and hydrogels, have been explored but only in limited scope[80].

One method to circumvent these issues and achieve stretchable conductive devices by DIW is by the printing of liquid metals, such as Eutectic Gallium-Indium (EGaIn)[81], [82]. Materials such as these remain liquid and can easily deform without cracking or breaking. EGaIn, especially, can be easily encapsulated using silicone and will remain stable after deposition as an oxide skin forms immediately in contact with air[81], [83]. While EGaIn is normally quite safe, it has been shown to be able to causes damage to human cells when mechanically agitated[84], making it a sub-optimal choice for wearables.

In brief, the choice of DIW printable inks is currently very limited, especially for conductive inks. A wide range of screen printing inks exist which can often also be used for DIW printing, as both printing methods require inks to be shear thinning and have a yield point[85]. Unfortunately, other than a few exceptions, many screen printing inks do not exhibit ideal DIW printing behaviours and are generally not developed for printing flexible and stretchable features.

2.1.3 Photopolymerisation Techniques

Vat photo-polymerisation, also sometimes known as resin 3D printing, is a popular technique for the creation of complex 3D printed structures. In this technique a vat is filled with a photocureable polymer precursor and selectively exposed in order to initiate local curing.

The remaining liquid is kept uncured by tuning the activation energy, or the energy required to start photo-polymerisation, to be above a certain level[86]. This means that the liquids have to be specifically developed for this technique. However, in this way the liquid supports the already printed structure and complex geometries can be generated that are not easy to produce using other layer by layer techniques.

The two most popular of these techniques are Stereolithography (SLA) and Digital Light Printing (DLP)[1]. In both techniques printed objects are cured per layer by photonic activation, before the stage is moved up to introduce new liquid for the next layer. In this way the 3D printed object is being "pulled" out of the liquid vat. Both techniques utilise a similar fabrication strategy, and as such, the main difference lies in how the photonic activation takes place. In SLA the resin is cured by a scanning laser that locally cures the exposed area. In contrast, DLP uses a projector to project a pixelated map onto the precursor to cure any exposed pixels while leaving the rest of the resin uncured.

Using this technique, a variety of materials can be printed, including silicones[59]. However, one key challenge for the fabrication of wearables is the printing of conductive composites using resin 3D printing. Rigid conductive composites (Figure 2.4 a) have been printed which could be used as compliant mechanisms[87], [88]. DLP printable polymer can be made conductive with Carbon Nanotubes (CNT), but have so far only been demonstrated with loadings below 0.1 wt% and only in rigid acrylate[89]. Soft 3D printed electronics have been demonstrated by DLP printing conductive hydrogels[90] or coating the finished object using a solution of silver nanoparticles (Figure 2.4 b)[91], resulting in devices with short lifetimes. Moreover, wearables are not easy to fabricate using this approach because multimaterial printing is made difficult due to restrictions imposed by the printing technique itself[23].

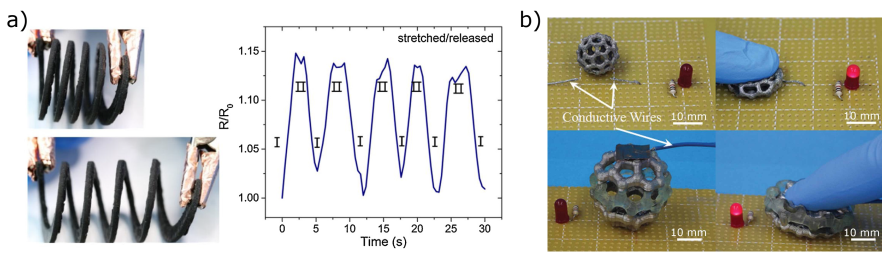

Figure 2.4 – Examples of conductive objects printed by means of resin 3D printing. **a**) 3D printed conductive compliant spring structure[87]. **b**) 3D printed soft and conductive buckyball[91].

To circumvent this, a solution is offered by a technique called polyjetting. In this technique micron sized droplets of UV curable polymers are dispensed by an inkjet printhead and immediately cured by an attached UV lamp. In this way, very thin layers of multiple UV cureable polymers can be dispensed to achieve multimaterial features[92]. However, the liquids that can be printed in processes such as these require very low viscosity values (< 40 cP)[93].

Even though these techniques are not ideal for 3D printing wearables, the advances in vat photo-polymerisation techniques are still very promising. Tomographic additive manufacturing is an upcoming technique in which 2D slices of a 3D object are projected onto a rotating liquid vat, resulting in a 3D copy of the object within seconds with a high resolution[94]. At this time, the number of materials that can be used in this process is still limited and multimaterial printing has not been explored.

2.1.4 Summary of 3D printing techniques

The previous sections gave an overview of the strengths, weaknesses, and advances made for the most popular printing techniques which can be used to fabricate soft wearables.

At this time, no single printing technique is currently suitable to produce a smart wearable by itself. The best strategy is to combine multiple techniques, also known as hybrid 3D printing[10], [11], to create highly integrated and multi-functional 3D printed objects. However, this can be challenging as materials and printing techniques are often not inter-compatible without serious modification. Combinations of certain materials are prevented by either their inter-incompatibility or by the inability to process them together and use them in devices. More often than not, materials are not compatible with one another in terms of thermoplasticity, viscoelasticity, topography, and adhesion[95].

However, new printing techniques are continuously being developed to be able to print novel material formulations. One example of such a novel technique is high viscosity drop on demand jetting[96], which is a printing technique that can print inks which are too viscous for standard inkjet printing. In this case study they showed the ability to print conductive silicones for functional sensors. Furthermore, an additional benefit of developing new techniques is that they could enable smaller resolutions and more precise printing.

2.2 3D printed sensors for mechanical motion sensing

The foremost requirement for realising smart wearables for motion monitoring is that they come with sensors, which are required to capture any data. To avoid having to introduce a large number of discrete components such as microcontrollers and batteries, the sensors should ideally be as simple as possible. Therefore the ideal sensors are low-powered or even self-powering. As such, a lot of research has already been done on these types of sensors which were not completely 3D printed[97], [98].

In this section an overview is provided of what mechanical sensing mechanisms are suitable to achieve these sensors. This is followed by a number of examples of fully 3D printed mechanical sensors. Lastly, a short overview of some of the challenges towards 3D printing soft and flexible smart wearables is provided.

2.2.1 Mechanical sensing

Mechanical sensing differs from other sensing mechanisms in that a mechanical deformation results in a change of signal. While many detection mechanisms exist, for wearable applications electromechanical sensors are especially of interest due to their high sensitivity and low power consumption[99].

In the case of electromechanical sensors, their implementation can be divided into two categories. Those which require external power sources and those which are self-powered. Within the first category of sensing mechanisms piezoresistive and capacitive sensors are considered, while in the latter category are piezoelectric and triboelectric sensors[100], [101].

Piezoresistive sensors especially have proven very popular over the years. Especially since they are often cost effective to manufacture, require simple electronics to readout, and are insensitive to environmental noise. Their working principle relies on the change of electrical resistance (R) expressed in Ohm (Ω) at a constant externally supplied voltage (V). Depending on the sensors design, when a sensing element deforms this either increases or decreases the resistance. These behaviours are called positive and negative piezoresistivity, respectively[102]. The working principles of several sensors are shown in Figure 2.5 . The performance of piezoresistive strain sensors is generally expressed using what is called the gauge factor (GF), which gives an indication of the change in resistance of the sensor at a certain elastic deformation. The gauge factor is defined as

$$GF = \frac{\Delta R}{R_0}\frac{1}{\varepsilon}, \tag{2.2}$$

with ε being the engineering strain, and R_0 and ΔR being the resistance at rest and after deformation, respectively. For an ideal sensor this relation is linear.

Capacitive sensors, on the other hand, make use of changes in electric fields. A capacitor stores electrical energy in its electric field, between two or more conductive features separated by a dielectric medium, with its density depending on the applied voltage supplied by a power source. The closer the plates are the stronger the electric field becomes for a given voltage, and the higher the energy density becomes. For these sensors their measurement capacity are indicated by the capacitance (C), expressed with the unit Farad (F). The capacitance, however, is the ratio of electric charge (Q) stored in the conductor with respect to the used voltage difference (V).

Piezoelectric sensors are of interest because they are the most geometrically simple self-powered sensors. They function by turning a mechanical deformation into a charge difference due to the material properties itself. As such, the signal is often expressed in the charge (I) that can be generated. Unfortunately few soft piezoelectric polymers are available with the most extensively studied amongst them being Polyvinylidene Difluoride (PVDF)[103]. Inks and precursors to 3D print these types of polymers are not readily available which limits their applicability to soft wearables at this time.

Currently, triboelectric sensors are the more promising self-powered sensors. They function by having two dielectric materials attached to conductors, or a dielectric material and a conductor, that build up triboelectric charges when they interact. The charge accumulation is caused by the materials having different charge affinities (or electron affinities) that lead to a difference in charge densities on the surfaces. When the materials separate or approach one another a potential difference is generated that drives a charge, which can be either harvested as energy or used as a signal[101]. This function can either be performed by touch and separation (vertical contact mode) or by "rubbing" of the materials (lateral sliding mode).

Schematic representations of all the treated sensing mechanisms are discussed in Figure 2.5.

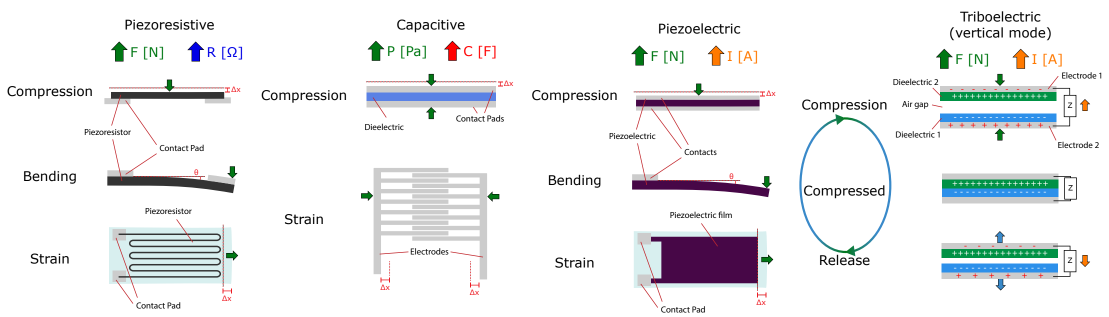

Figure 2.5 – An overview of the most common transduction mechanisms used for electromechanical sensors. Piezoresistive compression, bending, and strain sensing. Capacitive compression and strain sensing. Piezoelectric compression, bending, and strain sensing. Operation of a triboelectric sensor in vertical mode.

2.2.2 3D printed mechanical sensors and devices

As explored in the previous sections, due to the difficulties in material synthesis, processing, material incompatibility, and device fabrication few truly 3D printed sensors have been produced. Many researcher still prefer to use 3D printing in combination with more established techniques[104].

In this section an overview is given of 3D printed sensors which either make extensive use of printing or exploit 3D printing techniques to achieve novel fabrication workflows, sensing mechanisms, or geometries and patterns. A focus is placed on sensors which could be integrated into a wearable and made suitable for monitoring human motions. Within this category of motions the detection of normal pressures, shear forces, and angular deformations are considered. For these sensors it is important that they are sufficiently sensitive to avoid noisy data capture. Furthermore, they should have low hysteresis to avoid errors in dynamics measurements, have a repeatable response, and should be able to measure forces of intensities expected in human motions. Depending on the part of the body, this can range from a few pascal up to hundreds of kilopascal[17]. A table of all reviewed sensors and their performance is shown in Section 2.2.2 at the end of this subsection.

Piezoresistive strain sensors

As FDM printing was one of the first 3D printing techniques on the market, and is still one of the least expensive ones, many research groups have focused on creating custom FDM filaments to use them to produce piezoresistive strain sensors. By compositing TPU with carbon compounds, flexible and conductive filaments were created and used to FDM print low-cost strain sensors with varying performance[105]. Sensors with up to 100% stretchability, achieved by shape engineering, were reported but at the cost of low sensitivity (GF=0.16)[35]. Vice versa sensors with low stretchability (<2%) but gauge factors up to 1340 for strains up to 0.5% have been reported[106]. Christ et al. showed that the GF can be easily tuned by compounding the TPU material with different loads of multiwall carbon nanotubes (MW-CNT). Higher MW-CNT loads increase sensor performance, resulting in an increase of the GF from 8.6 at 5 wt% MW-CNT loading to 18.2 at 3 wt% MW-CNT loading, but at the cost of reduced stretchability due to the material stiffening.

While often strain sensors with traditional designs have been printed, Kim et al.[29] showed that a novel multi-axial strain could easily be produced by FDM printing as shown in Figure 2.6 a. To achieve this device, they exploited the capability of FDM printing to fabricate normal strain elements along multiple axis. The strain gauges had a sensitivity of 0.55 kΩ/N and a gauge factor of 2.29. While this is a reasonable performance, only a low load of up to 2.11 N was applied.

Even if FDM printed sensors are often used for normal force and strain detection they are not limited to this function. A 3D fingertip sensor developed by Wolterink et al.[107], [108] showed the capability of measuring both normal forces up to 10 N and shear forces up to 5 N under several different angles by differential measurement. This sensor, as shown in Figure 2.6 b, was found to have a gauge factor of less than 15 and a stretchability of 35%.

Very few fully DIW printed strain sensors exist. Instead, much research has gone towards using DIW printing to flexibly and rapidly print the functional parts while fabricating the rest using conventional techniques, such as by casting the silicone body on top of a 3D printed strain gauge[109], [110]. One such approach towards sensor fabrication was explored by Muth et al.[73] where conductive carbon grease was printed inside of a silicone medium that was cured after printing. In this way they fabricated simple tensile strain sensors for a simple glove with a gauge factor of 3.2-4.4. However, the sensor performance was strongly influenced by the strain rate.

While generally DIW printed layers have smooth surfaces, by playing with the line to line spacing rougher surfaces can be generated which can add functionality. Yuan et al.[111] demonstrated a device with piezoresisitive strain sensors integrated underneath a structured DIW printed cell well. Heart cells were grown inside of valleys formed between spaced DIW printed lines and their contraction recorded using the embedded strain sensors. This CB-TPU based sensor had a gauge factor of 2.42-2.6 and a reasonable hysteresis of 15%, which was sufficient to reliably measure tensile stresses of up to 15 kPa caused by cell contraction.

DIW printing can also be used to produce sensors with three dimensional overhang by printing a sacrificial structure from water soluble ink. Guo et al.[78] used this approach to produce the fully DIW printed silicone tactile sensor shown in Figure 2.6 c. Dragon Skin 10 RTV silicone was reinforced with silver flakes to create a sinter free ink that was used to print the functional parts of the piezoresistive tactile sensor. The sensor had a high sensitivity of 19.3%/kPa which resulted in a gauge factor of 180, and was sufficiently sensitive to measure the absolute difference in heart rate of a person before and after exercises. However, the response of the sensor was highly actuation dependent as the hysteresis could reach up to 82% at an actuation speed of 1 Hz and pressure of 200 kPa.

Peng et al.[112] demonstrated a hybrid DIW and DLP printing approach to produce a fully 3D printed piezoresistive strain sensor for low tensile strains (<2%). The device, with a high sensitivity (GF = 251), is shown in Figure 2.6 d. Dynamic cycling was only performed for strains below 1% giving no indication of the long-term stability of the device.

Since grippers are a hot topic within the field of soft robotics, many researcher have tried to exploit the benefits of 3D printing in their fabrication. Three dimensionally structured grippers have been completely 3D printed with integrated strain sensors, by means of a PolyJet printing, to measure the bending of the fingers of these devices[113]. The integrated sensors were printed from commercially available TangoBlackPlus FLX980 which possessed a gauge factor of around 40, hysteresis of 28%, and a maximum strain of 0.2%. This shows that sensors can be easily integrated into a device, but further material optimisation is required to create reliable sensors. The printed material was only reinforced by <0.1 wt% carbon black and is not necessarily designed for sensor fabrication.

Piezoresistive pressure sensors

Truby et al.[12] expanded on the work of Muth et al. by 3D printing shear thinning ionogels inside of a silicone medium to fabricate the functional parts of an air pressure powered actuator with DIW printed 3D features to allow for inflation and gripper contact pressures sensing, besides curvature strain sensing. These sensors were printed from an EMIM-ES ionogel with a linear sensitivity of 11.7%/kPa up to a maximum load of 152 kPa and with negligible hysteresis. As the body was created from standard cast silicone (EcoFlex 00-10), they showed that the functional material is by far the most influential on sensor performance. By combining three of these printed "fingers" together they fabricated a gripper which could identify several motions and objects (Figure 2.6 e).

True 3D structuring is hard to achieve outside of 3D printing, but through DIW printing this can be easily achieved as was demonstrated by Wang et al.[114]. In their work they created a fully DIW printed piezoresistive normal pressure sensor with a PDMS substrate, Ag-TPU electrodes, and CB-TPU piezoresistive element that has a geometry which is insensitive to small deformation strains such as those caused by bending. The piezoresistive element was printed with a hollow architecture, and further material porosity was introduced using sacrificial salt to achieve a slight 2.5% signal increase. The normal pressures response was exponentially declining and could be measured in different regimes leading to sensitivity values of 5.54 %/kPa below 10 kPa and which dropped down to 0.0048 %/kPa above 100 kPa of pressure.

In the work of Emon et al.[115] a multimaterial capacitive touch device was printed by DIW. The device was fabricated with a photopolymer substrate, CNT composited polymer electrodes and an ionic liquid pressure sensitive dielectric. All materials were reinforced with fumed silica to make them printable and the stack was cured in one shot by a combination of UV and thermal curing. This resulted in a fully printed stack with four "taxels" which could be individually operated to make a simple touchpad as shown in Figure 2.6 f.

Capacitive Normal Pressure Sensors

One advantage of capacitive normal pressure sensors is that they do not need to be entirely flexible nor elastic. FDM printed capacitive sensors have been developed with a printed flexible TPU dielectric and rigid electrode plates printed from carbon compounded Polylactic acid (PLA). Sensors printed using this approach have been demonstrated with sensitivity values of 9.1 fF/N[27], and 15.9 fF/N (0.71%/N)[116]. A similar device printed from TPU filaments only showed a lower sensitivity of 0.187%/N[32]. However, none of these devices were shown to be suitable for force detection above 35 N.

Using FDM, more freeform devices can be created. Loh et al.[26] designed a multi-layer flexible capacitive "net" to create a capacitive sensor with a sensitivity of 0.63%/N. Using the auxetic design, the sensor could be stretched up to 20% without the deformation having any effect on the sensor performance. By adding air gaps in the design, the sensitivity was increased significantly up to 5.21%/N.

So far, DIW printing has not been fully exploited to create capacitive sensors, as mostly only parts of sensors have been DIW printed. Examples of these include DIW printed silver nanowire ink electrodes[117] and PDMS dielectric layers[118]. One example being a fully printed capacitive sensor combining a DIW printed dielectric with inkjet printed silver electrodes[119]. At this time, Valentine et al.[120] produced one of the few only fully DIW printed capacitive normal pressure sensor. This sensor was created from custom TPU inks, one for the structural parts and another TPU ink compounded with silver flakes for the conductive features. By creating a DIW printed capacitive stack using these materials they produced a sensor with a linear sensitivity of 0.0853%/MPa and a maximum sensing pressure of 3 MPa for plantar pressure sensing.

Self powered sensors

To make sensors completely autonomous they ideally would be self-powered. Popular approaches to create self-powered sensors have been using either piezoelectric or triboelectric mechanism. However, many of the examples found in literature are not intrinsically made to be sensors, but are actually designed as energy harvesters, for which the power generation per surface area is reported.

Currently only a handful of printed piezoelectric and triboelectric devices have been demonstrated. The team of Zhou et al.[16] create a fully DIW printed normal pressure sensor by embedding Barium Titanate (BaTiO3) particles inside of P(VDF-TrFe) to make a DIW printable piezoelectric layer with silver flake reinforced P(VDF-TrFe) being used to print the electrodes. In this fashion a highly stretchable sensor was constructed that could detect normal forces up to 60 N. Furthermore, the device could also be used as a plantar pressure energy harvester during human gait with a power generation of up to 1.4 μW^2/cm. The same team used a hybrid DLP and DIW printing approach to create a nanogenerator, with a DLP printed BaTiO3 reinforced piezoelectric acrylate layer and DIW printed silver electrodes. Using this hybrid printing approach a harvester with a much lower power generation of only 57 nW^2/cm was realised.

Triboelectric bending and normal sensors have been fabricated by printing their parts by

PolyJet and assembling them manually. Using this approach a touch sensor has been constructed[121] with a root mean square voltage of 164.2 V. PolyJetting was also used to print a curvature sensor for a robotic finger[122]. A fully FDM printed triboelectric nanogenerator was developed by Qiao et al.[123] with three dimensional structures in order to increase its surface area, leading to maximum power density of 25.7$\mu W^2/cm$.

Zheng et al.[124] demonstrated that a soft silicone ink composited with Polytetrafluoroethylene (PTFE), has increased triboelectric properties. They used this composite to DIW print a triboelectric layer for a simple vertical contact sensor. A more complex soft triboelectric sensor was demonstrated by Chen et al.[125] which was DIW printed from UV curable resins. The device, however, was not entirely 3D printed as a conductive hydrogel was prepared and cured inside one of the 3D printed parts to create the counter electrode. Even so, the resulting device, shown in Figure 2.6 g, had a maximum voltage of 62 V and when used as energy harvester a power density of 10.98 W/cm^3. The device was soft and deformable, and could easily be integrated into a wearable as self powered sensor.

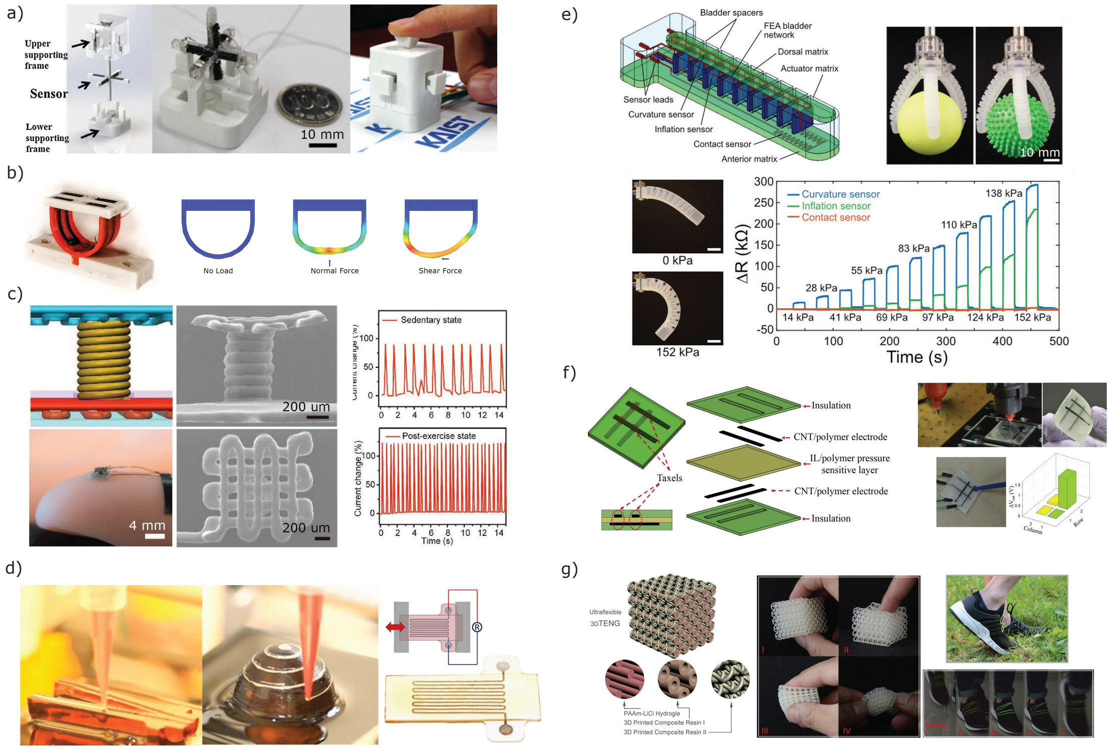

Figure 2.6 – Several examples of 3D printed mechanical sensors. **a**) FDM printed piezoresistive multiaxial strain sensor[29]. **b**) FDM printed fingertip sensor with normal and shear force sensing[108]. **c**) Freestanding DIW printed tactile sensor[78]. **d**) Hybrid DLP and DIW printed electronics and sensors[112]. **e**) Partially DIW printed pneumatic actuator with 3D structuring and motion recognition[12]. **f**) Fully DIW printed soft piezoresistive taxel[115]. **g**) Triboelectric nanogenerator (TENG) created partially by a DIW printing process[125].

Table 2.1 – Overview of sensors achieved using 3D printing methodology. Sensor performance was either retrieved or calculated from available data with - indicating a lack of data. MM and MA represent multi-modal and multi-axial sensors, respectively. Material shorthands include: CNT, carbon nanotubes; MW-CNT, multi-walled carbon nanotubes; CB, carbon black; Ag, silver; rGO, reduced graphene oxide; TPU, thermoplastic polyturethane.

Transduction	Motion(s)	MM/MA	Technique(s)	Material(s)	Functional Material(s)	GF	Performance	Hysteresis	Max. load	Max. strain	Source
Piezoresistive	Normal pressure	MA	FDM	TPU, CNT-TPU	MW-CNT	2.29	~0.55 kΩ/N	~20%	2.11 N	5.2% (flexural)	[29]
Piezoresistive	Flexural strain	-	FDM	NinjaFlex (TPU), PLA-TPU	Graphene	~0.16	-	-	-	8% (linear), 100% (non-linear)	[35]
Piezoresistive	Flexural/tensile strain	-	FDM	NinjaFlex (TPU), CNT-PLA-TPU	CNT (12 wt%)	20.6-1342	-	-	-	2%	[106]
Piezoresistive	Tensile strain	-	FDM	TPU-CNT	MW-CNT (3-5 wt%)	18.2-8.6	-	-	-	100%	[34]
Piezoresistive	Normal pressure, shear forces	MM	FDM	NinjaFlex (TPU), Palmiga PI-ETPU	CB	-	0.11 kΩ/N (0.79 %/N)	-	10 N (Normal) 5 N (Shear)	-	[107]
Piezoresistive	Normal pressure, shear forces	MM	FDM	NinjaFlex (TPU), Palmiga PI-ETPU	CB	< 15	-	-	10 N (Normal) 5 N (Shear)	35%	[108]
Piezoresistive	Normal pressure, bending	-	DIW + Casting	PDMS-CNT	MW-CNT (1.6-2.2 wt%)	~2	0.625 Ω/kPa (0.125 %/kPa)	-	600 kPa	40%	[109]
Piezoresistive	Tensile strain	-	DIW + Casting	([BMIM]BF4), PDMS	rGO	0.54-2.41	-	<3.5%	-	300%	[110]
Piezoresistive	Tensile strain	-	DIW + Casting	PDMS	Conductive Carbon Grease	3.2-4.4	~2.5-4 kΩ/%	~23.4%	-	450%	[73]
Piezoresistive	Pressures, Bending	MM	DIW + Casting	PDMS	EMIM-ES ionogel	-	~23.33 Ω/Pa (11.67 %/kPa)	-	152 kPa	-	[12]
Piezoresistive	Tensile strain	-	PolyJet	TangoBlackPlus	CB (<0.1 wt%)	~40	-	~28%	-	0.2%	[113]
Piezoresistive	Normal pressure	MM	PolyJet	TangoBlackPlus	CB (<0.1 wt%)	-	1.8 %/kPa	~12.5%	5 kPa	0.125%	[113]
Piezoresistive	Normal pressure	-	DIW	SiO2-TangoPlus, EMIBF4-TangoPlus, CNT-TangoPlus	MW-CNT (5 wt%)	-	~12.45 %/N	30%	7.8 N / 1 MPa	38%	[115]
Piezoresistive	Normal pressure	-	DIW	PDMS	Ag	180	~19.3 %/kPa	10-82%	500 kPa	200%	[78]
Piezoresistive	Tactile sensor	-	DIW	Sylgard 184, CB-TPU, Ag-TPU	CB (20 wt%) Ag (85 wt%)	-	5.54 %/kPa (<10 kiloPa), 0.123 %/kPa (10-100 kiloPa), 0.0048 %/kPa (0.1-0.8 MPa)	-	800 kPa	50%	[114]
Piezoresistive	Normal pressure	-	DIW	TPU, Ag-TPU	Ag Flakes (36 vol%)	13.3	-	~20%	-	15%	[120]
Piezoresistive	Tensile strain	-	DIW	TPU, CB-TPU	CB	2.42-2.6	-	~15%	15 kPa	0.1%	[111]
Piezoresistive	Tensile strain	-	DLP + DIW	Acrylate, DuPont ME603	Ag (50-53 wt%)	251	-	-	-	2.1%	[112]
Capacitive	Normal pressure	-	DIW	TPU, Ag-TPU	Ag Flakes (36 vol%)	-	0.0853 %/MPa	-	3 MPa	-	[120]
Capacitive	Normal pressure	-	FDM	NinjaFlex (TPU), PETG, ProtoPasta (PLA)	CB	-	9.1 fF/N	~12.3%	10 N	-	[27]
Capacitive	Normal pressure	-	FDM	NinjaFlex (TPU), Palmiga PI-ETPU	CB	-	0.63 %/N (Solid), 5.21 %/N (Air gap)	-	4.8 N	21.6%	[26]
Capacitive	Normal pressure	-	FDM	NinjaFlex (TPU), Palmiga PI-ETPU	CB	-	0.187 %/N	-	10 N	-	[32]
Capacitive	Normal pressure	-	FDM	eTPU-95A, ProtoPasta (PLA)	CB	-	~15.9 fF/N (0.71 %/N)	-	31.4 N	-	[116]

2.2.3 Full system printing and discrete component integration

As discussed in the previous section, a number of standalone sensors have been fabricated using 3D printing. However, to extend the 3D printing from single sensors to more complex wearable systems, integration and embedding of sensors and discrete component, such as batteries and microcontrollers, is required. So far, few wearable system have been entirely 3D printed. The work of Lin et al.[126] showed that hybrid printing could be used to fabricate a stretchable wireless electrocardiogram (ECG) measurement system. This device consisted of multiple DIW printed layers of silicone and conductive elements. Solid discrete electrical components were added by means of Pick and Place (PnP), which is an industrial technique that is used in the electronics industry for the placement of Surface Mounted Devices (SMD) onto Printed Circuit Boards (PCB). Although this device had no printed sensors, it demonstrated that rigid components could be integrated well within stretchable materials. In order to integrate the discrete electronics, they have to be placed during an interruption of the printing of the body either manually or by PnP[127], [128].

The PnP technique can be extended towards FDM based electronics. However, to realise this conductive functional layers or traces are required to link different electronic components together into a monolithic system. To integrate such conductive traces, the FDM printed bodies need to be combined with other electrically conductive materials such as metal based inks and pastes. Unfortunately, this makes them are hard to combine with FDM materials, since printable metal pastes require processing temperatures which can deform or damage the thermosensitive FDM printed material[13], [129]. This makes it not possible to use conventional curing methods such as curing the pastes in an oven. Alternatively, high throughput processing techniques such as laser sintering[127] or photonic sintering[130] have been explored to circumvent exposure of the FDM material to high temperatures for an extended duration.

A simpler strategy to avoid high temperature processing, when using FDM printed materials, is to intentionally leave behind voids or gaps and refill them with liquid metal to achieve conductors[25], sensing features[131], or even antennae[132]. Alternative methods to introduce these, such as feeding metal wiring directly into the liquid thermoplastic to create embedded cage like metal structures have also been explored to produce simple 3D printed capacitive sensors with discrete components[133], [134]

In contrast, DIW printed structural materials do not generally suffer from these thermal restrictions. Valentine et al.[120] demonstrated the integration of fully DIW printed piezoresistive strain and capacitive pressure sensors with discrete electronic components added by pick and place. This approach was used to fully additively manufacture a strain sensor, including microcontroller, and an insole demonstrator for the detection of plantar pressure as shown in Figure 2.6 g.

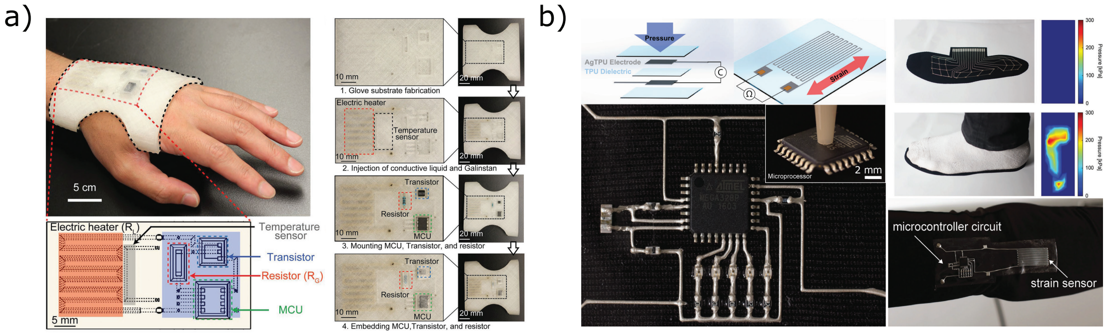

Figure 2.7 – Examples of fully printed devices with integrated components. **a**) FDM printed system with liquid metal sensors and discrete components[25]. **b**) Fully DIW printed sensors and systems with discrete components added by pick and place[120].

2.2.4 Achieving stretchable systems

As touched upon in the previous sections, creating fully 3D printed stretchable devices that provide smart functionality is a big challenge. A device that is required to be mounted on the body will undergo certain deformations that it will need to be able to tolerate. For example, skin around the joints of the leg can stretch by as much as 55% strain during walking[135]. Therefore, if to be able to design a device that can capture motion data from this body part both the structural and functional materials need to be able to withstand these strains. Especially if fatigue is to be prevented. Here the problem often lies in the fact that these materials are entirely different, they also have different material behaviours and properties. Viscoelasticity, hysteresis and material failure can all be the result of a material mismatch between two or multiple materials[95]. One example would be the integration of metal electrodes in a polymer body. As the former is much more rigid, it will not deform as easily as the soft material which can lead to cracking of the metal. Therefore, strategies need to be employed to add stretchability beyond the capabilities of the normal material.

As discussed in previous sections, compounding functional elements such as carbon analogues[55] or metals[136] into a 3D printable polymer matrix is a popular approach to create highly stretchable materials (>100% strain) while retaining good conductivity. However, this approach requires significant materials engineering by means of adding binders and crosslinkers which can negatively impact the material behaviour[55]. As such, an alternative and popular approach in the domain of stretchable electronics has been the fabrication of compliant features through designing deformable geometries.

Using deformable geometries to add stretchability into devices is done by adding features to the device such that they experience lower strains. This can be done by either adding compliance to the body or patterning the conductive features. Both methods rely on reducing the strain in the rigid parts caused by deformation of the surrounding material. A popular patterning approach to reduce strain on the metallic parts is by introducing serpentine features[137], [138], an example of which is shown in Figure 2.8 a. By designing conductive traces such that they "unfold" when strained linearly the material strain is significantly reduced. In this way metallic conductors can even deform in three dimensions. With the ease that digital manufacturing allows for making complex patterns, 3D printing is an attractive option to create conductive serpentine tracks[139].

An alternative strategy is to add strategic cuts, also called kirigami, in the body of the device[16], [140] as shown in Figure 2.8 b. Cuts are made to the body which that results in the gaps when the material is deformed linearly. The resulting deformation which can either be in-plane or out-of-plane results in a strain release. With the increased compliancy the material is able to stretch much more than the strain-stress relation of the material would normally allow for. Patterned materials can of course be easily fabricated using 3D printing[141].

Lastly, kirigami can also be combined with serpentine tracks to allow for extremely stretchable devices [142]. However, both kirigami and serpentine structures take up a lot of space which reduces how compact and feature dense devices can be made. Furthermore, complex devices often require multiple materials with different behaviours which can lead to significant materials integration challenges. This is especially true when the materials have mismatching strain rates. The differences can easily lead to fatigue of the devices and for them to become worn down[95] making sustained or long-term use not possible. So far no entirely 3D printed devices have been demonstrated making use of this approach.

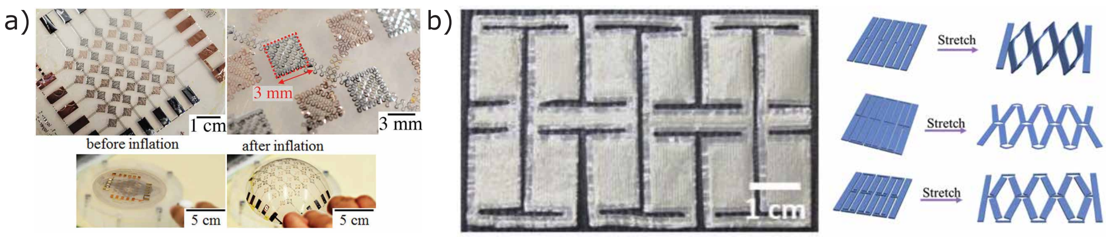

Figure 2.8 – Two general methods for adding additional stretchability to a device. Through means of **a**) serpentine patterning[138] or by **b**) adding strategic cuts (kirigami)[16]

2.3 Summary and conclusions

In this chapter the current state of the art regarding 3D printing of devices has been addressed. The discussion was centered around the available techniques to 3D print mechanical sensors and integrated systems. Addressed were the materials that can be printed, what types of printing techniques exist, what strengths and shortcomings each printing technique has, and what has already been demonstrated on both fabrication and device level. Furthermore, an overview of the types of sensing mechanisms has been given with respect to mechanical sensing. Lastly, a number of examples of 3D printed mechanical sensors and devices with integrated sensors was given to show in what direction research has been taking place. What follows is a brief summary of what has been achieved and what are the remaining challenges in the field.

2.3.1 Status on 3D printed electromechanical sensors

While proven to be a popular research methods among many researchers, a lot of research on 3D printing of wearable electronic devices and sensors is still missing. No 3D printing technique has been developed that could be easily adopted for mass electronics manufacturing. However, 3D printing can already realistically be used for the fabrication of customisable and personalised wearable electronics in combination with digital manufacturing. The latter technique allows for rapid adjustments to be made to a design and tailor devices on a single person basis. Furthermore, the ability to rapidly change the design and 3D print them allows for the flexible production of devices for research and prototyping.

Currently, material systems often have to be developed specifically towards the device being designed even if gradually more universal materials are becoming available. Of course, this also depends on the target application. Some soft materials suited for 3D printing are already readily available. However, materials which are easily tunable, deformable, conductive, and wearable still require more research. Furthermore, as many devices require multiple materials, with some parts being structural and others functional, all necessary materials need to be compatible and integratable. Due to this missing link in the materials department, a lot of research has gone towards the development of universal material systems. As such, less research has been done on the actual fabrication of sensors and electronic devices through 3D printing. Therefore, the processing steps to achieve 3D printed electronics are not well established. Moreover, few tools to create entirely 3D printed electronics are available. Only few 3D printers are available in which all processing steps can be performed, with many researchers resorting to customising existing bioprinters.

Even so, several research groups did tackle the development of 3D printed sensors directly, either by exploiting a single technique or a combination of multiple techniques, the latter which is commonly referred to as hybrid printing. Most of the research has focused on the fabrication of FDM printed piezoresistive strain sensors including those which are multi-axial. These sensors are unfortunately very limited in their stretchability. Therefore, other techniques such as DIW are far more suited for the 3D printing of wearable sensors with a motion monitoring application in mind.

2.3.2 Open challenges and research approach on 3D printed sensors

Current examples of 3D printed sensors include those with piezoresistive, capacitive, piezoelectric, and triboelectric mechanisms to measure tensile strain, normal pressure, shear forces, and bending deformations with mixed results. One key lack of development especially has been that geometries such as truly 3D features have been rarely produced. 3D printing makes fabricating these kinds of features much easier compared to conventional microfabrication methods. As such, 3D printing could be exploited to enable the fabrication of sensors with novel sensing mechanisms and enable new uses for electromechanical sensors. However, to realise this vision, the following challenges remain

- Conductive 3D printable soft materials need to be developed for the 3D printing of sensing layers for wearables with low hysteresis and high performance, while being less restricted in how they can be integrated.
- Processes are missing to integrate materials from different 3D printing techniques with one another, limiting what kind of materials can be combined and what kind of devices can be constructed.
- Many electromechanical sensors found in literature have only been partially 3D printed, with fabrication of other elements not considered. Printing the entire sensor could improve the sensor fabrication throughput and allow for more complex three-dimensional features.
- Few sensors have been completely 3D printed and most are only designed to measure normal deformations. Novel sensors could be designed exclusively for 3D printing that can capture shear forces, bending deformations or twisting motions.
- Most strain sensors in literature currently make use of conventional strain gauge patterns. Using 3D printing new types of strain sensors could be developed that exploit three-dimensional structuring.

To tackle the material issues we worked together with the Complex Materials Laboratory at ETH Zurich and the Wood and Cellulose Laboratory at EMPA. In cooperation with their researchers we developed and evaluated structural and conductive silicone materials that could be integrated into a multi-sensor device to monitor human gait. We designed sensors and developed the 3D printing approaches and processing steps to completely 3D print both standalone sensors and integrated devices. A design is proposed for a three dimensionally-structured piezoresistive sensor that can measure shear forces of the foot.

Furthermore, an investigation of the usage of laser sintering to integrate DIW printable metal pastes into thermosensitive flexible FDM printed materials was performed. Using this approach the embedding of highly conductive films of only several μΩ cm into the FDM structural material is enabled. This allowed for the creation of fully 3D printed sensors from materials which are usually incompatible.

Lastly, a material system and methodology were developed to 3D print soft sensing structures with three-dimensionality. This approach was exploited to create a novel capacitive sensor type that was able to measure angular bending differences with significant sensitivity.

3 Fused Deposition Modelling and hybrid 3D printing of mechanical sensors

Fused Deposition Modelling (FDM) is a cheap and accessible way to easily fabricate 3D structures from a 3D model[2]. Flexible FDM filaments are available to create elastomeric wearable sensors, however, as noted in Section 2.1.1, readily FDM printable highly conductive materials are not available. This makes it difficult to completely 3D print elastomeric sensors using this technique. Even though conductive filaments do exist, they are mostly rigid and reinforced with carbon particles which make for poor conductors. Integrating functional layers created from more conductive materials, such as metallic pastes or inks, would allow for highly conductive 3D printed features. However, these types of materials require post-processing treatments, often thermal, that can warp or even destroy the thermosensitive FDM printed materials[143].

Methods have been proposed to solve this problem such as photonic [130], [144] or laser sintering[145], which either rely on external and bulky equipment or used rigid and thermally stable materials. Alternatively, by refilling strategically positioned empty spaces in the FDM printed body with liquid metals[25], [146] with which highly conductive features can be created. But due to need for refilling and interfacing these liquid features after fabrication, it limits their use in an additive manufacturing process. An additive manufacturing suitable process is to use laser sintering to sinter highly conductive pastes, which has so far only been demonstrated for rigid FDM materials[127].

To solve this problem, multiple approaches were explored to embed conductive features into a 3D printed Thermoplastic Polyurethane (TPU) material, called NinjaFlex, to create flexible sensors. First we explored the FDM printing of a rigid carbon composited PLA into the flexible material to create piezoresistive and capacitive sensors. Whilst functional sensors were created, these layers did not prove to be sufficiently conductive for low-power electronics nor were they able to withstand flexion without leading to damage of the conductive layers. Therefore, we instead investigated if we could use laser sintering to embed DIW printed silver pastes into the thermosensitive FDM material using a cost effective LED laser to locally in-situ sinter the ink directly after printing. With this approach we prevent the warping of the FDM printed material, due to its low heat deflection temperature (HDT) of 60 °C which can lead to the release of material stress. An initial rigid prototype was created from FDM printed thermoplastic Acrylonitrile Butadiene Styrene (ABS) as a proof of concept of the proposed method. We then investigated if this approach could be also be used in combination with the NinjaFlex material. This investigation was performed by laser sintering DIW printed polyurethane based silver inks on top of FDM NinjaFlex substrates.

Within the study, effects of the laser power and scanning speed were studied for the sintering of silver single line and dogbone features. A wide range of parameters were tested to determine the influences of the substrate material, laser power, and scanning speed. Through this study, suitable sintering parameters were found and used to further investigate the sintering of larger DIW printed silver squares. For these structures we analysed the thermal behaviour during sintering, and the annealed structure and conductivity after sintering. With the developed methodology we enabled a cost-effective method to in-situ sinter DIW printed electrically conductive silver features with a resistivity in the range of 50-125 μΩ cm.

Using suitable sintering parameters, several flexible devices including a conductor and a capacitive pressure sensor were produced to demonstrate the effectiveness of fabricating and processing devices within a single machine. The sintering technique was also extended to cure a carbon black-silicone composite and DIW print it on top of a NinjaFlex substrate to create a piezoresistive bending sensor. Mechanical characterisation of these devices was performed to evaluate their performance and compare them to devices produced entirely by FDM printing.

With the developed hybrid methodology we enable the fabrication of flexible elastomeric sensors with highly conductive films embedded to enable low power mechanical sensors.

The research in this chapter is adapted from a conference proceeding[a] and an article published in the IOP journal of Flexible and Printed Electronics[b].

3.1 Fabrication of sensors using Fused Deposition Modelling

In this section the fabrication of proof of concept sensors printed using FDM and DIW is presented. As the printed surface of the FDM printed material is quite rough, a small study was also performed to see if a laser treatment could be used to planarise printed surfaces.

[a] *In-Situ Laser Processing for 3D Printed Mechanical Transducers* by Ryan van Dommelen, Olivier Chandran, Sébastien Lani and Danick Briand presented at Transducers & Eurosensors XXXIII

[b] *In-situ laser sintering for the fabrication of fully 3D printed electronics composed of elastomeric materials* Ryan van Dommelen, Rubaiyet Haque, Olivier Chandran, Sébastien Lani and Danick Briand - IOP Flexible and Printed Electronics - Vol. 6 No. 4.

3.1.1 Fully FDM printed sensors

A study was performed by a master student working on a semester project under my supervision to design and fabricate fully FDM printed sensors. For these sensors NinjaFlex was used as a base material and a conductive Polylactic acid (PLA) filament with embedded carbon particles (ProtoPasta) was used to print the conductive features. Two main transduction mechanisms were explored resulting in a number of piezoresistive (Figure 3.1 a) and capacitive pressure sensor (Figure 3.1 b) designs.

A proceeding[147] was published for the 20th International Conference on Solid-State Sensors, Actuators and Microsystems & Eurosensors XXXIII (TRANSDUCERS & EUROSENSORS XXXIII) held in 2019 in Berlin.

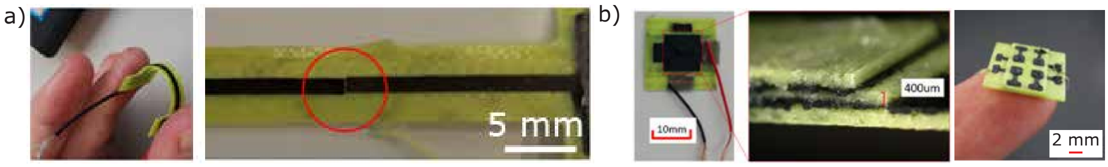

Figure 3.1 – The electronics and sensors produced using FDM multimaterial printing. **a**) Printed conductor/piezoresistive transducer with fractures visible after bending. **b**) Simple and multi-pad capacitive sensor designs.

Fabrication approach

The devices were printed using an Ultimaker S5 desktop printer. This printer comes equipped with two printing heads, to allow for multimaterial print jobs, such that integrated devices can be produced. The layers for the sensors were printed in a layer by layer approach where first one structural layer was printed before the functional conductive layer was printed on top of this. This process is shown schematically in Figure 3.2. Between the CAD model and the print a ±10 um error was found by optical interferometry. However, as this error remains the same for thicker prints the error percentage reduces when taller structures are printed.

Printed piezoresistive strain sensor

A simple 30 mm long linear conductor with two contact pads was designed to sit on top of a NinjaFlex substrate with a width of 1.05 mm. A minimum of 4 layers of 60 µm each of the carbon black reinforced PLA (PLA-Cb) were required to have good adhesion to the substrate and keep the error between print and CAD file to a minimum. The resistivity of the PLA-Cb was found to be 16.17±0.84 Ω cm which yielded conductive features with a 200-400 µm thickness and 1.2 mm width between 10-20 kΩ.

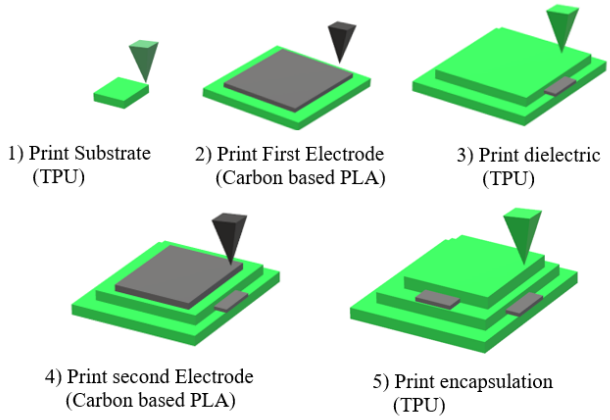

Figure 3.2 – The layer by layer printing approach as performed in the Ultimaker S5.

At 4 layers (240 um) the initial resistance was 13.3±8.9 kΩ which could be stretched linearly up to 2%. The effectiveness of a strain gauge can be expressed in terms of the gauge factor. This factor is derived for a linear-elastically deforming strain gauge as

$$GF = \frac{R - R_0}{R_0 \varepsilon}, \tag{3.1}$$

where R is the resistance at a certain strain (ε) and R_0 is the resistance when the gauge is undeformed. For the produced conductor a GF of 6 was found. However, as shown in Figure 3.2 a, the PLA-cb breaks quite easily when bending or straining it significantly, which limits its usage as a strain sensor.

The design could also be used as as simple thermistor which is able to sense temperatures up to just below 40 °C with a non-linear response and a resolution of at best 1°C. The material has a heat deflection temperature (HDT) of 60 °C, at which point it any residual stress in the material will be able to permanently deform the material. Any thermistor created from this material will be limited by this.

Printed capacitive pressure sensor

To avoid high strain forces, we instead investigated if the NinjaFlex-PLA-Cb material combination could be used to create flexible capacitive normal sensors. A capacitive sensor with a 1 cm^2 electrode overlap was designed consisting of a NinjaFlex substrate and dielectric, and two functional layer serving as plates created from PLA-Cb. This sensor functions by having normal compression squeeze the dielectric, which brings the two plates closer, leading to an increase in capacitance between them when a potential is applied. The formula that describes the capacitance for such a sensor with linear elastic material is given by

$$C = \frac{kA}{t(1-\varepsilon)}, \tag{3.2}$$

where k is the dielectric constant, A represents the surface area of the overlap of the plates, t the thickness, and ε the normal strain.

This sensor was tested on a custom made automated mechanical test bench with a Futek LRM200 load cell connected to a Futek IPM650 controller to read out the applied force and controlled using a LabView script. The capacitance-force behaviour of the sensor was determined using an Agilent Technologies E4980 Precision LCR Meter.

During printing, PLA-cb and Ninjaflex intermixed due carbon particles sticking to the nozzle which were reintroduced into the interface of the TPU resulting in higher dielectric values. While this can be beneficial, as it increases the base capacitance, the dielectric constant values became very spread out. As shown in Figure 3.3 a, dielectric permittivities lay between 10.0±1.2 and 7.4±0.3 for dielectric thicknesses of 200 and 1000 µm, respectively. This prevents the printing of devices with repeatable characteristics.

Of course, a thinner dielectric leads to higher capacitance with the average capacitance value being measured at 46.7±3.9 pF for a 200 µm dielectric while for a 1000 µm dielectric it was 6.53±0.3 pF. These base values have no real influence on the sensitivity as it is response is independent of the thickness, but it does reduce the signal to noise ratio. This behaviour is shown in Figure 3.3 b-c, where the force-capacitance responses for sensors with both dielectric thicknesses are shown. With the theoretical capacitance behaving the same for both thickness values, the deviations in response are due to variations in the dielectric permittivity and fabrication errors.

Independent of the dielectric thickness, the average capacitive sensitivities ($\Delta C/C_0$) were found to be 0.096±0.003 %/N which was slightly above the theoretical prediction of 0.087 %/N. This value is, however, low when compared to literature. In one paper a 0.1759 %/N FDM printed TPU based sensor was demonstrated[32]. A further smaller design was also tested with four separate plates to test touch detection including the direction of the force. This design had a total capacitance below 1 pF and could not be effectively tested without the fragile PLA-cb breaking.

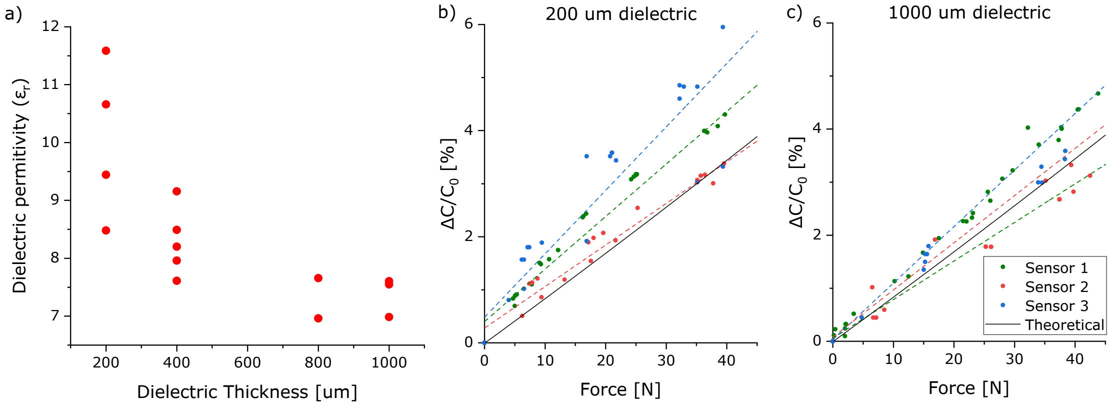

Figure 3.3 – Responses of the capacitive stacks produced by FDM printing. **a**) change of dielectric permittivity with layer thickness. Relative capacitance-pressure responses for a dielectric thickness of **b**) 200 µm and **c**) 1000 µm

Constraints and limitations

While functional devices can easily be produced using FDM, and sensor designs rapidly modified, they do come with some limitations. Devices suffer from reproducibility issues, are limited to certain dimensions, and lack highly conductive flexible features. As such they do not make the best candidates for low-power wearable soft devices. Therefore, we instead focused on embedding highly conductive silver features into FDM printed structures by local laser sintering to replace the fragile FDM printed conductive features.

3.1.2 Embedding silver conductive films into FDM structures

A simple proof of concept capacitive sensor was made from rigid materials to see if laser sintering could be effectively used to sinter silver pastes. The design, fabrication, and response of this sensor are shown in Figure 3.4.

The sensor was designed as shown in Figure 3.4 a, with a patterned infill to embed the silver feature. After deposition and sintering of the silver feature, the same structure rotated by 90° to be produced on top resulting in a simple capacitive sensor. The materials used to print this sensor were a FDM ABS filament called nGen for the structural parts, and Creative Materials 117-23 Medical Grade silver paste for the DIW printing of the conductive plates. This material combination was previously established by a master student working on making an embedded sensor. To print this sensor an Aether1 Bioprinter (Aether, San Francisco, CA, USA) was used equipped with a FDM head, a holder for several DIW cartridges, a M140 M-type Laser Diode (Barnett Unlimited, 445 nm, 2 W) with a spotsize of 125 um, and a heated printbed. To print the ink, 3 mL Luer-Lok syringes were mounted into one of the holders.

The nGen base structure was printed with a extruder temperature of 220°C, build plate temperature of 60 °C and print speed of 50 mm/s. The infill was designed and programmed to be 3 layers high with a layer height defined in the gCode to be 150 µm for a feature of 450 µm. The final infill depth was slightly reduced at a thickness of 378±1 µm, measured using a Veeco WYKO NT1100 Optical Profilometer. The silver was DIW printed into the infill pattern using a 25 gauge (Metcal, 254 µm inner diameter) needle dispensing tip, air pressure of 22 psi, printing speed of 2.4 mm/s, and a programmed line-to-line spacing of 250 µm. The ink was immediately sintered by passing the laser at a scanning speed of 5 mm/s with a laser power of 0.7W (35% of the available 2W). Two passes were used as the first pass did not completely cure the ink. Photographs of the DIW printing and sintering of the silver ink are shown in Figure 3.4 b-c.

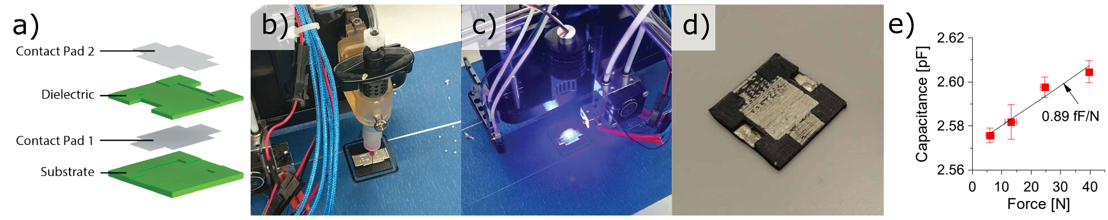

Figure 3.4 – Fabrication and testing of a rigid sensor prototype. **a**) CAD Design of the capacitive sensor. **b**) Printing of the silver ink and **c**) laser sintering after deposition. **d**) Photograph of the produced prototype and **e**) its response curve.

After printing, the silver layer had an average thickness of 285±43 µm. The average resistivity was measured to be 6.49±3.52 µΩ cm, showing a large spread as the ink deposition was not even in all locations. This uneven deposition is partially caused by the fact that the FDM surface is quite rough since it was measured to have a square root mean roughness of 4.53±1.09 µm and average profile height of 36.9±1.1 µm. The printing process was repeated to create a second layer to finalise the capacitive sensor shown in Figure 3.4 d. Capacitance and force data acquired was used to create the response curve shown in Figure 3.4 e.

A base capacitance of 2.42 pF was measured and by linearly fitting the response curve (R^2 = 0.95) an average sensitivity of 0.89 fF/N (0.0003 %/N) was found. While serving as a proof of concept, the performance of this device is far removed from sensitivity values demonstrated by FDM printed devices and literature. This mismatch can be partially attributed to the rigid nature of the materials resulting in low strain values.

This work was presented for the 20th International Conference on Solid-State Sensors, Actuators and Microsystems & Eurosensors XXXIII (TRANSDUCERS & EUROSENSORS XXXIII) held in 2019 in Berlin, and a proceeding[148] was published.

3.1.3 Laser planarisation of FDM printed surfaces

During the fabrication of the capacitive touch sensor prototype, the fabricated FDM layers were found to be very rough, which affects the deposition and minimum thickness of the silver layer. Previous work has shown that a FDM surface can be remelted to smoothen the surface by rapidly scanning it with an industrial 40 W CO2 laser[38]. We investigated if it would be possible to do the same using a low power LED laser at slower speeds.

3D printed nGen samples were prepared with an UltiMaker 3 FDM printer as it provided better quality prints than the Aether. The samples were then transferred to the Aether where 9 areas of 1x1 cm^2 per sample were treated using laser powers of 0.1, 0.3, and 0.5 W, and speeds of 5, 10, and 20 mm/s. The influence of the direction of the planarisation was also tested. These parameters and the resulting surfaces are shown visually in Figure 3.5.

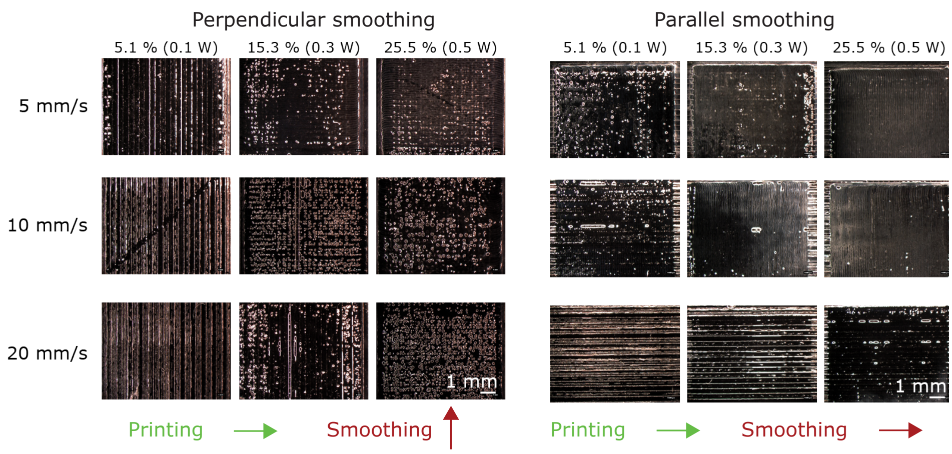

Figure 3.5 – Optical images captured after laser planarisation for several tested conditions.

The images captured by optical microscopy clearly show that perpendicular smoothing yields much smoother surfaces than parallel smoothing. However, the best way to quantitatively verify this was by means of surface measurements. To evaluate this, optical interferometry measurements were made of the planarised surface and Root Mean Square (RMS) roughness (R_q) and average profile height (R_t) were measured using Gwyddion.

By looking at the R_q values of both surfaces, shown in Figure 3.6 a-b it can be seen that while the surface roughness improves for the samples treated with parallel smoothing. For perpendicular smoothing the surface actually degrades as bubble-like structures appear on the surface, possibly due to overheating. While these again reduce at higher powers, the resulting surfaces are very uneven and wavy, resulting in a less planar surface. Overall, an increase in speed results in smoother surfaces for parallel smoothing (Figure 3.6 c-d), but a minimum amount of laser power is required in order to effectively planarise.

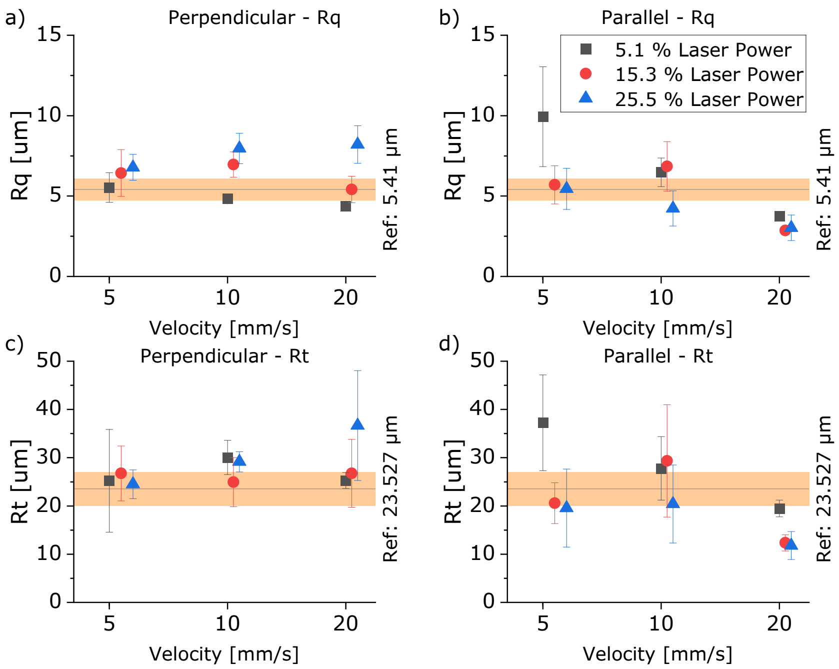

Figure 3.6 – Roughness of 3D printed nGen after laser planarisation. RMS roughness for **a**) perpendicular and **b**) parallel smoothing. Average profile height for **c**) perpendicular smoothing and **d**) parallel smoothing.

The best results for both directions are obtained at 0.51 W power (25.5%) at a speed of 20 mm/s. When planarising in the perpendicular direction R_q increases to a value of 8.20±1.17 µm, which is an increase of 51.6% compared to the non-treated nGen (5.41±0.54 µm). In the parallel direction, however, at the same power and speed R_q decreases to 3.03±0.79 µm which is a reduction of 44%. Similarly, the R_t increased to 36.67±11.39 µm (+55.9%) and decreased to 11.78±2.90 µm (-49.9%) for perpendicular and parallel planarisation, respectively.

The same test was carried out on a flexible FDM printed NinjaFlex (NinjaTek, Manheim, PA, USA) sample. The NinjaFlex was printed using a Prusa i3 MK II FDM printer with an extrusion temperature of 240 °C, a baseplate temperature of 40 °C and a writing speed of 25 mm/s, and with the layer thickness set to 100 µm. However, no significant changes to the structure were able to be made. In fact, the NinjaFlex sample was already much smoother than its rigid counterpart with a R_q value of 1.15±0.13 µm and a R_t value of 11.70±1.98 µm after printing.

These material properties thus also made it a more attractive material as a sintering target, since it is less sensitive. In order to create fully flexible devices, we instead focused on developing a laser sintering process for curing silver ink on the NinjaFlex substrate.

3.2 In-situ laser sintering of DIW printed conductive and flexible structures

Due to the unavailability of highly conductive FDM printable filaments, alternative materials are required to introduce highly conductive features. As demonstrate in section 3.1, localised in-situ laser sintering offers a solution for embedding rigid silver paste printed in a rigid FDM structure. While these structures can make for simple sensors, more complex wearables and flexible devices require the use of flexible or even soft materials. In this section the integration of a highly conductive and flexible ink, by means of a laser sintering technique, into a flexible FDM printed material is discussed. Experiments are performed to understand the influence of substrate, printing speed, laser power, laser speed, and bed temperature in order to optimise the printing and sintering protocols.

To achieve the flexible silver features, a polyurethane (PU) based silver ink (AG520EI, Chimet S.p.A.) intended for screen printing was used as received for the laser sintering experiments. The recommended annealing condition of this ink was given as 130 °C for 30 minutes in an oven, which should result in a resistivity of 50.8 μΩ cm as per the datasheet. A secondary diluted form of the original ink was made by adding 8 wt% thinner (0204IT, Chimet S.p.A.), to more consistently produce features with a sub 100 μm thickness which allow for easier integration into devices. This thinner is designed to dilute the PU based silver ink, and thus will react with any PU-based substrate as well. Line, dogbone and square features were printed from these inks on several substrates in order to determine which of the laser sintering parameters was most important.

3.2.1 DIW Printing and sintering of silver ink

In order to establish suitable DIW printing parameters for the laser sintering experiments, an initial analysis of DIW printed silver lines was performed. Both standard and diluted silver inks were printed using the Aether1 Bioprinter using 3 ml Luer-lok syringes with 25 gauge precision needles (Metcal, 254 μm inner diameter) for dispensing the inks by air pressure. These inks were printed on top of glass wafers cleaned with isopropanol and annealed at the recommended temperature of 130 °C. Sets of 9 silver lines of 20 mm in length were printed at a pressure increasing by 0.55 bar (8 psi) per line up to a final value of 4.96 bar (72 psi). Three different writing speeds (1.6 mm/s, 3.2 mm/s and 6.4 mm/s) were tested for a total of 27 lines per ink. After curing, their dimensions were measured by means of optical interferometry to find a relation between the pressure and speed. Their printing quality, determined in terms of the thickness and linewidth, was evaluated by calculating the coefficients of variation (COV) with respect for pressures where their dimensions increased linearly. The COV values were shown to be dependent on both the printing speed and pressure as shown in Figure 3.7. For the standard ink a printing speed of 3.2 mm/s was chosen as it showed the most reproducible result for printing layers less than 100 μm thick which would allow for integration within only one layer of FDM printed structural material. A pressure of 4.42 bar (64 psi) was chosen which resulted in a thickness of 72±1 μm and linewidth of 691±7 μm. Even though this is below 100 μm, the joining of multiple lines can lead to a thickness increase.

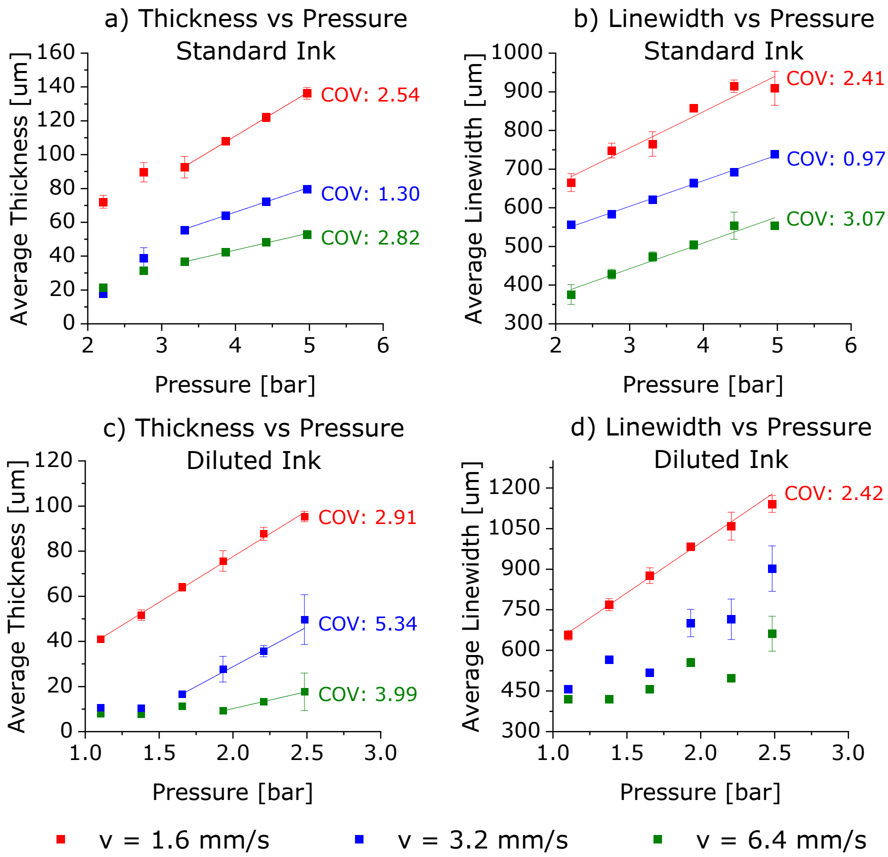

Figure 3.7 – Influence of pressure and speed on the dimensions of solidified lines printed on a glass wafer using **a-b**) the standard silver ink and **c-d**) the diluted silver ink.

Next, the diluted silver ink was tested. To ensure it could be reliably printed at all tested speeds a pressure of 2.21 bar (32 psi) was required. Even though both inks were characterised in the same way, the diluted ink was printed with less consistent dimensions due to its lower viscosity. The thickness and linewidth values resulted in higher COV values on average. The most consistent thickness was obtained at 1.6 mm/s. Even though the dimensions were less consistent at higher speeds, a speed of 3.2 mm/s had to be chosen for the diluted ink as a compromise. With the addition of the thinner the diluted ink reacts strongly chemically with the NinjaFlex substrate. As such, to minimise the chemical interaction between ink and substrate and achieve well defined lines a faster speed had to be chosen. At a pressure and speed combination of 2.21 bar (32 psi) and 3.2 mm/s, the thickness of the silver lines was reduced to about half that of the standard ink at the same speed with a value of 36±3 µm (Figure 3.7 c). The linewidth, however, increased slightly to a value of 715±75 µm as the ink spread more (Figure 3.7 d).

To be able to join the printed lines to print larger continuous features with either ink, a centre-to-centre spacing needed to be set. A value of 250 µm was chosen and, when printing at 3.2 mm/s, an increased thickness of 115±2 µm and 73±1 µm for the standard and diluted inks, respectively, was found. This signifies an increase for both inks by 88%. Increasing the spacing to 500 µm resulted in bifurcations and non-planar depositions (Figure 3.8).

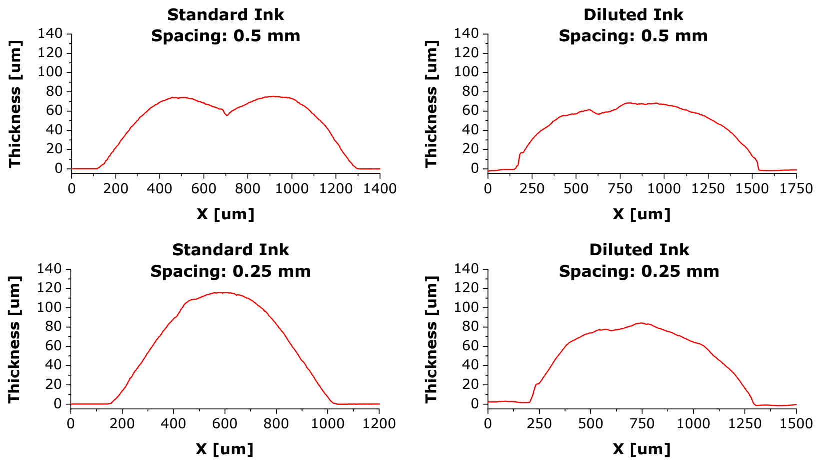

Figure 3.8 – Profiles measured when printing two lines with different amounts of spacing using both standard and diluted inks.

The Chimet ink is unfortunately not a truly shear thinning ink as it behaves too elastically. Even so, we chose this materials as it allows for the printing of flexible electrical conductors. Moreover, since it is also Polyurethane based it is expected to adhere well to the TPU material. However, the fact that it is not truly shear thinning will lead to less consistent thickness and linewidth values.

3.2.2 Influence of laser sintering power and speed on the resistivity of printed silver dogbone structures

Silver DIW printed dogbone test structures were fabricated in order to study the influences of the sintering parameters. Reference sintering experiments were performed by sintering silver features on top of a glass wafer to compare those sintered on top of the polymeric substrate.

Further laser sintering experiments were performed on DIW printed dogbone structures on top of a FDM printed NinjaFlex double layer substrate.

The goal of these experiments was to find the optimal laser sintering parameters without leading to degradation or damage of the substrate or printed features. The NinjaFlex substrates were printed using a Prusa i3 Mk2 FDM printer, as it allowed for better print quality with smoother printed surfaces, before being transferred to the Aether1 Bioprinter for DIW printing of the silver ink and in-situ laser sintering. However, the whole process could be envisioned to take place within a single tool. For the sintering a 445 nm M140 M-type Laser Diode (Barnett Unlimited) with a spotsize of 125 um and a maximum of 2 W was used.

Two experiments were carried out to evaluate the influence of the laser sintering parameters. First the influence of the laser power was evaluated by sintering the structures at laser powers between 0.5 W and 1.2 W. The latter power was set as a maximum to avoid damage to the diode from continuous operation. The influence of the scanning speed was evaluated by sintering at speed varied step-wise from 5 mm/s up to 40 mm/s at powers of 0.6, 0.8, 0.9 W, determined through the laser power experiment.

Dogbone test structure fabrication and characterisation

The dogbone test structure was designed as a single 4 mm long line joined by two 2 mm x 2 mm contact pads. These were printed at a speed of 3.2 mm/s with the pressures set at 2.21 bar (32 psi) and 4.42 bar (64 psi) for both the diluted and standard ink, respectively, as established in Section 3.2.1. After DIW printing these structures, they were immediately sintered using the laser LED.

Rows of five of these structures each were printed on glass wafers (Figure 3.9 a) and NinjaFlex substrates (Figure 3.9 b).

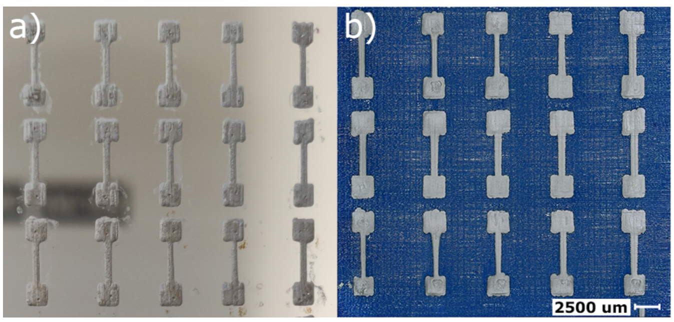

Figure 3.9 – The silver dogbone samples DIW printed **a**) on top of a glass wafer, and **b**) those printed on top of a FDM printed double layer NinjaFlex.

Optical interferometry was used to measure the dimensions of the features on glass. The features on NinjaFlex however could not be measured in the same way and were measured using a Keyence VK-X 3D Laser Scanning Confocal Microscope. As the substrate was at times non-planar and warped, whenever necessary cross-sections were made of the features and captured using a Keyence VH-X Digital Microscope to verify their dimensions. Their resistance was measured by means of four point probing, as their resistance was below 1 Ω, with an Agilent 34410/11A Digital Multimeter and their resistivity calculated as per the equation

$$\rho = \frac{RA}{l}, \tag{3.3}$$

where R is the resistance, A the cross-sectional area, and l the length of measured conductor. Since only the thickness and linewidth were measured, and not the area directly, the areas of lines were assumed to be ellipsoid and were calculated using the formula

$$A = \frac{\pi t w}{4}, \tag{3.4}$$

where t is the thickness and w the linewidth.

Reference dogbone structures were DIW printed on the glass wafer and annealed in an oven at 130 °C for 30 minutes. The features were found to have an average thickness of 65±10 µm and a resistivity of 214.2±26.2 µΩ cm which is significantly higher than the one calculated from the datasheet (50.8 µΩ cm).

Influence of laser sintering power

The influence of the laser power was determined by varying the intensity of the diode, which had a spotsize of 125 µm, from 25% to 60% of the total 2 W of power available translating to a power of 0.5 W to 1.2 W. The laser power was increased in increments of 5% (0.1 W) per row and the scanning speed was fixed at 10 mm/s. Single and double sintering passes were performed to test the influence of repeated sintering.

On the glass substrate the laser was passed twice over the dogbone features, as a single pass did not fully solidify the features. This resulted in features with a thickness of 64±9 µm, comparable to the oven annealed samples. Their resistivity was found to be slightly lower than the thermally annealed samples with an average value of 171.1±34.4 µΩ cm. The decrease is likely due to laser sintering providing a high amount of energy locally in a short amount of time. This could promote solvent evaporation and decomposition of the polymeric binder present in the ink, resulting in higher percolation compared to oven annealing[149], [150].

The same dogbone structures were printed on top of NinjaFlex substrates using the standard ink. An average thickness of 69±9 μm was found for the features sintered with a single pass irrespective of the applied power, matching the reference samples on glass. Figure 3.10 shows that, compared to the glass substrate, the resistivity of the dogbone features was lower.

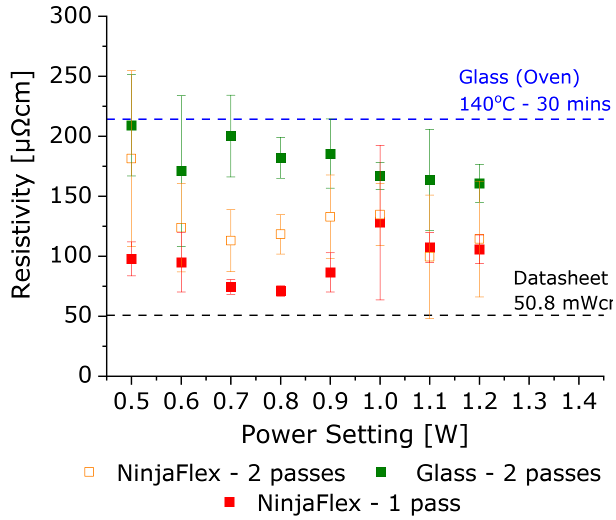

Figure 3.10 – Mean resistivity values found after laser sintering the silver dogbone structures for different substrate materials and power settings.

For the full power range, the mean resistivity was found to be 98.0±28.5 μΩ cm when sintering with a single pass. The decrease in resistivity for the features sintered on NinjaFlex is likely due its different optical properties compared to glass. Non-transparent substrates, such as NinjaFlex, absorb more energy from exposure to a visible laser source than glass substrates[149], resulting in more heat being transferred to the ink during sintering. Additionally, sintering the features on the NinjaFlex substrate twice carried no benefit as the average resistivity actually instead increased to 137.7±61.0 μΩ cm. As the ink was already solidified after a single sintering pass, any additional passes potentially damage the structure resulting in higher resistivity.

As shown in Figure 3.10, the lowest resistivity when sintering with a single pass was found at a sintering power range of 0.7-0.8 W with a value of 72.8±5.3 μΩ cm. When the power was either reduced down to 0.6 W or increased to 0.9 W, the resistivity increased to 95.1±24.8 μΩ cm and 86.6±16.4 μΩ cm, respectively. Nonetheless, these values are still significantly lower than those found for the structures on the glass substrate.

Influence of laser sintering speed

Next, the influence of the scanning speed was determined by varying the speed during sintering while keeping the power fixed. A speed sweep ranging from 5 mm/s to 40 mm/s was performed at three different powers (0.6, 0.8, 0.9 W), the values of which were guided by the results of the power test. The outer powers of 0.6 and 0.9 W were chosen as these powers led to the resistivity going up from the lowest values found at 0.7-0.8 W. Therefore, to understand if this was only due to the power or a combination of the power and speed, a speed sweep was also performed for these powers.

Figure 3.11 a shows that the minimally achievable electrical resistivity is coupled to both the speed and power. For the standard ink, sintering at 0.8 W at the slowest speed (5 mm/s) resulted in the lowest achieved resistivity with a value of 41.9±8.3 μΩ cm. Increasing the laser scanning speed by a factor two (10 mm/s) increased the mean resistivity up to 58.2±7.7 μΩ cm. Increasing the laser speed further resulted in a continuous increase in the resistivity. Lowering the power to 0.6 W increased the overall resistivity for the same speeds (5 and 10 mm/s), indicating that at this power the sintering effectiveness was reduced. Increasing the laser power to 0.9 W resulted in an increased resistivity of the same magnitude, but with the plateau shifted to the 20 to 30 mm/s range. For the latter power, a significant increase of the resistivity was observed at lower speeds indicating that the sintering was too intense.

The diluted ink was tested in the same way but forgoing the test at 0.9 W power, due to the poor resistivity values obtained in comparison to the lower powers. The resistivity values obtained for these features are shown in Figure 3.11 b. For both the 0.6 and 0.8 W laser power, the resistivity followed the same trend in relation to the speed as for those created out of the standard ink. At a sintering power of 0.8 W and a laser scanning speed of 5 mm/s, a minimum resistivity of 82.9±7.1 μΩ cm was achieved. Increasing the speed by a factor two resulted in an increased resistivity of 131.2±14.6 μΩ cm. At a laser power of 0.6 W, a resistivity below 100 μΩ cm could not be achieved.

In conclusion, we observed that the sintering speed, and by definition the total time spend sintering, is more influential on the final resistivity than the power. The best resistivity values for both inks were obtained at a speed of 5 mm/s and at 0.8 W laser power. However, at this speed the NinjaFlex structural layer was significantly affected by the laser resulting in severe damage to the structural integrity as seen in Figure 3.11 c.

As such, any further reduction in speed was not investigated. At the same power but at a speed of 10 mm/s these effects are significantly reduced to negligible surface damage. Therefore, in order to achieve an as low as possible electrical resistivity, while preserving the integrity of the structural layer, a speed of 10 mm/s with a power of 0.8 W should be maintained for both the standard and the diluted inks. For more thermally robust substrates a lower sintering speed

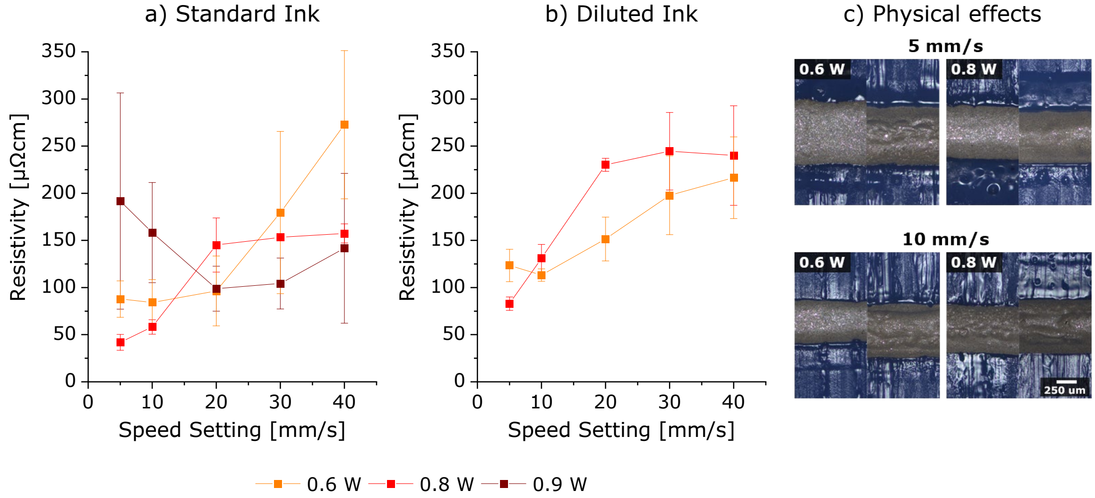

Figure 3.11 – Resistivity values found when laser sintering the silver dogbone structures at different speeds. **a-b**) The effect of laser sintering speed on the resistivity of both sintered inks. **c**) The effects of sintering power on the substrate, with in the left halves the dogbone structures printed from the standard ink and in the right halves those printed from the diluted ink.

could be applied.

3.2.3 Influence of printing and laser sintering conditions on the resistivity of silver squares for creating conductive layers

We wanted to study how much of an influence the size of the target had on the outcome of the laser sintering process. To evaluate this, 12 mm x 12 mm squares (Figure 3.12) were DIW printed from both the standard and diluted inks. To create theses structures, multiple printed lines were printed in close proximity to join them into squares. The printing pressures remained unchanged at 4.42 bar (64 psi) and 2.21 bar (32 psi) for the standard and diluted ink, respectively. A printing speed of 3.2 mm/s was used with at a centre-to-centre spacing of 250 µm for the lines. As these squares were thicker than 100 µm, a printing speed of 6.4 mm/s was also evaluated in order to reduce the film thickness below 100 µm where necessary.

As the larger size of the squares led to stronger ink-substrate interactions, a heated printbed was used to assist with the evaporation of the solvent and reduce its interaction with the NinjaFlex substrates. A bed temperature of 50 °C was set, which is just below the heat deflection temperature of NinjaFlex (60 °C). For these features, the ideal laser power was determined by setting the range from a low power of 0.6 W in steps of 0.3 W to a high power of 1.2 W with a fixed scanning speed of 10 mm/s as determined in Section 3.2.2.

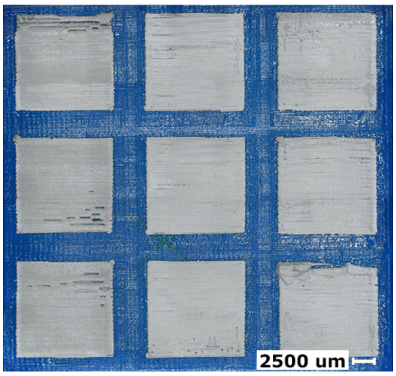

Figure 3.12 – Optical image of a square test structures printed from Chimet ink used for the laser sintering experiment of larger features.

Influence of printing speed and sintering conditions on standard ink

Since the printed square structures were composed of multiple lines, the resulting features were thicker than the single-line dogbone structures. Squares printed out of the standard ink at 3.2 mm/s had an average thickness of 247±76 µm, as shown in Figure 3.13 a. Heating the bed, to assist with the evaporation of the solvent, did not reduce the thickness. In contrast, when the printing speed was doubled to a speed of 6.4 mm/s the film thickness was significantly reduced to 90±19 µm after sintering.

The optimal sintering parameters as found in section 3.2.2 (0.8 W, 10 mm/s) were used in an initial test to sinter the squares printed at 3.2 mm/s from the standard ink. These squares showed a higher resistivity than for those found for the dogbone structures (72.8±5.3 µΩ cm) at an average value of 259.8±18.5 µΩ cm. As shown in Figure 3.13 b, increasing the laser sintering power, nor heating the bed during sintering, had any diminishing effect on the resistivity. However, Figure 3.13 c shows that when the printing speed was increased to 6.4 mm/s the resistivity was significantly decreased to a value of 136.1±32.3 µΩ cm at a laser power of 1.2 W. As these squares were thinner, this reduction indicates that decreasing the material deposition by increasing the speed is the most effective strategy to reach lower resistivity values for these square structures.

Influence of printing speed and sintering conditions on diluted ink

For the diluted ink, the printing speed was shown to be less influential on the final thickness. When printing at either 3.2 mm/s or 6.4 mm/s, the average thicknesses for these squares were 94±21 µm and 95±17 µm, respectively.

As the thickness was more consistent and independent of the printing speed, it made the diluted ink more suitable than the standard ink for printing features reliably with a thickness below 100 µm. Furthermore, printing at a speed of 6.4 mm/s speeds up the process and reduces the time of the ink-substrate interaction. The diluted ink squares were printed with the heated bed active to further reduces these interactions and avoid the formation of cracks and warping of the substrate.

The lowest resistivity for these sintered squares was reached at a laser power of 0.9 W, independent of the scanning speed. An average resistivity value of 104.2±21.0 µΩ cm was reached with this power, as shown in Figure 3.13 d.

Increasing the power to 1.2 W created a larger deviation of the average resistivity values. The best values obtained in this experiment lay below the lowest value found for the squares created from standard ink (136.1±32.3 µΩ cm). Furthermore, the laser sintering power required was also lower for the squares created from diluted ink. All silver squares, independent of the used laser intensity, bonded well enough to the substrate to stay adhered during a peel test using 3M Scotch Magic tape.

Temperature profile and effect of sintering on the microstructure

To better understand the sintering conditions, in-situ observations of the temperature were made during sintering. Cross-sections of the silver squares post sintering were made to analyse the quality of the sintered film.

Relative temperatures were captured using a FLIR A15 9 mm IR camera and recorded using the included ResearchIR software. For both inks the temperature values were extracted at a fixed 3x3 pixel point (150 µm x 150 µm) in the centre of the squares. The data was exported to a Python script to determine a Gaussian fit of the mean temperature over time. To perform the necessary temperature calculations on the data, the emissivity coefficient (ε) was determined to be 0.7 by means of a PeakTech 4950 IR thermometer with an integrated thermocouple for both inks in the liquid state.

These change of temperature during sintering indicated by the Gaussian plots for the squares printed at 3.2 mm/s from the standard and diluted inks are shown in Figure 3.14 a and Figure 3.14 b, respectively. A general temperature increase is seen as the laser is approaching the central point. Evidently, as the laser passes close to the point the temperature spikes in short bursts. A general decline in temperature is seen once the laser has passed the point of interest.

While the maximum temperature spikes for both inks remains about the same, a larger temperature difference (ΔT) between the two powers is present in the films printed from diluted ink. This indicates that the layer printed from diluted ink is able to more rapidly heat up and cool down, as a result of the smaller thermal capacity caused by the decreased film thickness.

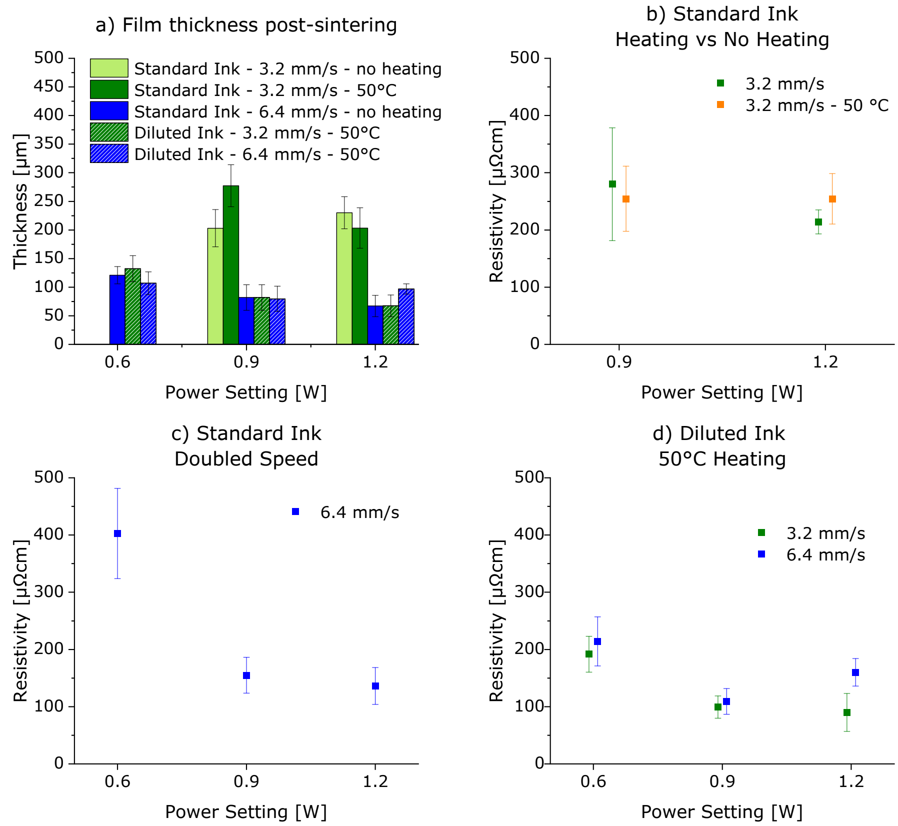

Figure 3.13 – Dimensions and values achieved by laser sintering of square structures at different sintering powers and printing speeds. **a**) Thickness values of all test conditions. Resistivity values of the sintered squares from **b)** standard ink with and without heating, **c)** standard ink printed at doubled printing speed, and **d**) diluted ink printed at two printing speeds.

However, as the recordings were indirectly captured it only provides the relative surface temperatures. To better understand the temperature changes during sintering, a more direct and rigorously calibrated analysis would need to be performed.

Indications on the quality of the sintering process can be obtained by looking at the physical influence of the laser on the microstructure of the ink after sintering. These are observed by looking at the cross-sections of the squares as shown in Figure 3.15.

The sintered thick squares printed at 3.2 mm/s from the standard ink showed cracking or localised delamination in their cross-sections. As the top layers for these squares detached from their respective bottom layers, it indicated that the features were not completely sintered leading to higher resistivity values. By heating the bed up to 50 °C these kinds of defects could be reduced, but the resistivity was not significantly lowered, and voids still appeared.

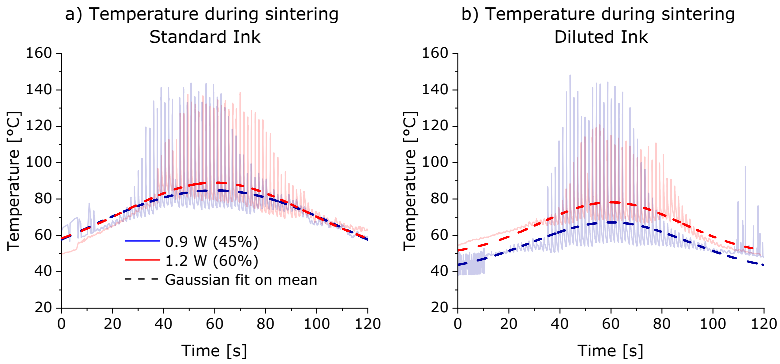

Figure 3.14 – Temperature distributions for the laser sintering of square structures at different sintering powers and printing speeds. **a-b**) Measured data and Gaussian fits for the standard and diluted inks sintered with the baseplate heated to 50 °C.

By reducing the thickness of the printed squares the damages in the microstructure could be significantly reduced. This reduction in thickness was achieved by printing the inks at a faster speed of 6.4 mm/s. The cross-sections with the best microstructural integrity were found when printing at this speed and with a sintering power of at least 0.9 W, irrespective of the ink. By using a higher printing speed less volume of ink is deposited, resulting in faster evaporation of the solvent as well as a reduction in time for solvent and substrate to interact during both printing and sintering.

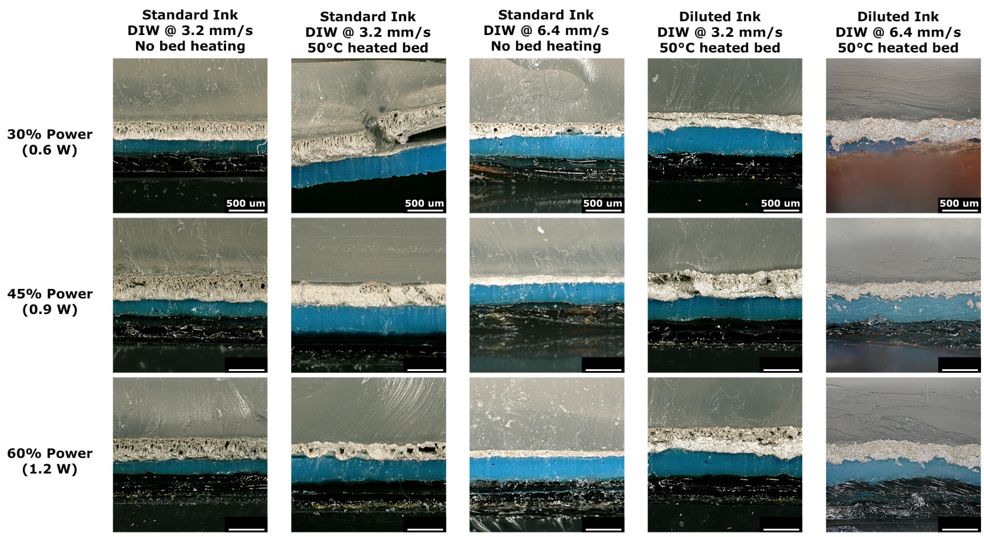

Figure 3.15 – Cross-sections of all tested squares with their respective printing and laser sintering parameters.

Optimal laser parameters for sintering of DIW printed silver layers

By combining the previously described results, a set of sintering parameters was established for the fabrication of components and sensors. As the diluted ink can be printed below 100 μm much more consistently, independent of the printed speed, it was the material of choice. To reduce the ink-substrate effects as much as possible, a printing speed of 6.4 mm/s with the bed heated to 50°C was used. To achieve the lowest possible resistivity values for larger multi-line features, a laser sintering power of 0.9 W at a laser scanning speed of 10 mm/s is advised. While slower scanning speeds leads to better resistivity values, at 10 mm/s no surface damage is observed which impedes the stacking of multiple layers.

3.2.4 Technique extension to soft silicone based piezoresistive material

To further extend the application of the developed technique, the method was applied to a carbon black silicone composite to create piezoresistive sensors. These composites were printed using a smaller 27 gauge needle (Metcal, 203 μm inner diameter), to allow for more control of the flow, at an extrusion pressure of 2.2 bar (32 psi) and a writing speed of 5 mm/s.

The material was created from commercial silicone (EcoFlex 00-20 Smooth on, PA, USA) and KetjenBlack-ec300J carbon black powder (Nouryon, Netherlands). To create this composite, the carbon black was added in a container with isopropanol and mixed at 2000 rpm for 7 minutes in a Thinky Mixer ARE-250. The dispersed mixture was then added to EcoFlex 00-20 Part A and again mixed at 2000 rpm for 7 minutes. The same process was repeated with EcoFlex 00-20 Part B. To create the final ink composition, the two mixtures containing part A and B were combined in a single container and mixed for 2 minutes at 2000 rpm and defoamed for 2 minutes at 2200 rpm. Two variants of the composite were tested with both 7.5 wt% and 10 wt% carbon black loadings. These values were previously determined to be in a suitable sheet resistance range for piezoresistive sensing (>1 kΩ/□) and are above the percolation threshold of 5 wt%.

To test the electrical properties of this composite, two layer films of the piezoresistive composite measuring 10 mm x 10 mm were printed. These films were then laser sintered at a power of 0.5 W (25%) and a laser scanning speed of 10 mm/s as shown in Figure 3.16. The power setting was determined by testing the maximum power that could be delivered before ablation of the composite occurred.

While the lower loading (7.5 wt%) could be fully sintered and would keep its structural integrity (Figure 3.16 a), the higher loading (10 wt%) started to flake and break apart (Figure 3.16 b). This might be caused by an increased absorption of the laser energy in the higher loaded composite, possibly due to it having more pigmentation. Therefore, the lower loaded composite was used for device fabrication. This piezoresistive film was measured with 4-point probing to exhibit a

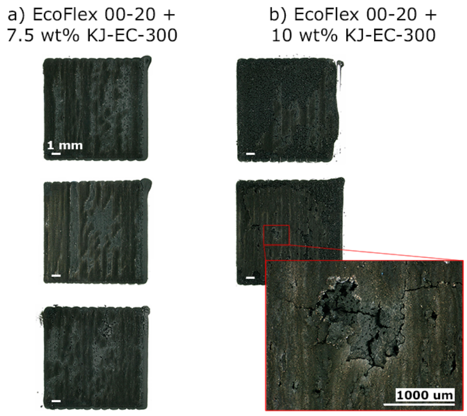

Figure 3.16 – Sintering of the Ecoflex-00-20 and Ketjenblack-EC-300 (Eco-CB) composite with **a**) sintering of the 7.5 wt% carbon black composite, and **b**) sintering of the 10 wt% carbon black composite.

sheet resistance of 1.32±0.10 kΩ/□ and a thickness of 369±68 μm.

3.3 Fully 3D printed sensors fabricated through hybrid printing

Several devices were fabricated using the highly conductive and three dimensional structuring realised by the hybrid printing method enabled by laser sintering. The parameters established in Section 3.2.3 were used for the curing of the silver layers.

In this section the fabrication approach, the device dimensions, and their characterisation are presented and discussed.

3.3.1 Hybrid printing approach and device designs

The hybrid printing approach is demonstrated in Figure 3.17 and consists of an initial base layer printing after which a repeatable process takes place to print, sinter, encapsulate, and print 3D structuring for additional layers.

All NinjaFlex layers were printed using the Prusa i3 Mk2. By printing a base layer on a glass slide the printed layer could be transferred to the Aether for DIW printing of the diluted Chimet ink and laser sintering. After this process was completed the glass slide was transferred back to the Prusa printer and a new FDM layer was printed on top of the base layer and conductive features to embed them.

To be able to embed any conductive features, patterned infills were created in the FDM

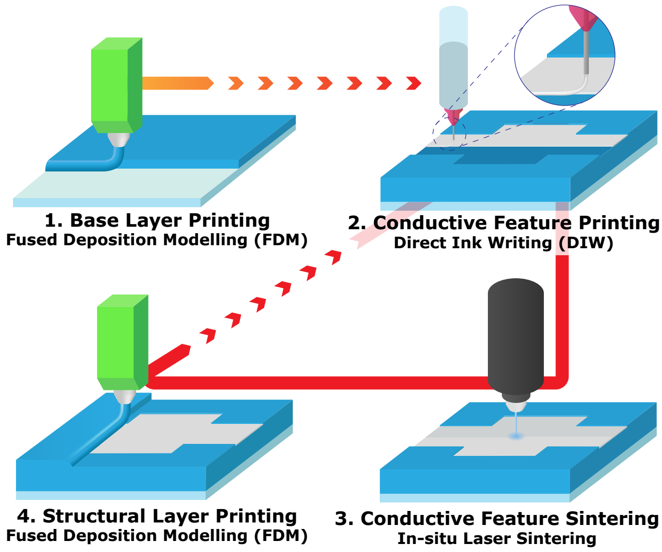

Figure 3.17 – Overview of the four step fabrication procedure: FDM printing of the base layer with a patterned infill, conductive ink filling through DIW, laser sintering of the ink, and printing of a second NinjaFlex layer for encapsulation or further fabrication.

structure with a depth of 200 µm which could then be filled with the silver ink. Three devices were fabricated as shown in Figure 3.18 using the technique with dimensions as outlined per Table 3.1. These were a flexible electrical conductor (Figure 3.18 a), capacitive pressure sensor (Figure 3.18 b), and a piezoresitive bending sensor (Figure 3.18 c).

The flexible electrical conductor and capacitive pressure sensor were fabricated using the hybrid printing approach shown in Figure 3.17 by embedding silver electrodes into NinjaFlex dielectric layers. To fabricate these embedded electrodes, the base layer of NinjaFlex was printed with a patterned infill.

The baseplate of the printer was heated up to 50 °C and left to stabilise for several minutes. Then the diluted silver ink was deposited into the patterned infill by DIW at 6.4 mm/s and 2.2 bar (32 psi), until completely filled. Immediately afterwards the ink was laser sintered once using the optimal parameters (0.9 W laser power and 10 mm/s scanning speed). After sintering, another NinjaFlex layer was printed on top of the electrode to act as an encapsulation layer, as in the case of the electrical conductor, or to act as the intermediate sensing dielectric layer. In the case of the capacitive sensor the intermediate layer was given a second patterned infill to create the top electrode of the capacitor, which was further encapsulated with a cover layer of NinjaFlex. The three devices were constructed with dimensions and layer thickness values defined in their respective CAD files as shown in Table 3.1.

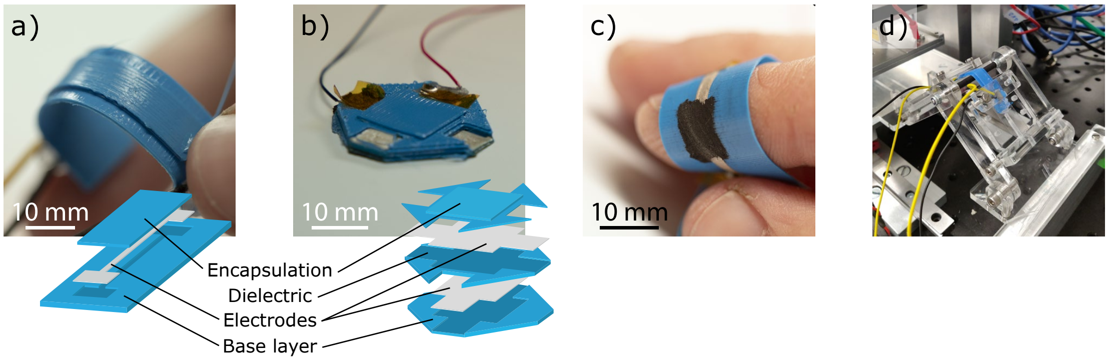

Figure 3.18 – Photographs of **a**) the flexible electrical conductor, **b**) the capacitive pressure sensor, and **c**) the piezoresistive bending sensor. **d**) The flexible electrical conductor mounted on the bending setup.

3.3.2 Fully 3D printed flexible conductor

The flexible conductor (Figure 3.18 a) was composed of a base FDM layer, embedded silver electrode, and an encapsulating top layer. The embedded electrode was designed as a single straight line interconnect 30 mm long and 750 µm wide, with an infill depth of 100 µm, and contact pads of 4 mm x 6 mm in size. The encapsulated structure measured 1 mm in total thickness.

Linear strain behaviour

The mechanical reliability of the conductor was tested in axial strain (Figure 3.19 a) as well as by bending (Figure 3.19 b). Before any strain was applied, the average resistance measured was 1.4±0.3 Ω.

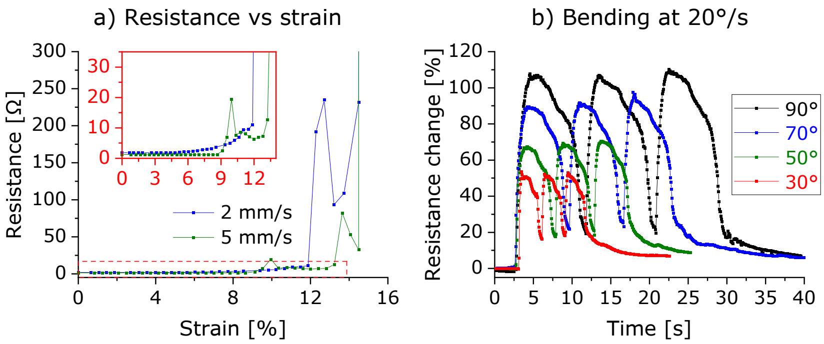

Figure 3.19 – Static and dynamic resistance responses of the conductor when **a**) straining linearly at 2 and 5 mm/s and **b**) bending at 20°/s.

Table 3.1 – Dimensions of the FDM layers of the sensors and devices as defined in the CAD files used for fabrication.

Feature	Layers (Thickness)	Patterned infill layers (Depth)
Flexible electrical conductor		
Base layer	7 (700 μm)	2 (200 μm)
Electrode	1 (100 μm)	-
Encapsulation	3 (300 μm)	-
Total thickness	10 (1.0 mm)	-
Capacitive pressure sensor		
Base layer	7 (700 μm)	2 (200 μm)
Electrode 1	1 (100 μm)	-
Dielectric	6 (600 μm)	2 (200 μm)
Electrode 2	1 (100 μm)	-
Encapsulation	6 (600 μm)	-
Total thickness	19 (1.9 mm)	-
Resistive bending sensor		
Base layer	2 (200 μm)	-
Electrode	1 (100 μm)	-
Piezoresistor	1 (200 μm)	-

The linear strain test was performed at two speeds, slowly at 2 mm/s and faster at 5 mm/s. The resistance increased negligibly, with a change below 1%, until the conductor experiences 5% strain as shown in Figure 3.19 a. At higher strains, the response at the two tested speeds diverged. The tested samples became non-conductive as they broke down at 12.6±0.7% strain with a resistance value of 11.9±0.8 Ω recorded just before failure.

Bending behaviour

The conductor was also tested under a bending deformation by bending it three times consecutively from a quasi-flat base angle (10°) to a set angle and back. The samples were bent successively from 10° to 90° with steps of 10° at a bending rate of 20°/s. While the conductor survived the bending test, it did experience a reproducible increase in resistance during bending as shown in Figure 3.19 b. On average, for the 3 bending cycles, the resistance at its peak value increased by 53.0±1.0% when it was bent at 30° and increased by up to 110.3±2.2% when it was bent at the maximum angle of 90°. For all the angles tested, the conductor did not recover to its initial baseline resistance after cycling. Once the tests were completed, at an angle of 20° and higher, the resistance of the sample was found to not recover to its initial base values when returning to the quasi-flat state. These values increased by 5.7% at 20° up to 17.4% after the sample was bent up to 90°. These effects are likely due to plastic deformation of the silver layer.

To minimise this behaviour and to achieve larger strains, design engineering could be applied for future versions. Different configurations, such as a serpentine design, could be implemented to release stress for both bending and linear strains[98]. Nevertheless, with its small resistance value, in comparison to the resistance of composite strain gauges, these conductors can be implemented as interconnects for the developed flexible piezoresistive sensors, since these sensors are significantly more resistive. Their response is demonstrated in section 3.3.4.

3.3.3 Fully 3D printed capacitive sensor

The capacitive sensor (Figure 3.18 b) was designed with a patterned infill base layer, two embedded electrodes, a dielectric sensing layer, and a structured top encapsulation. The embedded electrodes had a size of 12 mm x 12 mm, where the parallel plates overlapped, and two pads of 6 mm x 6 mm to allow for connections from either side. The dielectric was created as thin as possible measuring 400 µm (4 layers), which was the minimum thickness required to avoid pinholes. With the final encapsulation layer, the total structure had a thickness of 1.9 mm.

Force-capacitance characterisation

Characterisation of the sensor was performed by applying an increasing compressive force stepwise up to 45-50 N (450-500 kPa). Three of these sensors were tested in a step-response manner, an example of the force-capacitance response is shown in Figure 3.20 a. Among the three sensors, an average force sensitivity of 4.59±0.22 fF/N was found (Figure 3.20 b). The most linear sensors had a full-scale response of 1.26%, with the capacitance increasing from 15.91 pF up to 16.11 pF and a force sensitivity of 4.47±0.12 fF/N at a high degree of linearity (R^2 = 0.995). This corresponds to a capacitance change of 0.028±0.001 %/N (R^2 = 0.998) for the best sensor (Figure 3.20 c) and an average of 0.027±0.001%/N on average (R^2 = 0.956). These characteristics correspond to other printed capacitive sensors with similar geometries and dimensions [151] but still fall short of those create with micro-structured, softer, or thinner dielectrics[95]. A reduction of the dielectric thickness can further improve the response of this sensor design. After releasing the compressive force, the sensor completely recovered to its baseline value in less than 0.5 seconds.

Dynamic response

To test its dynamic behaviour, the sensor was repeatedly compressed at a force of 24.7±1.9 N at frequencies between 0.5 Hz and 4 Hz over a period of 10 seconds. As shown in Figure 3.21, the sensors were able to accurately follow the applied force in real time for these tested frequencies. The results indicate that this simple sensor design could easily be implemented

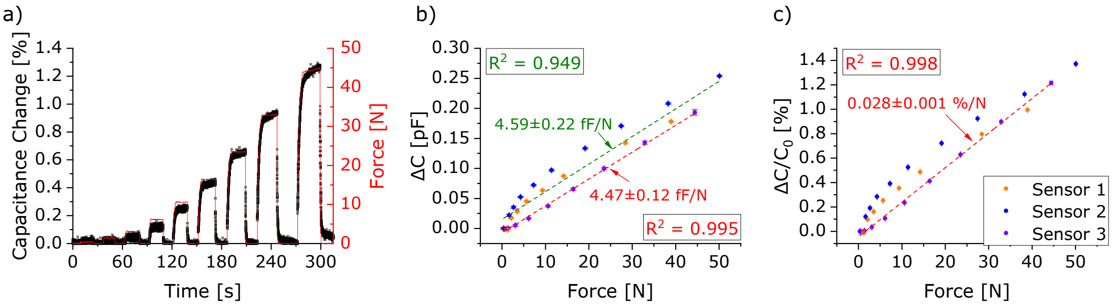

Figure 3.20 – Static behaviour of the fully 3D printed capacitive sensor. **a**) Example of a step response test performed on one of the sensors. **b**) Absolute and **c**) relative capacitance changes for the three sensors and extractions of the sensitivity values.

as an embedded pressure sensor within a customised 3D printed flexible structure.

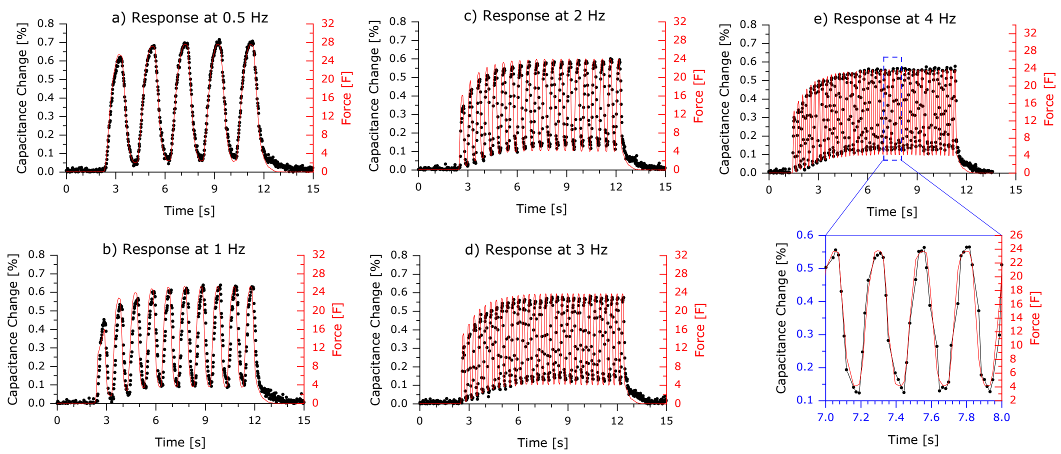

Figure 3.21 – Dynamic behaviour of the fully 3D printed capacitive sensor under a mechanical load of between 24.7±1.9 N at **a**) 0.5 Hz, **b**) 1 Hz, **c**) 2 Hz,**d**) 3 Hz, and **e**) 4 Hz with an enlarged view of the response.

3.3.4 Fully 3D printed piezoresistive bending sensor

The piezoresistive bending sensor (Figure 3.18 c) was designed to be printed on a 2 layer substrate of NinjaFlex such that it could be easily mounted on a bending test setup (Figure 3.18 d). Silver contact pads were printed with a gap of 5 mm, on top of which the piezoresistive feature was printed spanning the gap as a rectangle with a size of 15 mm x 5 mm and a thickness of 200 µm.

Piezoresistive bending response

The sensor with the piezoresistive film was mounted on top of the bending setup and actuated at several angles at a speed of 20°/s (0.11 Hz). In this fashion the sensor response could be reliably measured stepwise at an increase of 10° per test up to a bending angle of 90° (Figure 3.22). The baseline resistance was recorded at 1435 Ω and a peak resistance of 1885 Ω was reached at the maximum bending angle of 90°. The peak response of the sensor exhibited a linear behaviour at the bending states between 20° to 90°, with a sensitivity of 2.89±0.07Ω/° (R^2 = 0.998).

Dynamic bending responses

Subsequent dynamics tests were all performed using a bending angle of 90°. To test the dynamic behaviour of the sensor, it was cycled at angular velocities of 40°/s (0.22 Hz), 120°/s (0.66 Hz), and 360°/s (2 Hz) for 20 cycles each (Figure 3.22 d-f). The total angle travelled here was 180°, as within a single cycle the sensor is first bend up to 90° and then back to its starting position. It was observed that the peak resistance increase (ΔR) was slightly affected by the angular speed at the bending angle of 90°. The maximum resistance increases were found to be 525.4±12.2 Ω (40±0.9%) at 40°/s, 544.6±6.4 Ω (39.6±0.9%) at 120°/s, and 565.5±9.3 Ω (40.2±0.7%) at 360°/s. Some short-term drift occurred in terms of the peak response value at the maximum bending angle over the total number of cycles. Considering all angular speeds, an average change in the peak resistance value of 2.59±0.47% was determined.

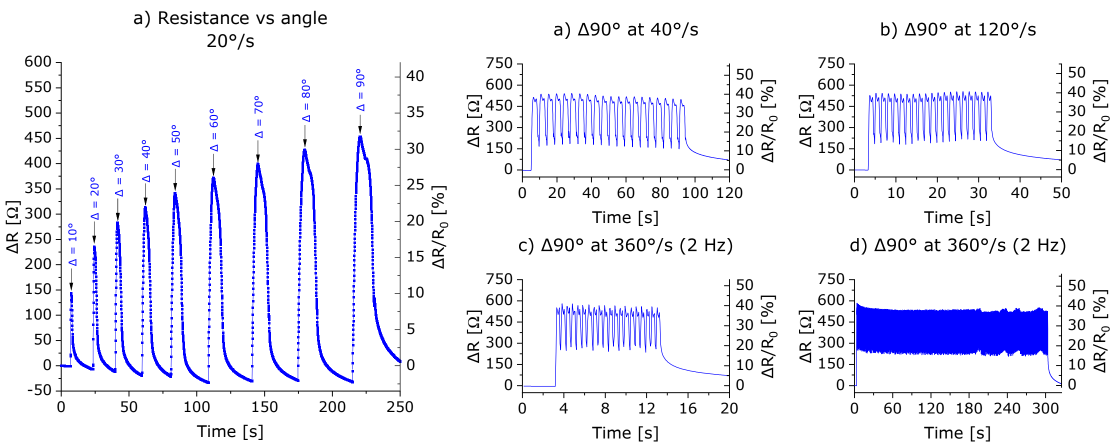

Figure 3.22 – Step response of the bending sensor when **a**) bending at subsequently increasing angles at 20°/s. Dynamic response of 20 cycles bending at an angle of 90° (total angle of 180°) at **b**) 40°/s, **c**) 120°/s, **d**) 360°/s, and **e**) 360°/s for 5 minutes.

A longer test of 600 cycles (5 minutes) was performed at 360°/s to study the resistance response over an extended time of operation (Figure 3.22 g), the maximum resistance increase here was 528.9±11.6 Ω (37.6±0.8%). Some drift of the peak response value was again observed in this test at a value of 1.92±0.14%.

Comparatively, the drift is small with respect to the peak resistance values. Considering this, we can conclude that behaviour of the simple sensor is repeatable for angles between 20° and 90°. Yet it was also observed that the bending angle speed had an effect on the measured response, and it is likely that it has an effect on the slope of the sensitivity of the sensor. Therefore, the response of the sensor should be evaluated for a number of bending speeds to fully understand its influence.

3.3.5 Comparison between printing approaches

The resistivity of the FDM printed plates was around 16.17±0.84 Ω cm which makes the material significantly more resistive in comparison to the embedded silver features by a factor of 10^6. Ideally to prevent high power consumption, the resistivity of the material should be as low as possible. Moreover, if we wish to integrate several sensing elements, such as piezoresistive sensors, in a single device the conductors connecting them should not be able to influence their readout. With the few conductive filaments available, none are available that are highly electrically conductive and flexible. This does not allow for the printing of highly electrically conductive and flexible sensors or devices by FDM only.

Furthermore, the electrically conductive features that can be produced are always limited to the nozzle size of the FDM printer. With a standard 400 µm nozzle, the linewidth will always be in this range with a layer thickness of around 100 µm. In fact, with FDM printing it is difficult to print thinner features, unless specialised equipment is used.

When printing capacitive sensors using FDM only, we observed the inadvertent result of conductive particles mixing in to the TPU dielectric. This did result in an increase in dielectric constant from plain NinjaFlex of about 2.3-3[152] to 7.1-11.2, which helps increase the response of the capacitive sensor. Indeed, this effect resulted in the sensor produced using laser sintering to have a lower sensitivity of 0.028 %/N versus the fully FDM printed one at 0.087 %/N which both had dielectric layers with a thickness of 200 µm. A further reason for the decreased sensitivity of the capacitive sensor produced using laser sintering is that the silver layer is slightly thinner than the surrounding FDM material. This could result in materials not bonding well and an air pocket being introduced, which reduces the capacitance due to a reduction in permittivity. Even if the fully FDM printed sensor had an increased sensitivity, the reproducibility for these sensors is not sufficiently high.

Lastly, with the laser sintering approach it is possible to incorporate more complex shapes and thinner layers into the material instead of only creating stacks. By printing layers in succession, 3D features such as vias and non-planar plates could be realised. Even so, this technique is still limited in dimension by the need to combine it with FDM material.

3.4 Summary and Conclusion

In this chapter a simple in-situ laser sintering process was developed using a low-cost commercial laser diode to sinter conductive inks and enable their integration into structural materials with a thermal processing mismatch. This was demonstrated using the laser sintering of highly conductive polyurethane based silver inks deposited by Direct Ink Writing (DIW) on top of thermosensitive layers printed by Fused Deposition Modelling (FDM). With this technique simple sensor prototypes could be rapidly constructed in a simple and easily adaptable fabrication process.

By investigating the sintering parameters, we showed that the influence of laser power, scanning speed, and number of passes played a significant role. For dogbone shaped structures, an ideal laser sintering power range was found at 0.7-0.8 W, with the scanning speed influencing the achievable resistivity values. A laser scanning speed of 10 mm/s was selected as a compromise to achieve a low resistivity value (58.2±7.7 μΩ cm) while preserving the structural material.

To achieve functional layers, square structures made up out of multiple joined lines were printed for which the found parameters were less effective due to an increased thickness of the ink during deposition. However, the resistivity values of these films could be reduced by increasing the printing speed and tuning the power appropriately. The correlation found between the resistivity and deposition thickness indicates that the effectiveness of our in-situ laser sintering is directly linked to the amount of material deposited and the thermal gradient present during sintering. By diluting the ink, a lower thickness was achieved and more precise control on the deposition thickness was obtained. With this ink the lowest resistivity values for the square features were achieved at 104.2±21.0 μΩ cm. In brief, the diluted ink proved more favourable due to its consistent thickness, independent of the printing parameters, but at the cost of a slightly increased resistivity. Comparatively to FDM printed conductive layers, the sintered silver layers had a resistivity which was a factor 10^6 lower.

Using the sintering parameters determined by our analysis, we fabricated an assortment of components and sensors to demonstrate the capability of integrating highly conductive layers through our fabrication technique. A low resistance conductor was realised, which was able to function up to 5% strain with a less than 1% increase in resistance. FDM printed conductors could only reach up to 2% strain before breaking and had a significant resistance increase.

We also fabricated a capacitive sensor with a highly linear sensitivity of 4.47±0.12 fF/N

(0.027±0.001 %/N) and the ability to accurately track an input force of tens of Newtons. This sensor functioned reversibly in dynamic operation in the low Hz range. FDM printing a similar design resulted in high dielectric values due to intermixing of the carbon particles into the dielectric. While this led to a more sensitive sensor (0.092±0.009 %/N) the varying dielectric permittivity made for sensors that could not be FDM printed in a reproducible manner.

Lastly, we extended our laser sintering technique to a piezoresistive PDMS composite which was implemented as a simple bending sensor. This sensor exhibited a linear response when detecting bending angles from 20° to 90°. When cycled 600 times at an angle of 90°, the peak resistance shifted by about 2% only.

The laser sintering technique presented here shows promise to be extended to a larger set of materials, in order to allow for more advanced sensor designs and other applications. Digital fabrication processes such as these are ideally suited for rapidly manufacturing custom tailored and integrated devices in a continuous manufacturing process. Even so, the combination with FDM always will retain some drawbacks, such as the high surface roughness, limitations in what geometries can be realised, and its thermosensitivity. Therefore, in the next chapter we decided to focus our attention on the DIW printing of silicone materials for structural purposes instead. These materials are thermally stable and allow for the annealing of silver features directly in an oven or on a hotplate, without requiring the use of laser sintering.

4 3D printing of mechanical sensors targeted at human gait analysis

Mechanical sensors are ideally suited for the monitoring of human motions as they are simple, reliable, and consume little power. So far, the most well established and popular ones used in soft and flexible electronics have been piezoresistive and capacitive sensors[97]. However, until this time only a handful of these sensors have been completely 3D printed[100]. Often the choice is made to make these sensors using a combination of 2.5D and 3D printing techniques or even with conventional soft material processing techniques[98]. Several soft sensors have been created entirely by Direct Ink Writing (DIW)[78], [120], but overall the topic is little explored. The digital nature of DIW printing would enable rapid fabrication, easy integration, and quick modification of soft sensors which could find their way into personalised smart objects.

One key challenge is that readily printable structural and functional materials to create such sensors are missing and require synthesis. Reinforced DIW printable silicone inks can be created using rheological additives such as fumed silica or other additives. Crystalline Nanocellulose (CNCs), a natural polymeric nanofiller used to make other polymers printable[57], could be integrated into silicones to give it the required printing properties.

In this chapter the results are presented on the development of a material system and the designs of soft DIW printed mechanical sensors. Using our developed processes we aimed to design sensors suitable for the detection of normal pressures and shear forces for gait monitoring. For this type of motion sensing, insoles with optical shear sensors have been previously demonstrated[153], but 3D printed shear sensors have not been utilised for real world gait monitoring. Due to the digital nature of 3D printing, these sensor designs can easily be altered on the fly[3], which we exploited to redesign parts of our sensors whenever required during their development. To test the sensors, protocols were developed to evaluate them in terms of static and dynamic performance. Test results on the static, hysteresis, and dynamic response of the created sensors are presented for several material combinations and design.

The work in this chapter was performed in collaboration with the Complex Materials Laboratory at ETHZ and the Cellulose and Wood Materials Laboratory at EMPA. This chapter is partially adapted from a conference proceeding submitted to the IEEE Sensors 2020 Conference[a] and a scientific article based on the work produced within this project which has been submitted for peer review[b].

4.1 Sensor designs and working principles

In this section the design and mechanisms of the produced sensors are highlighted. Both piezoresistive and capacitive normal sensors were developed. These sensors were designed to be able to measure normal pressures that occur during walking, which for an average person is between 325 to 460 kPa [154], [155]. High load activities, such as running, can increase these loads by a factor of at most 1.67-2.75 times[156], [157]. The large spread in this factor is caused by differences in body weight and running speed and leads to a large variation from person to person. Therefore, we decided to target a maximum pressure of 1000 kPa.

Furthermore, we also wanted to be able to measure shear forces between the foot and the ground as data on these forces is sparsely available. These forces can be anywhere from 20% of the bodyweight when walking on a flat surface up to 40% of the bodyweight when running on an incline[158]. However, these values were captured from test subjects wearing shoes and thus do not represent the actual shear forces between the foot and ground. Even so, researchers working at Swiss BioMotion Lab at the Lausanne University Hospital (CHUV) confirmed that these values were in the correct range. From this we established to target the sensing of shear forces in the range of 20% of the bodyweight.

Lastly, these sensor were designed such that multiple of these could be integrated into a personalisable wearable produced entirely through DIW printing. This is demonstrated further in Chapter 6.

4.1.1 Piezoresistive normal sensor

Piezoresistive sensors function by means of a strain gauge that, when deformed, results in a change in the electrical resistance. This can be used to couple a force to a normal pressure.

[a] Fully 3D Printed Mechanical Pressure Sensors: A Comparison of Sensing Mechanisms by Ryan van Dommelen, Julien Berger, Rubaiyet Haque, Marco R. Binelli, Gilberto de Freitas Siqueira, André R. Studart, and Danick Briand

[b] Digital Manufacturing of Personalised Shoe Insoles with Embedded Sensors by Marco R. Binelli and Ryan van Dommelen, Yannick Nagel, Jaemin Kim, Rubaiyet Haque, Gilberto de Freitas Siqueira, André R. Studart, and Danick Briand

Working principle

Piezoresistive sensors come in many forms but frequently take the form of either a meandering strain gauge, cantilever, or suspended film[159]. When the strain gauge is deformed it causes a strain that results in a change of resistance. These sensors typically display a resistance increase due to tensile strain (positive piezoresistivity) or a decrease due to compression (negative piezoresistivity). Piezoresistive sensor created from polymer composites can display either behaviour by tuning the conductive particle distribution inside of the composite gauge[102], as well as by the positioning of the electrodes. For our sensor we chose to exploit a tensile strain deformation, for which the change between resistance and strain is proportional ($R \propto \varepsilon$), such that it either increases or decreases with increased strain. For a piezoresistive tensile strain sensor the change in resistance ($\mathrm{d}R/R$) can be expressed per

$$\frac{\mathrm{d}R}{R} = \frac{\mathrm{d}L}{L}(1+2\upsilon), \tag{4.1}$$

which relates to the change in strain ($\varepsilon = \mathrm{d}L/L$) and is linked to the Poisson's ratio (υ)[159]. In this chapter we studied the use of a carbon compounded polymeric material for the creation of strain gauges. For such a compound, the applied strain results in a change of percolation which leads to a change in resistance.

Design

For our sensor design we wanted to create a strain gauge that converted normal pressure into tensile strain. This can be easily achieved using carbon compounded silicone[160] on top of two electrodes in the same plane. In this way both electrodes could be printed and processed within a single step. When a normal load is applied to our strain gauge design, the normal deformation leads to a tensile strain. For a linear elastic material, such as silicone, the tensile deformation due to a normal pressure is coupled by the Poisson's ratio and prescribed by

$$\upsilon = -\frac{d\varepsilon_{\text{normal}}}{d\varepsilon_{\text{tensile}}}, \tag{4.2}$$

where the ε_i components are the deformations with respect to individual directions. This is especially true for silicones, which do not change in volume under compression ($\upsilon \approx 0.5$). Therefore, any strain due to normal pressure results in an equal or close to equal tensile strain. A normal strain deforms the gauge in the orthogonal tensile direction which changes its resistance in the longitudinal conductive path, as shown in Figure 4.1 a.

For the sensors we resorted to a design with negative piezoresistivity, as it provides a more sensitive response than a positive one[102]. The chosen composite material requires careful tuning to prevent loss of conductivity through a lack of percolation. The negative piezoresistive normal pressure sensor design is shown in Figure 4.1 b-c.

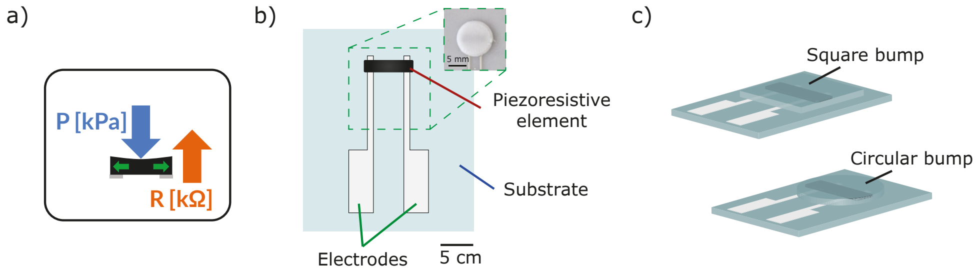

Figure 4.1 – **a**) Transduction mechanism and **b**) top view of the piezoresistive normal pressure sensor design and a **c**) 3D representations of the sensor with both rectangular and circular bumps.

Two electrodes are placed on top of a silicone substrate with a piezoresistive strain gauge measuring 2x7 mm^2 bridging these electrodes with contact pads of 4x10 mm^2. A simple rectangular bump measuring 1 cm^2 and 1.2 mm in height was added over the gauge to help with the force transfer and to assure that a pressure-force relation was established. The effectiveness of an increased force transfer, especially at lower forces, was demonstrated by a master student working on the evaluation of initial prototype sensors[161]. Improvements were made to the design by reshaping the bump to a 1.1 cm^2 circular bump to make it less sensitive to shear forces.

4.1.2 Piezoresistive shear sensor

The piezoresistive sensing principle was also used to create a shear force sensor. By reading out the resistance of two elements, and taking their differential, a sensor was designed that could detect these forces.

Working principle

The working principle of the shear sensor is based on the same resistance-strain relation between the normal pressure and tensile strain. For this load type we assume that both an unevenly applied normal pressure and a shearing force are exerted on the sensor. By using two parallel piezoresistive gauges, that deform at different rates due to both loads, a difference in tensile strains will occur. Subsequently, this leads to a resistance difference with the resistance of one gauge increasing more than the other. A schematic representation of this mechanism is shown in Figure 4.2 a.

Direction of the shear force can be distinguished by defining a "front" and "back" strain gauge and calculating a resistance differential between the two. The equation for this differential can be expressed in the form of

$$\Delta R_{\text{shear}} = (R_{\text{I}} - R_{\text{I},0}) - (R_{\text{II}} - R_{\text{II},0}), \tag{4.3}$$

where R_{I} and R_{II} represent the resistance values under compression of two strain gauges, and $R_{\text{I},0}$ and $R_{\text{II},0}$ their baseline values. When ΔR_{shear} is negative it means that the shear force is in the direction of gauge I, as $R_{\text{II}} - R_{\text{II},0}$ is the biggest term, while when it is positive it is in the direction of gauge II.

Design

An initial design for a shear sensor was made using the working principle with two parallel rectangular strain gauges. Two electrodes and a common ground are placed on the same substrate to bridge two 2x7 mm^2 piezoresistive strain gauges to measure a differential due to an applied shear force. The gauges were separated by a spacing of 3 mm between the two. A 1 cm^2 rectangular bump with a height of 1.2 mm was printed on top of both gauges to aid with the force transfer and shear deformation.

Due to the proximity of the strain gauges the tensile strain would often be very similar and the shear forces hard to extract. As such, a redesign of the sensor was made to introduce strain gauges with compliancy in a single direction. The piezoresistive elements were given a chevron shape with an angle of 135° between the two parts of the V-shape. When a shear is applied in the direction of the shape it will deform easily but will resist deformation in the other direction. As such, larger tensile strains will occur in the more resistive gauge which leads to an increased differential. The dimensions of the gauges were altered slightly for it to fit in a width of 8 mm such that it could fit under the same bump. A spacing of 3 mm between the two gauges was attained.

Both versions of the sensor design are shown in Figure 4.2 b-c.

4.1.3 Capacitive normal sensors

Capacitive transduction is an interesting approach for normal pressure sensing due to its simple transduction mechanisms which prevents the needs for functional materials such as piezoresistive composites. Furthermore, these sensors can yield very sensitive responses. However, they are also quite sensitive to noise and require tailored shielding and electronics to function well. This makes their execution more difficult than a piezoresistive sensor. However,

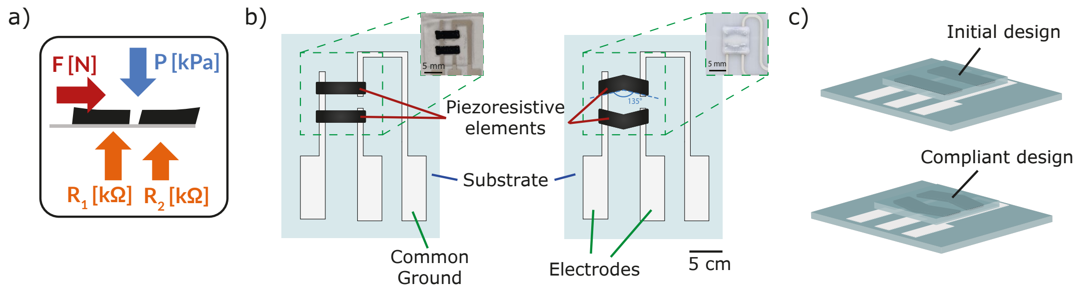

Figure 4.2 – **a**) Transduction mechanisms and **b**) sensor design of the piezoresistive shear sensor and the **c**) 3D representations of the two versions.

to compare the effectiveness of both sensing mechanisms, capacitive normal sensors were also created.

Working principle

The working principle of a capacitive sensor relies on a voltage difference between separated conductive features. By retaining this separation either by geometry, or by a non-conductive material that prevents current flow, an electric field forms. The intensity of this field is called capacitance (C) and is measured in Farad (F). The capacitance increases the closer the features are and decreases when they are removed from each other. Capacitive sensors come in many forms with the most popular being those with parallel plates or finger electrodes[162]. The parallel plate capacitor is, due its simplicity, one of the most popular capacitive sensors. The capacitance of this sensor can be described per the equation

$$C = \frac{\varepsilon_0 \varepsilon_r A}{d}, \tag{4.4}$$

where ε_0 is the permittivity of free space, ε_r the relative permittivity, A the plate surface area, and d their separation. This relation is reciprocal, but with small deformations the response of the sensors can usually be approximated to be linear which makes it attractive for normal pressure sensing. Furthermore, the relative permittivity can be tuned by means of the dielectric material separating the plates, which is a non-conductive material that can be polarised by an electric field to increase its energy density. By using a soft linearly elastic dielectric, normal deformations of this material can be coupled by linear elastic theory to a change in capacitance to create a simple but highly effective sensor as shown in Figure 4.3 a.

Design

A simple sensor was designed consisting of a capacitive stack composed of two parallel electrodes with an overlapping area of 10x10 mm^2, as shown in Figure 4.2 b-c. A bottom electrode was printed on top of the substrate after which a patterned dielectric was printed. The top electrode which overlapped with the bottom electrode was printed on top of this dielectric. No further design improvements were made for this sensor.

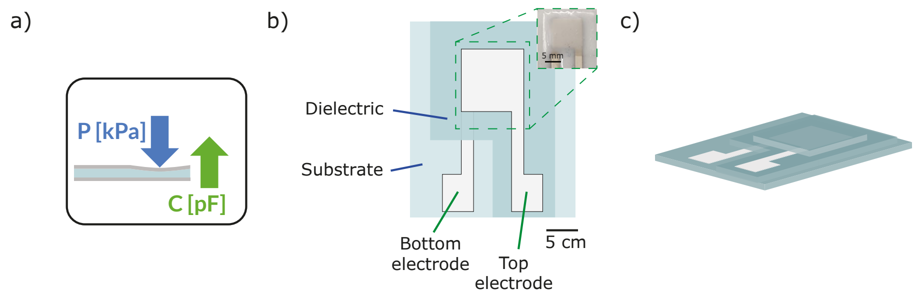

Figure 4.3 – **a**) Transduction mechanisms and **b**) sensor design of the capacitive normal pressure sensor and its **c**) 3D representation.

4.2 Processing and material system development

In this section a brief overview is given of the materials development that enabled the DIW printing of the sensor designs presented in Section 4.1. Two material types were developed to enable the printing of these sensors. A structural self-supporting ink was developed to form the soft material for substrates, dielectric layers, and encapsulation. To enable functional piezoresistive layers, a carbon-black reinforced ink was developed. All electrical connections were made using the commercially available AG520EI silver ink (Chimet S.p.A., Italy) thinned with 5 wt% Chimet 0204IT thinner to allow for better control during printing. Lastly, the fabrication steps and processes are outlined used to produce the sensors using the developed material systems.

4.2.1 Structural material development

As was explained in Section 2.1.2, for inks that are printed by means of DIW it is important that they maintain their shape after deposition. This means that the inks need to exhibit shear thinning, the reduction of viscosity under a shear force such as extrusion from a printing nozzle, and display viscoelastic or gel-like behaviour. Many soft materials exist for the fabrication of wearables but these generally do not display this behaviour. As such, inks need to specifically developed to enable the printing of soft materials in three dimensions.

Our partners at the Complex Materials Laboratory at ETH Zurich and at the Cellulose & Wood Materials Laboratory at EMPA developed a method to reinforce polymers with cellulose particles in the form of Crystalline Nanocellulose (CNC). Therefore, their task in the SFA funded D-Sense project was to develop and synthesise the DIW printable inks required for the sensors, including a silicone ink that could be used to print self-supporting structures. They had previously demonstrated to be able to introduce CNCs into a variety of polymers to make them suitable for DIW printing[57]. A first ink formulation used the surfactant propylene glycol methyl ether (PGME) to stabilise the CNC particle dispersion inside the silicone. Due to curing and processing issues, this surfactant was later switched to the silanisation agent methyl trimethoxy silane (MTMS) which renders the CNC more hydrophic, and resulted in the CNC adhering directly to the PDMS.

Before the improved CNC reinforced ink formulation was established, a simpler to synthesise and readily available ink formulated from 10 wt% fumed silica (HDK 30) reinforced Sylgard 184 silicone (FS-PDDMS) was used to print the first prototype sensors. While complete sensors can be 3D printed with this ink, it does not retain its shape very well after deposition and will deform during curing. Therefore, these inks were only used to build sensor prototypes for the evaluation of the carbon loading in the strain gauges.

CNC reinforced silicone composites were created from multiple commercially available platinum silicones including EcoFlex and Dragonskin (Smooth-On, Inc., Macungie, PA, USA). However, these silicones had major adhesion issues both between printed layers and other materials leading to delamination under compression. Due to these issues a structural ink composed of CNC reinforced Sylgard 184 (Dow Inc. Midland, MI, USA) was developed instead.

To enable the printing of this Sylgard 184 based ink, the ink had to be reinforced with at least 5 wt% CNCs (CNC-PDMS) which were functionalised using methyl trimethoxy silane (MTMS) such that they change the ink from a fluid to a viscoelastic material to achieve printability (Figure 4.4 a-b). Furthermore, the amount of CNCs incorporated into the silicone matrix results in different mechanical material properties after curing (Figure 4.4 c). Due to the shear and extensional forces the particles experience inside the ink, they align along the printing path during extrusion resulting in anisotropic mechanical properties. Furthermore, the resulting ink is self supporting and can be printed with infill densities down to 10% (Figure 4.4 d).

To be able to print more rigid multi-layer structures, such as the bump, a 12.5 wt% CNC reinforced silicone ink was required to prevent flowing and retain a stable structure. Inks with a lower CNC concentration of 5 wt% flow more, in comparison to inks with higher loads, which leads to smooth surfaces (R_q = 4.16±1.53 µm) with a roughness at least 8 times lower than surface printed from inks containing 12.5 wt% CNCs Figure 4.4 e. Features which require a flat surface can be more easily printed on top of this material such as conductive films.

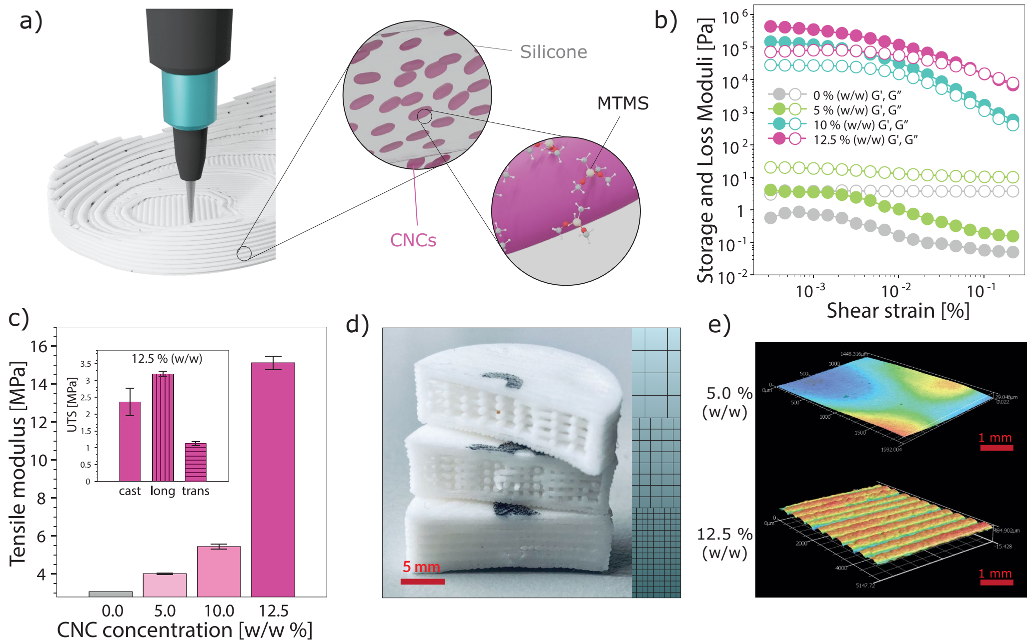

Figure 4.4 – Crystalline nanocellulose (CNC) reinforced silicone ink and its printing. **a**) Reinforcement with MTMS silanised CNCs allows for the printing of 3D silicone structures. **b**) Rheological properties and **c**) tensile moduli at different CNC loadings. **d**) Stack realised using different infill densities, from bottom to top: 100%, 50%, 25%. **e**) Confocal microscopy measurement of silicone inks with 5 and 12.5 wt% CNC reinforcement.

4.2.2 Piezoresistive material development

A formulation using Sylgard 184 as a base material infused with EC-300 KetjenBlack carbon black (CB), using isopropanol to disperse the particles within the composite, existed in our laboratory and has been frequently used for the manufacturing of soft electrodes for stretchable Dielectric Actuators[163], and strain sensors[70]. By finely tuning its CB loading percentage it becomes possible to decrease its electrical conductivity and increase its piezoresistivity.

To print the strain gauges for the piezoresistive sensor, we wanted to develop a DIW printable ink. We developed this ink by compounding the existing formulation with 10 wt% fumed silica, a widely used rheological modifier, to give it the necessary shear thinning properties. In order to understand the influence of the concentration of carbon black on its conductivity, we explored the compounding of several percentages up to 10 wt% CB.

Films were created from this ink by stencil printing that showed that when the CB loading was increased from 5 to 10 wt% the resistivity decreased from $0.35\pm0.02\ \Omega\,\mathrm{m}$ to $0.04\pm0.00\ \Omega\,\mathrm{m}$, a difference of $0.31\pm0.02\ \Omega\,\mathrm{m}$. In comparison, when increasing the loading from 4 to 5 wt%

the resistivity changed by a value of 1.84±0.2 Ω m. The piezoresistive effect is linked to the base resistivity, and lower loadings will result in more sensitive sensors. To understand the influence of CB loading on the resistivity we developed inks with a maximum CB loading of up to 5 wt%.

Using the same ink developed for stencil printing, we DIW printed several normal sensor prototypes with piezoresistive gauges. However, we found that the ink was very liquid and unable to hold its shape well, even with the addition of fumed silica. The prototype sensors printed from this material showed a variance in response of up to 30%. The main suspect was the isopropanol used to disperse the CB in the ink, as it has a short chain length, and the solvent polarity and dielectric can have an effect on the CB dispersion and particle agglomeration[164]. Therefore, we decided to investigate the role of the solvent on the printing of the ink and resistivity of the material.

Sedimentation test

To start, several alcohol-CB mixtures were tested and their stability checked by a simple sedimentation experiment. For this test several alcohols were tested including isopropanol, ethanol, butanol, pentanol and octanol. As shown in Figure 4.5, isopropanol and ethanol based suspensions sedimented more rapidly than the other alcohols, and octanol was observed to be the most stable. In part this is due to the difference in chain length between ethanol and octanol, the latter which has a longer chain length, resulting in a difference in polarity.

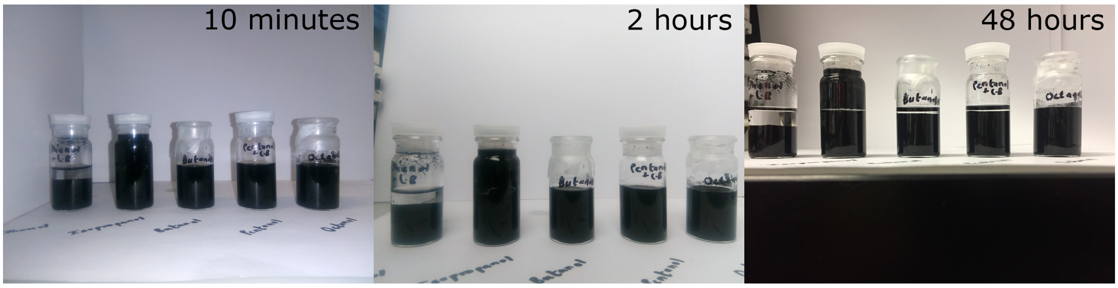

Figure 4.5 – Sedimentation experiment of carbon black (CB) suspended in, from left to right, ethanol, isopropanol, butanol, pentanol and octanol, which were inspected at several time checkpoints.

To understand the particle distribution and electrical characteristics, we evaluated DIW printed films made from silicone inks compounded with solvent dispersed carbon black (CB-PDMS). To disperse the carbon black in the silicone mixture we selected octanol as it was the most stable. We then compared the DIW printable inks created with this solvent to the isopropanol formulation and one without any solvent. The latter ink was analysed as a way to understand the influence of the presence of alcohol during printing.

CB-PDMS ink preparation, film printing, and resistivity evaluation

CB-PDMS mixtures were prepared with a CB loading set at 3.75 wt% and 4.25 wt%. First these were mixed by Thinky Mixer, then refined by three-roll mixer and finally mixed in the Thinky Mixer one last time to create a homogeneous paste. Squares measuring 12.5 mm x 12.5 mm were printed at ETH using a RegenHu 3D Discovery, dried and fully cured for several hours at 80 °C in an oven to evacuate any remaining solvent completely from the composite films. The printed samples were then analysed at EPFL by bisecting them and photographing their cross-sections using a Keyence VH-X Digital Microscope. Within the cross-sections of the films (Figure 4.6) a difference in particle dispersion can be seen. Inks created using alcohol show a stratification that is not present for those created without any solvent (Figure 4.6 a). This indicates that the presence of alcohol influences the particle dispersion of the cured printed films.

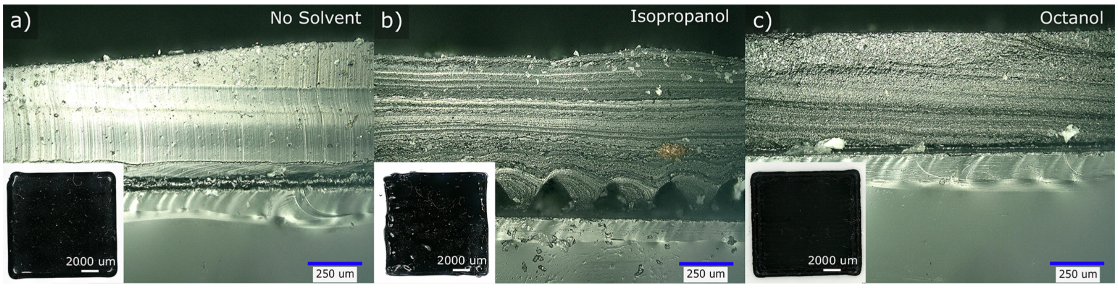

Figure 4.6 – Cross-sections and optical images of the cured CB-PDMS composites for inks **a**) without any solvent, with **b**) isopropanol as a solvent, and **c**) octanol as a solvent.

The sheet resistance of each printed film was measured with an Agilent 34410/11A Digital Multimeter in 4 point probe mode by directly placing the probe on the printed surface. An average thickness of 499.5±105.4 µm was measured using a Keyence VK-X 3D Laser Scanning Confocal Microscope. This thickness was used to calculate their resistivity. However, among all tested samples only for those created with octanol, conductivity was seen with their average resistivity measured to be 3.2±0.6 Ω m with no clear influence of the CB loading. The other films showed no detectable conductivity. It is likely that either the lack of alcohol, or by using a volatile alcohol such as isopropanol, the percolation of the carbon network is reduced which results in an non-conductive material. This was further corroborated by experiments performed for inks which had part of their alcohol removed before printing during processing by vacuum extraction, which were not electrically conductive either.

CB-PDMS films with pentanol based inks

Further tests with octanol based CB-PDMS did not result in DIW printed films with reproducible resistivity values. Therefore, we decided to investigate if instead pentanol, one of the solvents found to be stable during the sedimentation test, could be used instead. Pentanol is similar to octanol but has a shorter chain. Furthermore, it has previously been shown to effectively disperse carbon particles within DIW printable inks without the inks drying out during printing[165]. Another advantage over octanol is that pentanol has a lower boiling point, at 138 °C compared to 194 °C for octanol, meaning that it will evaporate faster from the ink during curing and potentially reduce processing time. Furthermore, we extended the range of CB loading to check its influence.

Pentanol based CB-PDMS inks were developed with three CB loadings of 3, 3.75, and 5 wt% to evaluate its influence on the resistivity. Films printed from the pentanol based CB-PDMS inks had resistivity values of 18.3±5.2 Ω m, 11.2±7.6 Ω m, and 0.9±0.1 Ω m for the 3, 3.75, and 5 wt% CB loadings, respectively. These resistivity values are significantly higher than for the octanol ink, with a larger spread of data. Comparatively, films stencil printed from the old CB-PDMS isopropanol ink had a resistivity of 0.35±0.2 Ω m at 5 wt% CB, which means that the pentanol based ink had a resistivity of a factor 2.52 higher.

A full overview of the resistivity values found for the tested inks in comparison to the resistivity evaluations of stencil printed films created from the isopropanol CB-PDMS ink formulation are shown in Figure 4.7.

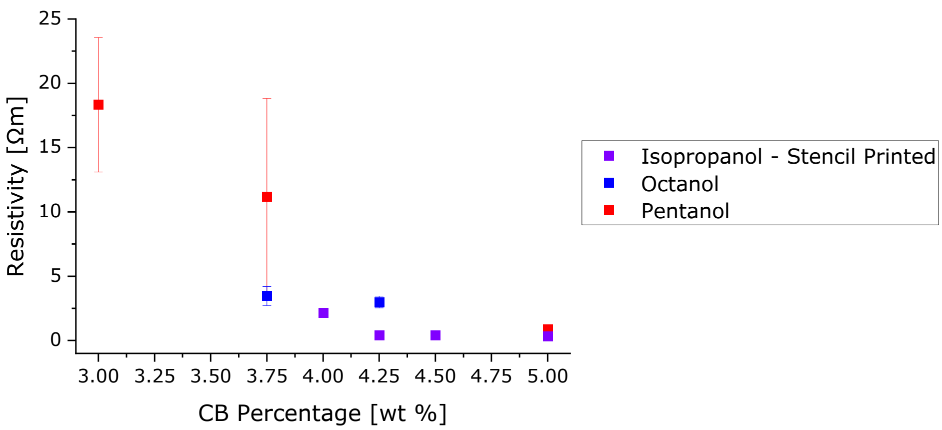

Figure 4.7 – Resistivity values measured for the DIW printed CB-PDMS squares printed from inks with octanol and pentanol as dispersion agents and compared to stencil printed isopropanol based ink.

It should be noted that the evaluation of the electrical properties of the material can be influenced by the manner it is contacted. Directly interfacing silver contact pads to the film allowed for a less noisy read out than probing the film directly. Using a contact pad likely creates a more conformal and larger contact surface with the uncured silicone.

This experiment only provided us with the resistivity data, which is limited to giving an indication of what the piezoresistive behaviour of the ink will likely be like through the status of the CB network percolation. Films with a higher resistivity will result in materials with weaker networks which are likely more sensitive to manipulation of their electrically conductive network. Therefore, we decided to use the stable pentanol based CB-PDMS inks. These were integrated into strain gauges with CB loadings of 3.5, 4, 4.5 and 5 wt% to be able to directly evaluate their piezoresistive properties. As such, the CB-PDMS and sensor development continued in parallel. To further understand the influence of alcohol and CB loading on the DIW printing of piezoresistive and conductive silicone ink, and the resulting structural compositions of the cured films, a larger study could be envisioned.

4.2.3 Fabrication cycle and processing steps

Sensors were fabricated from both the FS-PDMS and CNC-PDMS inks at the ETHZ Complex Materials Laboratory either by myself or by two members of the lab using a RegenHu 3D Discovery equipped with pressure driven direct ink writing extruders from the developed materials treated in the section before. For sensor incorporated directly into a multisensor platform, the printing was performed using a custom build StepCraft 420 3D printing platform with integrated Direct Ink Writing tools, a heated bed, and a plasma gun. Both printers are shown in Figure 4.8. The full fabrication process, which will be described here, is illustrated in Figure 4.9.

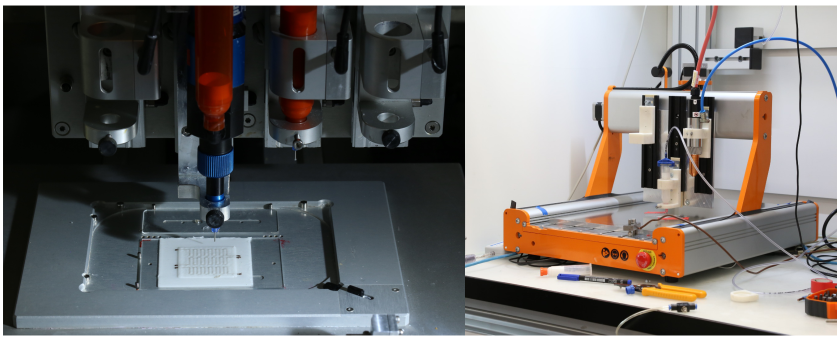

Figure 4.8 – The RegenHu 3D Discovery (left) and Stepcraft 420 (right) DIW printing platforms used to produce the sensors at the Complex Materials Lab at ETHZ.

Substrate and dielectric fabrication

Initial sensor prototypes had their substrates created from Sylgard 184 reinforced with 10 wt% fumed silica. This material was printed using a 20 Gauge (ID = 0.61 mm) conical metal nozzle at a pressure of 4.5 bar, printing speed of 15 mm/s, and a tip to substrate distance of about 450 µm. The substrate was cured for 1 hour at 80°C in an enclosed oven until it was no longer tacky.

For sensors composed of CNC reinforced Sylgard 184 (CNC-PDMS) a preeflow EcoPen (ViscoTec GmbH, Germany) precision dispensing tool was used. Using this tool the flow of ink could be finely controlled to allow for more uniform deposition. The CNC-PDMS ink was printed using a pressure of 3-5 bar, and a flowrate of 120-200 µm/min was selected depending on the CNC content and the flow of the material. This content varied during the development of the ink and lay between 5-22.5 wt% and was highly dependent on the surfactant used to introduce the CNCs into the silicone. A printing speed of 10 mm/s, tip distance of 500 µm, and centre-to-centre spacing of the printed lines of 600 µm were used during printing. The CNC-PDMS was cured for 30-60 minutes at 80 °C on the integrated heat bed depending on the step in the process. Dielectrics of the capacitive sensors were printed in the same way.

All inks were printed using a infill orientation that changed by 90° every layer, such that the layers formed a cross-hatched pattern which reinforced the final material strength.

Plasma activation

To improve bonding between the CNC-PDMS and other materials the substrates and dielectrics were treated in a Harrick Basic Plasma Cleaner using atmospheric gas at a power of 18 W for 2 minutes. When printing the sensors using the StepCraft a Relyon plasmabrush PB3 was used to activate the surface without having to remove the samples. The plasma gun was supplied with atmospheric gas at 1 bar with a 70% of its maximum power supplied at a plasma frequency of 54 Hz. A working distance of 20 mm, linespacing of 5 mm, and a scanning speed of 70 mm/s were used to scan the entire surface and provide a total surface activation.

Electrode fabrication

After the plasma treatment, the electrodes were printed on substrates and dielectrics using the thinned (10 wt%) Chimet silver ink by depositing it through a pressurised luer lock syringe with a 0.5" (12.7 mm) long 25 gauge (ID = 0.26 mm) needle. A printing pressure of 1.7-1.9 bar, printing speed of 8-10 mm/s, and center-to-center spacing of 100 µm were used to create continuous lines. The tip distance was set to 100 µm. After deposition the samples were returned to an enclosed oven and cured at 120 °C for 30 minutes.

Piezoresistor fabrication

For the piezoresistive sensor, a second plasma treatment was performed using either the plasma cleaner or plasma gun to increase the bonding between the silicone substrate and the silver electrodes with the piezoresistive strain gauge. The CB composited Sylgard 184 silicone (CB-PDMS) was prepared as per the steps described in Section 4.2.2 with pentanol as a solvent and printed using a conical 25 gauge (ID = 0.26 mm) plastic nozzle at a pressure of 0.75 bar, printing speed of 10 mm/s, tip distance of 200 μm, and a centre-to-centre spacing of 200 μm. Two layers of 200 μm each were deposited on top of each other to achieve a 400 μm thick strain gauge. The entire sensor was then put in an oven at recommended temperature of 80 °C as per the datasheet for a duration of at least 3 hours to evaporate the pentanol and fully cure the material. An increased temperature can speed up the curing process but also could lead to introduction of air bubbles.

Capacitive sensor fabrication

For the capacitive sensor, after the printing of the electrodes on the substrate, a dielectric was printed on top of these after plasma activation using the same method as used for printing the substrate. Then, a second plasma treatment was performed using the plasma cleaner to print a second electrode overlapping the first which was processed in same way as the first electrode.

Bump fabrication

For both sensors, a final plasma treatment was performed before the printing of the bump. For the fumed silica sensors the bump was again printed from 10 wt% fumed silica reinforced Sylgard 184, while for the CNC-PDMS bumps were printed using 12.5-22.5 wt% CNC content. The bump was given a height of 1.2 mm, to have a 0.8 mm layer on top of the strain gauges. The first layer was printed using a tip distance of 300 μm, which was increased to 400 μm for the second layer. Two layers were printed to achieve the final height of the bump after which the sensor was put into an oven for 1 hour at 80 °C to finalise the devices.

4.3 FS-PDMS and CNC-PDMS based normal pressure sensors

In this section the responses of soft normal pressure sensors created from our developed FS-PDMS and CNC-PDMS inks are discussed. First the testing methodology is explained. This methodology was applied to the piezoresistive sensors to retriever their static and dynamic responses, as well as their hysteresis. Finally, the same metrics are presented for the capacitive sensors.

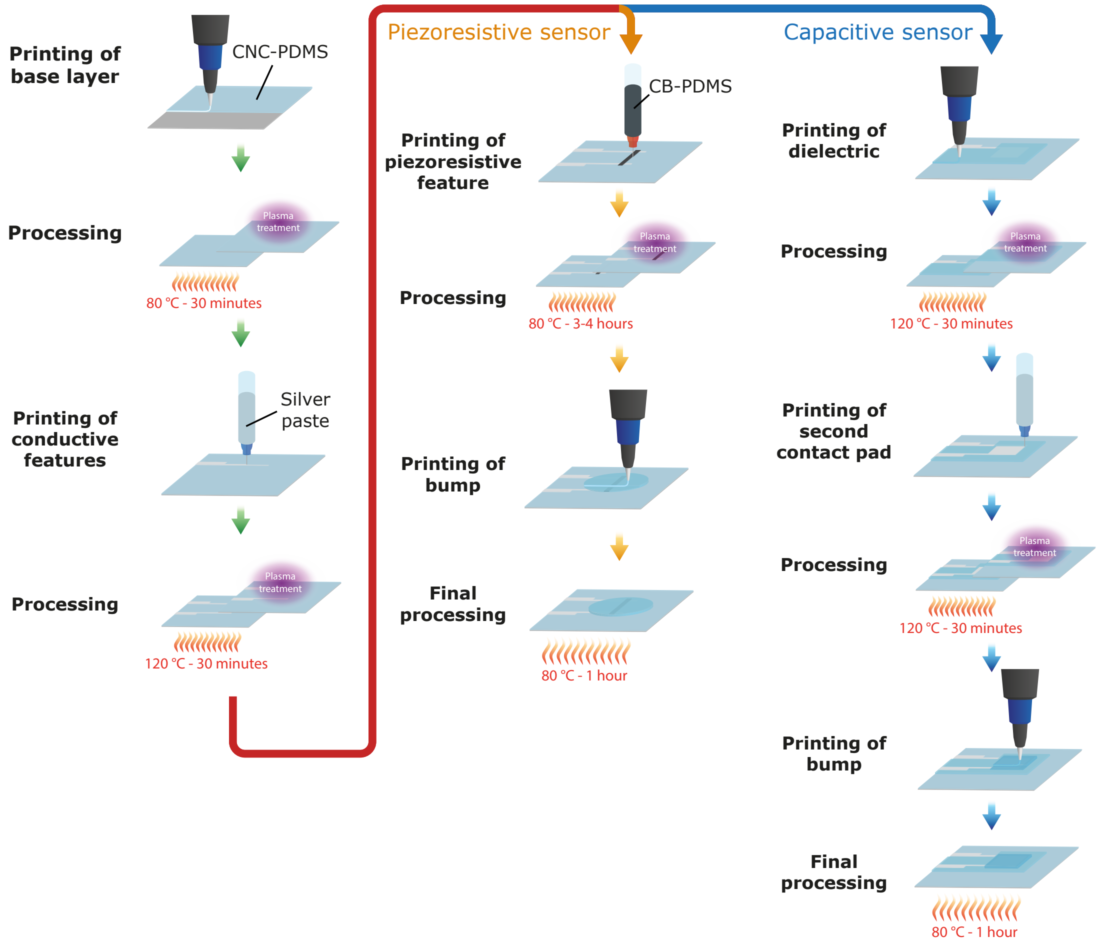

Figure 4.9 – Schematic of the DIW printing and processes used to fabricate the fully 3D printed piezoresistive and capacitive sensors.

4.3.1 Developed testing methodology

Several types of static and dynamic tests were performed to evaluate the performance of the sensors. These tests were performed using an Instron 3340 pull-tester with custom made compression pistons matching the shapes of the bumps. The resistance values were recorded using Agilent 34410/11A Digital Multimeters which were recorded using a LabView script.

Static pressure test

The performance of the sensors was tested by applying a load at 20 kPa/s until a predetermined static load was achieved. This load was applied for a duration of 90 seconds before the pressure was gently released again and the sensor was allowed to recover for 5 minutes. These tests were performed in series, starting at a load of 200 kPa which was increased subsequently by 200 kPa per test up to a final load of 1000 kPa. Later tests included a reversed load application to simulate both a loading and unloading condition.

Hysteresis test

To determine the hysteresis of the sensors pressure cycling tests were performed at constant pressure rates of 20 kPa/s and normal pressures of 200, 600, and 1000 kPa. Starting at 200 kPa, the sensor was cycled three times after which it was allowed to recover for 5 minutes. The same procedure was then repeated at 600 and 1000 kPa. The test were carried out in series to reduce the influence of material relaxation.

Dynamic test

Dynamic responses of the sensors were tested at compressive pressures of 200, 600, and 1000 kPa using a Bose Electroforce 3400 at cycling speeds of 0.5, 1, and 2 Hz. The signals were processed using a Python script to determine the time dependent characteristics of the signal.

4.3.2 FS-PDMS based piezoresistive sensor evaluation for static loads

In this section the results of the piezoresistive sensors printed with fumed silica reinforced silicone (FS-PDMS) as structural material are discussed. To evaluate their performance, they were tested under static loads as described Section 4.3.1. Response curves were created from the force reported by the pull-tester, which was converted into pressure, and the sensor resistance measured by multimeter.

Influence of carbon content for pentanol CB-PDMS strain gauges integrated into FS-PDMS piezoresistive normal sensors

The initial CNC-PDMS based formulation resulted in inconsistent printing results as the ink was very liquid and sometime did not fully cure. Therefore, further development of this material was required before we could create sensors using this type of PDMS ink. As an alternative, a printable Sylgard 184 reinforced with 10% wt fumed silica (FS-PDMS) was used instead to print the substrate and bumps, while we focused on the development of the CB-PDMS ink with pentanol for the printing of the strain gauges.

Several sensors were fabricated using the new CB-PDMS formulations, and their performance was tested and compared to the initial prototypes printed using the isopropanol ink formulation.

The static tests were performed as per the protocol lined out in Section 4.3.1. We evaluated sensors with strain gauges printed from 3.5, 4, 4.5 and 5 wt% CB pentanol inks. The curves of the resistance changes under normal pressure of several of these sensors during the static tests are shown in Figure 4.10.

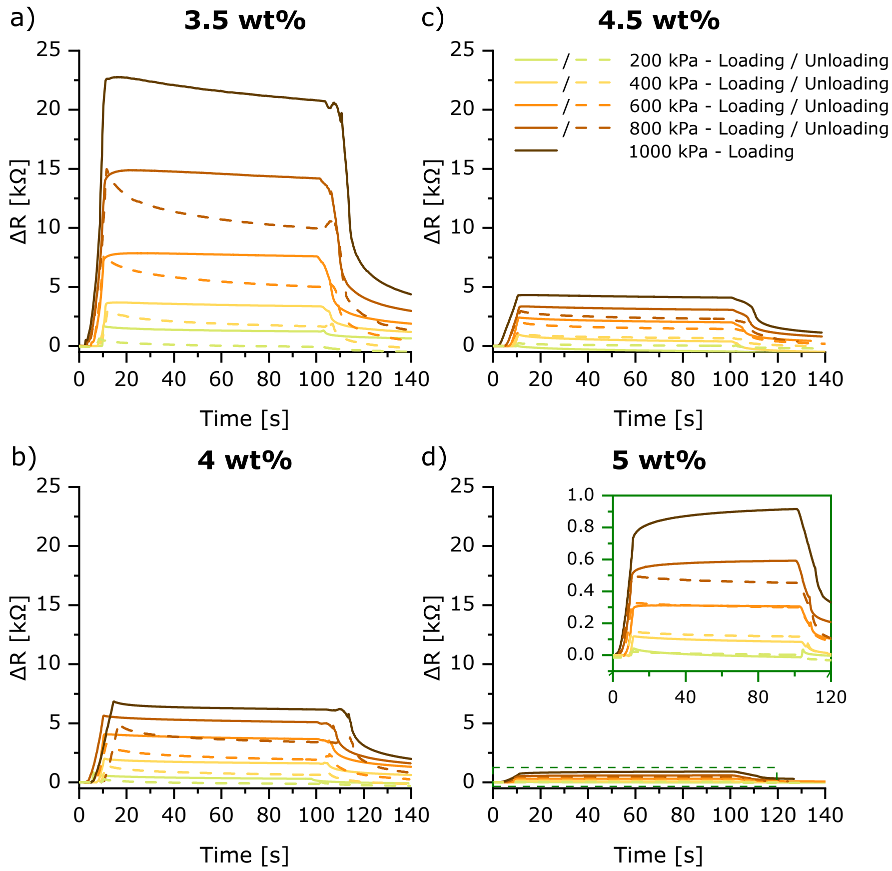

Figure 4.10 – Relative sensor responses during static testing for piezoresistive strain sensors printed from 10 wt% fumed silica Sylgard 184 (FS-PDMS) with strain gauges printed from pentanol based CB-PDMS ink with CB loadings of **a**) 3.5 wt%, **b**) 4 wt%, **c**) 4.5 wt%, and **d**) 5 wt%.

All sensors showed time-dependent responses which decrease slightly over time under the static load. This change over time is most pronounced for the low CB loadings. For the 3.5 wt% carbon loading (Figure 4.10 a) the loading and unloading responses show a significant difference, while this effect diminishes at higher loadings above 4 wt% (Figure 4.10 b-d).

Response curves can be constructed by determining the resistance values from the responses by extracting quantified values 30 seconds after full load application. This allowed us to extract response curves to evaluate the sensor performance as shown in Figure 4.12. From the resistance curves we further quantified R_{max}, the maximum response at 1000 kPa, R_0 which is the value before any load is applied, and S_{abs} and S_{rel} which are the absolute and relative sensitivity values which are expressed in Ω/kPa and %/kPa, respectively. The latter which is calculated as per

$$S_{\text{rel}} = \frac{\Delta R}{R_0}. \tag{4.5}$$

The full characterisation for the strain gauges printed from the developed pentanol based CB-PDMS inks are presented in Table 4.1, and compared with initial prototypes created from the isopropanol based ink formulation.

Table 4.1 – Characterisation of sensors fabricated using pentanol based CB-PDMS ink formulations and a comparison to the sensors fabricated with the isopropanol formulation. Sensitivity values are evaluated for a range of 0 to 1000 kPa.

CB wt%	**Solvent**	$\mathbf{R_0}$ **Preload** kΩ	$\mathbf{R_{max}}$ **(@1000 kPa)** kΩ	$\mathbf{S_{abs}}$ Ω/kPa	$\mathbf{S_{rel}}$ %/kPa
4.08	Isopropanol (Old ink)	15.7±4.3	82.0±26.3	66.3±26.9	0.466±0.222
3.5	Pentanol	13.2±3.6	46.1±18.5	36.2±18.8	0.262±0.072
4	Pentanol	5.0±0.2	8.2±1.0	3.2±0.8	0.063±0.015
4.5	Pentanol	6.8±1.5	10.3±0.8	3.5±0.7	0.058±0.027
5	Pentanol	2.7±0.3	4.5±0.6	1.8±0.6	0.070±0.028

Comparatively to the readily available isopropanol based ink, the pentanol based CB-PDMS ink at the same CB loading had both lower sensitivities (S_{abs}), maximum responses (R_{max}), and initial resistances (R_0). The maximum response decreased by a factor 10 at CB loading of 4 wt% when switching the solvent from isopropanol to pentanol, however this reduced the standard deviation between the sensors from 26.3 kΩ (32.1%) down to 1.0 kΩ (12.2%). This shows that the pentanol based CB-PDMS strain gauges can be more replicably DIW printed.

With the reduction in the initial resistance and and maximum response, the absolute sensitivity of the pentanol based CB-PDMS strain gauges also decreases, compared to the sensors printed using the isopropanol based ink. However, the former sensors had a deviation of 26% between each other, irrespective of the loading, while the latter showed a deviation of 40.6%. It is likely that this change is due to the fact that evaporation during or before printing of the gauges using the less stable isopropanol ink results in the ink drying out[165], which can result in a less optimal carbon distribution. Therefore, the pentanol makes for a better dispersion agent for CB with regards to DIW printable CB-PDMS inks.

The influence of the CB loading could be clearly seen from the sensitivity values in Table 4.1, which are visualised in Figure 4.11.

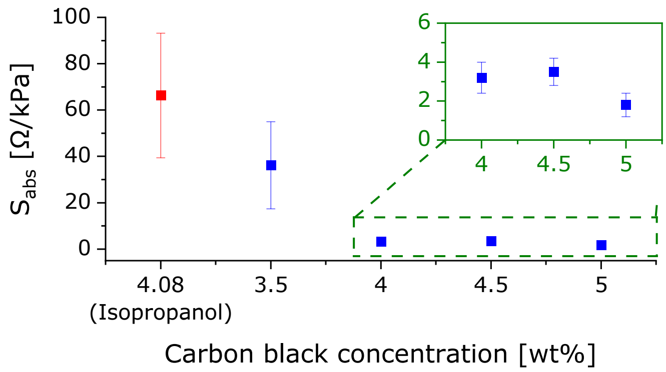

Figure 4.11 – Absolute sensitivity values of the tested sensors with strain gauges printed from the isopropanol based ink formulation and the newly developed pentanol based inks.

With an increasing CB loading the absolute sensitivity reduces as the gauges become more electrically conductive. The 3.5 wt% CB loading produced the most sensitive gauges, while sensitivities were very similar for 4 and 4.5 wt% loading, and reduced again for the 5 wt% loading.

To understand how these distributions in sensitivity occurred we looked at the response curves of the sensors for all pressures both in the loading and unloading phase as shown in Figure 4.12.

The distribution in sensitivity for the 3.5 wt% CB sensors stems from a significant difference in the slopes in-between different sensors. In retrospect, above 4 wt% CB loading the sensor responses are more linear and repeatable, especially for the unloading phase. The responses retain similar slopes for sensors with 4 and 4.5 wt% CB loading, with the response and absolute sensitivity significantly reduced when the CB loading was increased to 5 wt%.

The relative sensitivity remains roughly the same at 0.061±0.018 %/kPa for 4-4.5 wt% CB loading sensors and 0.070±0.028 %/kPa for those at 5 wt% CB loading. This is likely due to the sensors with lower loadings having a large overlap in R_0 values, which likely also influences the obtained sensitivity values, while for the higher loading sensors its decrease leads to a clear change in sensitivity.

Even so, to be able to accurately read out the sensors the absolute sensitivity is more important, which becomes easier with an increased response. Considering this, we decided to further investigate strain gauges printed from inks with 3.5 and 4 wt% loading to try to find a balance between sensitivity and linear performance.

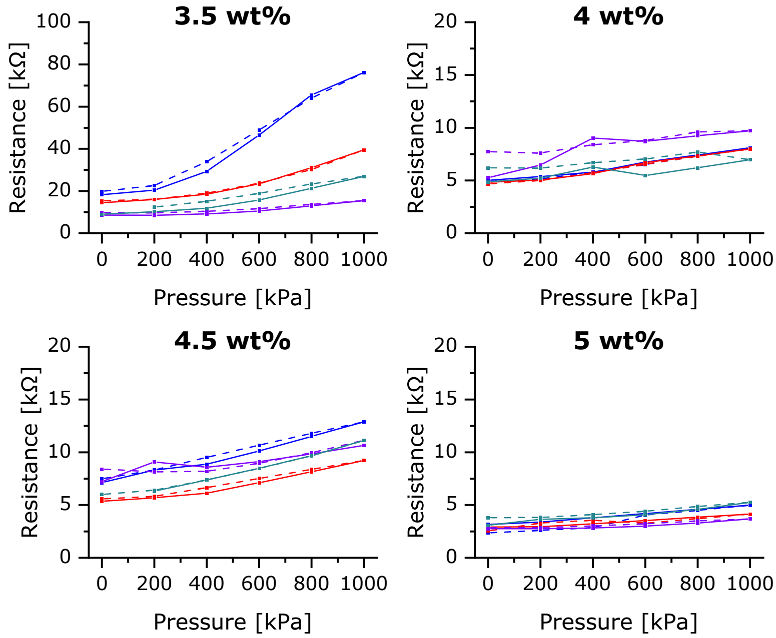

Figure 4.12 – Response curves for selected strain sensors printed from 3.5 wt%, 4, 4.5 wt%, and 5 wt% pentanol based CB-PDMS inks.

4.3.3 CNC-PDMS piezoresistive static sensor response

The effects of the 3.5 and 4 wt% pentanol based CB-PDMS gauges were studied further. However, we now integrated them into sensors that were created from a newly optimised CNC-PDMS formulation. For this ink to disperse the CNCs, the surfactant propylene glycol methyl ether (PGME) was switched in favour of the silanisation agent methyl trimethoxy silane (MTMS), that allowed for better dispersal of the CNCs and their reinforcement in the PMDS. The MTMS-PDMS ink displays ideal shear thinning parameters and better shaped fidelity during DIW printing, which will result in less variance between sensors. The CNC content was tweaked during the production of the sensors to arrive at a balance between printability and fidelity.

Influence of structural material on sensor response

Since the structural material changed, we wanted to evaluate if this had any effect on the sensor response. Two types of sensors were printed, one with a 4 wt% CB-PDMS strain gauges and the other with 3.5 wt% CB-PDSM strain gauges. The sensors were created from highly reinforced CNC-PDMS ink with a CNC content above 18 wt% of which both substrates and bump were printed. The CNC content had not been optimised yet and was tweaked during the production of the sensors. Figure 4.13 shows the static response of both FS-PDMS and

CNC-PDMS sensors.

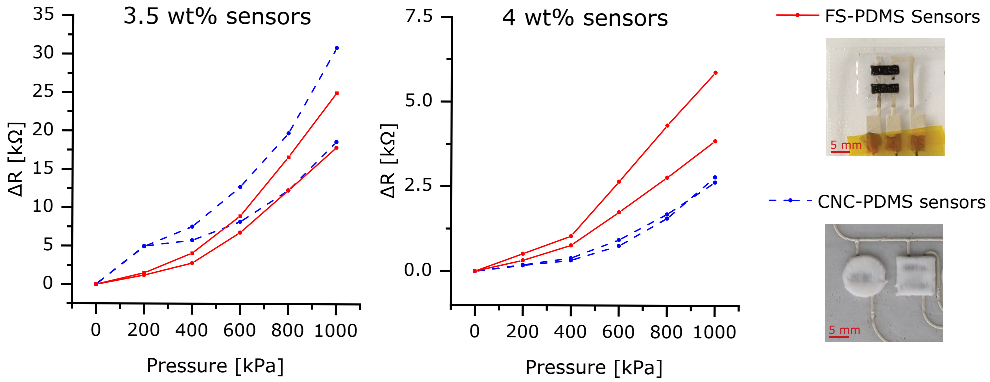

Figure 4.13 – Comparison of sensors printed from 10 wt% fumed silica reinforced PDMS (FS-PDMS) and >18 wt% crystalline nanocellulose (CNC) reinforced sylgard 184 PDMS (CNC-PDMS) for sensors with strain gauges printed from 3.5 and 4 wt% CB inks.

Both sensors with the lowest loading of 3.5 wt% did not show a significant difference in response after the change of the material system. For the 4 wt% CB loading CNC sensors an improved but slightly lower response of 2.7±0.1 Ω/kPa was found. Since the R_0 values remained the same, at values of 4.6±0.3 kΩ for the CNC-PDMS sensors versus 5.0±0.2 kΩ for the fumed silica ones, the error reduction for the sensitivity is most likely the result of the improved printing process with the CNC-PDMS being a much more stable ink. The CNC-PDMS ink flows less after printing than the fumed silica reinforced composite as it is well tuned for printing by shear thinning. This allows for more replicability during printing which allows us to make sensors applicable for human gait sensing.

Based on these resulted we used the new CNC reinforced materials to continue to produce sensors with strain gauges printed from the pentanol based 4 wt% CB loaded ink.

Influence of preconditioning on static response of CNC-PDMS piezoresistive normal sensors

As was already observed from Figure 4.12, the sensor responses were slightly different during the unloading than the loading phase. The reason for this is that the materials that make up the sensors are created from silicones which have long mechanical relaxation times which can influence the sensor performance. Therefore, we investigated the influence of preconditioning the sensor prior to subjecting them to any tests. The preconditioning took place in the form of loading and unloading the sensors 10 times consecutively up to the maximum applied pressure of the test at a pressure rate of 20 kPa/s.

After the 10 cycles were applied, the sensors were left to rest for 5 minutes before starting the test. In order to investigate the influence of this on the sensor response, we performed the static pressure tests on the same sensors both without preconditioning and then, after a 24 hour cool-down period, with the preconditioning performed. The resistance and response curves of these tests are shown in Figure 4.14 .

These tests were all performed on CNC-PDMS sensors with a substrates printed from 5 wt% CNC-PDMS, resulting in a smooth surface, and with bumps, on top of 4 wt% CB-PDMS strain gauges, printed from 12.5 wt% CNC-PDMS, allowing for high fidelity prints. This ink combination was used for all subsequent CNC-PDMS sensors.

Figure 4.14 a-b shows the resistance curves of these sensor under static loads before and after preconditioning. In comparison, the sensors which have been preconditioned have loading and unloading response curves which lay much closer to each other in terms of absolute resistance. Part of this can be explained by the looking at the value of the resistance just before application of a static load (R_N). This value increases with the applied load as it is dependent on the material relaxation and serves as an indicator of the effect of the preconditioning. Post preconditioning the average R_N has a value of 7.24±0.46 kΩ while for the ones without preconditioning it has a value of 6.53±1.04 kΩ.

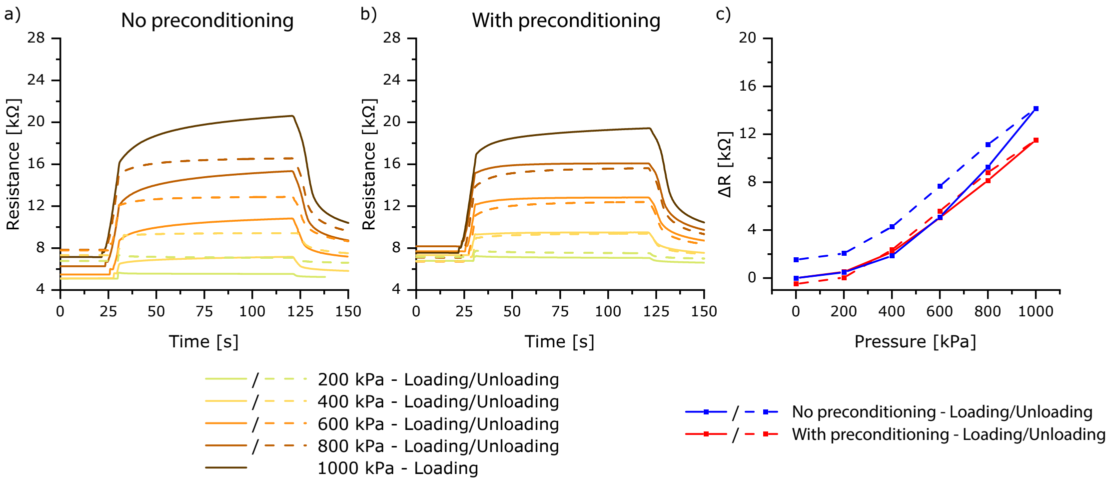

Figure 4.14 – Response curve of a CNC-PDMS sensor with a 4 wt% CB-PDMS strain gauge before and after preconditioning.

Furthermore, for the sensors without preconditioning a larger difference of R_N is seen between the loading and unloading of the sensors as this value significantly increases after being actuated at 1000 kPa. During the loading cycle the average R_N for these sensors is 5.82±0.79 kΩ while during unloading it is 7.43±0.43 kΩ. This means that R_N, even after 5 minutes of relaxation between tests, recovers less well after the maximum load of 1000 kPa is applied. By applying the preconditioning cycles this effect can be diminished.

However, the reduction in resistance before loading, both R_0 and R_N result in a decrease of the absolute response from 15.3±1.4 Ω/kPa to 13.8±0.8 Ω/kPa. However, as was shown in Figure 4.14 c, due to this the linearity improves with the linear fitting quality of the response curve improving from R^2 of 0.975 to 0.993.

Due to this improving the sensor behaviour, we decided to always precondition the sensors before running any tests.

Optimised sensor sensitivity

Further CNC-PDMS sensors were printed with substrates printed from the 5 wt% CNC-PDMS ink and with strain gauges printed from the pentanol based 4 wt% CB-PDMS underneath a 12.5 wt% CNC-PDMS bump using optimised printing parameters. These sensors were tested using the developed protocol including performing preconditioning, a loading cycle, and an unloading cycle. The recorded resistance values (Figure 4.15) show that most sensors responses have similar shapes but have varying response ΔR values for the same pressure.

This divergence influences the sensitivity as it is dependent on the change of resistance with respect to the pressure. The majority of the tested sensors had an increasing response over time, with most drift occurring at 1000 kPa. However, this change is minor in comparison to the increase in response due to the applied pressure. Response curves created from the resistance plots are shown separately (Figure 4.16 a) and in an averaged fashion (Figure 4.16 b). A linear fit was performed to determine the average sensitivity which can be used as a model for the sensor response, excluding the response between 0 and 200 kPa as it had a slightly lower slope.

The sensors had an averaged total resistance change (ΔR) of 12.3±3.8 kΩ (79.8±29.2%), and resistance without load of (R_0) of 6.8±1.5 kΩ. Using linear fits, the average slope was determined to find a global sensitivity (S) of 14.9±0.4 Ω/kPa with a fit of R^2 = 0.997 indicating very little residual. While the fitting matches the average data closely, a reasonably larger difference in sensitivity remains. This difference can be partially attributed by the fact that the full sensor response can vary by as much as 3.8 kΩ. The data of the separate sensor and a summation of the average can be found in Table 4.2.

The main difference in sensitivity thus comes from the resistance difference (ΔR) from one pressure level to the next. This is likely due to the fact that 3D printing is an error prone process, especially when it comes to multimaterial printing. Printing multiple materials introduces errors either due to different material behaviours or by small differences in the printed

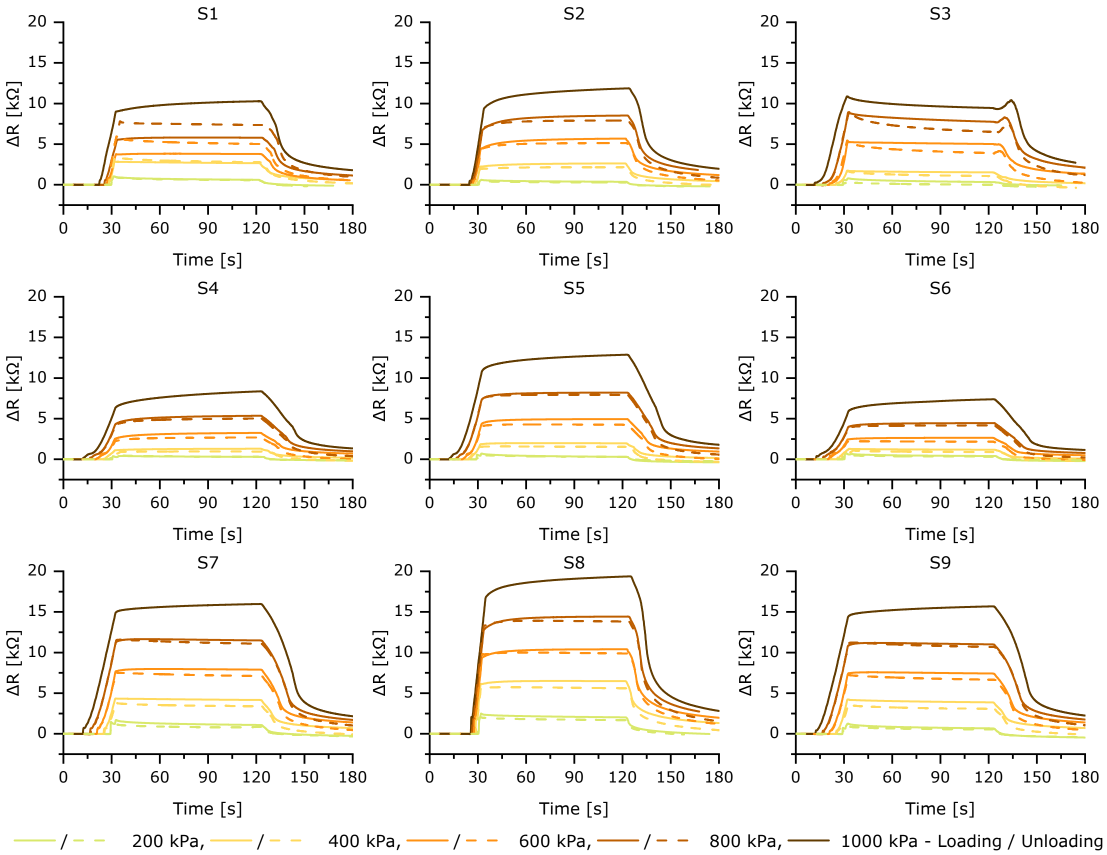

Figure 4.15 – Resistance curves for several CNC-PDMS sensors with 4 wt% CB-PDMS strain gauges.

geometry[166]. Some of these errors can be reduced by tweaking the printing parameters. However, optimisation of these requires a significant study and even then some variation will always be present from one printed sensor to another.

Gauge factor

As previously explained in Equation (2.2), the performance of a piezoresistive strain sensor can be evaluated through the gauge factor (GF). This factor gives an indication of the change in resistance of the sensor at a certain elastic deformation. The gauge factor is defined as

$$GF = \frac{\Delta R}{R_0}\frac{1}{\varepsilon}, \tag{4.6}$$

where ε is the strain. This factor is often used for the evaluation of tensile strain sensors but

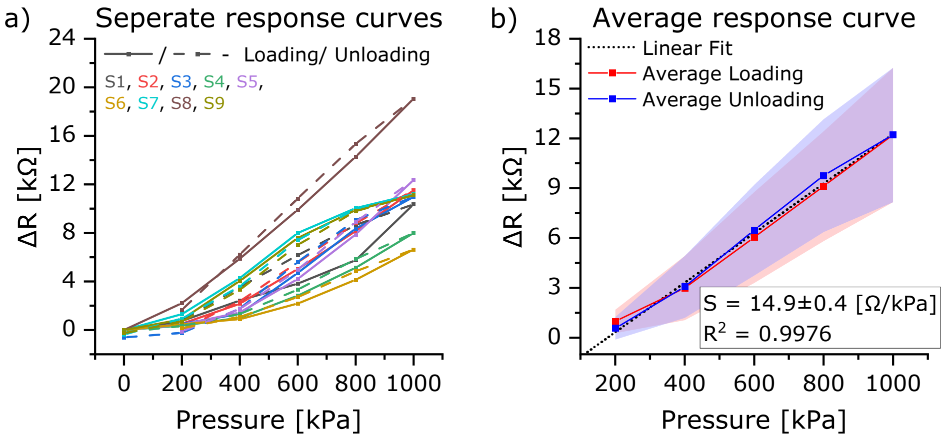

Figure 4.16 – Response curves of CNC-PDMS sensors with 4 wt% CB-PDMS strain gauges with **a**) the individual sensor response and **b**) their average for both the loading and unloading phase.

can also be applied to our normal pressure sensor as it too functions by a change in tensile strain. To evaluate the GF of our sensor design we determined its value through looking at the compressive behaviour of the strain gauges under the bump, neglecting any deformation of the substrate. Since the Poisson's ratio (v) of silicone is close to 0.5, we assumed that the tensile strain was of a similar magnitude as the compressive strain as per Equation (4.2).

Since the strain gauges are encapsulated by a CNC-PDMS bump the strain gauge will not deform at the same rate as the bare material, since the CNC-PDMS and CB-PDMS have mismatching moduli. To tackle this, we first determined the individual compressive moduli, and then calculated their simultaneous compressive behaviour.

First, the 12.5 wt% CNC-PDMS and pentanol based 4 wt% CB-PDMS materials were tested separately to determine their individual elastic compressive moduli. Both moduli were evaluated using a Autograph AGS-X Series (Shimadzu, Japan) at the ETH lab which measured both the compressive strain and stress. From the resulting graphs we used linear fittings to extract the moduli.

During materials development, the compression modulus of the 12.5 wt% CNC-PDMS was already measured to be 7.7 MPa. The compression modulus of the CB-PDMS was determined by measuring its longitudinal strain of a plasma bonded stack of 3D printed 4 wt% CB-PDMS films under compressive stress as shown in Figure 4.17. A linear slope was fitted for the CB-PDMS of 9.22±0.06 MPa for the 400 to 1000 kPa range which represents the compressive strain at a certain stress.

When the sensors is under compression the bump and strain gauge deform at the same time.

Table 4.2 – The initial resistance, resistance change in ΔR and $\Delta R/R_0$, and slopes or sensitivity (S_{abs}) of all tested CNC-PDMS sensors and their averages with standard deviations.

Sensor	R_0 [kΩ]	ΔR [kΩ]	$\Delta R/R_0$ [%]	S_{abs} [Ω/kPa]
S1	6.5	10.4	60.0	11.7
S2	7.1	11.5	62.0	14.4
S3	8.2	11.0	34.1	14.4
S4	4.5	8.0	77.8	9.8
S5	5.8	12.4	113.8	15.6
S6	4.4	6.7	52.3	8.0
S7	7.9	16.2	105.1	19.3
S8	8.4	19.1	127.4	21.5
S9	8.4	15.6	85.7	19.1
Avg. response	6.8±1.5	13.3±3.8	79.8±29.2	14.9±4.3

However, due to the geometrical and material mismatch the stress in the strain gauge (σ_{CB}) will be different under compression than in the case if it was not encapsulated. To calculate the actual stress, we assume that the material system is linearly elastic ($\varepsilon = \sigma/E$). Therefore, to be able to determine the strain in the composite we need to calculate the internal stress in the strain gauge. For this we first we need to calculate the internal force (N_{CB}).

To find this force we assume that both the CNC-PDMS and CB-PDMS strain gauge deform at the same rate and that therefore the strain is continuous ($\delta_{CB} = \delta_{CNC,12.5}$). The strain continuity equation for this two material system is then given as

$$\frac{N_{CNC,12.5}}{E_{CNC,12.5}A_{CNC,12.5}} = \frac{N_{CB}}{E_{CB}A_{CB}}, \tag{4.7}$$

where N represents the internal forces, E the compressive moduli, and A the cross-sectional areas of the bump and CB strain gauge. By assuming that the total internal force for the sensor is a summation of the internal forces in both materials ($N_{bump} = N_{CB} + N_{CNC,12.5}$) we can rewrite Equation (4.7) into an expression of internal force of the strain gauge

$$N_{CB} = N_{bump}\left(\frac{E_{CNC,12.5}A_{CNC,12.5}}{E_{CB}A_{CB}} + 1\right), \tag{4.8}$$

with N_{bump} being the total force applied on the sensor. At a pressure of 600 kPa a force of 66 N is exerted on the 1.1 cm^2 circular bump of the sensor resulting in an actual stress on the strain gauge of 695.12 kPa. From this pressure a normal strain of 7.54±0.04 % is calculated.

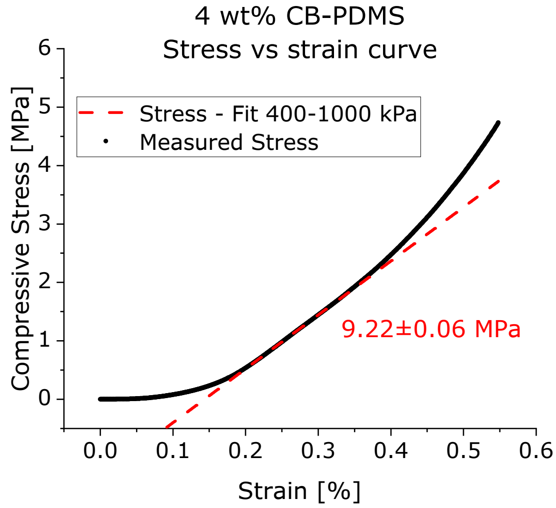

Figure 4.17 – Compressive stress versus strain test of the 4 wt% carbon black-fumed silica-PDMS (CB-PDMS).

To find the tensile strain we need to use Equation (4.2) which couples the normal and tensile strain. The Poisson's ratio for CB reinforced Sylgard 184 has previously been determined to be in the range of 0.4-0.5[167], and using experimental data for a 4 wt% CB-PDMS the Poisson's ratio will be around 0.46. However, it should be noted that this Poisson ratio does not take into account the presence of fumed silica in the silicone and its influence should be further analysed.

With a resistance change (ΔR) of 12.2±4.0 kΩ and an initial resistance (R_0) at 400 kPa of 9.46±2.7 kΩ a gauge factor of 34.0±0.1 is calculated. Not taking into account the multimaterial system, and considering a general E modulus of 9.22±0.06 MPa, leads to an overestimated gauge factor as shown in Table 4.3.

To put this into perspective, our sensors show a higher GF than other printed tensile strain sensors using carbon nanotube (CNT) reinforced FDM filaments of 2.3[29] and 3.7[168], or DIW printed silver-polyurethane inks at 13.3[120]. Normal pressures sensors with electrodes underneath created by partial DIW printing using carbon nanotube-PDMS composites showed a GF of around 2[109]. However, the GF of our sensor is below tensile strain sensors printed using a hybrid printing combination of Digital Light Printing (DLP) and DIW at 251[112]. Even if this signifies that our sensor is more sensitive than most 3D printed tensile strain sensors, the GF is lower those created from doped silicon which can attain factors of 100 and higher[159].

Table 4.3 – Influence on calculating the gauge factor with the influence of the modelling of the material system.

	No correction	With correction	
GF	36.4±0.2	34.0±0.1	-
σ_{CB}	600.0	695.1	kPa
σ_{PDMS}	-	580.4	kPa
ε_{normal}	6.51	7.54	%
$\varepsilon_{tensile}$	2.99	3.46	%
E_{CB}	9.22±0.06		MPa
E_{bump}	7.7		MPa
R_0	9.45±2.7		kΩ
ΔR	9.19±4.0		kΩ

4.3.4 Hysteresis response of the CNC-PDMS piezoresistive normal sensors

Hysteresis analyses were performed for 5 wt% CNC-PDMS DIW printed sensors with 4 wt% strain gauges underneath a 12.5 wt% CNC-PDMS bump. The sensors were tested for their hysteresis by the protocol described in Section 4.3.1. A pressure rate of 20 kPa/s was used, and slowing this rate down showed no significant change. The resulting resistance over time for such cycles at pressures of 200, 600, and 1000 kPa are displayed in Figure 4.18 a.

To evaluate the hysteresis we ideally want to evaluate the sensor response versus the applied force or pressure. For this we analyse the resistance-pressure loops of the sensors between a zero-load and a maximum load point after the first cycle. To process the data a custom python script was written to construct the datasets for the resistance versus force plots. The mechanical hysteresis was then calculated from this data by the formula

$$\delta_h = \frac{R_U - R_L}{R_{max} - R_{zl}}, \tag{4.9}$$

where R_{max} is the resistance at the peak load, R_{zl} the resistance at which the sensors is unloaded (0 kPa). R_U and R_L are the resistance values where the absolute difference in resistance between the loading and unloading cycles is the largest. This point is called P^* and for a sensor with symmetric hysteresis will lay exactly in the middle. In reality, however, this can lay anywhere along between P_{max} and P_0. A visualisation of an ideally symmetric hysteresis curve with all discussed points of interest is shown in Figure 4.18 b.

The python script was also able to calculate the hysteresis for each test by a developed algorithm that categorises and sorts the resistance data per integer value of pressure. For each pressure value the resistance difference in loading and unloading ($R_U - R_L$) is calculated, the

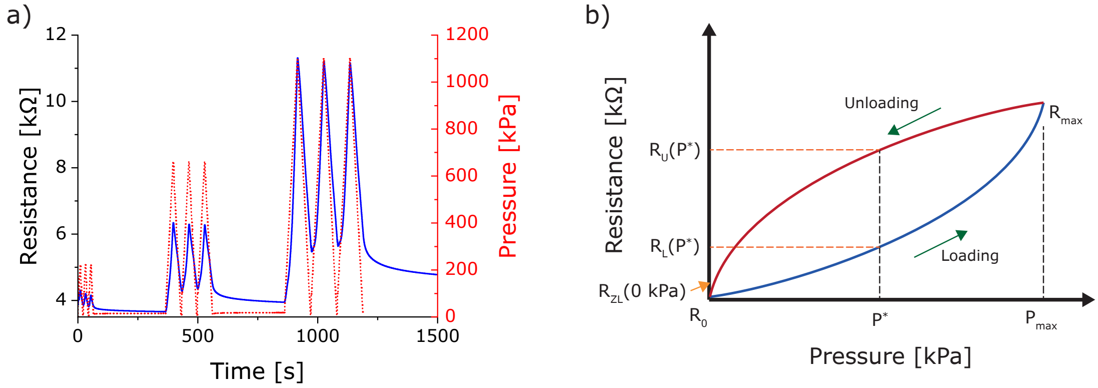

Figure 4.18 – Basic elements of the hysteresis tests with **a**) the resistance and pressure versus time for a hysteresis test and the **b**) a visualisation of an ideally symmetric hysteresis curve including points of interest for evaluation of the hysteresis of the sensors.

maximum was determined from which the percentage of hysteresis could then be calculated.

Influence of preconditioning and hysteresis values

As previously discussed in Section 4.3.2, performing a preconditioning step had a significant influence on the drift and repeatability of the sensor response. Figure 4.19 shows the hysteresis curves of two sensors before and after preconditioning.

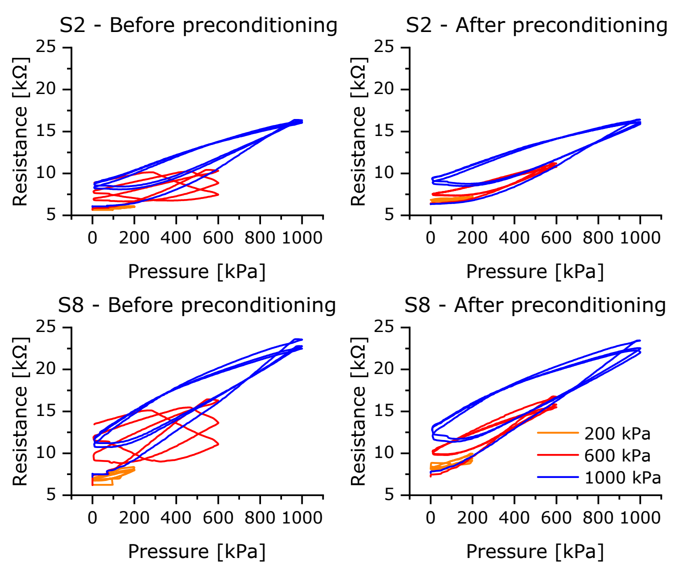

Figure 4.19 – Hysteresis loops extracted from piezoresistive normal sensors with on the left the sensors before and on the right sensors after the preconditioning was applied.

In both sensors it is very clearly demonstrated that the hysteresis loops do not show the expected hysteresis loops before the sensors are preconditioned for cycling pressures of 200 and 600 kPa. Only once at an actuation pressure of least 1000 kPa do these sensors show the expected loops. The hysteresis can be quantified by calculating the actual values both before and after preconditioning as is shown in Table 4.4.

Table 4.4 – The evaluated hysteresis (δ_h) values of the CNC-PDMS piezoresistive normal sensors with 4 wt% CB-PDMS both before and after preconditioning.

	Pressure	R_0	R_max	R_U	R_L	δ_h
	kPa	kΩ	kΩ	kΩ	kΩ	%
	200	6.25±0.53	7.23±1.13	6.99±0.58	6.38±0.58	62.87±0.37
No preconditioning	600	8.02±1.14	13.27±2.96	12.72±1.16	7.97±1.16	95.06±12.79
	1000	9.50±1.25	19.94±3.60	15.68±2.21	12.76±2.21	28.17±1.04
	200	7.35±0.66	8.59±1.36	8.10±1.06	7.70±0.93	37.82±10.17
After preconditioning	600	8.74±1.24	13.97±2.77	11.90±2.35	10.18±1.87	32.96±0.54
	1000	10.32±1.49	19.91±3.52	16.15±2.70	12.93±2.12	33.71±1.08

Evidently from the last column on the hysteresis values (δ_h) the preconditioning does not necessarily always result in a lower hysteresis. For low pressures (<600 kPa) there is a significant improvement while at a pressure of 1000 kPa there is little change. However, over the entire pressure range the average hysteresis dropped from 62.0±28.3%, without the preconditioning, to down to 34.8±6.3% after preconditioning. Furthermore, the hysteresis values are more consistent for the different pressures. Whereas without preconditioning the hysteresis values are in a range of 28-63%, this range reduces down to 33-37% after preconditioning.

It is possible that reinforcing the CB-PDMS with CNCs instead of fumed silica could further reduce the hysteresis since it also stiffened the CNC-PDMS material (Figure 4.4). This could reduce the variation between sensors by reducing the loss in fidelity of the printed strain gauges.

4.3.5 Dynamic response

Lastly we evaluated the responses of the 5 wt% CNC-PDMS sensors with 4 wt% CB-PDMS strain gauges underneath a 12.5 wt% CNC-PDMS bump for dynamic loads, as per the protocol described in Section 4.3.1. The tests were performed using a Bose Electroforce 3400 which was able to cycle at faster speeds and with higher pressures than the Instron pull tester. Several frequencies were tested which were based on slow walking speeds of less than 3 km/h (< 1 Hz), up to running speeds faster than 18 km/h (2 Hz)[169]. The tests were carried out at several pressure and speed combinations for a duration of 30 minutes each to analyse how both factors influenced the sensor response.

Dynamic actuation of piezoresistive sensors

Dynamic responses of the sensor were tested at actuation speeds of 0.5, 1, 2 Hz and pressures of 200, 600 and 1000 kPa. A short stabilisation period was required as the sensor showed higher amplitudes when starting to actuate them. The signals resemble harmonic waves with maximally loaded (peaks) and unloaded responses (valleys). The difference between these two is defined as the dynamic amplitude.

A 60 second close up of the response of the sensor at a low actuation speed (0.5 Hz) is shown in Figure 4.20 a. The amplitudes were found to be stable over extended amounts of time as can be seen in the full response shown in Figure 4.20 b.

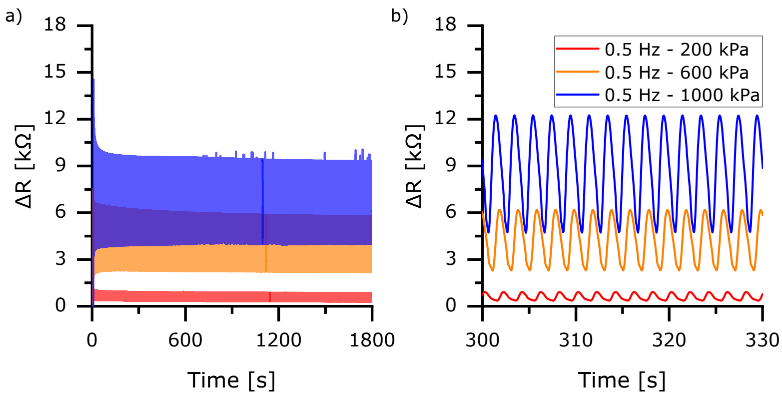

Figure 4.20 – Relative dynamic response of the CNC-PDMS piezoresistive sensor at an actuation speed of 0.5 Hz for **a**) normal pressures of 200, 600, 1000 kPa for 30 minutes and **b**) the responses zoomed in for 30 seconds.

Further tests were carried out at increased speeds of 1 and 2 Hz at the same pressures. A 15 second close up can be seen in Figure 4.21 a of both the full responses of the 1 Hz (Figure 4.21 b) and 2 Hz (Figure 4.21 c) actuation speeds.

Again, all amplitudes were found to be stable over time a peak drift of less than 2% over the 5 to 30 minutes interval. Therefore, to determine the actual behaviour of the responses versus the pressure and actuation speed an analysis was carried out of the dynamic data.

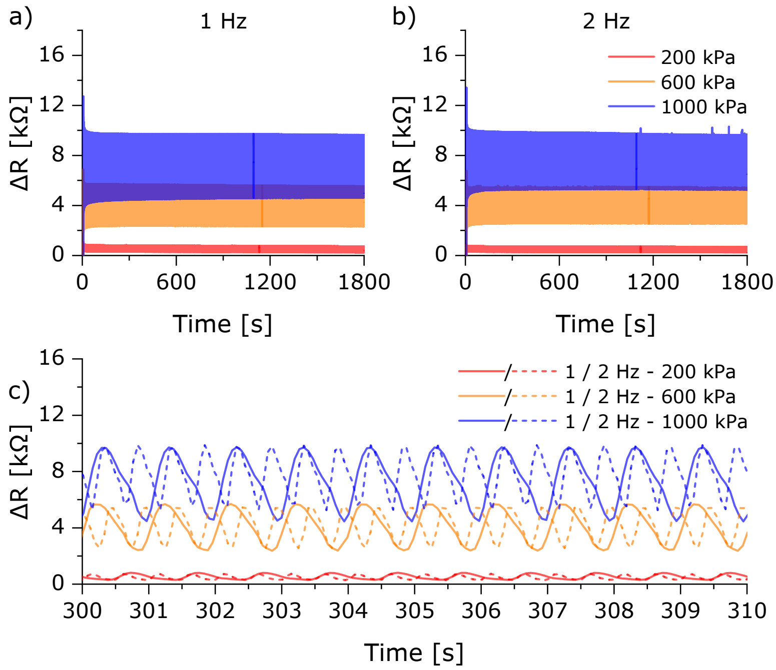

Figure 4.21 – Relative dynamic response of the CNC-PDMS piezoresistive sensor at 1 and 2 Hz for normal pressures of 200, 600, and 1000 kPa. Full signals at **a**) 1 Hz and **b**) 2 Hz of actuation as well as a **c**) 10 second sample with both frequencies plotted for all pressures.

Evaluation of dynamic piezoresistive sensor behaviour

To quantify the dynamic characteristics of these sensors and their stability the data was analysed by a python script. Every five minute period, eighteen data points were evaluated at the extremes of the waves and processed to determine the peak, valley, and amplitude values. This resulted in a total of 6 measurement periods for the 30 minutes of data.

An increase in the actuation pressure resulted in a heightened relative peak response ($R - R_0$), which increased linearly resulting in a S_{rel} of 16.9±0.8% per 100 kPa ($R^2 = 0.999$), as shown in Figure 4.22 a. This sensitivity is slightly lower than the one for the static test which was S_{rel} = 21.6±6.5% per 100 kPa. As the nature of the applied load is transient and takes some time to stabilise, as was shown in Figure 4.15, the sensitivity during the dynamic test was expected to be slightly lower.

The relative valley values follow an upward trend, as shown in Figure 4.22 a due to the baseline increasing with increased pressure, but with a lower variation of 10.1±2% per 100 kPa (R^2 = 0.989). As the peak and valley values increase at different slopes this results in a non-linear increase of the amplitude versus the pressure which is shown in Figure 4.22 b.

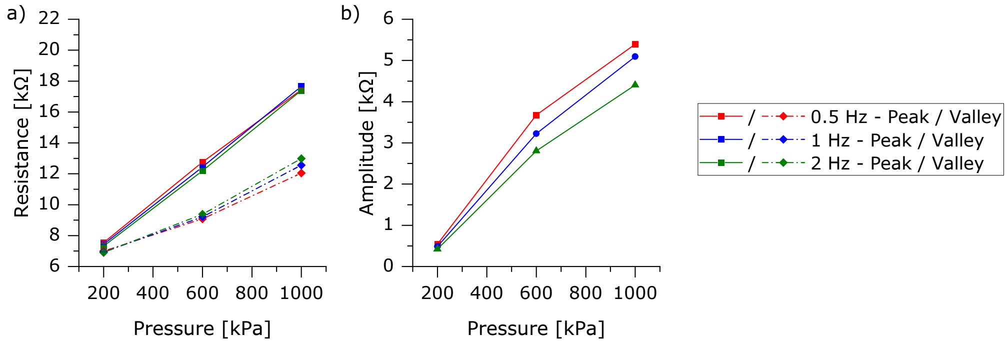

Figure 4.22 – Analysis of the dynamic signals versus the pressure in terms of **a**) resistance values and **b**) amplitude.

The actuation speed did not significantly influence either the peak or valley sensitivities but did have some effect on the magnitude of the responses. Figure 4.23 a, shows that the peak values overall decreased slightly, while the valley values increased slightly with increased frequency. Per frequency step this increase was observed to be between 1.1-3.7%, which is much smaller than the increase due to the pressure (Figure 4.23).

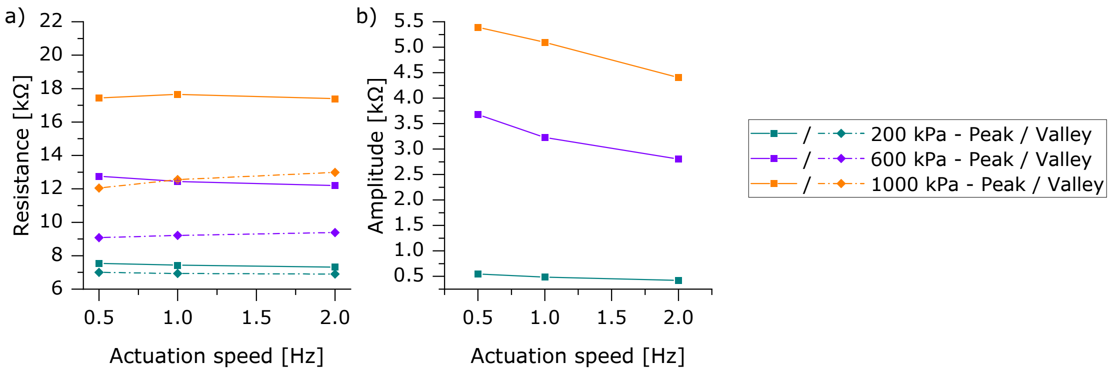

Figure 4.23 – Analysis of the dynamic signals versus the actuation speed in terms of **a**) resistance values and **b**) amplitude.

The viscoelastic properties of the material of the sensor cause some transient behaviour. Effects of these are most pronounced at higher dynamic pressure rates, when the sensor has less time to relax and does not fully recovers to its initial state. As discussed in the section 4.3.4 and Section 4.3.3, this relaxation behaviour and its influence on the dynamic response, is likely due to the hysteresis experienced by the strain gauge material and less due to the surrounding CNC-PDMS. When DIW printing, the CNC-PDMS is reinforced in the tensile direction by the aligning of the CNC particles which adds a stiffening effect[57]. To fully understand if this also reduces the relaxation of the strain guages, a CNC reinforced CB-PDMS should be created and its mechanical characteristics compared to the one reinforced with fumed silica.

The dynamic results indicate that the sensor is suitable for detecting a wide range of repetitive motions at a variety of speeds and pressures relevant for gait monitoring. For the detection of gait pressures, only the peak responses needs to be monitored which were found to be linear and repeatable. The intensity of the physical activity can also be determined with the dynamic amplitude of the signal which has a slight error of a few percent on the measured pressure values. The most significant reduction in amplitude was found to occur with an increase in speed. Lastly, a small amount of drift over time was observed which was strongest at a slower actuation speed. This dependency on frequency and the drift could be corrected for by developing an appropriate signal processing algorithm.

4.3.6 Capacitive normal sensor

To show that our materials could also be used to create other mechanical sensors, capacitive normal sensor prototypes were also created using an unoptimised CNC-PDMS ink. These were used as a comparison to evaluate the performance of a piezoresistive sensing mechanisms versus a capacitive one. These capacitive normal sensors were DIW printed per the design as outlined in Section 4.1.3 and fabricated from 10 wt% CNC-PDMS ink for the substrate, top layer and bump, and the 20 wt% CNC-PDMS for the dielectric. The percentage of CNC content was higher as the propylene glycol methyl ether (PGME) surfactant used to disperse the CNCs in the silicone resulted in an ink with less optimal shear thinning properties and shape fidelity. Top and bottom electrodes forming the sensor were printed from the 10 wt% Thinned Chimet Ag520 EI silver ink. The sensors were evaluated for their static response, hysteresis, and dynamic performance.

Static response

Capacitive sensors shown in Figure 4.24 a were evaluated by means of the static test protocol as described in Section 4.3.1. With a base capacitance at zero load of 8.2±1.7 pF, the sensitivity of these sensors was linear for the full response at a value of 0.41±0.02 fF/kPa (4.13±0.17 fF/N) and with a fit accuracy of R^2 = 0.994. At the stated sensitivity, and a full-scale response of 5.2±0.9% (0.052±0.007 %/kPa), the sensors are less sensitive than those obtained by other researchers using FDM printing (9.5 fF/N[27]) but significantly more so than those printed by DIW (0.853 %/MPa[120]).

As these sensors were created from the unoptimised CNC-PDMS formulation, imperfect printing led to defects being introduced in the dielectric layer resulting in a reduced capacitance. Furthermore, as the thickness of the dielectric layer was unoptimised in this prototype, the response could be significantly improved by reducing its thickness. However, even with an

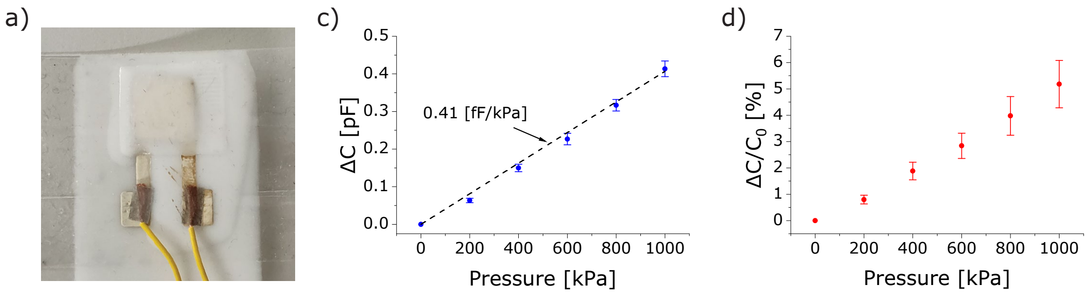

Figure 4.24 – Static responses of the 3D printed 10-20 wt% CNC-PDMS capacitive normal pressure sensor. **a**) Photograph of the printed sensor and its relative static responses in **b**) femtofarad, and **c**) percentage change.

improvement in signal the capacitive sensors would remain quite sensitive to noise, and to reduces this, shielding would have to be incorporated into its design.

Hysteresis

The 3D printed capacitive sensors were also tested to compare their hysteresis to the piezoresistive sensors. The hysteresis loops of two sensors are shown in Figure 4.25.

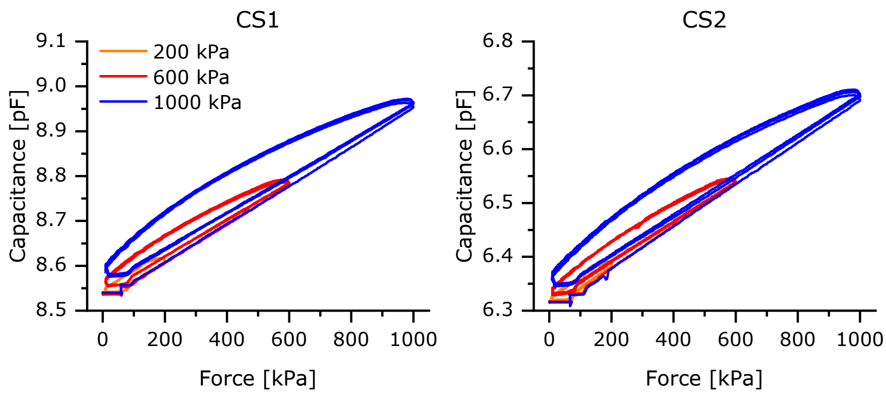

Figure 4.25 – Hysteresis loops of two 3D printed 10-20 wt% CNC-PDMS capacitive sensors

These loops display much less hysteresis than the ones for the piezoresistive sensors, but still a significant amount remains. Average hysteresis (δ_h) values were measured of 39.6±1.0% at 200 kPa and 19.9±3.2% for pressures between 600 and 1000 kPa. Considering this is without any preconditioning, this implies that the hysteresis of the capacitive sensors is significantly less than for the piezoresistive sensors. In fact, preconditioning could reduce the hysteresis further. Even so, some hysteresis is likely to remain due to the relaxation of the PDMS dielectric.

Dynamic response

The dynamic response of the capacitive sensors was only tested at an actuation speed of 0.5 Hz as it was the maximum compression speed that the Instron pull tester could reach. Actuation pressures of 200, 600, and 1000 kPa were used in this test.

Figure 4.26 a-b shows the performance of these sensors during the full dynamic actuation and for a 10 second window. Over the 60 second test time the sensors stabilised much faster than the piezoresistive ones. A peak drift of 0.61±0.12% was found for pressures between 200 to 600 kPa and 1.17±0.21% for a pressure of 1000 kPa. However, the values of the valleys do not fluctuate significantly at a difference between them of 10.3±9.0 fF for all tested sensors. As such, the amplitude drift in-between sensors for all pressures is quite low at a value of 0.39±0.08%.

As these sensors do not suffer the same amount of relaxation as the piezoresistive sensors, we also tested their response to a varying load, actuating them several times at speed of 0.5 Hz with a stepwise increasing pressure. First a pressure of 400 kPa was applied, then 600 kpa, and finally 1000 kPa before going stepwise back down to 400 kPa and repeating the process a second time. Figure 4.26 b shows the response of this sensor versus the applied load. Evidently, the sensors follow the actuated pressure well, with no significant hysteresis being observed. However, the first cycles do show a small difference in amplitude.

Even so, the error in amplitude between the first and second test is just 6.8±9.0 fF. This does not have a significant impact on the response as this is an error of about 2.8-6.5 kPa as per the sensitivity determined in Figure 4.24. This makes the error much lower than the average applied load.

It should be noted that these sensors were tested in an optimum condition with as little as noise as possible. When a dynamic test was executed by pressing the sensor down with a foot, the resulting dynamic results were very noisy. Signals would get dominated by the noise which had capacitance values often exceeding 50% of the baseline value. This implies that even if the transduction mechanism is promising, especially with regards to its performance, at the current state it was the sub-optimal choice in comparison to the piezoresistive normal sensor which showed no influence on its performance due to the environment. To reduce the noise and improve the importance a significant redesign of the capacitive sensor is necessary which incorporates shielding. The latter is especially crucial if we wish to integrate multiple of these sensors into a device without generating noise due to interaction with the environment or cross-talk.

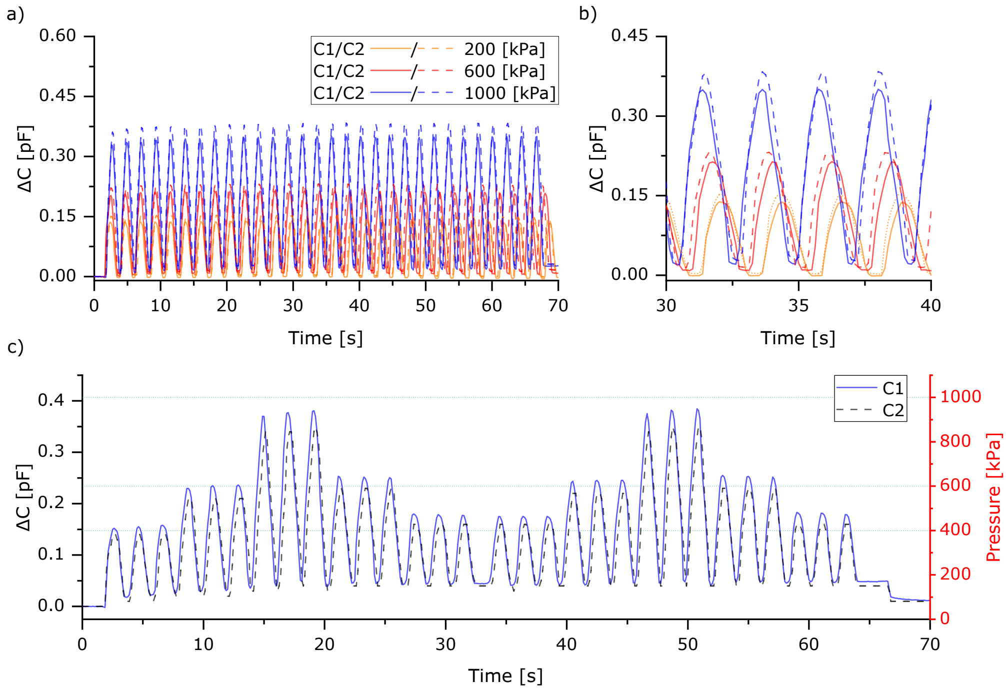

Figure 4.26 – Dynamic response of 3D printed 10-20 wt% CNC-PDMS capacitive sensors. **a**) Dynamic response at constant pressure. **c**) Dynamic response with varying pressure.

4.4 Silicone based shear force sensors

We explored the 3D printing of shear force sensors by using two strain gauges with parallel and chevron configurations, of which the designs were outlined in Section 4.1.2. The strain gauges of these were DIW printed from the 4 wt% pentanol based CB-PDMS ink on top of a 5 wt% CNC-PDMS substrate and enclosed within a 12.5 wt% CNC-PDMS bump.

4.4.1 Developed testing methodology

Shear tests were carried out on the Instron pull tester under compressive loads of 400, 600, and 800 kPa. A minimum load of 400 kPa was required to be able to avoid slipping of the sensor at shear forces above 5 N. As discussed in Section 4.1, the shear forces can be of an intensity of 20% of the bodyweight (for an average person around 800 kPa) when walking on a flat surface. Therefore, we wanted to apply a shear stress of at least 160 kPa on the 1 cm^2 bump, which translated to a shear force of about 15 N. These values agree with shear forces measured using optical sensors integrated into an insole[153].

As such, shear forces of 5, 10, 15, 20 N were tested, which translates to a maximum of about

25% bodyweight. These were applied successively and separately for two sensing directions using a custom built shearing bench (Figure 4.27 a). Shear force loads were recorded using a Futek FSH00096 load cell and Futek IPM650 controller. A square 1 cm^2 piston was used to compress the bump. However to improve the transition of shear force to the bump a PMMA piston (Figure 4.27 b) with sandpaper was used to avoid slipping of the bump and allow for more stable shear measurements. The positive shearing direction was assumed as a shear force applied from the back direction of the sensor towards the front (Figure 4.27 c).

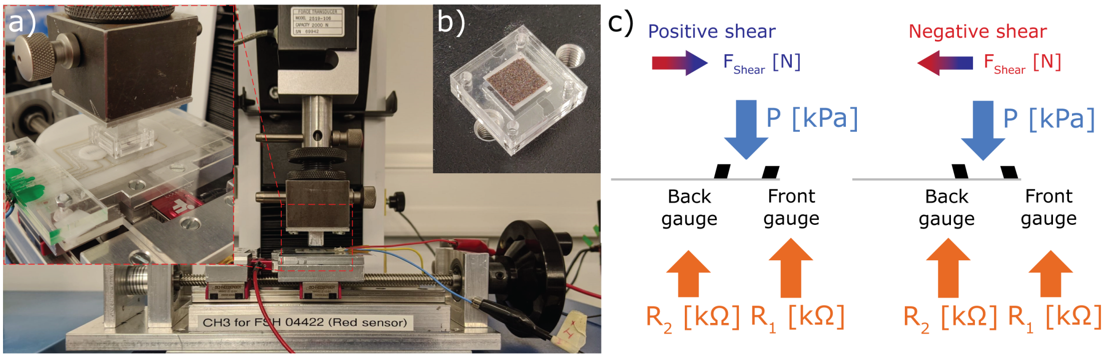

Figure 4.27 – Images and measurement principle of the shear tests. **a**) The custom made shear bench with a **b**) PMMA piston designed to shear the sensors. **c**) Shear sensing principle and directionality.

Sensors were first actuated with a compressive normal load and allowed to relax for 1 minute. The sensors were then manually sheared using the test bench and once the targeted force was reached the shear force it was released slowly back its neutral position. A 30 second pause was taken after which the next targeted shear force was applied. In this fashion shear forces between 5 to 20 N were applied in steps of 5 N.

Two shear directions were tested to be able to tell, through means of the differential signal, which direction the shear forces were occurring in. To characterise the directionality the shear sensors were first completely characterised in one direction. After the last force was applied they were unloaded completely and allowed to rest for 5 minutes before starting the test in the other direction. The two designs which were evaluated for the shear sensors were those designed with parallel (Figure 4.28 a) and with chevron-shaped (Figure 4.28 b) strain gauges.

4.4.2 Static pressure response

Both sensors were evaluated to understand how the shape of the strain gauges can influence the sensing of force and direction of the shear.

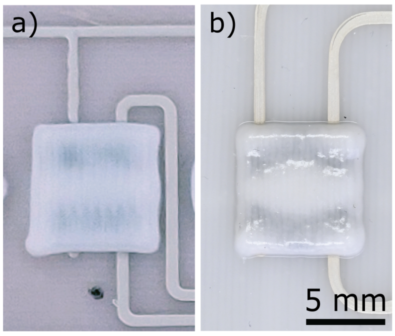

Figure 4.28 – Images of the two shear sensors with the two 4 wt% CB-PDMS strain gauges covered underneath a 12.5 wt% CNC-PDMS bump with **a**) the parallel design and **b**) the chevron design.

Influence of strain force direction

A preemptive shear test was performed to understand if there was a difference in response versus the direction of the strain force. Normal sensors with a single rectangular strain gauge were tested both under transversal and longitudinal shear deformation. Figure 4.29 shows the response under shear deformation up to 15 N in the positive direction only at compressive normal loads of 400 kPa and 800 kPa.

In figures Figure 4.29 c-d the resistance changes of the tested sensor are shown for the two applied normal loads. No significant relation was found between the shear force sensitivity and the direction from which the shear force was applied. Sensors under transversal shear showed a sensitivity of 51.2±6.5 Ω/N while those under longitudinal shear showed a sensitivity of 38.5±9.8 Ω/N, independent of the compressive load. Furthermore, the clamping pressure showed no real influence on the shear force magnitude either. An average shear sensitivity of 44.9±10.5 Ω/N was found independent of shear direction and clamping pressure. As such, to achieve directional shear sensing the design should be adapted to include features that can allow for different behaviour in the two directions.

Influence of strain gauge shape

The two sensor designs were tested on the test bench at a compressive load of 800 kPa to avoid slipping. The sensors were first sheared in the negative direction, towards the back sensor, with transversal forces of up to 30 N before restarting and repeating the test in the positive direction. Figure 4.30 shows the responses for both design to shear at a compressive normal load of 800 kPa.

In both sensors a clear increase in resistance can be seen and all forces, except for the 5 N

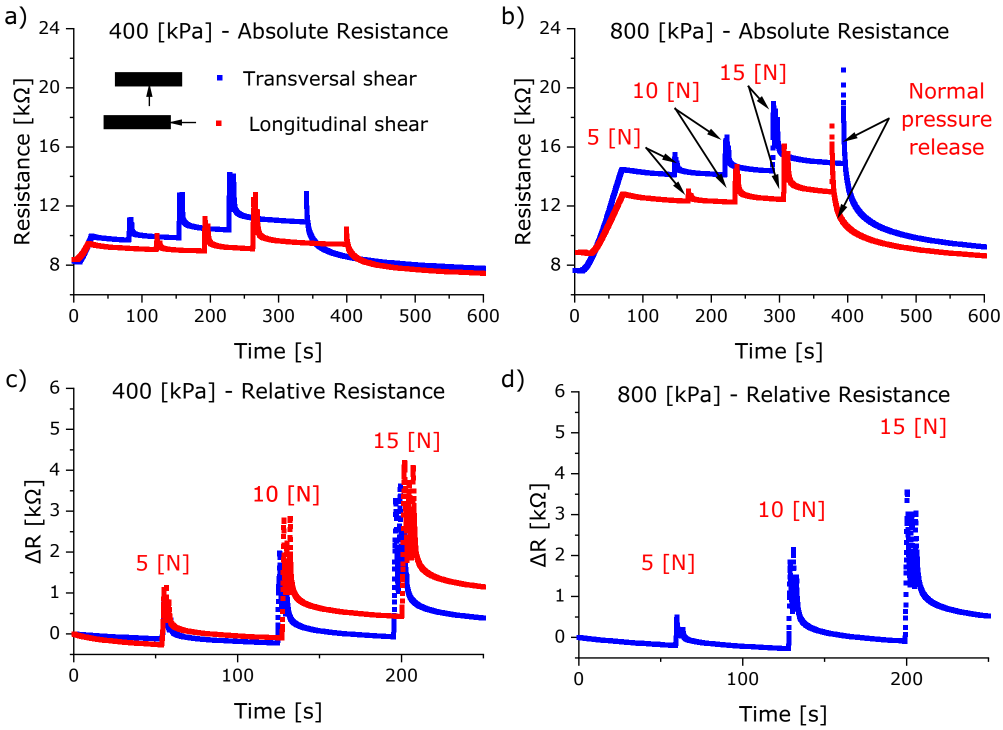

Figure 4.29 – Responses due to shear forces of 5, 10, and 15 N applied in the transversal and longitudinal directions tested on a single strain gauges under normal compression. Raw resistance values at normal pressures of **a**) 400 kPa and **b**) 800 kPa. Resistance changes due to shear with respect to the compressed state at pressures of **c**) 400 kPa and **d**) 800 kPa.

shear force, show up as clear peaks in the signal. For the chevron design the base resistance before the next shear force is applied (R_N) also increases. In fact, for the parallel design the R_N increased by 8.6±3 kΩ ($\Delta R/R_{10}$ = 46.2±13.7%) while for the chevron one it increases by 54.1±18.4 kΩ ($\Delta R/R_{10}$ = 82.3±30.7%) when increasing the shear force from 10 N to 30 N. This suggests that the strain in the chevron shaped strain gauge increases faster under the same shear force.

Sensor resistance change and sensitivity

To further quantify the response of the the two designs we evaluated the resistance change per shear force as

$$\Delta R_N = R_{pk} - R_N, \tag{4.10}$$

where R_{pk} is the peak resistance at a certain shear force and R_N the baseline value just before shearing. In this fashion the responses of both sensors were evaluated as shown in Figure 4.31

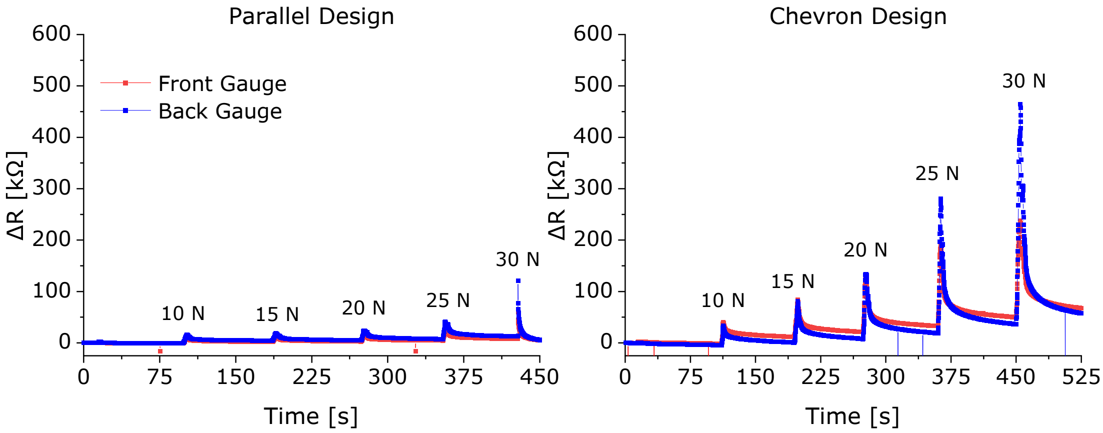

Figure 4.30 – Comparison of resistance increase for positive shearing of the sensors with parallel and chevron strain gauge designs at a compressive load of 800 kPa.

a-b.

By these responses sensitivity values ($\Delta R_N / F_{shear}$) can be found of 0.95±0.33 kΩ/N and 7.79±3.64 kΩ/N for the parallel and chevron configurations, respectively, independent of the shearing direction. This indicates that the chevron design was much more sensitive to shearing forces than the parallel design. However, a strong non-linear and divergent behaviour starts to set in after a shear force of 25 N. As such, a maximum shear force of 20 N was used to prevent this behaviour and also avoid damaging the sensor during testing.

Further tests were done with chevron-shape strain gauges only to determine how repeatable the performance was from sensor to sensor. These sensors were tested at 400, 600, and 800 kPa of compressive pressure and at shear forces from 5 to 20 N. In Figure 4.31 c the relative shear force sensitivity values are shown for the sensors expressed as the resistance change per force ($\Delta R_N / R_N$) in percent up to 15 N of shear force.

By evaluating these sensitivity values shown in the previous plot, a linear response can be found of 2.59±0.16 %/N ($R^2 = 0.992$) independent of the compressive load. Considering only the pressures between 0-400 kPa this sensitivity has a value of 2.96±0.11 %/N ($R^2 = 0.99$) and reduces down to 2.37±0.18 %/N ($R^2 = 0.987$) for compressive loads of 600-800 kPa. the fact that there is a small, but not insignificant, response drop off makes sense as the higher normal load already results in an increased initial resistance. As such, the demonstrated sensor design is suitable for measuring shear forces up to 20 N with a high degree of linearity. However, the shear behaviour at lower loads is currently not understood. To determine shear forces at these levels of compressive pressure a redesign of the test setup is required to prevent slipping of the bump.

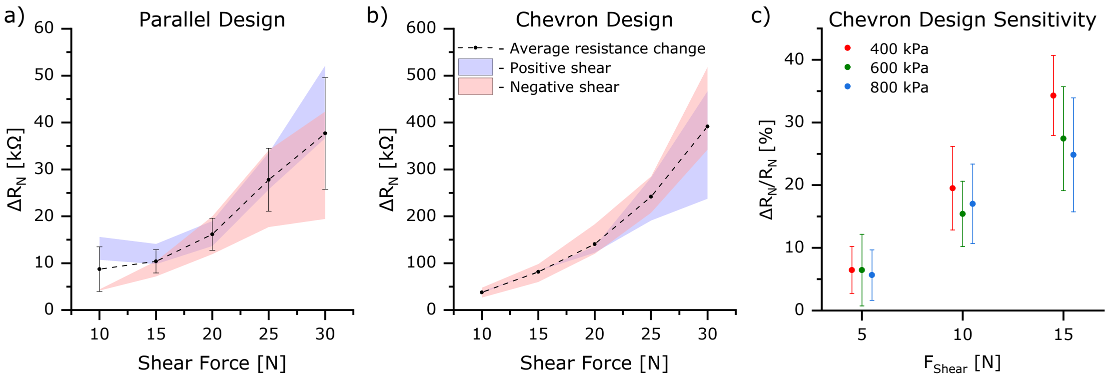

Figure 4.31 – Comparison of resistance increases (ΔR_N) at the tested shear forces for **a**) chevron and **b**) parallel sensors designs with the average resistance change, positive, and negative shearing results. And Average shear force sensitivity ($\Delta R_N / R_N$) of the chevron sensor design for different compressive normal pressures.

4.4.3 Differential response

So far we only evaluated the response of a single element under a shear force, with the chevron shape strain gauge proving to be more sensitive than the parallel design. However, the working principle for measuring shear sensor during gait relies on calculating a differential between the two elements such that the magnitude and direction of the shear force can be determined. Therefore, we investigated if differentials of the chevron design shear force sensors could be used to determine directionality and shear force magnitude.

Differential shear signals

Figure 4.32 shows how the differential and raw shear signals look like for a shear test under compressive pressures of 400, 600, and 800 kPa for shear forces up to 15 N. To determine if the results were repeatable, each force was applied three times in a row and the tests were performed in both directions.

These differentials were determined as per Equation (4.3), with the differential ($\Delta R_{\mathrm{shear}}$) being determined by subtracting the signal of the "back" gauge from the "front" such that when a positive shear is applied the resulting differential is also positive. To calculate the differential its formula was expressed as

$$\Delta R_{\mathrm{shear}} = \Delta R_{\mathrm{back}} - \Delta R_{\mathrm{front}} = (R_{\mathrm{back}} - R_{\mathrm{back,0}}) - (R_{\mathrm{front}} - R_{\mathrm{front,0}}), \tag{4.11}$$

where R_{front} and R_{back} are the resistance values of the front and back gauges, respectively,

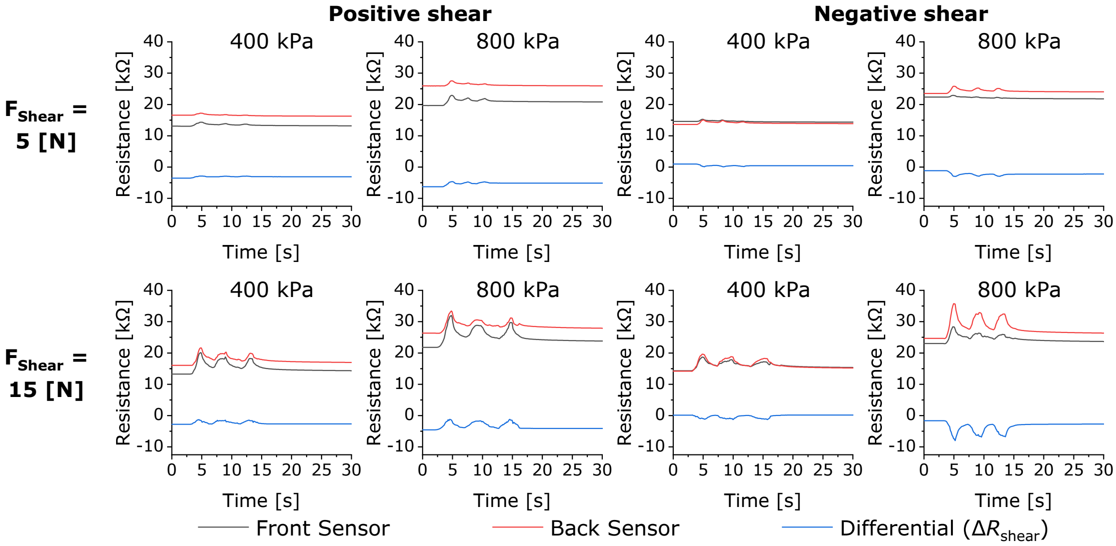

Figure 4.32 – Resistance responses and differential signals of the 4 wt% CB-PDMS piezoresistive shear sensors with chevron design for both positive and negative shear at 5 and 15 N of shear force.

during the shear tests. $R_{\text{front},0}$ and $R_{\text{back},0}$ are the resistance values under normal compression before shearing and serve as a reference.

The resulting differentials gave a clear indication of the direction of shear force. Evidently, the resistance values of all gauges is higher at a higher normal pressure. However, the magnitude of the differentials also is influenced with it being larger for 800 kPa of clamping pressure. Furthermore, the applied shear force directly influences the magnitude and amplitude of the differential signal. Even though the single element sensitivity is not the highest in this case, as was shown in Figure 4.31, the differential signal has a bigger amplitude due to a larger difference in resistance between the gauges at higher clamping pressures.

Shear directionality

To better quantify the amplitudes of the differentials shown in Figure 4.31, their average values were determined using the responses of three sensors. and plotted in Figure 4.33 versus the applied shear forces.

Before shearing, the sensors exhibited an average baseline resistance of 7.0±0.8 kΩ. At all tested compressive pressures it was possible to detect the direction of the shear forces. However, the peak values overlap significantly and it is not possible to tell the exact shear force magnitude at compressive pressures of 400-600 kPa.

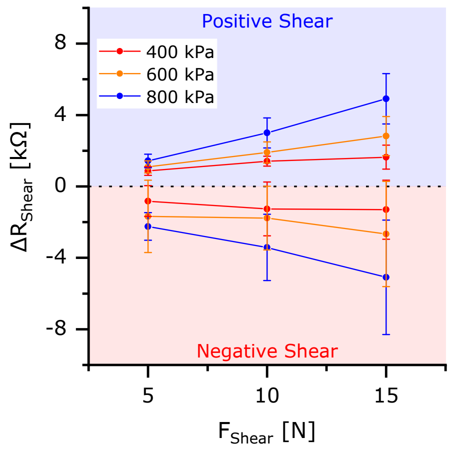

Figure 4.33 – Differential behaviours of the 4 wt% CB-PDMS piezoresistive shear sensors with chevron design for different shear forces at compressive pressures of 400, 600 and 800 kPa.

By increasing the compressive pressure to 800 kPa, the slope of the resistance change versus force increased in comparison to the lower pressures. Using linear fits, for a negative shear a sensitivity of 297.7±30.0 kΩ/N (R^2 = 0.998) was determined while for positive shear the sensitivity is -355.9±20.2 kΩ/N (R^2 = 0.997). This thus allows for an indication of the magnitude of the shear force to be determined at high normal pressures, such as during running.

While the chevron design proved to be function better than the parallel design, other strain gauges could be designed that show even more directionality. Of further interest would also be to tune the carbon loading of the ink to see if this influences the shear measurements. As these sensor were positive piezoresistors, a negative normal force piezoresistor could be less influenced by the normal compression and yield more sensitive shear sensing.

4.5 Summary and Conclusion

In this chapter we have discussed the design, evaluation, and performance of fully 3D printed piezoresistive and capacitive sensors created from silicone materials by means of Direct Ink Writing (DIW) which were designed for the evaluation of human gait.

Piezoresistive sensors were enabled using a developed fumed silica based PDMS inks loaded with carbon black (CB) at loadings between 3.5-5 wt%. By printing a single gauge from this material on top of two electrodes, a sensor was created that converted normal pressure into a tensile strain with a positive piezoresistive response. The most suitable solvent to disperse the carbon black in this composite was pentanol. In comparison to isopropanol and octanol, pentanol based inks yielded a piezoresistive material with good conductivity and printing characteristics. Due to the low boiling point of pentanol, it could be fully evacuated during curing.

Using the pentanol based CB-PDMS inks, normal pressure sensors with piezoresistive strain gauges with several CB loadings were DIW printed to evaluate the piezoresistivity of the material. By evaluating these during static normal pressure tests, we arrived at a 4 wt% CB loading as a balance between sensitivity and repeatability.

Using this ink, and a crystalline nanocelluslose (CNC) reinforced PDMS (CNC-PDMS), developed by our partners at ETH Zurich and EMPA, we enabled the DIW printing of highly replicable piezoresistive normal sensors. These sensors were evaluated in terms of their static pressure, hysteresis and dynamic performance. In terms of the static response we found that the piezoresistive sensors had a linear response above 200 kPa of 14.9±0.4 Ω/kPa (0.216±0.065 %/kPa). This is less sensitive than ionogel strain gauges printed inside of cast PDMS[12], but more sensitive than a DIW printed CB-Silver Thermoplastic Polyurethane (TPU) based normal sensor[114]. A gauge factor (GF) of 34.0±0.1 was calculated for our sensors, making it more sensitive than most 3D printed carbon tensile sensors by a factor of 2-3.7[29], [109], [168] and slightly better than silver-polyurethane inks at 13.3[120]. However, doped silicon tensile strain sensors commonly achieve a GF of 100 and above[159].

Preconditioning was required to reduce the effects of relaxation in the piezoresistive sensors, which was applied before testing. Its effects were especially evident when looking at the hysteresis of the sensor. By performing the preconditioning, the hysteresis was decreased from 62.0±28.0% down to 34.8±5.2%, However, since the sensors are created from silicones they have inherent material relaxation such that some hysteresis will always remain.

The dynamic responses of the piezoresistive sensors were evaluated by actuating them at normal pressures of 200, 600, and 1000 kPa, at frequencies of 0.5, 1, and 2 Hz. Initial cycles showed an increased response that stabilised after actuating for about 30 seconds. This effect was less prominent at lower pressures and higher actuation speed (> 1 Hz). Since pressures of 1000 kPa rarely occur in gait, and as we wish to monitor for extended amounts of time, these effects are negligible. Overall dynamic responses were found to be stable, with only an on average 5% peak drift over several 25 minute tests. While the amplitude increased with the compression pressure, the actuation speed had a comparatively negligible effect on the amplitude. This makes our sensors applicable to the monitoring of human gait, in which plantar pressures above 400 kPa are common.

CNC-PDMS based capacitive sensors were also DIW printed to be able to compare its performance to the piezoresistive sensor design, and evaluate its applicability for normal pressure sensing during gait. For these sensors, a static response of 0.41±0.02 fF/kPa (0.052±0.007 %/kPa) was measured. Even if the relative change of the signal is much higher for the piezoresistive sensors, the response of the capacitive sensors is more linear due to small deformations of the dielectric, with larger deformations likely resulting in a reciprocal response. Furthermore, the responses of the capacitive sensors deviate less at higher pressures. This is due to its response only being dependent on a geometrical change and not the material properties, unlike the piezoresistive sensor, which relies on a change in the percolation network of the strain gauge. The hysteresis of the capacitive sensor was also lower at an average value of 29.8±10.0%, without needing to apply any preconditioning. For the dynamic response, the capacitive sensors had a very low peak drift of only 0.89±0.31% and could even follow dynamically altering pressure quite well. With this high performance, these sensors should be great for normal pressure sensing. Unfortunately, they are very sensitive to external perturbations, especially in dynamic situations such as gait, making them less directly suitable for human motion monitoring.

Lastly, using the 4 wt% CB-PDMS and CNC-PDMS formulations, piezoresistive shear sensor designs were DIW printed to enable shear force measurements. A sensor design using two normal strain gauges in parallel resulted in a low response to shear forces with its direction not always possible to be determined. Therefore, a redesign with two chevron-shaped strain gauges was created which showed a higher sensitivity and could distinguish the direction of shear. Shear forces could be measured up to 20 N with sensitivities of 2.96±0.11 %/N and 2.31±0.28 %/N at compressive forces of 0-400 and 600-800 kPa, respectively. Directionality was measured through differential measurements between the two gauges, which showed a negative shear sensitivity of 296.7±30.0 kΩ/N and a positive shear sensitivity of 355.9±20.2 kΩ/N up to 15 N.

With these performance metrics in mind, the piezoresistive normal and shear force sensors were utilised in a fully 3D printed insole presented in Chapter 6 to test the monitoring of human gait. Previously gait monitoring was only achieved using non 3D printed sensors by optical[153] or piezoelectric[170] sensing. Neither solution, however, provided an easy method to implement sensor designs and easily adjust their position within the wearable.

Still, further improvements of the sensors could be envisioned by reinforcing the CB-PDMS with CNCs instead of fumed silica to add material stiffening[57], possibly reducing hysteresis and relaxation times, which would improve the dynamic response of the sensor. Furthermore, by optimising the design of the shear sensor, its response could be further improved such that the shear force magnitude could be detected as well. A more accurate shear sensing setup could also be developed to increase the quality of the measurements.

As capacitive sensing also showed good performance metrics, this transduction mechanism was further investigated in Chapter 5 for the creation of a fully 3D printed bending sensor suitable for human motion monitoring.

5 Capacitive sensors for angular motion monitoring enabled by 3D printing

By 3D printing three dimensional and non-planar features, it becomes possible to design new types of sensing mechanisms and electronics. This has been demonstrated for solid state electronics through combining stereo-lithographic resin printing and DIW printing[13], [145]. In this fashion, a high degree of functionality can be introduced in a printed object by printing electronic components in three dimensions and in a miniaturised fashion. So far this has only been demonstrated by printing inside of a pre-cast silicone bath that was fully cured afterwards to finalise the device[12]. This method enabled the creation of a air pressure driven gripper with integrated sensors capable of measuring pressures and deformations. Fully 3D printed silicone objects and devices with three-dimensional features have been realised, but without any electronic components[60], [171], or by using liquid metals[172]. However, a fully 3D printed soft device with integrated mechanical sensors utilising 3D structuring has not yet been demonstrated.

Direct Ink Writing (DIW) is ideally suited for the printing of shear thinning materials[51], [52], which can enable the printing of freestanding and non-planar structures[60], [63], [172]. Currently, this technique and the compatible materials have not used frequently in the creation of novel 3D printed sensors. In fact, to create complex three dimensional structures researchers often rely on printing on top of existing 3D printed resin moulds[41].

In this chapter we explore the development of a UV curable silicone material system that can be used for the fabrication of truly 3D printed and three-dimensional sensing features. This system was used as a basis for the design of a capacitive bending sensor with asymmetric angular sensing behaviour when measuring bending motions. Models were developed and experimentally verified to design and manufacture a completely 3D printed version of a bending sensor design.

5.1 Design and modelling of a capacitive bending sensor

3D printing angular features could open ways for new sensing mechanisms. From this general idea the concept of a bending sensor with directionality was conceived which could be realised by 3D printing. In this section the design of the sensor, the developed models, and a prototype to validate the models are discussed.

5.1.1 Sensing mechanism and sensor design

Capacitive sensors function by monitoring the change in an electric field due to physical separation of two charged features such as plates. As outlined in Chapter 2, the most common capacitive sensor designs are those with either parallel plates or electrode fingers. To measure angular motions, parallel rotating disks with specific layout designs[173] have previously been proposed. Printed capacitive pressure and strain sensors[151] have also been demonstrated for the monitoring of angular motions, the latter of which has been applied for wearable motion monitoring[174]. However, unless these sensor are directly laminated to the skin the detection of actual joint angles is limited[19], as stretching of the skin can influence the sensing performance and introduce errors. Furthermore, these sensors do not take into account the large range of motion of certain joints. For example, the angular displacement of a knee can be 90-120° in day to day activities[175], including in a negative direction from the neutral plane. The effects of micron sized slanted plates have previously been investigated for capacitive sensing[176], but features of this size have not used in a bending sensor.

Proposed sensing mechanism

In this frame, a novel angle sensing mechanism was conceived that display a non-linear response depending on the angular separation between plates. By making use of plates that are already under an angle, an asymmetric bending behaviour can be introduced to sense the direction of bending and target negative angles as well.

In Figure 5.1 the sensing principle is illustrated with plates oriented in a V-shape manner at an angle (θ_i) with a small spacing (S_{int}) at the bottom to separate them.

By bending the plates such that they come closer (positive bending) the capacitance increases, while when increasing the angle between them (negative bending) the capacitance decreases. An external spacing (S_{ext}) is required to be larger than the internal spacing such that the sensor displays asymmetric behaviour.

To develop the sensing mechanism, analytical and finite element method (FEM) models were developed to evaluate its effectiveness. In these studies the influences of the internal spacing

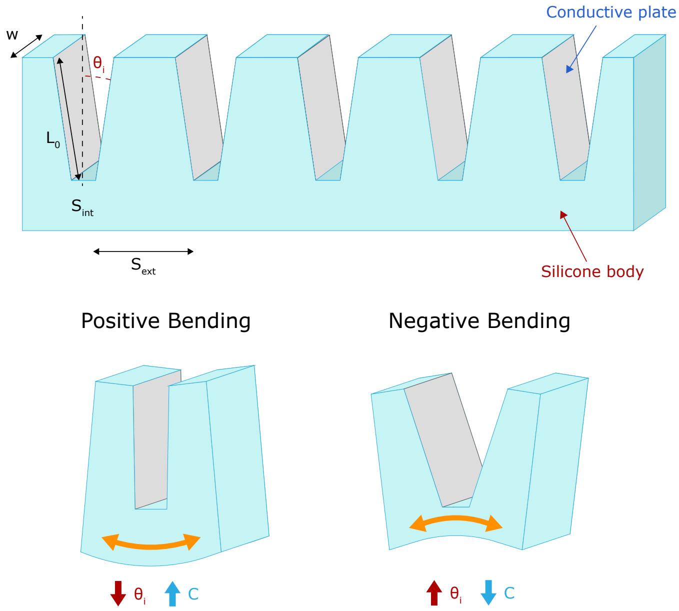

Figure 5.1 – The proposed sensing mechanism for a capacitive bending sensors. By either bending the plates inwards (positive) or outwards (negative) the capacitance will increase or decrease, respectively. This allows for a bending sensor with directionality.

(S_{int}), external spacing (S_{ext}), plate length (L_0), plate thickness (t), and sensor width (w) were investigated. Furthermore, the influence of an encapsulation layer covering a part of the plates, to increase the capacitance through a dielectric material, was also tested.

Design considerations and targets

As previously mentioned, the sensor was targeted to be able to monitor angular motions of 90-120° which are common in day to day activities[175]. For wearable solutions angular errors have been demonstrated at a level below 2.7-3° [7], [174].

A wearable bending sensor, composed of two 4x4 cm^2 flat fabric conductive plates, was previously explored by mounting them on the top and bottom part of the arm[177]. This wearable setup was able to detect changes up to 180° with a sensitivity of about 45 fF/°, but with a response below 30° which was reciprocal. Taking into account the surface area of the sensor, this is a normalised sensitivity of 2.81 fF/°cm^2.

Previously, a wearable inkjet printed carbon based strain gauge was demonstrated with an angular sensitivity of 0.086%/°, and a film thickness below 2 mm [96]. However, while this strain gauge was very unobtrusive it also suffered from high viscoelastic effects. Non-printed thin wrinkled capacitive strain sensor have been demonstrated with nano-meter gold films which could detect changes ($\Delta C/C_0$) up to 1.25 %/°[178]. However, none of these solutions demonstrated an asymmetric sensing capability or the ability to differentiate between tensile and bending deformation.

For our sensor design we targeted for it to operate in the picofarad range. For the sensor to operate in this range, and not become too bulky to wear, a plate to plate spacing of less than 1500 µm was required if we consider a parallel plate capacitor. To be able to wear the sensor on most larger joints of the body, its width should not exceed 15 mm. Lastly, for it to remain unobtrusive and conformal, its height should be a few millimeters at most.

As we wanted to verify our model with a sensor prototype, we used FDM moulding to achieve this geometry. This choice of manufacturing technology, however, limited our fabrication resolution to 400 µm. Therefore, we also used this value as a constraint in the modelling and simulation of the design, while with DIW printing lower fabrication resolutions can be achieved.

5.1.2 Analytical and FEM models

Two types of models were developed to analyse the behaviour of the capacitive bending sensor. First an analytical model was derived and programmed into python to allow for the evaluation of the influence of the design parameters. Then this design was translated into a COMSOL Multiphysics model with which it was verified to see if these models agreed.

Derivation of the analytical equation

We can model the plates of the sensor as two parallel plates within a cylindrical coordinated system such that we have an electric field which can be expressed in this space as $\vec{E}(r,\theta,z)$[179]. We assume that this electric field only has a component in the direction θ from one plate to the other as shown in Figure 5.2 a. This electric field depends on the voltage difference $\vec{V}$ between the two bodies by means of the relation

$$\vec{E} = \vec{\nabla} V = \begin{pmatrix} \frac{\partial}{\partial r} \\ \frac{\partial}{r\partial\theta} \\ \frac{\partial}{\partial z} \end{pmatrix} V \tag{5.1}$$

where V is the voltage as a scalar[180]. The voltage for the system can be expressed by assuming the condition that it is symmetric on both sides such that we arrive at the relation

$$V = \frac{V_{\mathrm{max}}}{\theta_{\mathrm{i}}}\theta, \tag{5.2}$$

where V_{max} is the voltage of the plate, θ_i the angle at this maximum voltage and θ the angle between the plates. If we substitute Equation (5.2) into Equation (5.1) then the resulting differential becomes

$$\vec{E} = \begin{pmatrix} 0 \\ \dfrac{V_{\mathrm{max}}}{r\theta_{\mathrm{i}}} \\ 0 \end{pmatrix} \tag{5.3}$$

Therefore, the electric field between the two plates is only dependent on the r coordinate and can be written as $E(r) = \dfrac{V_{max}}{r\theta_i}$. From this electric field we can also determine the charge density (σ) on the plates as per

$$\sigma(r) = \varepsilon_{\mathrm{r}}\varepsilon_0 E(r), \tag{5.4}$$

where ε_r and ε_0 are the relative permittivity and permittivity of vacuum, respectively, the latter which is a constant with a value of 8.854 pF/m. The charge between the two plates can be calculated from the charge density as per

$$\mathrm{d}Q = \sigma(r)\mathrm{d}S = \sigma(r)\,w\,\mathrm{d}r, \tag{5.5}$$

with the S being surface over which the charge accumulates. This can be decomposed into w which is the width of the plate and remains constant, and dr which is the radius over which the charge varies. Both sides of this equation can be integrated such that we get

$$Q = \frac{V_{\mathrm{max}}\varepsilon_{\mathrm{r}}\varepsilon_0 w}{\theta_{\mathrm{i}}} \int_{r_1}^{r_2} \frac{\mathrm{d}r}{r}. \tag{5.6}$$

The limits r_1 and r_2 represent the length of the plate ($r_2 - r_1$) and the distance from the start of the plate to the centrepoint around which it rotates (r_1). By integrating this function we can find the relation which describes the charge

$$Q = \frac{V_{max}\varepsilon_r\varepsilon_0 w}{\theta_{\mathrm{i}}} [\ln r]_{r_1}^{r_2} \tag{5.7}$$

$$= \frac{V_{max}\varepsilon_r\varepsilon_0 w}{\theta_{\mathrm{i}}} [\ln r_2 - \ln r_1] = \frac{V_{max}\varepsilon_r\varepsilon_0 w}{\theta_{\mathrm{i}}} \left[\ln \frac{r_2}{r_1}\right] \tag{5.8}$$

Finally we use the relationship between voltage and charge ($C = \frac{Q}{V}$) to arrive at a final equation which describes the change of capacitance (C) with respect to the angle between the plates (θ_i). Considering that we only evaluate the voltage at $\theta = \theta_i$ we can substitute $V(\theta_i) = V_{max}$ and arrive at the equation

$$C = \frac{\varepsilon_r \varepsilon_0 w}{\theta_i} \left[\ln\left(\frac{r_2}{r_1}\right) \right] = \frac{\varepsilon_r \varepsilon_0 w}{\theta_i} \left[\ln\left(\frac{L}{r_1} + 1\right) \right]. \tag{5.9}$$

This analytical equation is in agreement with another model derived for the evaluation of capacitance between thick non-parallel plates simulated by FEM[181].

Analytical model

Equation (5.9) only described the capacitance between two single opposing plates. Using this as a basis, it is possible to construct a model that contains the internal and external fringe fields for the plates, as well as those of the connectors. Furthermore, gaps were added to introduce flexibility in the sensor at the cost of reducing the capacitance. For this part it was assumed that the fields through the encapsulation and the air could be added as capacitors in series. The full model was based on the geometry as in Figure 5.2 b with the electric fields as shown in Figure 5.2 c and was composed as follows.

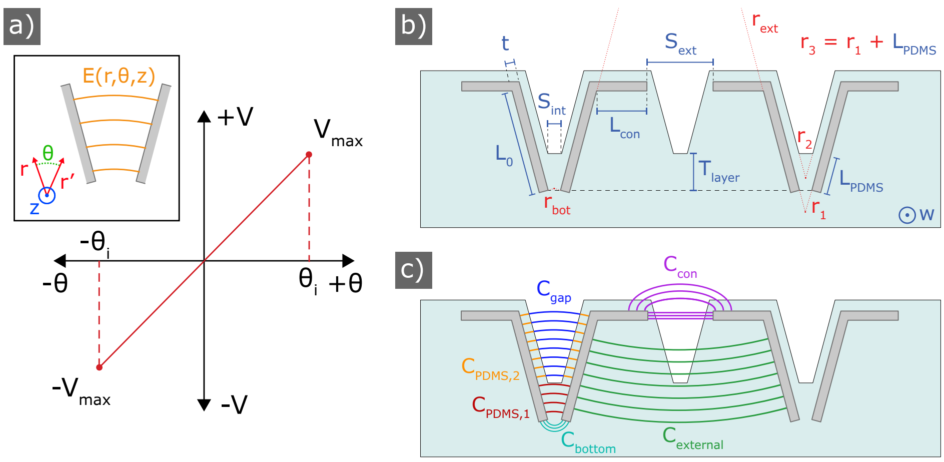

Figure 5.2 – Aspects of the capacitive sensor model. **a**) The electric field between two plates can be described in cylindrical coordinates with a magnitude of the voltage on the plates prescribed as V_{max}. **b**) Dimensions drawn for the side view of the model of the bending sensor that can be manipulated (blue) and those that are calculated (red). **c**) The electric fields that are considered in the full model to calculate the total capacitance.

First the capacitance due to the main internal and external fields is determined,

$$C_{\text{gap}} = \frac{\varepsilon_{\text{PDMS}}\varepsilon_0 w}{\theta_{\text{i}}} \ln\left(\frac{L_{\text{air}}}{r_1} + 1\right), \tag{5.10}$$

$$C_{\text{PDMS,1}} = \frac{\varepsilon_{\text{PDMS}}\varepsilon_0 w}{\theta_{\text{i}}} \ln\left(\frac{L_{\text{PDMS}}}{r_2} + 1\right), \tag{5.11}$$

$$C_{\text{PDMS,2}} = \frac{\varepsilon_{air}\varepsilon_0 w}{\theta_{\text{i}}} \ln\left(\frac{L_{\text{PDMS}}}{r_3} + 1\right), \tag{5.12}$$

$$C_{\text{internal}} = C_{\text{PDMS,1}} + \left(\frac{1}{C_{\text{PDMS,2}}} + \frac{1}{C_{\text{gap}}}\right)^{-1}, \tag{5.13}$$

$$C_{\text{external}} = \frac{\varepsilon_{\text{PDMS}}\varepsilon_0 w}{\theta_{\text{i}}} \ln\left(\frac{L_0}{r_{\text{ext}}} + 1\right). \tag{5.14}$$

Next the fringe fields at the bottom of the plates are added

$$C_{bottom} = \frac{\varepsilon_{\text{air}}\varepsilon_0 w}{90° - \theta_{\text{i}}} \ln\left(\frac{L_{\text{PDMS}}}{r_{\text{bot}}} + 1\right). \tag{5.15}$$

Lastly, any fields due to the connectors are added assuming that these remain static and bending does not influence their orientation. The extremities of the two ends are assumed to act like a parallel plate capacitor

$$C_{\text{connector}} = \frac{3\varepsilon_{\text{PDMS}}\varepsilon_0 w t}{s_{\text{ext}}} + \frac{\varepsilon_{\text{air}}\varepsilon_0 w}{90°} \ln\left(\frac{3L_{\text{con}}}{s_{\text{ext}}} + 1\right). \tag{5.16}$$

By assembling these capacitance values all together the final model is realised

$$C_{\text{model}} = \left[\frac{n}{2}\right](C_{\text{internal}} + C_{\text{bottom}}) + \left[\frac{n}{2} - 1\right](C_{\text{external}} + C_{\text{connector}}), \tag{5.17}$$

where n stands for the total number of plates that face each other which should always be an even number. This model was programmed into Python to determine the influence on the capacitive for the individual parameters shown in Figure 5.2 b, which were sweeped one by one as per Table 5.1. Fixed values were set for the parameters not being sweeped.

In Figure 5.3 the results of these sweeps with respect to the angle (θ) are shown. The most influential parameters are the internal spacing, plate width and length of the plate. The reason for this is that larger values for these directly increase the capacitance that can be generated in harmony with the V configuration of the plates. As would be expected, the highest capacitance gain that can be made is by increasing the width of the plates.

Attention should be paid to certain parameters such as the thickness of the plate. When the

Table 5.1 – Overview of the parameters and the minimum, maximum, and fixed values used for the sweeps performed using the analytical model programmed in python.

Parameter		Min	Max	Fixed	
Internal spacing	S_{int}	100	5000	1000	um
External spacing	S_{ext}	0.5	25	5	mm
Plate length	L_0	1000	10000	5	mm
Plate thickness	t	400	4000	500	um
Encapsulation thickness	T_{layer}	5	90	35	$\%L_0$
Width	w	0.1	2.5	1	cm

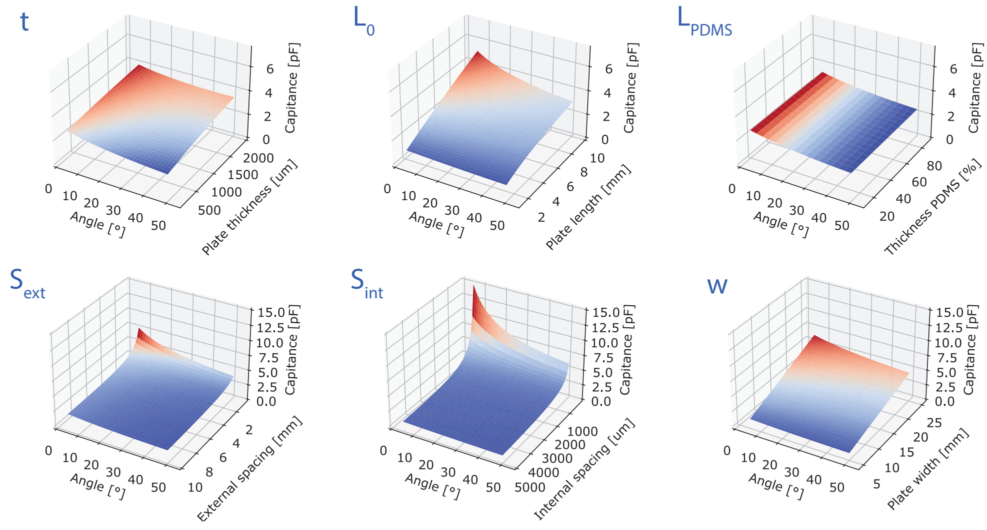

Figure 5.3 – Capacitance values for angles of 5-50° for several parameter sweeps including the plate thickness (t), plate length (L_0), amount of encapsulation (L_{PDMS}) in terms of the length of the plate, external spacing (S_{ext}), internal spacing (S_{int}), and plate width (w).

thickness exceeds a critical threshold the fringe fields will dominate those in-between the plates, causing a reversion of the intended sensing direction.

Static FEM model

A static Finite Element Method (FEM) model was built in COMSOL Multiphysics to simulate the geometry of the analytical model to validate it. This model was build using the electrostatics module to simulate an electric field between the two plates with a voltage applied on one plate and the ground on the other. The capacitive plates are assumed to be in parallel such that they can be summed. By changing the angle from the plate to the centre-line (θ_i) the bending of the sensor is simulated. However, this only simulates a change of the geometry and not the real bending of the sensor. An example of how the geometry changes can be seen when changing the angle from 15° (Figure 5.4 a) to 45° (Figure 5.4 b).

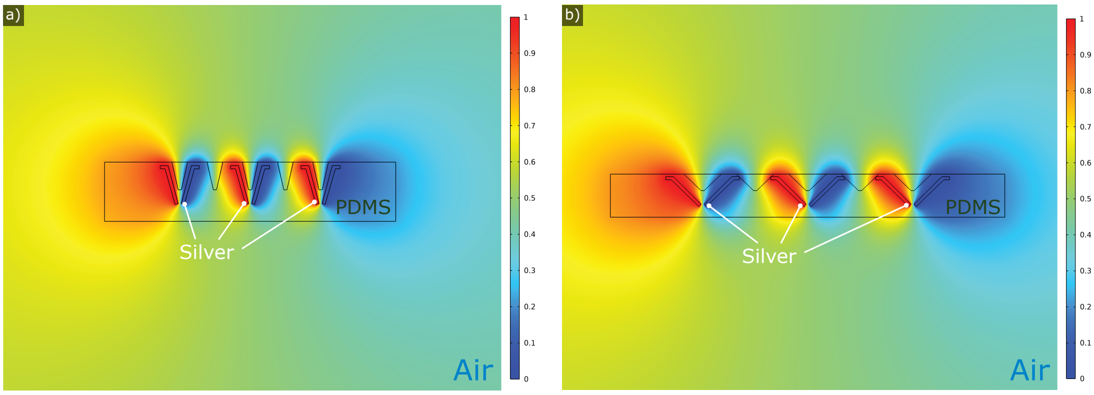

Figure 5.4 – The static FEM model simulated in COMSOL showing the electrical field between six plates at angles of the V-shape of **a**) $\theta = 15°$ and **b**) $\theta = 45°$ from the centre-line.

Parametric sweeps were carried out for several parameters chosen per the results from Figure 5.3. These were the plate length (L_0), internal spacing (S_{int}), and the plate width (w) at three different values. The standard values for the parameters when not being studied were 10 mm for L_0, 800 µm for S_{int}, and 10 mm for w. The latter configuration has a reduced capacitance due to a lack of external fields from the connectors. As expected, the capacitance increases by increasing the size of L_0 and w, and reducing S_{int}. A comparison between the two static models, one with a single pair of plates and the other with six, is shown in Figure 5.5.

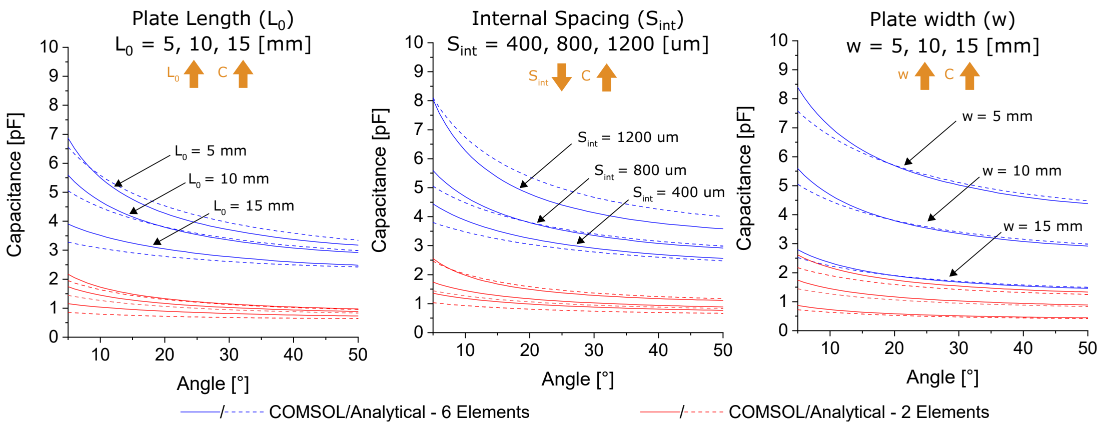

Figure 5.5 – Comparison of the analytical and static FEM model in COMSOL for different values of the plate length (L_0), internal spacing (S_{int}), and the plate width (w). The simulations were carried out for 6 plates (blue) and 2 plates (red).

From these sweeps it can be seen that the models are matching well with one another and there are only small errors between the two. By calculating the R^2 between the two datasets it is possible to determine how big the error between them is. For these sweeps an average R^2 of 0.996±0.002 is found which indicates that overall the shapes of the models are matching well. Therefore, any difference is within the magnitude, and most likely stems from the fact that within the analytical model not all geometric constraints can be taken into account, leading to over and underestimation for certain fields.

Bending FEM model

As the actual bending of the sensor is not taken into account for the static models, a second model was created in COMSOL. In this model the body of the sensor was deformed, instead of changing the angles between the plates, to further investigate how the sensor would actually behave, and how well the other models estimated this. The model was set up in the same way as before but using a deforming mesh, static deformation, and multiphysics coupling for the electromagnetic forces. A rotating boundary condition with an angle Φ_{act} was applied to both sides of the sensor to bend it, resulting in an angular deformation of γ_{bend} (90 - Φ_{act}).

As the aim of this model was to use it as a basis for verifying a sensor prototype, the dimensions were based on those which could be effectively achieved using the proposed manufacturing technique. These were an external spacing (S_{ext}) of 5 mm, an internal spacing (S_{int}) of 1200 µm, plate width (w) of 1 mm, a plate length (L_0) of 1 mm, layer thickness (t_{layer}) of 4.5 mm (45%), and plate thickness (t_{plate}) of 800 µm. The results of each model are shown superimposed in Figure 5.6 in terms of both the absolute and relative capacitance change in picofarad and percentage, respectively.

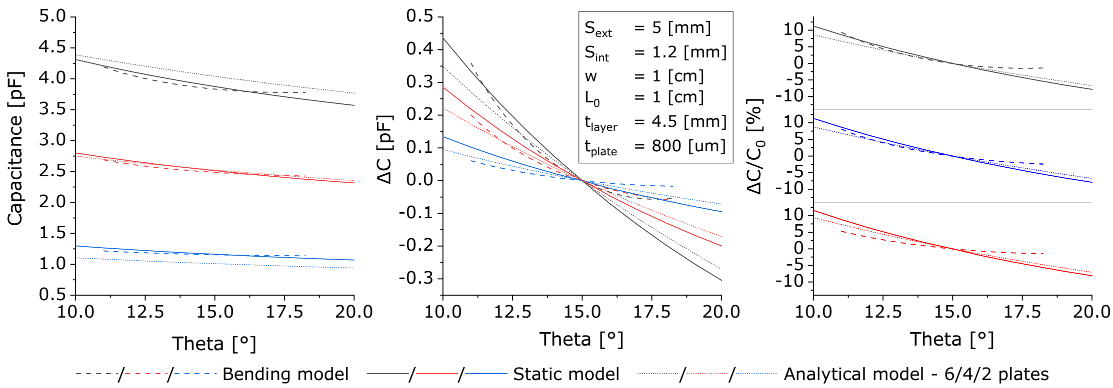

Figure 5.6 – Comparison of the developed models for a set of parameters including the bending, static, and analytical model with a single, two, or three sets of plates.

The choice was made to start with a 15° angle between the plates, such that the total angle between plates was 30°, and to determine the relative capacitance and its change from this angle.

The bending, static, and analytical models all matched well in terms of the capacitance change. Due to the change in curve a lower R^2 value of 0.946±0.023 was found when comparing the analytical model to the bending one. Furthermore, the bending model showed the influence of an aspect that could not be taken into account for in the other models. As is demonstrated in Figure 5.7, when bending the sensor at the sides and keeping the center fixed it results in a non-equal change of the angles of the plates. The plates on the inside bend further inwards leading to a non-equal change of capacitance between the sets of plates.

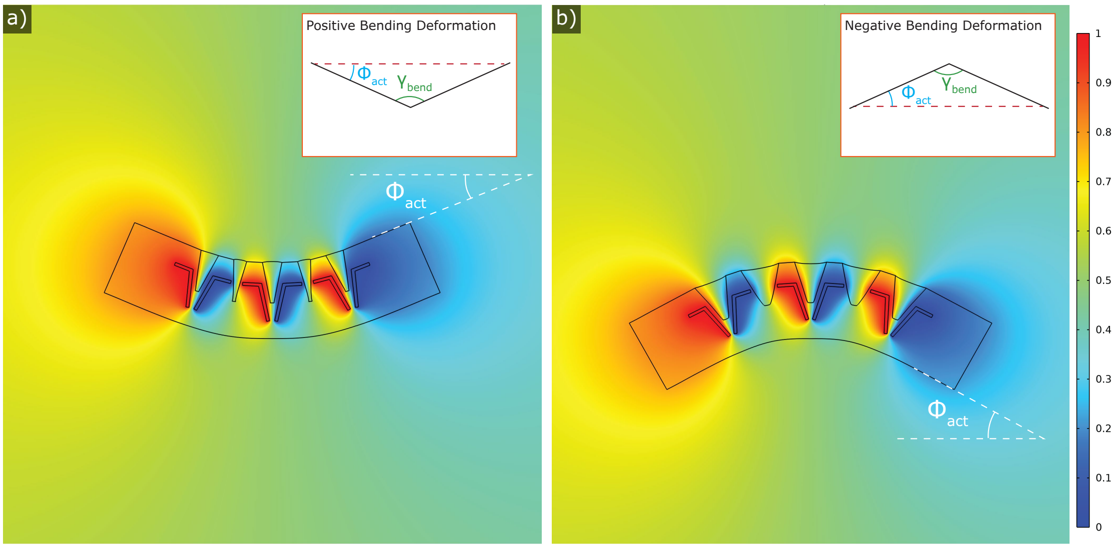

Figure 5.7 – The bending FEM model programmed in COMSOL with the actuation angle Φ_{act} and actual bending angle (γ_{bend}) indicated for **a**) positive and **b**) negative bending.

For this model the plate to midline angle (θ) was to 15° as established at the start. This would allow the reciprocal part of the curve to be used for finely estimating small angles of adduction, while resulting in an approximately linear response for larger bending angles.

In the bending model the actuation angle of the sensor was 29.5° in the positive direction, and 23.5° in the negative direction, for a total angular translation of 73°. This results in a total bending angle γ_{bend} of 146°. This was the maximum angular difference that could be simulated in the bending model as beyond it would run into convergence errors. The actual angles of the plates, with respect to the mid-line, are at 11 and 18.3° for actuation angles of 29.5° and 23.5°, respectively.

Sensitivity values were calculated with respect to bending angle (γ_{bend}) of the sensor for a sensor design with the dimensions as shown in Figure 5.6. To simulate its use as a bending sensor for a human joint, a range of motion between 90-120° was required, which could not be simulated due to convergence errors. The estimated sensitivities are therefore for angular deformations of 59° and 47° for positive and negative bending, respectively.

With a base capacitance of around 3.8 pF, for a 6 plate capacitive sensor, the model gives a sensitivity of 5.99±0.13±fF/° (0.16±0.00 %/°) for positive bending, and 1.11±0.07 fF/° (0.03±0.00 %/°) for negative bending when approximated linearly. For a 2 plate sensor the base capacitance was 1.15 pF and the sensitivity values went down to 1.03±0.02±fF/° (0.09±0.00 %/°) and 0.36±0.00±fF/° (0.03±0.00 %/°) for positive and negative bending, respectively. Therefore, a multi-plate sensor is preferred as not only does it add base capacitance, which reduces the influence of any noise, it also increases the sensitivity significantly.

Summary of model evaluation and importance of design parameters

In this section, analytical and FEM models were developed to understand the sensing mechanisms of the proposed bending concept, and evaluate the influence of the design parameters.

These models were used to determine the influence of certain parameters with different plate angles (θ), which could be used to approximate the bending behaviour. A secondary bending model was created to actually evaluate the behaviour of the sensor for the actual bending angles (γ_{bend}).

The analytical model was used to sweep the thickness (t), plate length (L_0), plate encapsulation (L_{PMDS}), internal and external spacing between plates (S_{int} and S_{ext}), and sensor width (w). Each parameter influenced the behaviour of the bending sensor differently, as was demonstrated in Figure 5.3.

For the plates, their lengths determine the shape of the response of the sensor, with longer plates resulting in a higher reciprocal response when bending the sensor positively. This has to do with the fact that a longer plate leads to a longer arc length, and capacitance building up faster when the plates have a small angle in-between. A more approximately linear sensor can thus be achieved with a shorter plate. This means that the sensor mechanism is well suited for a low-profile miniaturised version.

The thickness of the plates showed little effect on the capacitance. Encapsulating the plates increased the capacitance slightly, but too much thickness did not result in a significant addition. Therefore, only a small encapsulation should be added at the bottom where the plates are closest and the electric fields are strongest. Adjusting the width of the sensor is an easy way to increase the capacitance, as its scaling effect is entire linear, and allows for the capacitance to be finely tuned.

The dimensions of the internal and external spacing both exhibited a significant effect on the shape of the response due to the change of the arc length. The internal spacing was found to be the most influential and changing its values allows for tuning of the base capacitance. However, as the external spacing added base capacitance as well, its dimensioning should be exploited due to it remaining mostly static during the bending deformation.

Using the bending model, the actual behaviour of the sensor was simulated for bending angles (γ_{bend}) of 59° and 47° for positive and negative bending, respectively. The bending behaviour was simulated for a sensor design with six plates, with an internal and external spacing of 1.2 and 5 mm, plate length of 10 mm, layer encapsulation of 4.5 mm, plate thickness of 800 µm, and plate angle of 15°, which could be replicated using FDM moulding for its validation. This sensor showed positive bending and negative bending sensitivities of 5.99±0.13±fF/° (0.16±0.00 %/°) and 1.11±0.07 fF/° (0.03±0.00 %/°), respectively. Convergence issues with the simulation did not make it possible to evaluate larger angular deformations.

With these metrics, this makes the current sensor design less sensitive than both capacitive and resistive strain sensors used for angular bending measurements. However, neither of these sensors were able to demonstrate asymmetric sensing[96], [178]. When considering the form factor, a normalised sensitivity of 37 fF/°cm^2 was determined, which is a factor 13.2 higher than a similar fabric based bending sensor[177].

For the 3D printed miniaturised version, the sensitivity values are reevaluated and compared to the state of the art in Section 5.4.5.

5.1.3 Model validation through FDM moulding

To validate the models, a sensor prototype was created using conventional microfabrication techniques. A sensor prototype was fabricated using a tested and proven method for producing the non-planar geometries. A negative two-part mould was printed using a Prusa i3 MkIII FDM printer which could print at a minimum resolution of 400 µm. Therefore, to print features which were sufficiently stable at least two lines (800 µm) were used to print free-standing plates to acts as negatives for the conductive features of the sensors. The mould was designed composed of two parts as shown in Figure 5.8 a. By assembling the mould and injecting PDMS through the side port, as shown in Figure 5.8 b, the entire chamber was filled. Any excess PDMS could flow through the overflow port in the top.

The two parts of the mould were printed from a UV transparent Purefil PETG filament (Fabru GmbH, Switzerland) at an extruder temperature of 240 °C, bed temperature of 80 °C, and printing speed after the first layer of 80 mm/s. A microscopy image of the mould after printing

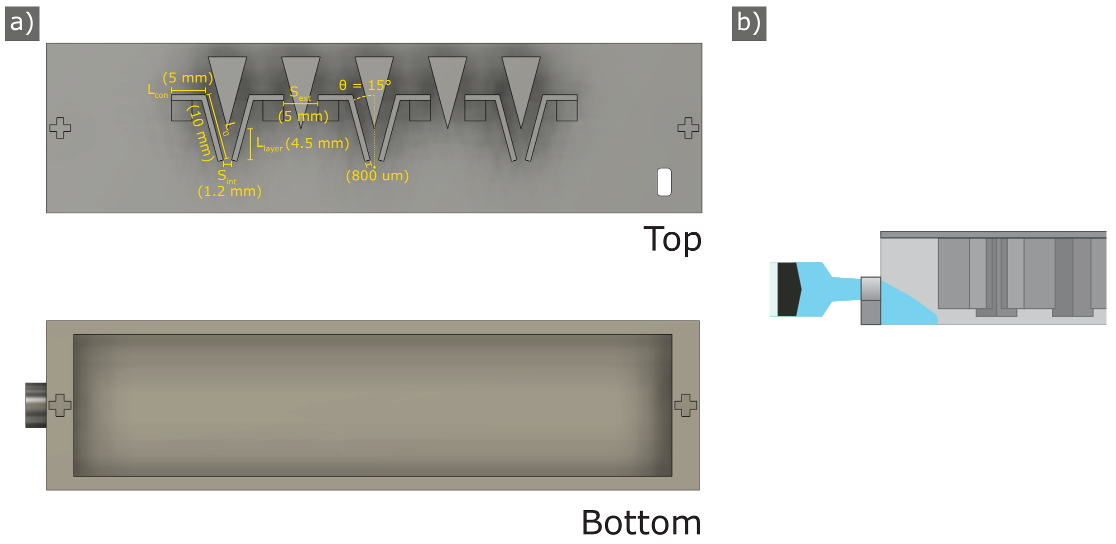

Figure 5.8 – **a**) The CAD design of the two part mould with its dimensions. **b**) Filling of the mould with silicone by injecting it from the side.

is shown in Figure 5.9 a, with the printed dimensions shown.

Filling of the mould

Before casting, the mould was cleaned using isopropanol and placed inside of a Zepto oxygen plasma cleaner (Diener electronic GmbH & Co. KG, Germany) and plasma treated for 1 minute at full power (60 W @ 40 kHz) to reduce the surface energies as much as possible. In the meantime, Silopren^{TM} UV Electro 225-1 silicone was prepared by mixing it with its curing agent first manually and then in a planetary mixer. The prepared PDMS was then slowly scooped into a syringe before being placed into a desiccation chamber for 5 minutes to remove as much air as possible. Once the PDMS was inside of the syringe, the plunger was added and the PDMS was inserted into the mould.

Three strategies were tested for comparison, including, casting the material and then desiccating it (Figure 5.9 b), injecting the material through the side port of the closer mould using the syringe (Figure 5.9 c), and first casting a thin film before adding the top cap and injecting the rest of the material (Figure 5.9 d).

In each technique the mould was filled until PDMS caused overflow. Desiccation after filling the mould should be able to reduce the bubbles but only resulted in air bubbles merging into larger ones inside of the mould. Bubbles were especially prevalent in the spaces between the triangle shapes and the plates, which reduces capacitance and could potentially short-circuit the plates. Therefore, the best technique among the three was to add a thin cast layer inside of the mould, before adding the top part and injecting the rest of the material.

After filling the mould, it was placed inside of the ProMA 140 UV exposure device for 10 minutes to ensure that the entire body was cured. To remove the body of the sensor the lid was gently pried off using a razor blade with the use of isopropanol as lubrication. After removal of the lid, the PDMS body was removed from the mould and allowed to dry. The negative cavities to allow for the plates had an average width of 824±29.9 µm which represents an error of less than 3% compared to the programmed values.

Creation of the plates

The plates of the sensor were created from SS-24 EMI/RFI Conductive Adhesive (Silicone Solutions, Ohio, USA) which is a nickel graphite reinforced silicone with a volume resistivity of 0.09 Ω cm. Before injecting this in negative spaces of the PDMS body, its surface was activated by use of the plasma cleaner described previously. The SS-24 adhesive was then carefully added into the voids by filling it from the bottom up using a small syringe with a thin needle. The entire device was then allowed to cure for at least 72 hours at room temperature (20°C) before use to allow the adhesive to cure completely. Several devices were produced this way, with one of the final prototypes is shown in Figure 5.9 e. Silver and carbon based inks were also tested but these shrunk too much during curing, leading to fragile and broken plates.

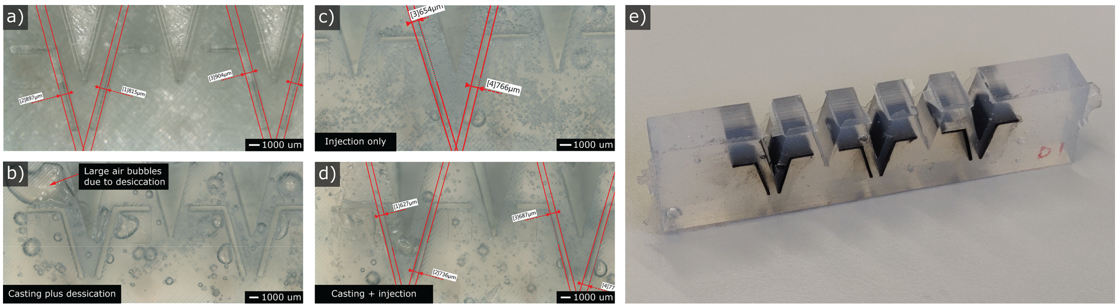

Figure 5.9 – Comparison of the tested strategies to fill the FDM mould. Optical images of **a**) the FDM mould, PMDS body using **b**) only injection, **c**) casting plus desiccation, and **d**) casting plus injection. **e**) A photograph of a final prototype bending sensor with the conductive plates made from the nickel-silicone compound.

5.1.4 Characterisation of the prototypes

Prototypes were characterised by connecting their plates in parallel fashion to a USB CapMeter (JLM Innovation GmbH, Germany) which is able to read out capacitance changes within a range of 4 pF at an accuracy of 4 fF. To avoid noise, all cabling was grounded and the sensors were put in a Faraday cage during testing. A PMMA plate was cut which forced the sensor under predetermined bending angles of the sides of the sensor (θ_{act}) at values of 15° and 30°. Multiple sensors were bend under these angles of which the measurements are shown in absolute (Figure 5.10 a) and relative values (Figure 5.10 b). The prototypes displayed the intended bending behaviour but do not entirely match the predicted capacitance. Most likely this discrepancy stems from production errors, such as bubbles inside the PDMS and incomplete filling of the cavities of the plates. The relative capacitance change shows that, in terms of percentage change ($\Delta C/C_0$), the sensors follow the models well but with some error. A R^2 value of 0.944±0.043 was found for the datasets. Images from a sensor being bend are shown in Figure 5.10 c and were captured using a Dino-Lite Digital USB microscope. The image shows that, since the plates are also made of a flexible material, they bend along with the sensor body. Since this results in a non-linear deformation it further explains for the small differences in slope at larger bending angles.

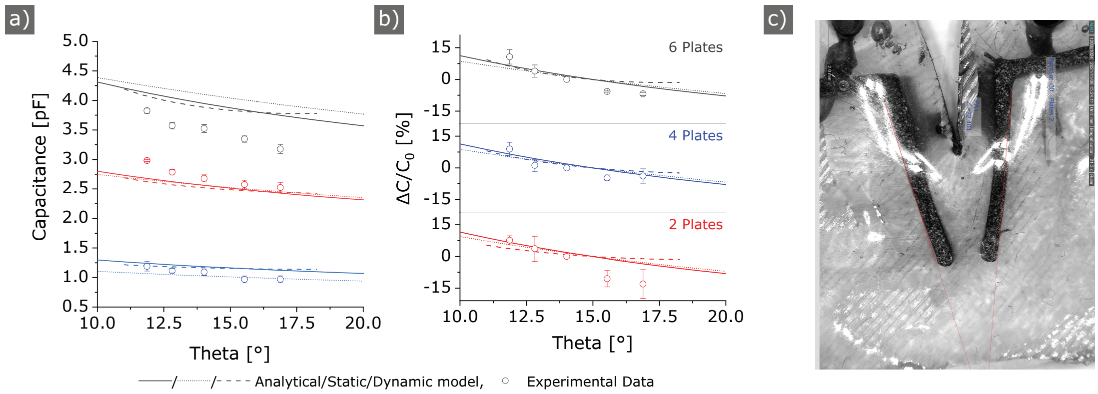

Figure 5.10 – Experimental results of the capacitive bending sensor prototype versus the model for **a**) the absolute capacitance, and **b**) relative capacitance ($\Delta C/C_0$). **c**) Non-linear deformations of the bending plates during bending of the sensor.

5.2 3D printing of soft silicone with planar geometry

Creating a 3D printable silicone bending sensor required that techniques be developed to realise its production. Above all else, the techniques to DIW print angular structures were missing to realise the slanted plates for the sensor. However, to reach this overarching goal first the development of a protocol to print 2D features is discussed in this chapter.

5.2.1 Printing Methodology

To 3D print silicones, we decided to reinforce them with fumed silica to introduce the shear thinning conditions outlined in Section 2.1.2. Initial tests were carried out with the same thermoset silicone (Sylgard 184) which was extensively used in Chapter 4. An additional UV curable silicone (UV Electro 225-1) was also explored to quickly in-situ cure the printed silicone structures through UV exposure. In this section the characterisation and utility of both inks is discussed.

All silicone materials were printed using a nScrypt (Orlando, Florida, USA) Direct Ink Writing (DIW) printer. This highly advanced 3D printed can be equipped with DIW printing devices called smartpumps which allow for precise control of the flow by means of a programmable valve that can precisely release small amounts of ink. By tuning the pressure, speed, valve opening, and distance to the substrate, the deposition of inks of varying viscosity can be finely controlled. As the pressure is constantly applied there will be no backflow, which makes the printing more reliable than for most DIW printers.

The printing process was established as follows. First a thin layer of Sylgard 184 silicone (Dow Inc., MI, USA) was doctor bladecast using a Zehntner ZAA 2300 film applicator on top of a cleaned and plasma activated 125 µm thick PET sheet. This film was cast at a blade height of 200 µm and at a speed of 3 mm/s and then allowed to cure for at least 3 hours in an oven at 80 °C. The resulting film had a thickness of about 110-115 µm, resulting in a base layer thickness of about 235 µm when taking the PET layer underneath into account. This film was activated using a Diener Atto plasma cleaner at 150 W (@ 13.56 MHz) for a duration of 1 minute before printing.

Silicone inks were inserted into luer-lock syringes that were attached to the printer and pressurised. Then, by bringing the inter-exchangeable printing tip of the smartpump close to the substrate, the material could be deposited onto the doctor bladecast silicone. Thermoset silicone was cured by using the heated bed of the printer and curing it for 3 hours at 80 °C. UV curable silicone was cured using either the build-in UV LED or an external ProMA 140 UV exposure device for at least 3 minutes, as specified by the datasheet. A schematic of these processes is shown in Figure 5.11. All silicone inks were printed using the 125 µm ceramic dispensing tip.

5.2.2 Ink preparation

The silicone inks were prepared by reinforcing them using fumed silica, which is a commonly used rheological modifier to create shear thinning inks[51], [55]. Two silicones were used in the 3D printing experiments which were the thermoset Sylgard 184 and a UV curable PDMS called Silopren UV Electro 225-1 (Momentive Inc., NY, USA). Both silicones consist of a base

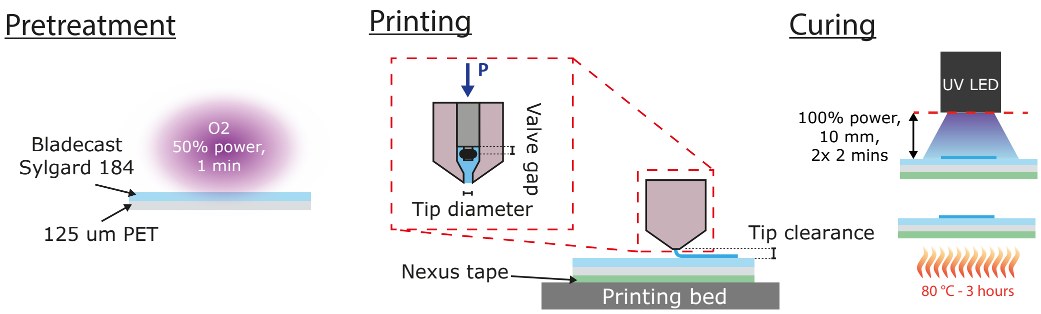

Figure 5.11 – The three step fabrication process for printing silicones. A thin layer of Sylgard 184 silicone was activated using a plasma cleaner before the smartpump was used to print silicone ink on top of this. Finally the printed silicone was cured either thermally or by UV exposure.

precursor (Part A) and a curing agent (Part B).

First Part A of the silicone was put in a measuring cup and weighed. Then Part B was added at 10 wt% for Sylgard 184 and 2 wt% for UV Electro 225-1 and mixed thoroughly by hand. After this step inks were mixed in a planetary Thinky Mixer ARE-250 and mixed for 2 minutes at 2000 RPM and defoamed for 2 minutes at 2200 RPM. Any unreinforced silicones were prepared by the same protocol but without the addition of fumed silica.

To create reinforced silicones, HDK H30 fumed silica (Wacker Chemie AG, Germany) was added carefully to a cup. The Part A precursor was added on top and the materials were gently mixed to avoid dispersion of the fumed silica into the air. The mixing continued until all fumed silica was inside of the precursor, which resulted in a significant volume decrease. Subsequent mixing was performed by using the planetary mixer using the same program as for mixing silicones. After mixing, the mixture was inspected, and if the resulting ink was not homogeneous, was once more mixed by hand and by planetary mixer. Several loadings of fumed silica (9.1, 11.6, and 16.5 wt%) were tested to evaluate the printability. For loads of fumed silica above 10 wt% it was often necessary to perform multiple mixing steps. Since the mixing was only performed using Part A, the process resulted in a fumed silica reinforced precursor.

To create the final DIW printable silicone ink, the respective curing agent was added to the precursor. The curing agent weight percentages were not altered. First the complete mixture was mixed once using the silicone program for the planetary mixer. Then the mixture was inserted into a a large syringe that was connected to a 2 ml luer-lock printing syringe using a female-female connector. This procedure was done to reduce the amount of bubbles in the ink. Finally the printing syringe was mixed for 30 seconds at 2000 RPM using the planetary mixer to further decrease the amount of bubbles.

Characterisation

Printed features were measured using a Keyence VK-X 3D Laser Scanning Confocal Microscope to determined their dimensions. As the inks were transparent, gold sputtering was used to make certain features scanable. Optical images both top-down and cross-sectional were taken using a Keyence VH-X Digital Microscope.

5.2.3 DIW printing of thermally curable silicone

As we used DIW printing to create sensors from Sylgard 184 reinforced with fumed silica, as was demonstrated in chapter 4, we investigated if it would be possible to 3D print similar structure using the nScrypt smartpump. We investigated how suitable this method was for the fabrication of multilayer structures that could be cured in one shot to create 3D structured sensors.

Influence of plasma treatment before printing

To understand the influence of plasma on the deposition of the fumed silica reinforced Sylgard 184 silicone ink, print tests were performed on top of polyimide foil. The substrate material was chosen to be able to visualise the deposition of the silicone ink, and as surface interaction energies between silicone and polyimide are high but can be reduced through plasma activation[182]. A 9.1 wt% fumed silica reinforced Sylgard 184 ink was used.

Single lines of 12.5 mm long were printed at pressure between 0.69 and 1.1 bar (10-16 psi) at speed of 10 and 20 mm/s. A distance of 125 µm was maintained to the substrate and the valve opening was set to 75 µm, which was sufficient to allow for a continuous flow of silicone at the set pressures. The printing results for both treatments are shown in Figure 5.12 which shows that the deposition of the material on non plasma treated films is erratic and inexact.

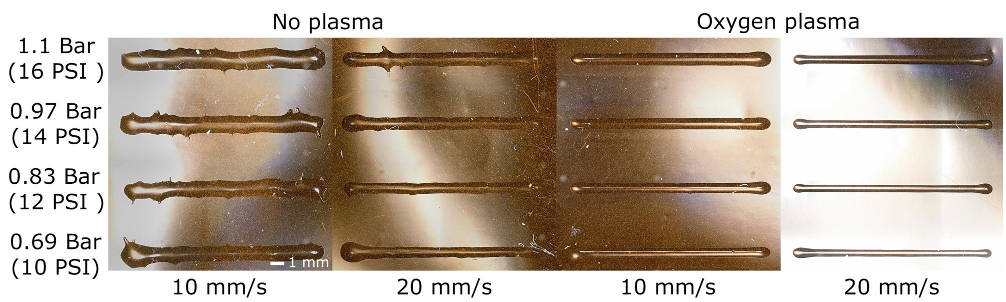

Figure 5.12 – Influence of plasma treatment and printing speed on DIW printed lines of 9.1 wt% fumed silica reinforced Sylgard 184 on top of a Kapton film.

The effects were verified using confocal microscopy and the measured dimensions are plotted in Figure 5.13.

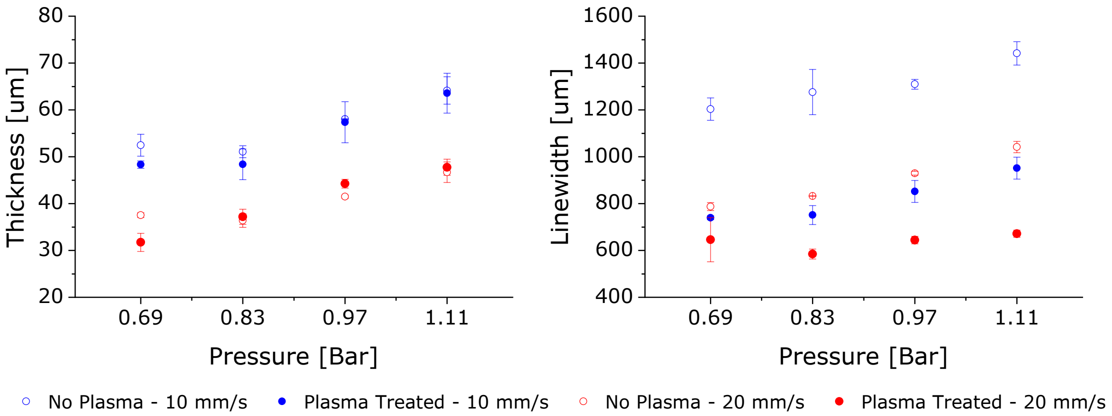

Figure 5.13 – Thickness and linewidth values of lines printed with and without plasma treatment printed at 10 and 20 mm/s.

The thickness of the printed lines is not significantly affected at average values of 55.4±5.9 µm and 40.4±5.2 µm for lines printed at 10 and 20 mm/s, respectively. However, the dimensions of the linewidth changed significantly. This effect was the most drastic for the lines printed at 10 mm/s, where their linewidth was measured to be 1307.6±256.9 µm without plasma treatment and 823.58±85.9 µm without. Therefore, in further experiments the substrates were always treated with plasma before printing.

Influence of addition of fumed silica

To understand the influence of adding more fumed silica to the ink, a comparison print was made by printing the same 12.5 mm lines using an ink that was reinforced with 11.6 wt% on top of plasma activated Kapton. As this ink had more fumed silica added to it, it also had an increased viscosity. Therefore, slight tuning of the printing parameters was required and the valve gap was increased from 75 to 120 µm. The printing gap and printing speed were kept the same. A linear dimensional increase is still observed as shown in Figure 5.14. For the thickness this was at rates of 54.9±5.1 µm/bar and 42.8±11.4 µm/bar for inks reinforced at 9.1 and 11.6 wt%, respectively. Both the thickness and linewidth reduced at average rates of 12.2±2.7% and 51.9±5.3%, respectively, when switching to the 11.6 wt% ink for the same set of pressures but with a larger valve opening. This makes it evident that the increased viscosity of the ink reduces the flow of the ink out of the tip and the amount being deposited.

To improve printing results we resorted to using a substrate that did not curl up, with less surface energy than the Kapton, in subsequent tests. A silicone substrate was created by

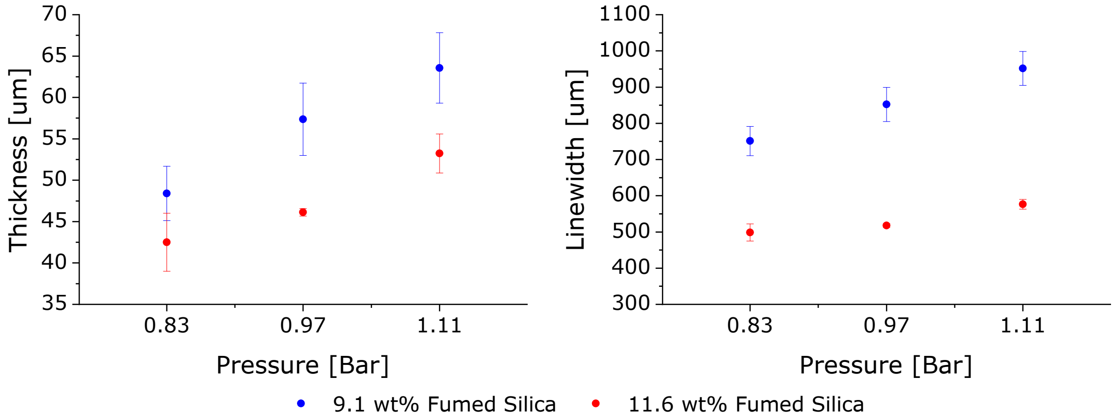

Figure 5.14 – Comparison of the addition of additional fumed silica to Sylgard 184 on the cured thickness and linewidth of printed lines.

doctor bladecasting Sylgard 184 using a Zehntner ZAA 2300 film applicator on top of a plasma activated 125 µm PET sheet at clearance of 200 µm a speed of 3 mm/s. This resulted in films of about 110-115 µm.

Printing multilayer structures

Even with 11.6 wt% fumed silica added to the silicone it was not possible to print multilayer features which held their shape during curing. Curing the structure instead layer by layer was unfeasible since the curing time of Sylgard 184 is in the range of 3 hours. While this might not be a problem for devices created with single or double layers, such as the normal pressure sensors created before, for more miniaturised devices created out of several layers stacked on top of each other, this adds significant processing time.

Therefore, we tested if reinforcing the silicone with a maximum amount of fumed silica would result in a stable depostion. The silicone was reinforced with 16.5 wt% fumed silica as any further reinforcement made a paste so viscous that it could no longer be mixed thoroughly. The resulting ink had such a high viscosity that the pressure range had to be increased from 0.69-1.11 bar (10-16 psi) to 3.59-4.41 bar (52-64 psi) with other parameters kept the same. Lines printed at 10 mm/s had an average thickness of 107.4±4.5 µm and linewidth of 215.5±10.7 µm for this pressure range without a linear relation discernible for their dimensions.

To print larger features, first two lines were printed at 4.14 bar (60 psi) and 10 mm/s in close proximity at a linespacing of 50, 100, 200, 300 and 400 µm. A linespacing of 100 µm was required to create a continuous single line as can be seen in Figure 5.15 a. Confocal microscopy measurements revealed that for the lines printed in proximity the thickness increased to 129.4±1.1 and 134.4±1.3 µm for spacing values of 50 and 100 µm, respectively. This is an average increase of 17.1±0.2% compared to the single lines. Subsequently, 12.5x12.5 mm^2 squares were printed with spacing values of 100 and 200 µm. Figure 5.15 b-c shows how influential this is on the printing of squares, as squares printed with a 100 µm linespacing are continuous.

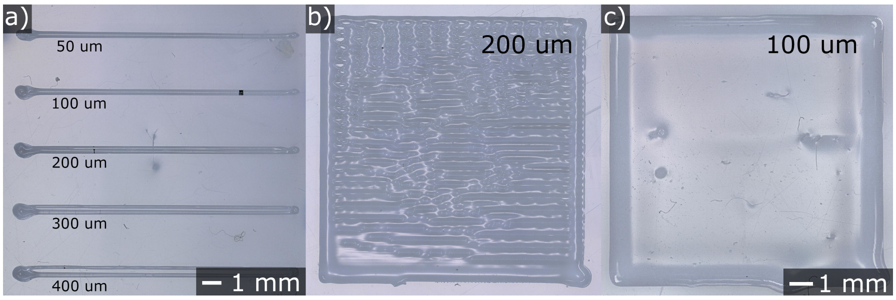

Figure 5.15 – Printing tests of the 16.5 wt% fumed silica reinforced Sylgard 184. **a**) Spacing tests between two lines to create a continuous feature. Square structures printed using **b**) 200 µm and **c**) 100 µm linespacing.

To try and print multilayer structures, several square layers of the silicone ink were printed with a 150 µm z-offset on top of one another. This value is slightly higher than the layer thickness as the deposited Sylgard 184 layers shrink slightly due to curing and flow after deposition. A pyramidal structure was printed consisting of 3 square layers of 12x12 mm^2, 10x10 mm^2, and 8x8 mm^2 with a final circular structure 5 mm in diameter on top. The printing pattern (.gcode) of this structure and the resulting print after curing are shown in Figure 5.16.

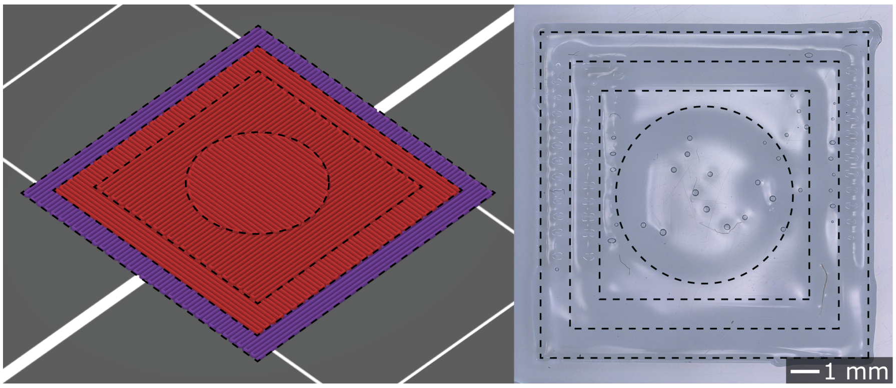

Figure 5.16 – 3D printing pattern and the final DIW printed structure of a multistack structure created from Sylgard 184 silicone reinforced with 16.5 wt% fumed silica.

As the ink flowed after deposition, as well as during curing, the feature loss between layers was unfortunately too significant to be able to use this ink to print 3D structures. Since the layers blended into each other, the resulting structure did not resemble the preprogrammed shape. Coupled with long processing times, this suggested that a different ink should be selected. Therefore, we decided to test other base silicones to achieve the desired 3D structures.

5.2.4 DIW printing of UV curable silicone

As the thermoset Sylgard 184 silicone ink could not be used to create 3D structures, we decided to use a different silicone ink. The selected candidate was a UV curable silicone called UV Electro 225-1 which can be cured using a UV lamp in atmospheric conditions. This ink was reinforced using fumed silica to achieve the desired printing characteristics.

Influence of fumed silica on rheology

To analyse the printability of this ink a more encompassing approach was chosen by determining the viscosity of the silicone at different loadings of fumed silica. The silicone was loaded using 2.5, 5 and 10 wt% fumed silica and compared to the plain material. Viscosity tests were performed using a Discovery HR-2 (TA Instruments, DE, USA). Both a shear rate and oscillation strain test were performed on the material.

The shear rate test provides information on the viscous behaviour of the material at different intensities of shear. An ideal DIW printable material will reduce in viscosity when a higher shear rate is applied, an effect called shear thinning[51]. The oscillation strain test was performed to evaluate the time-dependent material behaviour, by shearing the material back and forwards at different material strains, and then evaluating the viscoelastic properties. From the resulting stresses, the storage modulus and the loss modulus can be calculated which express the elastic and viscous behaviours of the ink, respectively. The evaluation of the moduli versus oscillation strain is shown in Figure 5.17 a and the viscosity versus the shear rate in Figure 5.17 b, for several amounts of fumed silica added to the silicone.

All inks showed shear thinning behaviour albeit not at the same rate. The 10 wt% ink has a far higher shear thinning rate than the other inks, which is due to the fact that this ink undergoes a phase transition indicating that they were more liquid than solid. A yield point, which indicates a phase transition from a more elastic phase to a more liquid one is shown only for the 10 wt% ink, indicating a transition from a elastic material to a more viscoelastic one. Therefore, at this loading the ink will not flow after deposition. The next ink down at 5 wt% ink had storage and loss moduli which were very close to each other. This ink will not undergo a phase transition but is still very gel-like and will flow slightly.

From the storage and loss moduli the phase angle, defined as $\delta = G''/G'$, can be calculated to determine how close the materials are to more elastic or more viscous material behaviour. The

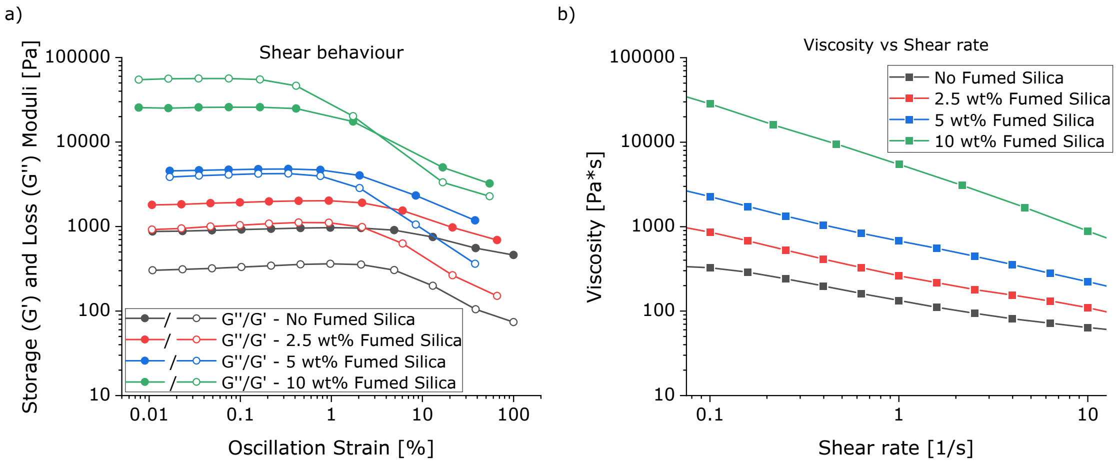

Figure 5.17 – UV Electro 225-1 silicone with several amounts of fumed silica added into it and its influence on the **a**) storage G' and loss G" moduli, and **b**) viscosity.

closer the value of δ to 90° the less elastic and the more viscous the material becomes, and vice versa when δ approaches zero. The phase angles and their development versus the fumed silica loading are shown in Figure 5.18.

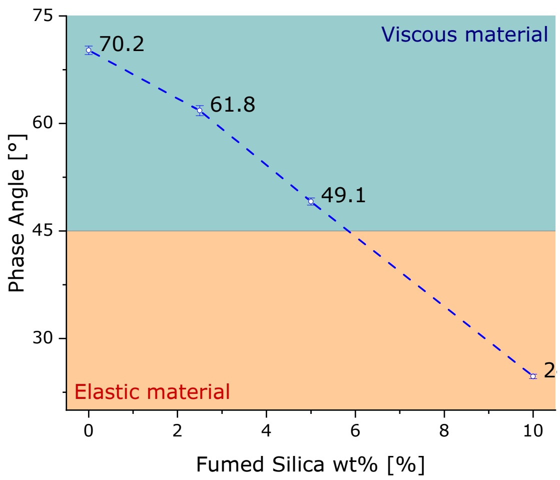

Figure 5.18 – Addition of different amounts of fumed silica into UV Electro 225-1 silicone and the influence on the phase angle.

A value of $\delta < 45$ deg indicates the material is viscous and will flow. The 5 wt% ink is very close to the transition point in where it will become a shear thinning elastic material, and thus acts like a slightly flowing gel. In fact, this behaviour can be exploited to create smoother features. The ink does not immediately settle after deposition and will blend with the surrounding ink leading to less rough surfaces. As the UV curable silicone cures in less than 3 minutes of exposure we could have control on how much the silicone flows before it is set. With this in mind we decided to continue by printing features created from the 5 wt% ink. If a truly shear thinning elastic ink is required it can already be produced at a loading of at least 6 wt% fumed silica.

Initial printing study of 5 wt% reinforced ink

To improve the overall printing quality, we needed to ensure that the distance of the tip was always within the same range of the substrate. A 95 µm GP20 Nexus tape (NEXUS, Republic of Korea) electrostatic foil was placed on top of the printing bed before adding the doctor bladecast Sylgard 184-PET substrate on top.

Initial characterisation experiments were performed by printing the 5 wt% UV curable silicone ink (UVE225-R5) on this substrate using a smartpump with a 125 µm tip. A valve gap of 150 µm was set and the lines shown in Figure 5.19 were printed at a printing speed of 20 mm/s. These lines were printed at pressures of 1.65 to 2.48 bar (24-36 psi) with a clearance between the tip and substrate of 75 µm. After printing they were briefly exposed for 1-2 minutes to UV light using the build in UV LED and then completely cured in a ProMA 140 UV exposure device for 5 minutes. The dimensions of the lines measured by confocal microscopy as are shown in Figure 5.19.

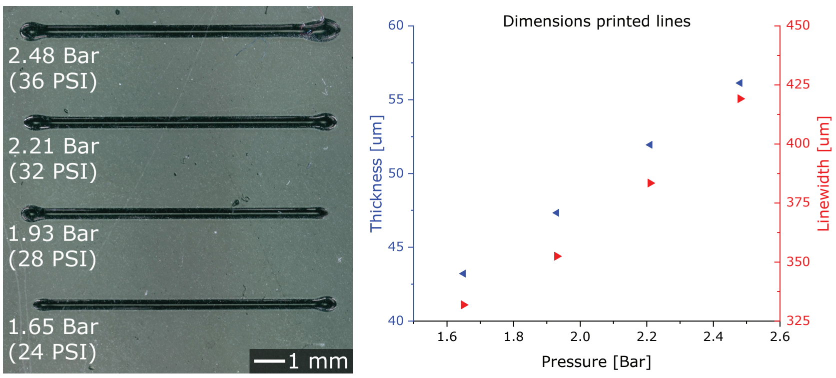

Figure 5.19 – Printed lines to determine the pressure-thickness relation using the UV curable silicone ink with 5 wt% fumed silica loading.

Initially a layer thickness of around 100 µm was targeted, however this could not be achieved using the shear thinning fumed silica reinforced Sylgard 184 silicone. With the UVE225-R5 silicone this was easily achieved as the thickness printing rate was 15.7±0.2 µm/bar. To print features of at least 50 µm, we decided to use a pressure of 2.21 bar (32 psi) and speed of 20 mm/s.

To achieve larger features, the next step was to test in tandem the influence of the clearance between tip and substrate, as well as the spacing between the lines. Three test lines with linespacing values of 100, 125, 150, 175 and 200 μm were printed at clearances of 25, 50, 75, and 100 μm. The resulting lines are shown in Figure 5.20.

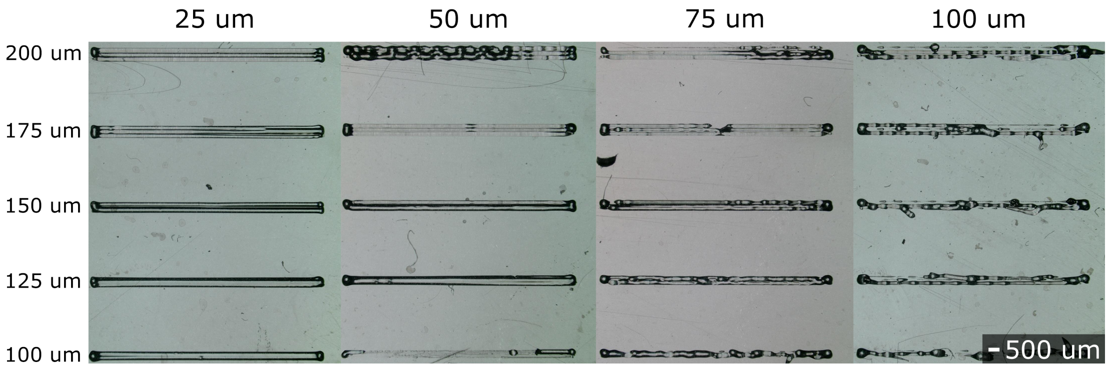

Figure 5.20 – Sets of DIW printed lines from 5 wt% fumed silica reinforced UVE225-1 Electro silicone with different linespacing values and tip to substrate clearances.

As was already observed, the UVE225-R5 silicone ink, has a particular behaviour that was not seen for the Sylgard 184 ink. Instead of adhering to the substrate, the ink would instead stick to the tip and curl around it causing a build up of ink if the clearance was too large. This is especially visible for lines printed with a 100 μm clearance, where the deposition of the ink is incomplete and discontinuous. As such, a clearance of at least 50 μm is recommended for printing. To ensure that features composed of many lines have planar surfaces, the lines require a linespacing of between 100 and 125 μm. These features had an average thickness of 52.3±2.7 μm, independent of the clearance, which is an increase of just 3.6±2.2 μm.

UV curing study

To cure the UVE225-R5 ink, it was exposed for 2-3 minutes using the build in 365 nm UV LED with 3 mm focusing lens, which has an irradiance of 14 W/cm^2 at a working distance of 10 mm from the silicone substrate (Figure A.1). However, a secondary curing step was performed where the features were transferred from the nScrypt to a ProMA 140 UV exposure device. In this device the samples were exposed to 120W UV radiation for 5 minutes to ensure complete curing. If instead the silicones are cured in-situ, the process flow is improved and alignment errors resulting from removing and reintroducing any samples into the printer are reduced. A small study was performed to determine the influences of curing parameters of the build in UV LED. For this study Design of Experiment (DoE) strategies were employed to analyse several samples and determine their trends using statistics.

The aim of the study was to evaluate the influence of curing conditions on the mechanical properties of the silicone in terms of its stress-strain behaviour. The experiments were performed by printing dogbone structures using the nScrypt, curing them at different UV exposure conditions, and then testing them in tensile strain on an Instron 3340 pull-tester (Figure 5.21 a). The dogbone structure design was created to be in accordance with the ASTM D638 standard which is explicitly designed to determine the ultimate tensile strength of plastics. The shape and dimensions of the dogbone design are shown in Figure 5.21 b. This design was printed on top of a plasma activated Sylgard 184 base layer with a 125 µm tip at a pressure of 32 psi, printing speed of 20 mm/s, linespacing of 100 µm, and a clearance of 50 µm. To reduce discontinuities in the printed dogbone structures, the valve gap was set to 200 µm. An example of a 3D printed dogbone is shown in Figure 5.21 c.

Several UV curing conditions were tested which included altering the supplied power, distance to substrate, and number of passes. The time of exposure was fixed at 5 minutes, as an initial test at the minimum power of 50% revealed that the ink was not fully cured at a shorter exposure time. The full set of tested parameters is shown in Table 5.2.

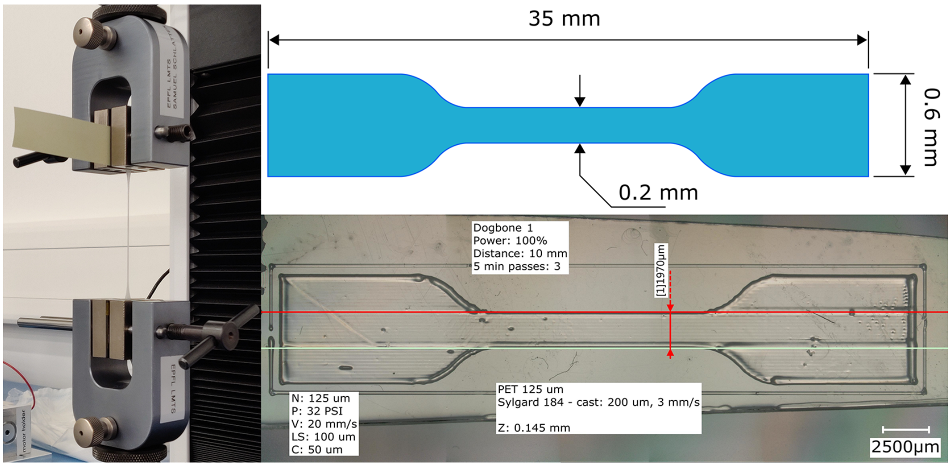

Figure 5.21 – Overview of the mechanical test setup and the samples with **a**) a sample being stretched using the Instron 3340 pull-test with tensile test clamps. **b**) Dimensions of the dogbone per the ASTM standard and **c**) a optical microscopy image of a dogbone printed using the nScrypt 3D printer.

After curing, the samples were dusted with talc powder to reduce their stickiness and aid in their removal from the substrate. To evaluate the samples, they were mounted in a Instron 3340 pull-tester and slowly stretched at 150 µm/s to reduce the influence of the strain rate as much as possible. The tensile tests were stopped when the samples underwent tensile failure. Internal forces and strains were recorded during this test. Using the recorded data the Young's

Table 5.2 – Tested conditions UV exposure conditions to test the curing of the UVE225-R5 silicone ink.

	Condition 1	Condition 2	Condition 3
Power (%)	50	75	100
Distance (mm)	5	10	20
Passes (#)[a]	1	2	3

[a]Each pass was programmed to expose the printed material for 5 minutes and used a .gcode that followed the printed pattern.

modulus (or E modulus) of the tested materials were determined by

$$E = \frac{\sigma}{\varepsilon} = \frac{(F_{\text{int}}/wt)}{\varepsilon}, \tag{5.18}$$

where F_{int} represents the internal force, w the thinnest width of the dogbone, t its thickness, and ε the strain. The slope of which will be linear as long as the ratio between stress (σ) and strain remains the same, a behaviour called linear elasticity. The resulting E moduli and the associated testing conditions are shown in Table 5.3.

Table 5.3 – Testing conditions and resulting E moduli of dogbones printed by the nScrypt from UVE225-R5 silicone ink found by means of the tensile test.

Sample	Passes	Distance	Power	E modulus
[#]	[#]	[mm]	[%]	[kPa]
1	1	10	50	671
2	1	20	75	774
3	1	5	100	810
4	2	10	75	587
5	2	20	100	614
6	2	5	50	625
7	3	10	100	602
8	3	20	50	565
9	3	5	75	685

Using this data, or the responses, we determined a constant coefficient model to understand the influence of each parameter. A constant coefficient model takes the form of

$$Y(i,j,k) = \mu + \alpha_i + \beta_j + \gamma_k + \varepsilon_{ijkl}, \tag{5.19}$$

where Y is the response, μ the global mean and α_i, β_j, and γ_k represent values for the individual factors, or parameters. Finally, ε_{ijkl} represents the residual, or error, of the model and will contain any value of the response that can not be explained by the model. To determine the coefficients an action known as sweeping is performed, where the mean values of select groups are calculated to determine their individual difference with respect to the global mean. The global mean was calculated to be 665.2 kPa. The factors are calculated by taking the mean of their respective grouping and then subtracting the global mean. In this fashion the linear equation given in Equation (5.19) is slowly build by reducing the error $\vec{\varepsilon}$ step-wise. By summing up the vectors of each group (i.e. distance, power, passes) the constant coefficient model is obtained as

$$Y(i,j,k) = 665.2 + \begin{pmatrix} -44.8 \\ 2.3 \\ 42.5 \end{pmatrix} + \begin{pmatrix} 103.3 \\ -56.0 \\ -47.3 \end{pmatrix} + \begin{pmatrix} -44.6 \\ 33.4 \\ 11.1 \end{pmatrix} + \begin{pmatrix} -8.2 \\ 10.4 \\ 18.5 \end{pmatrix}. \tag{5.20}$$

Using this model it becomes possible to perform an Analysis of Variance (ANOVA), which makes it possible to determine if the parameters in the model are statically significant in comparison with the global mean with a confidence of 95%. The table consists of sums of squares (SS) of the coefficients, the degrees of freedom (DoF), mean square (MS) or the SS divided by the number of DoF, and the F ratio or the ratio between MS of a factor and the global residual. Using this information the p value can be obtained to determine if the parameters are of statistical significant or not. Table 5.4 shows these values and from this it can be seen that all variables were influential.

Table 5.4 – Analysis of Variance (ANOVA) table of the model for the influence of UV exposure on the mechanical properties of the printed UVE225-R5 silicone test samples, and the resulting statistic significance.

Factor	Sum of Squares (SS)	Degree of Freedom (DoF)	Mean Square (MS)	F Ratio (MS/DoF)	p value
Intercept	3982058.8	1	3982058.8	5127.73	<0.001
Passes	48139.9	2	24070.0	31.00	<0.001
Distance	11462.6	2	5731.3	7.38	0.014
Power	9684.9	2	4842.4	6.24	0.019
Residual	1553.1	2	776.6	1.00	0.250

Lastly we can evaluate the effect size, or influence of each group, by means of the Cohen D value which explains how many standard deviations of difference there are between two data groups. This can be calculated using the formula

$$\frac{\mu_{\mathrm{all}} - \mu_{\mathrm{g}}}{\sigma_{\mathrm{p}}}, \tag{5.21}$$

where μ_{all} is the mean of all samples, μ_{g} the mean of the group or category, and σ_{p} the pooled standard deviation of the two compared groups. To calculate this pooled standard deviation we use the formula

$$\frac{(N_{\mathrm{g}} - 1){\sigma_{\mathrm{g}}}^2 + (N_{\mathrm{all}} - 1){\sigma_{\mathrm{all}}}^2}{N_{\mathrm{g}} + N_{\mathrm{all}} - 2}, \tag{5.22}$$

where σ_{g} and N_{g} are the standard deviation and number of entries for a group, respectively, while σ_{all} and N_{all} are those for all samples. These values were calculated and are displayed in Figure 5.22. The effect sizes indicates the influence of a single group.

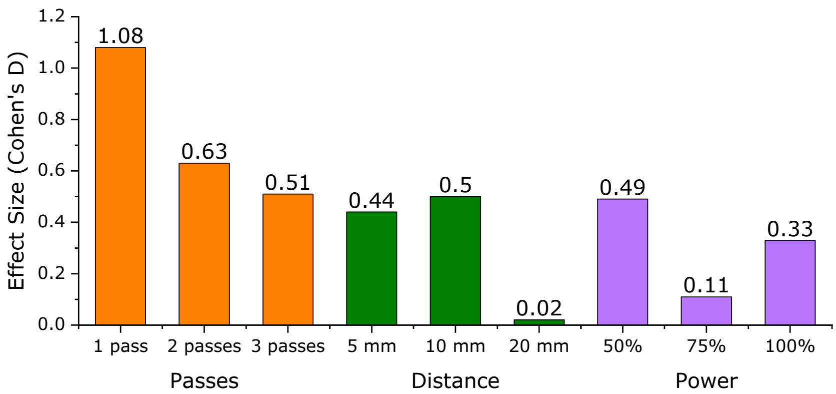

Figure 5.22 – Cohen's D effect sizes for the UV LED curing conditions of all tested DIW printed UVE225-R5 silicone test samples.

Values above 0.5 are generally regarded as having a medium effect, while those above 0.8 have a large effect. These values are only an indication, but this means that for this experiment there is a very significant difference in the number of passes. In fact, a single pass seems to yield a significantly different result than performing more passes. This likely stems from the fact that samples might not have been fully cured after a single pass at a lower power. Therefore, using an as high as possible power is recommended to reduce the total curing time. In terms of the distance, there seems to be little influence past a distance of 10 mm. However, there is a trade-off in-between the total area irradiated and delivered power as the UV spot of the lamp grows larger with a removed distance. Therefore, we decided to keep the distance at 10 mm and use a power of 100%. Exposure times of 1 minutes were used for curing in-between layers to retain some inter-layer adhesion and 5 minutes to perform a full cure. To avoid underexposing certain regions of the silicone ink, two passes were performed using the UV

LED. The travelling speed of the LED was programmed in .gcode such that the UV spot would expose the material only for the set amount of time.

5.2.5 Design of Experiments (DoE) to determine the influence of the printing parameters

There are numerous parameters that can be tuned when printing with the nScrypt smartpumps including, but not limited to, the pressure, printing speed, linespacing, tip clearance, valve gap, and various waiting times. Therefore, a Design of Experiments (DoE) approach was used to study the statistical influences of the printing parameters previously already shown to have an influence, which were the printing pressure, speed, and linespacing.

To optimise the printing of the UVE225-R5 silicone ink, an experimental design was employed that reduces the number of variables to be tested. For an experiment with three parameters, or factors, a full factorial design needs a N^3 number of experiments, where N is the number of levels or values of the parameters. For example, for an experiment with 3 factors and 3 levels per factor a total number of 27 experiments would have to be executed. Using a more strategic design, such as a Composite, Box-Behnken, or Doehlert design, experiments can be performed solely at strategically chosen levels of the factors. For a 3 factor and 3 level experiment a Box-Behnken or Doehlert design (Figure 5.23 a-b) would result in 13 experiments instead of 27 while maintaining enough statistical power to evaluate the experiment. Using this framework, an experiment was set up which consisted of the printing of three lines in close proximity with varying printing parameters. The geometry of the printed lines is shown in Figure 5.23 c.

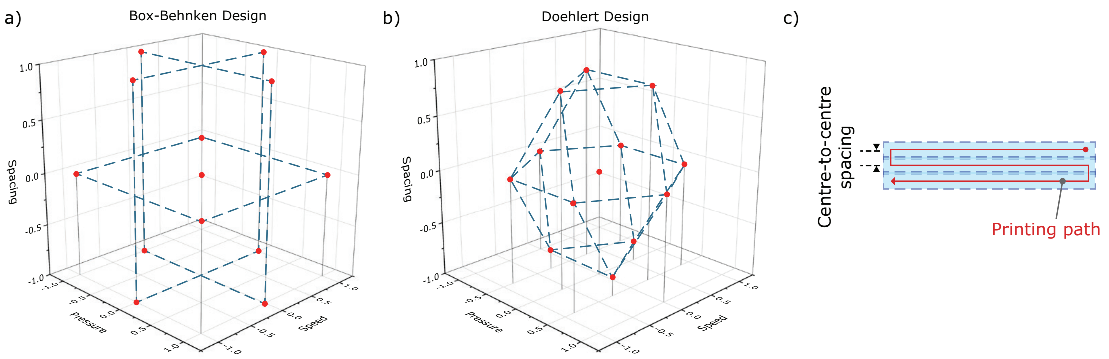

Figure 5.23 – The most effective design of experiments designs spaces with **a**) The Box-Behnken design and the Doehlert Design with 3 factors. **c**) The printed feature used in these tests.

In this experiment, the Box-Behnken strategy was used which is an ideal design as long as nonlinear model is not expected, which from the previous dimensional results had not been observed. In this design three equally spaced levels are strategically placed for each factor and labelled as -1, 0, and 1 in a design matrix. Experimental parametric values can then be assigned to these as long as they are evenly spaced such that the design space remains symmetric. In our case the pressure, speed, and linespacing were evaluated with values for the experiments as in design matrices shown in Table 5.5. Both the actual values and the normalised design matrices are shown here. Normalising prevents the actual parametrics values to influence the ANOVA calculations.

Table 5.5 – Designs matrices used for the DoE experiment to determine the influence of the printing parameters on the DIW printing of UVE225-R5 silicone ink.

Experiment no.	**Design Matrix**			**Normalised Design Matrix**		
	Pressure (psi)	Speed (mm/s)	Spacing (um)	Pressure (P)	Speed (V)	Linespacing (S)
1	20	10	110	-1	-1	0
2	20	40	110	-1	1	0
3	32	10	110	1	-1	0
4	32	40	110	1	1	0
5	20	25	100	-1	0	-1
6	20	25	120	-1	0	1
7	32	25	100	1	0	-1
8	32	25	120	1	0	1
9	26	10	100	0	-1	-1
10	26	10	120	0	-1	1
11	26	40	100	0	1	-1
12	26	40	120	0	1	1
13	26	25	110	0	0	0

Using this experimental framework four samples were produced per set of experiments such that a total of 52 features could be characterised. The clearance between the tip and the substrate was not included in the experiment, as printing could be performed with a tip clearance of both 25 and 50 µm, and printing at 75 µm was unreliable. This made only two levels available for this parameter such that they could not be included in the DoE framework. To still study its influence, the DoE experiment was performed twice, once at a clearance of 50 µm and then again at a clearance of 25 µm. All DoE test features were printed from UVE225-R5 silicone ink on top of cleaned and plasma activated Sylgard 184-PET substrates. An optical image of the printed samples is shown in Figure 5.24. The samples were scanned using the confocal microscope to measure their thickness.

Figure 5.24 – Set of 3 DIW printed UVE225-R5 silicone lines of 4 mm long printed using the parameters settings outlined in Table 5.5 at a clerance of 25 and 50 µm.

Linear models

First a linear regression for a predetermined thickness model was performed using an ordinary least squares algorithm. This model could either take the form of a linear, linear with interactions, or quadratic formulation. For the tested parameters we can write these equations as

$$\begin{aligned}
\text{Linear:} \quad & t = a_1P + a_2V + a_3S, \\
\text{Interactions:} \quad & t = a_1P + a_2V + a_3S + a_{12}PV + a_{13}PS + a_{23}VS, \\
\text{Quadratic:} \quad & t = a_1P + a_2V + a_3S + a_{12}PV + a_{13}PS + a_{23}VS + a_{11}P^2 + a_{22}V^2 + a_{33}S^2.
\end{aligned} \tag{5.23}$$

The parameters in the models P, V, and S, represent the pressure, speed and, linespacing, respectively, and the coefficients are represented by a_i, a_{ii}, and a_{ij}. The response for these models was the measured thickness t. These were validated by evaluating their fit using the R^2 factor that gives the ratio of variance of the model versus that of the residual (remaining data). The closer this value is to 1, the better the model fits onto the experimental data. An ANOVA is then performed to determine if the independent variables of the model are statistically significant towards explaining the measured data. First a linear model was analysed for which R^2 values of 0.273 and 0.419 were found for tip clearances of 50 µm and 25 µm, respectively.

The resulting ANOVA tables for these models are shown in Table 5.6. The p-values in these tables have to be below 0.05 in order for the parameters to be statistically significant within the model with a confidence of 95%

Table 5.6 – ANOVA tables for the linear model describing the printed thickness of features DIW printed from UVE225-R5 silicone.

50 µm clearance					25 µm clearance				
	SS	DoF	F Value	P Value		SS	DoF	F Value	P Value
Pressure	2752.23	1	17.497	<0.001	Pressure	1151.98	1	22.995	<0.001
Speed	43.92	1	0.279	0.6	Speed	558.7	1	11.152	0.002
Spacing	34.72	1	0.221	0.641	Spacing	25.1	1	0.501	0.482
Residual	7550.07	48			Residual	2404.65	48		

From these tables it shows that the influence of some parameters can not be explained by the fitted linear model with respect to the data. These factors are the spacing for the 25 µm clearance test and the speed for the 50 µm clearance test. Therefore, it was decided not to take these factors or any terms that dependent on them into account for the interactions and quadratic models.

Non-linear models

The interactions and quadratic models were constructed and fitted again using OLS. The R^2 values for these fitted models are shown in Table 5.7.

Table 5.7 – R^2 values for the fitted models describing the printed thickness of features DIW printed from UVE225-R5 silicone.

Clearance	50 µm	25 µm
Linear	0.273	0.419
Interactions	0.492	0.441
Quadratic	0.584	0.504

The same ANOVA analysis can be performed for these extended models to show which parameters are influential on the outcome of the data as shown in Table 5.8.

For the 25 µm clearance tests there is no influence of quadratic and interaction terms, meaning there will be no influence of non-linear terms. For this model, only the pressure and speed are shown to be dependent variables. However, for the 50 µm clearance model there is significant influence of interactions and quadratic terms even if the linear parameters are not significantly

Table 5.8 – ANOVA table for the interactions and quadratic models for the thickness of DIW printed UVE225-R5 silicone. P-values coloured in red are above the 0.05 threshold and are not statistically significant.

50 µm clearance					25 µm clearance				
	SS	DoF	F Value	P Value		SS	DoF	F Value	P Value
Interactions									
Pressure	2752.2	1	23.994	<0.001	Pressure	1152.0	1	22.42	<0.001
Speed	43.9	1	0.383	0.539	Speed	558.7	1	10.87	0.002
Spacing	34.7	1	0.303	0.585	Spacing	25.1	1	0.49	0.488
Pressure*Speed	1708.8	1	14.897	<0.001	Pressure:Speed	63.5	1	1.24	0.272
Pressure*Spacing	564.8	1	4.924	0.031	Pressure:Spacing	26.5	1	0.52	0.476
					Speed:Spacing	1.9	1	0.04	0.847
Residual	5276.5	46			Residual	2312.7	45		
Quadratic									
Pressure	2752.2	1	28.692	<0.001	Pressure	1152.0	1	24.11	<0.001
Speed	43.9	1	0.458	0.502	Speed	558.7	1	11.69	0.001
Spacing	34.7	1	0.362	0.550	Spacing	25.1	1	0.53	0.472
Pressure*Speed	1708.8	1	17.814	<0.001	Pressure:Speed	63.5	1	1.33	0.255
Pressure*Spacing	564.8	1	5.888	0.019	Pressure:Spacing	26.5	1	0.56	0.460
Pressure^2	959.9	1	10.007	0.003	Speed:Spacing	1.9	1	0.04	0.841
					I(Pressure ** 2)	111.1	1	2.33	0.135
					I(Speed ** 2)	70.8	1	1.48	0.230
Residual	4316.5	45			Residual	2054.3	43		

influential. There are many reasons for why this could be, and some of them can be related to the scope of the experiment. One possibility is that the design space chosen is possibly too large and if the spacing between parameters is chosen to be too high there might be no clearly defined linear or non-linear response. Furthermore, any errors due to the error prone nature of printing will also influence any statistical analysis.

Effect sizes of the parameters

With the formulas for the models obtained by linear regression with quadratic terms, we arrived at two final models. One being for a clearance of 25 µm and the other for one of 50 µm, that can describe the outcome of the printed thickness. These models also provide coefficients respective to their parameters, which can be used to determined the effect size of each parameter. These effects are plotted in a normalised fashion in Figure 5.25 with the significant parameters indicated in green and those not in red.

From this we can tell that, by far, for both experiments and models the pressure is the most influential effect with a coefficient of 0.17-0.18. The speed also has an influence in the 25 µm clearance model but does not have as much of an effect on the thickness as the pressure. It should be noted, however, that these are only relative as for any non-linear effects the

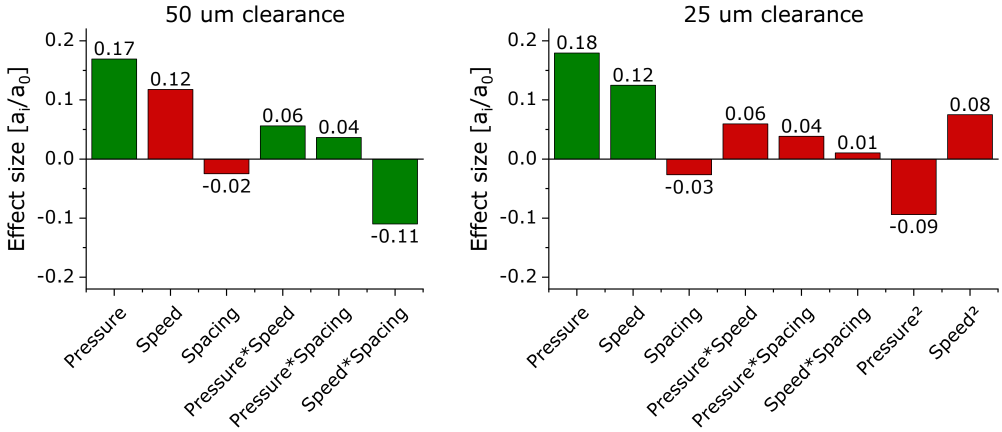

Figure 5.25 – Effects sizes of predictive models developed by the DoE analysis. These were normalised with regards to the intercept for lines DIW printed from UVE225-R5 silicone ink at 50 and 25 µm tip clearances. The statistically significant parameters are indicated in green.

coefficient is less important with regards to the magnitude of the response.

The 50 µm clearance model showed that several non-linear parameters were statistically influential. Since this was not the case for the 25 µm clearance model, and the effect of pressure and speed were significant contributors to the thickness, printing parameter optimisation was continued for these parameters.

5.2.6 Optimization towards DIW printing sub 100 um silicone layers

Using the results obtained from the DoE analysis, further steps were taken to optimise the printing of the UVE225-R5 silicone ink. The intention was to used this material to create sub 100 µm silicone layers to allow for sensor miniaturisation and precise control of angular structures. Experiments were carried out, with a 25 µm clearance gap, to determine suitable printing parameters which included the speed, pressure, and valve gap. The optimisation test features were printed on top of cleaned and plasma activated Sylgard 184-PET substrates. All printed features were cured using the built-in UV LED for 5 minutes at 100% of the available power and a distance of 10 mm.

Influence of speed and linespacing on printed films

First the speed was studied as its influence was smaller on the thickness, and varying it should result in a less drastic change of the thickness than varying the pressure. To determine its influence, 5x5 mm^2 squares were printed using different printing speeds. A printing pressure of 32 psi was used with a valve opening of 200 µm. To validate that the linespacing had no effect on the thickness, as predicted by the models, each square was printed at a linespacing of 100, 110, and 120 µm.

Figure 5.26 shows the development of the printed squares from a printing speed of 40 mm/s down to 20 mm/s, 10 mm/s, and finally 5 mm/s. While the thickness definitely increases, the surface roughness improves as there is more material to fill in any gaps that might result from under-deposition.

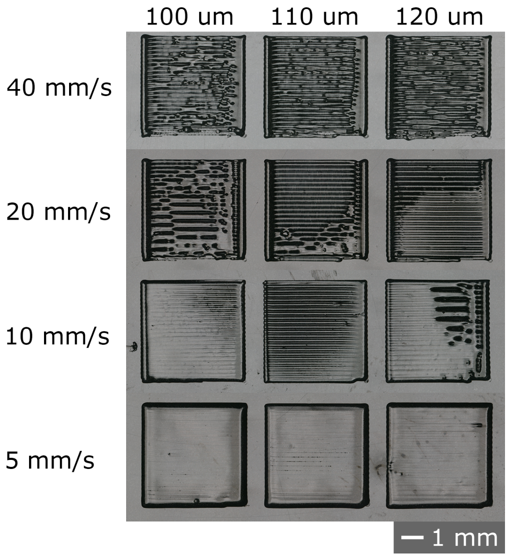

Figure 5.26 – Squares DIW printed from UVE225-R5 silicone ink at speeds of 40, 20, 10, and 5 mm/s with a linespacing between the lines of 100, 110, and 120 µm.

A clear improvement in the printing of squares can be seen as large gaps are clearly visible at higher speeds, while printing at 10 mm/s and below yields smooth surfaces. The linespacing showed no clear optical influence and so the squares were measured using a confocal microscope. A linear increase in thickness and a decrease in surface roughness can be seen in Figure 5.26 a and Figure 5.26 b, respectively. As shown by the analysis before, the linespacing did not show a significant difference as the values for the thickness overlapped at all speeds. A fitting reveals that the thickness increases exponentially with regards to the speed. An exponential decay of the form $t = ae^{-v/b} + t_0$ can be found for this range with a R^2 of 0.999, indicating a close to perfect fit. With the coefficients obtained the formula for the thickness becomes $t = 166.94e^{-v/4.73} + 51.36$ in micrometer.

The squares printed at 5 mm/s yielded the best print quality in terms of surface roughness. By choosing a spacing of 120 µm the printing process was slightly sped up, by printing fewer lines, without leading to a loss in quality. Even so these squares were above the targeted 100 µm film thickness. Therefore a range of pressures was tested to see if the film thickness could

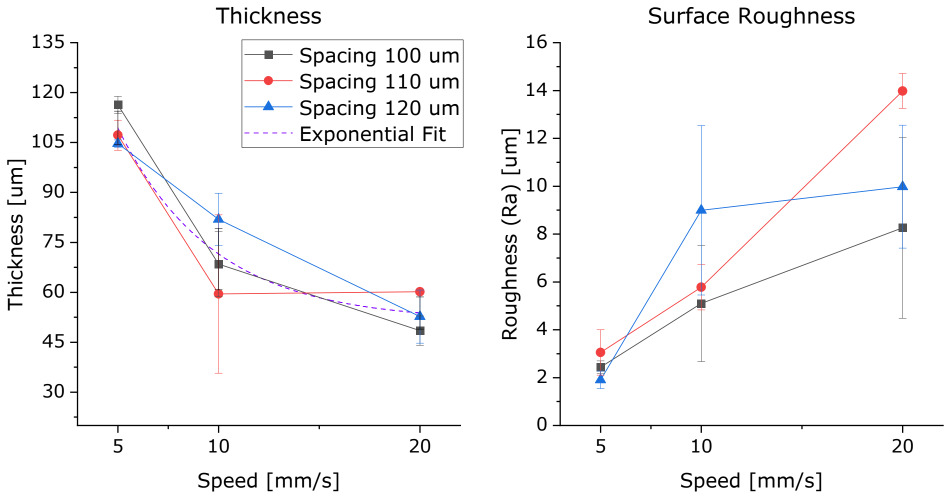

Figure 5.27 – Thickness and surface roughness plots of the squares DIW printed from UVE225-R5 silicone ink at speeds of 20, 10, and 5 mm/s.

be reduced in this fashion.

Influence of pressure on printed films

An initial trial print was performed at pressures ranging from 0.55 to 2.48 bar (8 to 36 psi) at steps of 0.28 bar (4 psi). These squares are shown in Figure 5.28 a which reveal that at least 1.10 bar (16 psi) of pressure is required to print coherent features. When more than 2.21 bar (32 psi) of pressure is used it results in over-extrusion, thus establishing a range of usable printing pressures between 1.10 and 2.21 bar 16-32 psi. Several more squares were printed using this range of pressures (Figure 5.28 b) of which the film thickness values were measured which are shown in Figure 5.28 c.

The pressure increases in a quadratic fashion at a rate of $t = 205.4 - 189.5P + 68.7P^2$, in micrometer, with a R^2 of 0.985. Comparatively, a linear fit only reaches a fit quality with a R^2 of 0.876, indicating that with an increased pressure the thickness increases non-linearly. To print films below 100 µm a pressure of 1.93 bar (28 psi) should be used. After this pressure the film thickness increases by 116.5 µm/bar compared to 30.8±1.7 µm/bar before which is a 3.7 times rate increase. Therefore when printing at 5 mm/s a maximum pressure of 1.93 bar (28 psi) is recommended to be used.

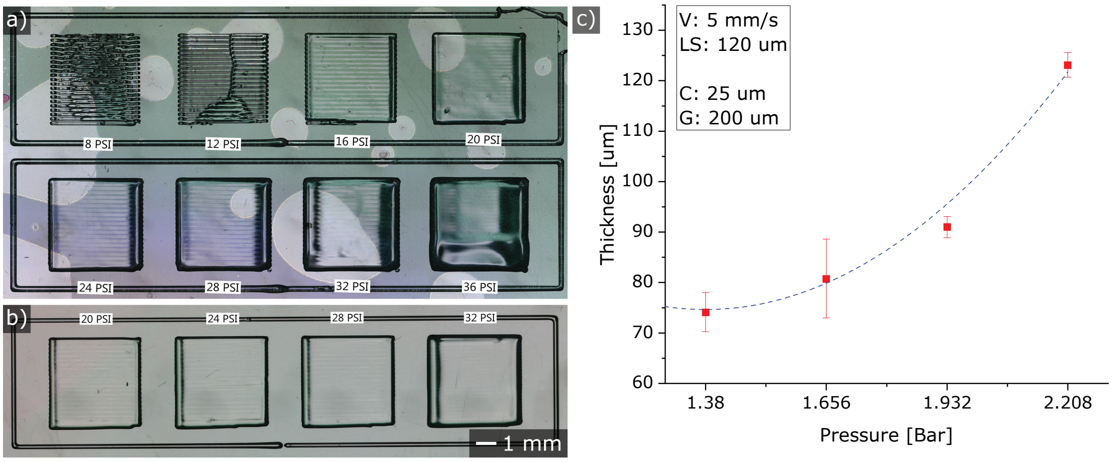

Figure 5.28 – Squares printed from UVE225-R5 silicone ink for pressures between **a-b**) 0.55 to 2.48 bar (8 to 36 psi) and **c**) their resulting thickness.

Optimisation towards sub-100 µm layers by valve gap tuning

Lastly, with the pressure, speed, clearance, and linespacing established we wanted to see if we could tune the thickness, and feature continuity, by playing with the valve gap which controls the flow of the ink. Squares were printed using the standard valve gap of 200 µm, used in all previous experiments, as well as with gaps of 175, 150, and 100 µm. The resulting squares were measured and their thickness values are shown in Figure 5.29.

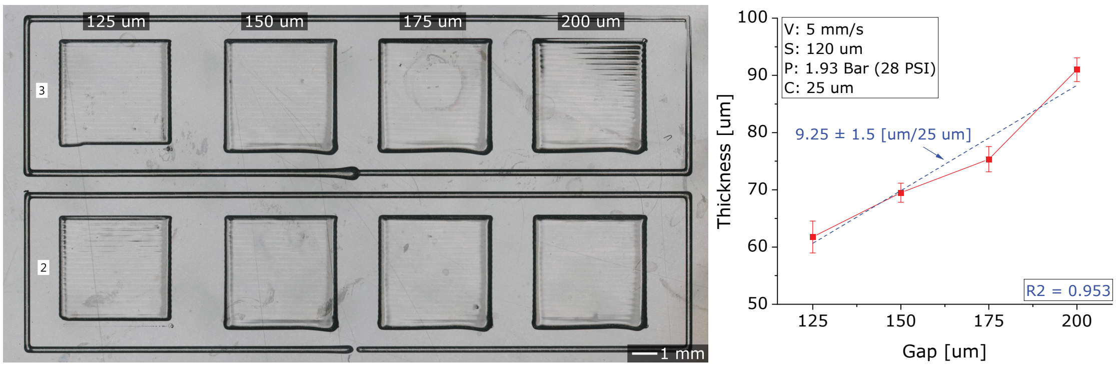

Figure 5.29 – DIW printed squares from UVE225-R5 silicone ink printed with different valve gaps and their measured film thickness.

This experiments shows that the thickness can be finely controlled by managing the valve gap, as it allows for the thickness to be changed by 9.25±1.50 µm per a 25 µm reduction of the valve gap. Furthemore, adjusting the valve gap does not influence the surface as the roughness (R_a) remained unchanged at an average value of 2.79±0.46 µm.

For the printing of these films, with a clearance of 25 µm, the printing tip was always inside of the ink during printing since the clearance was lower than the final film thickness. Therefore, we decided to set the valve gap to 150 µm to achieve a film thickness of around 69.5±1.7 µm to avoid the printing tip being too deep inside of the printed film.

Summary of the optimisation experiments

In summary, the following parameters shown in Table 5.9 were found to print homogeneous, flat, and reliably printable sub 100 µm films from the 5 wt% fumed silica reinforced UV Electro 225-1 silicone, that could be cured in-situ with the build-in UV LED.

Table 5.9 – Final printing parameters for printing films of UVE225-R5 silicone ink established after optimisation of the printing parameters.

Parameter	Value
Pressure (P)	1.93 bar (28 psi)
Speed (V)	5 mm/s
Linespacing (S)	120 µm
Clearance (C)	25 µm
Valve gap (G)	150 µm

It should be noted that while these settings allow for the printing of replicable features, the printing process is quite slow. As the layers are thicker than the tip clearance is higher, it means that the ink flows out around the tip and also acts as a mechanisms for controlling the flow. It is entirely possible that with further fine-tuning of the speed, gap, and pressure it becomes possible to print similar features at faster speeds.

Further tests at higher clearances could be envisioned, as having such a small clearance makes the printing more sensitive to misalignment and uneven surfaces. However, increasing the clearance will lead to the printing parameters influencing the thickness of the printed features in a different way, as indicated per the models determined by Design of Experiments.

5.3 3D printing of soft silicone with three dimensional geometry for creating slanted conductive features

To DIW print a full capacitive bending sensor, based on the concept and design presented in Section 5.1, we needed to print the angular conductive features required for its design. However, no printing strategy existed to achieve this. Therefore, a process was developed using the UVE225-R5 ink to print multilayer structures to introduce 3D printed structures with angular faces. All printing was carried out using the printing parameters defined as per Table 5.9. All test features were printed on top of cleaned and plasma activated Sylgard 184-PET substrates previously described.

5.3.1 Multilayer printing

When 3D printing multilayer structures, generally the printing orientation is changed per layer, as it adds to the strength of the material even if it is not loaded with any particles such that asymmetric material behaviour can be introduced[183]. However, the direction of printing can still influence the final geometry, as the material is deposited in the form of a filament which blends with previously deposited material.

Therefore, two deposition strategies were tested. One was to print the layers on top of each other in a parallel fashion, keeping the printing direction the same. The other was to create a crosshatched pattern by changing the printing direction by 90° every layer change. The resulting printed stacks, composed of multiple layers, are shown in Figure 5.30.

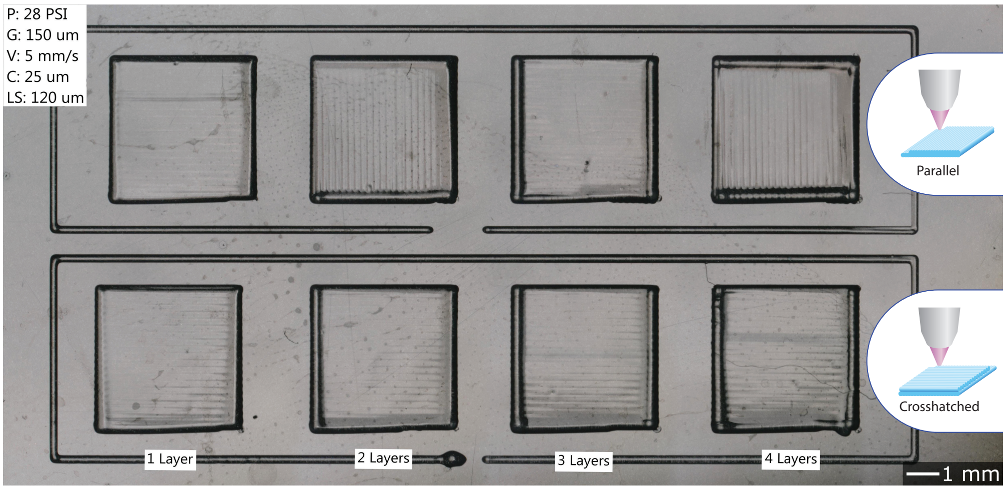

Figure 5.30 – Optical images of up to 4 layers of DIW printed UVE225-R5 silicone ink stacked on top of each other in parallel and crosshatched fashion.

The z-height offset per layer was set to 70 µm. To avoid curing the ink solid, and reducing the adhesion between layers, every layer was individually cured for 1 minute at 100% of the power at a distance of 10 mm. A final 5 minute cure was performed at the same settings to fully solidify the structure.

Visually it is not possible to distinguish the difference between the two printing patterns. Therefore, the features were scanned using a confocal microscope and both the thickness (Figure 5.31 a) and profile (Figure 5.31 b) of all stacks at all layer heights were measured.

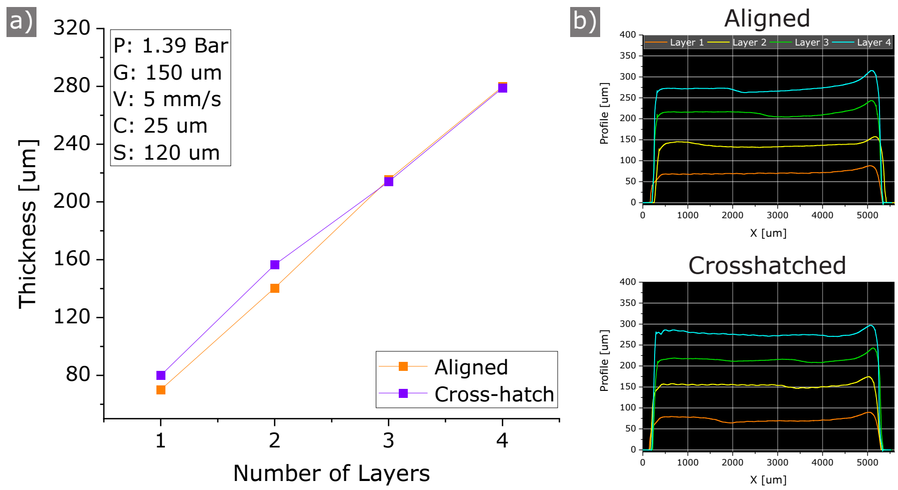

Figure 5.31 – Thickness evaluation when stacking multiple DIW printed UVE225-R5 silicone films with **a**) the thickness increase and **b**) the profiles for both printing orientation techniques.

No distinguishable difference in thickness can be found between the two printing directions, with both stack strategies showing the same linear increase at an average rate of 71.9±2.9 µm per layer. However, what is visible from the profile development is that any faults in the printing get smoothed out when printing in a crosshatched fashion. Even so, when errors are smoothed out it does not necessary lead to a decrease of surface roughness. Repeating the cross-hatch printing test several times showed a linear increase of the layer thickness of 63.9±1.3 µm with a R^2 of 0.999, which is within the range of the previous tests with the same settings. Small amounts of variance can be attributed to the flatness of the printing substrate.

5.3.2 Printing 3D angular structures

To create 3D conductive plates we first needed to create a strategy to create a slanted face. First we investigated if the fabrication order and curing strategy had any effect on the resulting structure. Four layer 5x5 mm^2 square structures were printed on top of each other using one of three curing strategies. In the first strategy, called Layer-by-Layer curing, the films are printed and cured separately. In-between layers a 1 minute cure is performed and after printing everything the structure is fully cured for 5 minutes. With the Support Layer technique a single layer is printed and cured for 1 minute before printing the rest of the structure and curing it for 5 minutes. This support layer can pin any flow of the material on its edge. The last strategy was called Single Shot in which the full structure was printed before curing it for 5 minutes without any intermediate curing steps.

Evaluation of curing strategies

None of the strategies had an effect on the printed layer thickness as on average the four layer structures had a final thickness of 266.6±2.9 µm, which is an average layer thickness of 66.7±2.9 µm. However, as the printed surfaces were flat, the choice of curing strategy could have an influence on structures with angular faces as the ink can flow more freely.

To create these angular features, the surface area of each stack was reduced in small steps. For the first test a single line, or 120 µm, was removed from each side to create a staircase feature that through re-flow of the ink would result in an angular face. The three strategies described above were applied the results of which are shown in Figure 5.32.

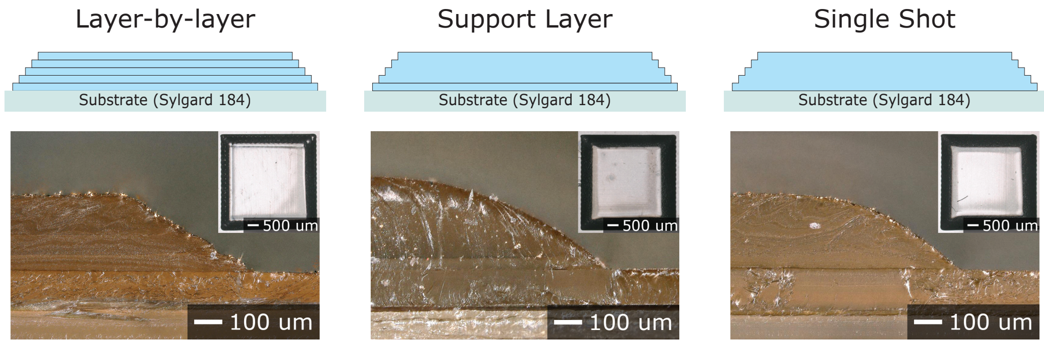

Figure 5.32 – The three tested strategies tested for DIW printing angular faces using the UV curable UVE225-R5 silicone ink.

From these cross-sections it can be seen that the layer-by-layer approach leads to a flat surface on the top but with a well defined staircase pattern on the slope. In contrary, using either the single shot or support layer techniques allow for a smooth angular features on the side face. Therefore, these two techniques were selected for further experiments to understand what type of angle could be realised. As the linespacing of the lines was set at 120 µm the minimum offset that could be programmed for the printing path was 60 µm. Therefore, offset values of 60, 120, and 180 µm were tested which resulted in the angular structures shown in Figure 5.33 a.

Evaluating angular structures

The angles were determined by measuring the angle of the steepest slants with respect to their base layers in the cross-sections. In Figure 5.33 b the angles for all tested conditions are shown.

Linear regression of the angle data shows a decrease of the angle by 7.70±1.04° per 60 µm of

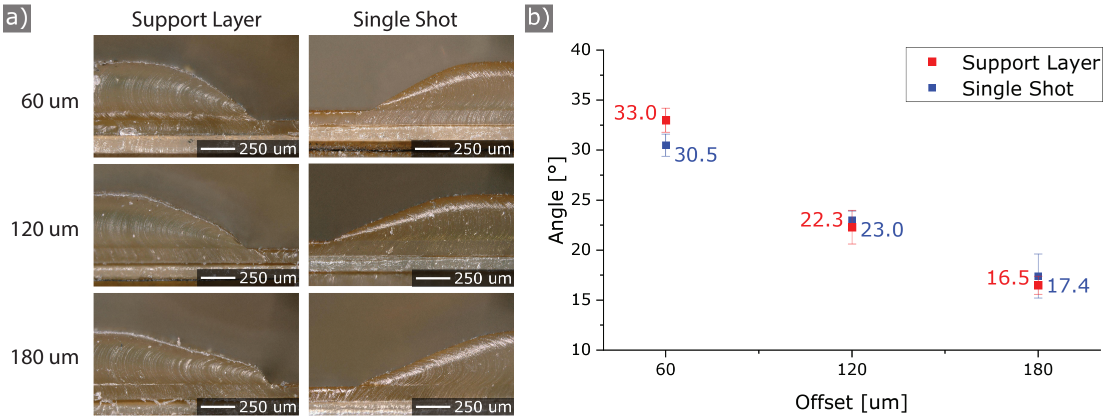

Figure 5.33 – Printing angular faces using the UVE225-R5 silicone ink with **a**) optical images of the cross-sections of the printed structures and **b**) the resulting angles.

offset at a fit of $R^2 = 0.982$. While there is observable difference between the angles achieved using either technique, the support layer technique is less error prone. The coefficient of variation (COV) can be used to evaluate the error which is the rate of the mean value divided by the standard deviation. For the support layer strategy this value was 5.6±1.6% while for the single shot strategy it was 6.7±4.2%. The reason for this is most likely the pinning effect due to the support layer which prevents any flow past the edge, which is especially clear from the cross-sections at an offset of 180 µm.

For the previous experiments the offset was kept equal for all sides. However, this would often result in ink sticking to the tip (Figure 5.34 a) especially for smaller offsets. To understand if this had any effect on the angle and the printing quality we printed several rectangular structures (n=9) with asymmetric offsets per the design shown in Figure 5.34 b. Making this design improvement increased the angle of the faces up to 41.2±2.3° which is an increase of 24.8±2% without the asymmetric offset. To print angular structures with slopes of around 40° it was decided to use an asymmetric off-set in combination with the support layer.

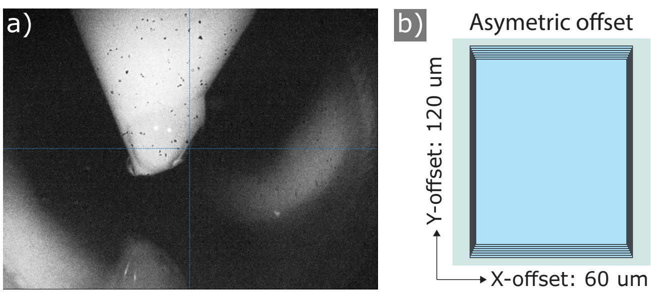

Figure 5.34 – **a**) Camera capture of the UVE225-R5 silicone ink stuck to the tip, and **b**) a schematic top view of the developed strategy to increase the angle of the side face.

5.3.3 DIW printing of silver ink on UV curable silicone

In order to enable the electronic functionality needed for a 3D printed sensors, a conductive material needs to be printed on top of the silicone. As we had quite some experience using the AG520EI silver paste (Chimet SpA, Italy), used for the creation of the sensors in Chapter 4 as well, we decided to use this ink to create conductive features for the bending sensor. Since the material is quite viscous, and slightly elastic, it was thinned using the 0204IT thinner provided by the same company. As the standard nTip is quite large, and does not allow for printing in small spaces, a 30 gauge stainless steel needle (Adhesive Dispensing Ltd., UK) with an inner diameter of 150 µm and a length of 6.35 mm was used. The samples were cured on a hotplate at 120°C for a duration of at least 30 minutes.

Printing of silver lines and pads

First a set of suitable printing parameters was determined to DIW print the silver, the results of which are shown in Figure 5.35. A test substrate was prepared by taking the UVE225-R5 silicone and doctor bladecasting it on a cleaned and plasma activated PET sheet. Using a very slow speed of 1 mm/s, with a gap of 200 µm, a film with at thickness of around 180 µm was cast. The films were irradiated for 5 minutes using the ProMA 140 UV exposure device to cure them. Before printing they were cleaned using isopropanol and activated using oxygen plasma at a power of 150 W (@ 13.56 MHz) for 1 minute.

First a speed and pressure test was performed with a needle to substrate clearance of 50 µm. Printing speeds of 10 and 20 mm/s were tested at pressures of 1.10-2.21 bar (16-32 psi) with steps of 0.28 bar (4 psi). As the viscoelastic ink needs to travel through the thin needle the valve gap was set to 1100 µm. Even so, additional wait time had to be added to avoid printing discontinuous lines, which also depended on the pressure used. Lines printed at 10 and 20 mm/s are shown in Figure 5.35 a. Confocal microscopy measurements were made to measure the thickness and linewidth of these lines of which the development is shown in Figure 5.35 b. The thickness of the lines increases linearly by 5.72±0.47 µm (R^2 = 0.987) and 3.72±0.55 µm (R^2 = 0.959) for those printed at 10 and 20 mm/s, respectively, between pressures of 1.38-2.21 bar (20-32 psi). At a printing speed of 20 mm/s and pressure of 1.65 bar (24 psi), continuous lines could be printed of a thickness of 8.4±0.8 µm and linewidth of 203.6±23.1 µm. Next, using these settings the linespacing between the lines had to be determined to be able to print continuous films.

Four linespacing values were selected at 100, 125, 150, and 175 µm. Increasing the spacing beyond 175 µm resulted in discontinuities and corrugated sides as the lines blended less well with one another. Figure 5.35 c shows the resulting film thickness for all these spacing values. For a linespacing of 150 µm a film with a thickness of 9.0±0.2 µm could be effectively achieved.

At most, this is a 14.3% increase of the thickness versus the measured thickness of the lines and was therefore chosen in order to print functional layers. By measuring the electrical properties in 4 point mode an average resistivity of 21.3±3.3 μΩ cm is found.

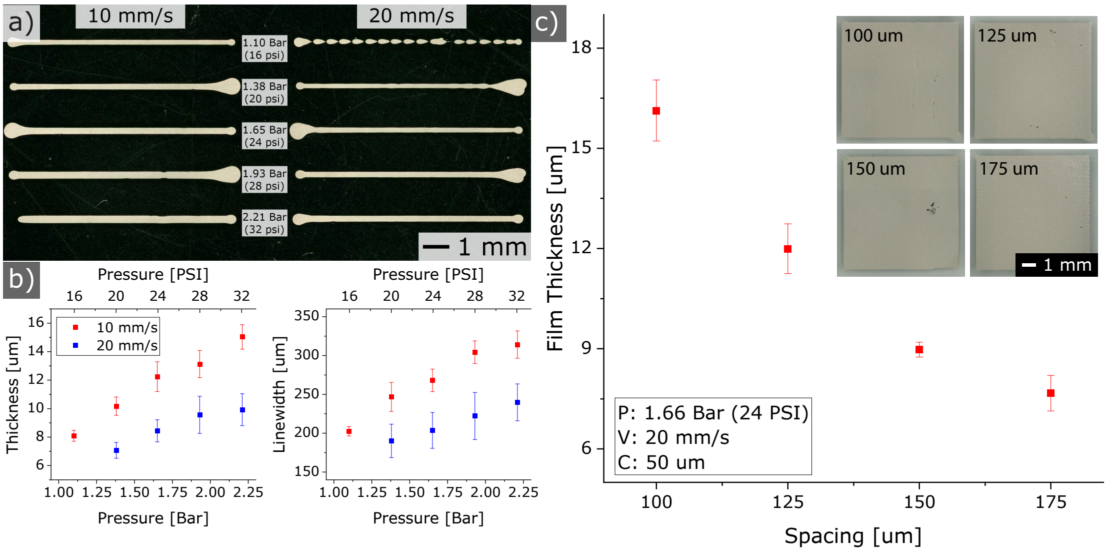

Figure 5.35 – Lines and pads, DIW printed using the nScrypt, from 5 wt% thinned Chimet silver paste on top of a UVE225-R5 silicone substrate. **a**) Lines printed at several speeds and pressures with **b**) their thickness and linewidth. **c**) Printing of squares with a linespacing of 100, 125, 150, and 175 μm.

5.3.4 DIW printing of silver plates on angular faces

To fully realise the sensor, we wanted to be able to print conductive features on a non-planar structures. We tested printing silver on DIW printed slopes by first printing two parallel pyramidical structures using the process described in Section 5.3.2. With an X-offset of 60 μm and Y-offset of 120 μm, silicone slopes could be printed with an angle of around 41.2°. A script was programmed to follow such a slope and print a silver plate at a 40° angles using a spacing of 150 μm between the printed lines, as shown in Figure 5.36. As the ink does not stick to the surface it will flow, resulting in some residue on the bottom of the pyramids. Therefore, a minimum spacing between the two pyramids is required. We tested spacing values of 400, 800 and 1600 μm to see what would be the minimum achievable spacing between the two pyramids.

After printing and curing the pyramids the printed structures were activate using oxygen plasma to reduce the surface energy. As this required the samples to be moved it introduced some small alignment issues. The alignment errors, slant, and the surface activation resulted

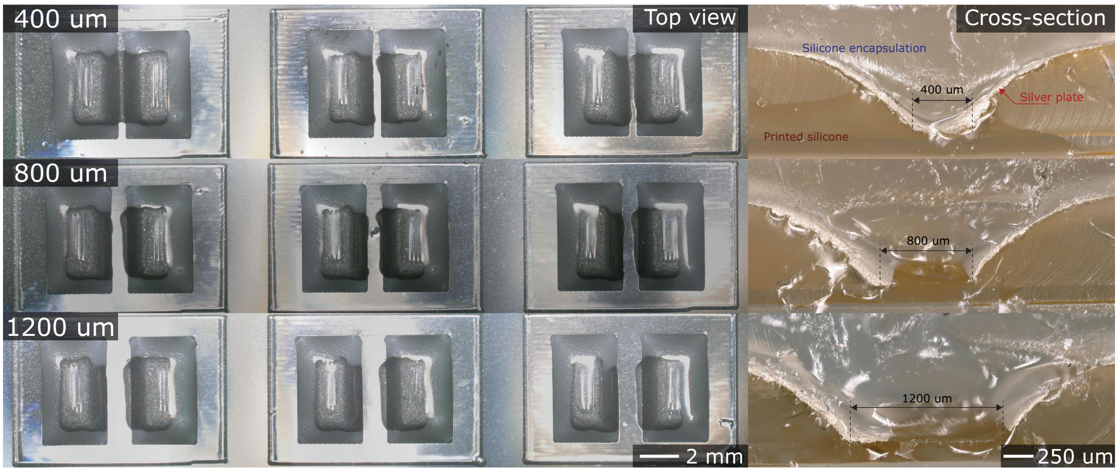

Figure 5.36 – Top down and cross-section views of DIW printed UVE225-R5 silicone pyramids with Chimet silver plates printed on top of them at 3 different spacing values.

in an overflow of ink at the bottom of the slants. This could result in the two plates merging together when the pyramids were too close as was the case for a spacing of 400 µm.

For the a spacing larger than 400 µm, an overflow of the ink of 313.0±24.5 µm was measured. A spacing of 800 µm can be used to effectively keep the plates separated by about 500 µm. Utilising a less flowy ink, the spacing could probably be reduced and the feature density increased further.

5.4 Fully 3D printed capacitive bending sensor

A completely 3D printed bending sensor was created using the printing techniques developed in section 5.3, with its dimensions guided per the developed models discussed in section 5.1. The main advantage of 3D printing is that a much thinner device can be created with a longer form factor, which gives a linearly controllable increase in the capacitance. For the sensors produced using FDM moulding there was a practical limit to how long the plates could be made (w) and how close they could be positioned, which had a significant influence on the total capacitance. Furthermore, the sensors can easily be created by printing without significant defects such as air bubbles.

5.4.1 Dielectric constant evaluation

As the printed silicone was reinforced with fumed silica, a small experiment was carried out to determine if this reinforcement had any influence on the dielectric constant. UVE225-R5 silicone was doctor bladecast at a gap of 200 µm with a very slow speed of 1 mm/s after which it was cured by UV exposure for 5 minutes. The surface was then activated using the Zepto plasma cleaner at maximum power (60 W @ 40 kHz) for 1 minute. The silicone surface was wetted using DI water and a PET stencil mask of a 20x20 mm^2 plate was placed on top before drying the surface again. Undiluted Chimet silver paste was then bladecast on top using a razor blade until a solid plate was achieved. The ink was cured by placing the sample on a hotplate at 120°C for 30 minutes before repeating the same procedure on the other side of the cast PDMS film. In this way a rudimentary capacitive stack was created. Using an Agilent Technologies E4980 Precision LCR Meter the capacitance was recorded for three samples at a frequency of 100 kHz and voltage difference of 1 V. The thickness was measured for each sample, by micrometer at 3 seperate points, just outside of the conductive plate. Applying the parallel plate capacitor theory ($C = \varepsilon_0 \varepsilon_r A/d$), the dielectric permittivity (ε_r) was calculated for all samples at a value of 3.46±0.28. This value is slightly increased from the unreinforced PDMS at a value of 3.31. The range of error, due to the uneven thickness of the bladecast silicone, can probably be reduced further by improving the fabrication of the capacitive stack. This could be performed either through printing the entire stack using the nScrypt, or even more so by spincoating to achieve a high degree of film uniformity.

5.4.2 Design, dimensions and fabrication flow

A miniaturised version of the sensor developed in Section 5.1.3 was created by printing it completely using the nScrypt. The sensor is entirely composed out of UVE225-R5 silicone, with a baselayer, four pyramdical structures, and an encapsulation covering six slanted silver plates created from an infill and top cap. The design with all the relevant dimensions is shown in Figure 5.37.

The plates of the sensor were each 12 mm long, with a programmed spacing of 800 µm in-between plates. Its design was based on maximising the capacitance while maintaining a flat sensor that could be easily placed on the body. Guided by the analytical model, the expected capacitance was in the range of 2.06±0.06 pF.

The fabrications steps needed to realise this sensor are shown in Figure 5.38 . First a double layer of 140 µm UVE225-R5 silicone base layer is printed and cured for 3 minutes using the UV LED at 100% power. Pyramids were printed one after another from 10 layers of silicone, at 700 µm in height, and with a subtraction of 60 µm per layer of the sloped side and 120 µm on the short edge. After printing, each pyramid was cured for 3 minutes at 100% power before the next pyramid was printed, for a total of four pyramids with a spacing of 800 µm between them.

The pyramidical structure was removed from the printer and its surface was activated by oxygen plasma at a power of 150 W (@ 13.56 MHz) for 1 minute. Then the structure was placed back in the printer and aligned using prefabricated cross-hair marks. Using a 30 gauge (0.15

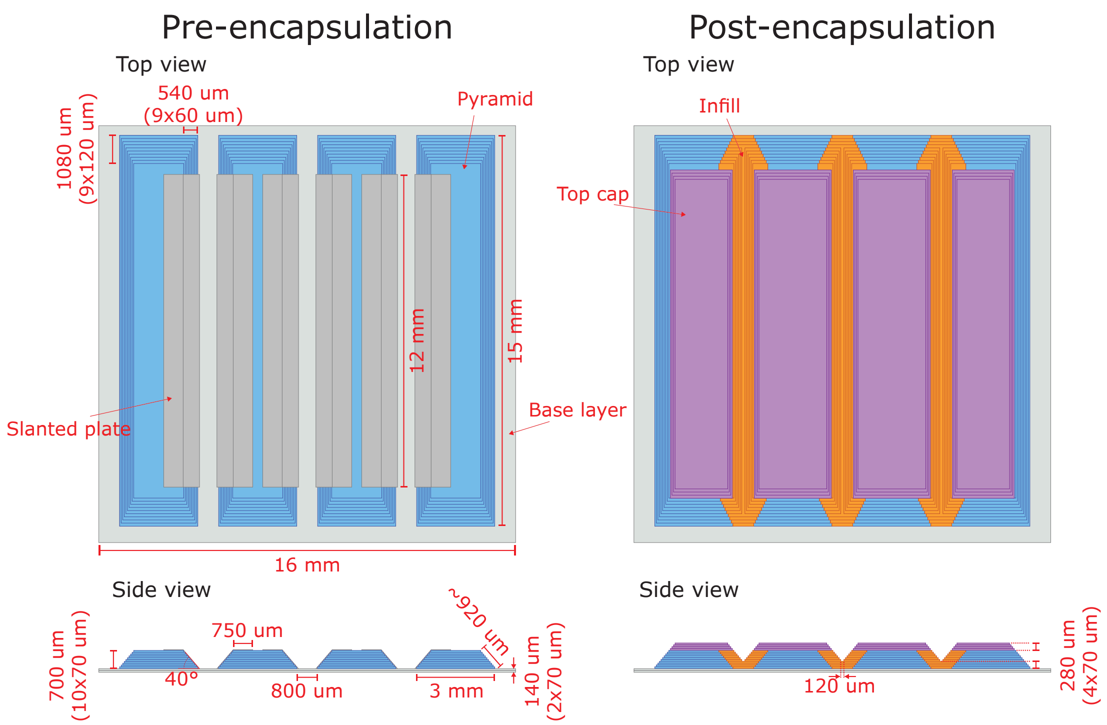

Figure 5.37 – Design and dimensions of the fully DIW printed bending sensor, with and without the encapsulation step.

mm) needle, silver plates were printed on the slanted sides before curing it at 120°C for 30 minutes on a hot plate. The dimensions of these plates had a width (w) of 12 mm and a length (L_0) of about 920 µm, which was dependent on slope of the pyramid. The connectors on the top were 750 µm long, which resulted in a spacing between the top plates of about 420 µm.

To encapsulate the device, an infill was printed on top of the cured silver in the shape of a V groove with an bottom spacing of four layers, 280 µm in height, and a spacing of 120 µm at the bottom that opened up into a 720 µm spacing on the top. The infill was designed to follow the shape of the pyramids exactly and were all printed before being cured simultaneously for 3 minutes at 100% power. A final silicone cover was printed on top of infill and the pyramids to fully encapsulate the sensor and cured for a duration of 5 minutes at 100% power to ensure that the entire structure was fully cured. The fully printed sensors is shown in Figure 5.38.

5.4.3 Static behaviour of the printed sensor

The prototype was connected to a readout circuit to measure the capacitance of the plates in parallel using a USB CapMeter. Undeformed the sensor had an average capacitance of

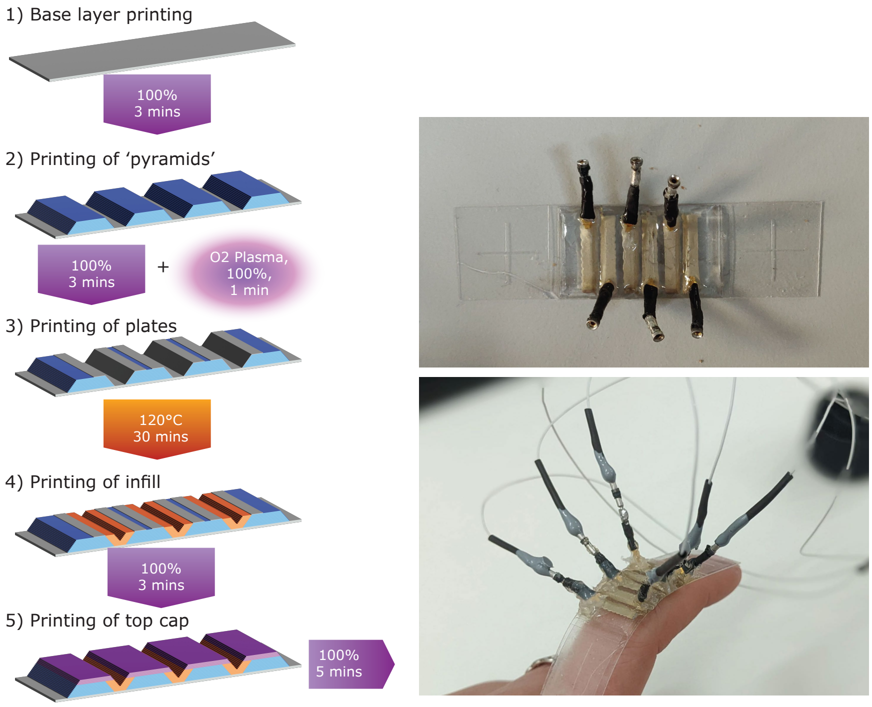

Figure 5.38 – The printing steps to create the fully 3D printed capacitive bending sensor including photographs of the sensor after production.

2.36±0.06 pF. This is slightly higher (15%) than the predicted capacitance. However, this increase is likely due to any fabrication errors as well as any additional capacitance due to connectors that could not be properly grounded.

To evaluate the sensing of the bending direction, the sensor was placed on a PMMA cutout with a either a negative or positive bending radius of 30 mm. As shown in Figure 5.39 a, when the plates bend towards each other (positive bending) the capacitance increased by 193.9±72.8 fF (8.2±2.4%). When the plates bend away from each other (negative bending) the capacitance decreased by 52.9±34.5 fF (-2.3±1.2%). This matches the same behaviour as was seen in the prototype produced through FDM moulding.

To quantify the sensitivity of the sensor (Figure 5.39 b), it was actuated several times from a stationary position to several preset actuation angles using a bending setup (Figure 5.39 c). The sensor matched the bending FEM model well for negative bending with a sensitivity of 2.50±0.04 fF/° (0.11±0.00 %F/°) using a linear fit (R^2=0.998). With an accuracy of 4 fF for the CAPMeter, the bending angle will have an error of 1.6°.

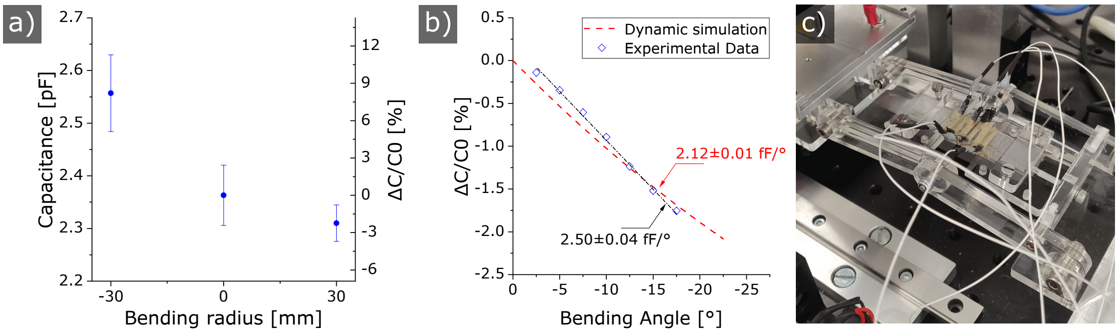

Figure 5.39 – Evaluation of the fully DIW printed bending sensor with **a**) its assymetric sensing ability demonstrated by a 30 mm bending radius, **b**) evaluation of the sensor sensitivity by bending at several angles, and **c**) the bending setup used to evaluate the sensitivity.

5.4.4 Dynamic behaviour of the printed sensor

To test the dynamic performance, the sensor was automatically bent using the automated test setup shown in Figure 5.39 c, and by mounting it on a human joint. The results of these tests are shown in Figure 5.40.

Figure 5.40 a shows the capacitance change ($\Delta C/C_0$) for actuation angles up to 15 and 22.5° and actuation speeds of 0.2 and 0.5 Hz. For either angle, a difference of less than 0.25% of the peak-baseline capacitance difference was measured when increasing the actuation speed from 0.2 to 0.5 Hz, showing that the speed has little influence on the performance for these angles. However, at a speed of 0.5 Hz the sensor doesn't have time to fully return to its relaxed state, likely due to the relaxation time of the silicone sensor body.

To evaluate the applicability of real-life use for the sensor, it was attached to an elbow and tested to detect the capacitance change when extending and and flexing the arm several times (Figure 5.40 b). Starting from a flat position with the palm facing outward towards the ground, the elbow was flexed up to about 90 degrees and extended back several times. Using the sensitivity determined in the static test, the sensor estimated an angular change of between 70-85°. From this data we can infer that the sensor is able to keep up with an angular speed of 87.6±9.1°/s, which is sufficient to be able to track the gait for paralympic athletes when walking and running[184].

5.4.5 Realised sensor comparison to state of the art and limitations

A fully 3D printed sensor was produced with six plates each of a length of about 920 µm, width of 12 mm which had an internal and external spacing of 800 and 420 µm, respectively. The full sensor had a height of 1.12 mm, making it flat and easy to unobtrusively mount on a

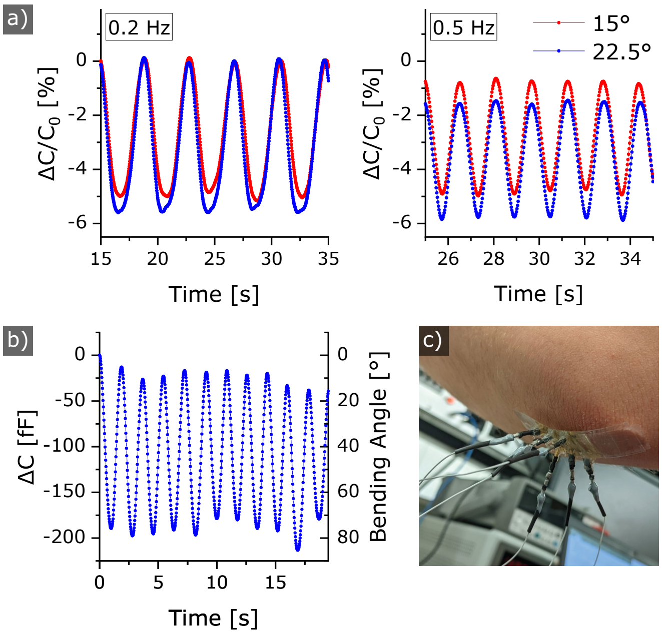

Figure 5.40 – Dynamic test done with the fully DIW printed silicone capacitive bending sensor with **a**) actuation at 0.2 and 0.5 Hz. **b)** Capacitance change of the sensor due to flexion-extension of an elbow with angle estimation. **c**) Picture of the the sensor mounted on an elbow.

person. The sensor was characterised to have a sensitivity of 2.50±0.04 fF/° (0.11±0.00 %F/°) for negative bending, which correspond to a normalised sensitivity of 7.55 fF/°cm^2. With the smaller form factor of the sensor it was 2.7 time more sensitive, when normalised to the surface area, than a much larger two part wearable capacitive sensor[177]. Moreover, this is the first time a bending sensor was demonstrated which had asymmetric sensing behaviour and could distinguish between a positive and negative bending deformation.

The sensitivity of our device was higher than a wearable inkjet printed carbon based strain gauge which had an angular sensitivity of 0.086%/°[96]. Still, more bulky wearable devices equipped with resistive flexural sensors showed much higher sensitivities up to 1.2±0.2%/°[185]. It is likely that using a small form factor will always result in a reduced capacitance. However, by employing nanostructuring gold films a sensitivity up to 1.25 %/° was previously demonstrated[178]. Nano- or micro structuring could, therefore, be applied to increase the base capacitance and increase the sensitivity.

One limitation of the current design is that the plates are orientated at a starting angle of around 40°. By increasing this angle, a steeper slope can be generated such that the baseline capacitance is higher and the sensitivity becomes increased for negative bending. However, this requires the development of a process to print even steeper slopes. Possible methods could include increasing the layer thickness of the layers of the pyramids, or by utilising a smaller printing tip to allow for smaller printed lines and a reduced offset between them.

While the simulations did not account for this, a range of motion of 90° was able to be tracked by testing it on the body, making it suitable for the dynamic evaluation of the knee[175]. This measurement, is however, not without error due to the CAPMeter used to read out the capacitance. This device has an error of 4 fF, resulting in an error in measurement of 1.6°. This error could be further reduced with more robust electronics, or by increasing the base capacitance, such as by printing a wider sensor. Even so, errors in angular detection are regularly demonstrated at a level of 2.7-3° [7], [174], indicating a small improvement with regards to the state of the art for wearable devices. However when using MEMS based Inertial Measurement Units (IMU) this error can be brought down to as low as 0.7° [186]. It should be noted that these results are only for static evaluation, and that the tracking of dynamic movements could introduce further errors. However, to evaluate this for our sensor a more comprehensive study is required of its dynamic performance.

5.5 Summary and Conclusion

In this chapter, the design and simulation of a capacitive bending sensor with a novel sensing mechanism, that could be enabled by 3D printing, were discussed. Based on this design, DIW printing techniques were realised to be able to fully print a sensor prototype.

The capacitive bending sensor was based on the idea of having parallel plates with an angle between them which changed by a bending motion. By separating the plates, due to an increased angle (negative bending) the capacitance decreases while, when the angles come closer (positive bending), the capacitance increases. By spacing multiple plates with a difference in their horizontal spacing between the bottoms and tops of the plates, a bending sensor design was created with bi-directional angle sensing capabilities. An analytical model was constructed and compared with Finite Element Analysis (FEM) models to evaluate the sensor mechanism, which showed good agreement in-between all models. Verification of these models was performed by creating a prototype sensor from UV curable silicone by moulding it with a FDM printed mould and evaluating its capacitance.

The commercially available UV curable UV Electro 225-1 (UVE225) silicone was reinforced with 5 wt% fumed silica to create a gel-like shear thinning ink suitable for 3D printing. Using Design of Experiments (DoE), an analysis was performed for this ink to understand the influence of the printing parameters on the thickness. With a 25 μm clearance between printing tip and , the pressure and speed were shown to have a direct linear influence on the thickness for pressures between 1.38-2.21 bar (20-32 psi) and speeds between 10-40 mm/s. Through further optimisation a set of parameters was found to print films with a consistent thickness of 69.5±1.7 µm.

Multiple square layers from the silicone ink could be stacked with a cross-hatched pattern to form 3D square structures. By reducing the surface area of each subsequent square layer, angular features could be created on their sides. Using an offset of 60 µm on one side and 120 µm on the other, stacks with an angular face of 41.2±2.3°, with respect to the substrate, were achieved. By printing a silver paste, a conductive slanted plate could be printed on this slope with a thickness of around 30 µm.

Using the models, the dimensions of a flat 3D printable design were determined. By using the developed printing techniques a fully 3D printed version was created with a capacitance of 2.36±0.06 pF. This version too showed the desired directionality and was demonstrated to have a sensitivity of 2.50±0.04 fF/° (0.11±0.00 %F/°), which agreed well with the bending FEM model. By normalising it with regards to the plates and their size, a sensitivity of 7.55 fF/°cm^2 was found. Using the CAPMeter, the error of measurement for this device is now 1.6° which could be further reduced with more robust electronics.

By testing the sensor in dynamic situations it showed a repeatable response for the same angular deformation, and the ability to measure the angles of a body part up to at least 90°. With this sensor we have for the first time demonstrated a fully 3D printed capacitive bending sensor suitable for motion monitoring.

While the sensor design shows potential, sources of noise, such as the connections, can still influence the sensor performance. These are currently created out of standard parts and not miniaturised. Future versions of the sensor should include all connections and shielding to be integrated. Errors resulting from certain production steps influence the sensor performance, which could also be reduced by performing the surface activation and curing steps in-situ, in a fully automated fashion.

6 Design and evaluation of a fully 3D printed insole demonstrator for human gait analysis

A growing demand exists for more accurate and personalised health monitoring systems[187]–[189] from clinicians, athletes, and sports enthusiasts alike[189], [190]. To address this demand, personalised soft wearable sensing systems are under development that provide physiological health metrics over extended time[187] without sacrificing the comfort of the user[191], [192]. One target application for continuous health monitoring is gait analysis, which can provide insight into overall health[193], aging[194], [195], and sports performance and injury recovery[196]. The current gold standard for measuring gait uses stationary instrumentation[192], [197], which limits the data collection and usage. Extensive gait monitoring could be better performed with a personalisable wearable system.

Advances have been made in wearable development[187], [191], but no complete gait monitoring solutions exist that can be easily custom personalised. While the sports industry has expressed much interest in such wearables[4], research on their fabrication and characterisation has been lagging behind. Elastomeric smart plantar gait sensing systems have previously been developed using integrated capacitive[120], [198], piezoresistive[199], and triboelectric[200], [201] sensors. However, such systems have been produced using conventional manufacturing workflows[202]–[204] that cannot meet the demands for personalisation. Creating personalisable insoles with integrated sensors for gait sensing remains an open manufacturing challenge, that could be solved by utilising 3D printing to enable their rapid manufacturing[2], [23].

Using the materials systems and mechanical sensors discussed in Chapter 4, developed in partnership with ETH Zurich and EMPA, we produced an elastomeric insole with embedded piezoresistive sensors. The design considerations, real-time data monitoring, and results from several free-living tests are discussed in this chapter.

This chapter is partially adapted from a scientific article submitted for peer review based on the work produced within the D-Sense project[a].

6.1 Gait analysis using smart insoles

Using the piezoresistive sensors developed in Chapter 4, we set out to create a fully 3D printed insole with embedded normal and shear sensors to enable plantar pressure and shear force measurements. In this section the design consideration of the insole layout and its fabrication are discussed. We also discuss the usage of a wearable electronics system for monitoring the sensor response during physical activities.

6.1.1 Insole design, layout, and fabrication

The outer shape of the smart insole was designed to fit inside of a Asics® GT-2000 running shoe which has a flat bottom once the supporting insole is removed. The flatness of the shoe reduced non-normal deformations and allows for more accurate calibration, which was performed on a pull tester with a flat testing bed.

Anatomical normal pressure maps were made for a test subject at The Lausanne University Hospital (CHUV) to determine the best positions for the sensors, as shown in Figure 6.1 a, with the sensor postions indicated in yellow. This placement was verified in agreement with the researchers from CHUV, based on bony markers in the feet. This resulted in the design shown in Figure 6.1 b, with the interconnect network created to read out the sensors separately, and a common ground running along the border of the insole.

Since we wanted to determine both normal and shear forces, we used the piezoresistive normal and shear forces sensors design from Chapter 4 and placed these at the positions of interest.

Fabrication

The insoles were fabricated at the Complex Materials Laboratory by our partners on a custom build StepCraft 420 3D printing platform with integrated Direct Ink Writing tools and a Relyon plasma gun.

The fabrication flow to DIW print the insole was as follows. First a smooth base layer was printed and cured onto which the interconnects of the design shown in Figure 6.1 were printed. At the predetermined positions, piezoresistive strain gauge elements were printed to be able to determine the normal pressures. Two sets of piezoresistive strain gauges designed for shear

[a]Digital Manufacturing of Personalised Shoe Insoles with Embedded Sensors by Marco R. Binelli and Ryan van Dommelen, Yannick Nagel, Jaemin Kim, Rubaiyet Haque, Gilberto de Freitas Siqueira, André R. Studart, and Danick Briand

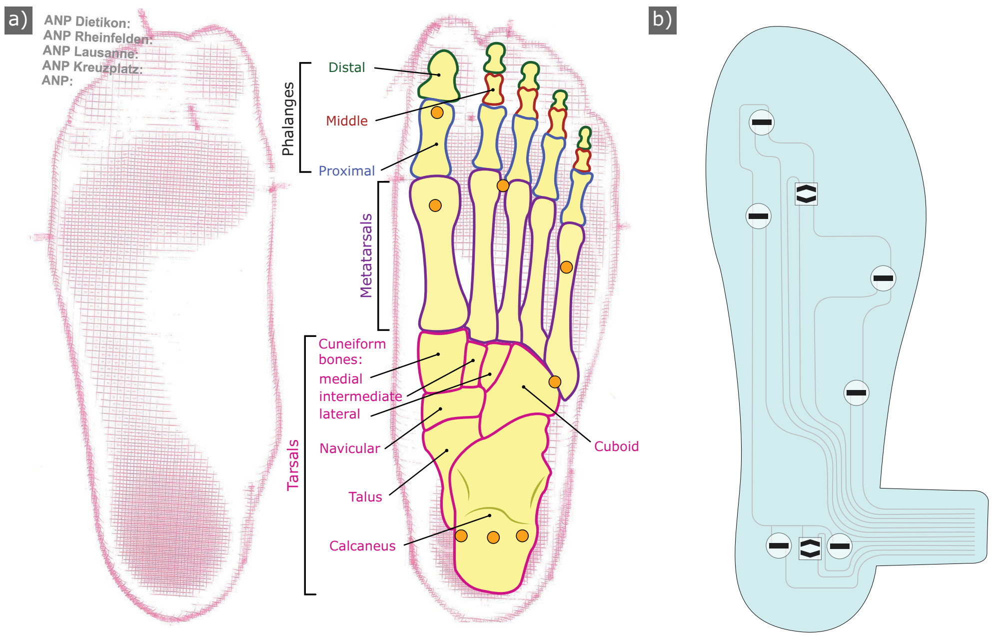

Figure 6.1 – **a**) Pressure map for a test subject, with bones in the foot (plantar view) and sensor positions indicated (yellow). **b**) The design of the DIW printed insole with the sensors positions according to skeletal positions of interest.

sensing were printed towards the heel and front of the foot to evaluate shear difference at these locations. The normal pressure gauges were covered with a DIW printed circular 1.1 cm^2 bump to aid with force transfers and prevent shear, and the shear gauges were covered with a DIW printed square 1 cm^2 bump. As a last step, an encapsulation layer was printed on top of the entire insole to protect the sensors and interconnects from interaction with the foot.

The base layer was printed from three layers of 5 wt% Crystalline Nanocellulose (CNC) reinforced Sylgard 184 silicone (CNC-PDMS) at a pressure of 5 bar resulting in a thickness of 1.5 mm. The ink was deposited using a preeflow EcoPen (ViscoTec GmbH, Germany) precision dispensing tool to finely control the flow of the ink. A flowrate of 175 µm/min, printing speed of 10 mm/s, tip distance of 500 µm, infill orientation of 90° and linespacing of 600 µm were used to print this layer.

After printing, the substrate was cured for 1 hour at 80°C in an oven. Then, using the Relyon Plasma Gun, the surface was treated at 70% of its maximum power supplied at a plasma frequency of 54 Hz, a working distance of 20 mm, linespacing of 5 mm, and a scanning speed of 70 mm/s. After the plasma treatment, all electrodes were printed from thinned (10 wt%) Ag520EI Silver paste (Chimet S.p.A.) by depositing it through a 250 µm needle twice at a printing pressure of 2.4 bar, printing speed of 10-20 mm/s, linespacing of 250 µm, and tip distance of 100 µm. The electrodes were cured in an oven at 120°C for 30 minutes which resulted in them having an average thickness of 50 µm.

A second plasma treatment was performed to increase the adhesion between the silicone substrate and the silver electrodes with the to be printed piezoresistive strain gauges of the sensors. Two layers of the 4 wt% carbon black (CB) composited Sylgard 184 (CB-PDMS) reinforced with 10 wt% fumed silica (FS) were printed using a conical 0.41 mm plastic nozzle at a pressure of 1 bar, printing speed of 5-8 mm/s, tip distance of 200 µm, and linespacing of 200 µm, resulting in strain gauges with a thickness of 400 µm. The gauges were then cured in an oven at 80°C for a duration of 4 hours.

The sensors were finalised by performing another plasma treatment before printing the bumps on top of the gauges to aid with force transfer. Three layers of 12.5 wt% CNC-PDMS were printed to form the bumps using a 0.41 mm plastic conical nozzle at a pressure of 5 bar, a flowrate of 70 µm/min, a printing speed of 10 mm/s, tip distance of 250 µm, infill orientation of 90° and linespacing of 400 µm. The resulting bumps of 900 µm in thickness were cured for 1 hour at 80°C in an oven.

To finalise the insole, an encapsulation layer with a thickness of 300 µm was printed from 5 wt% CNC-PDMS on top of the entire insole to protect it from wear and tear. The same printing parameters were used as for the substrate and the material was cured for 1 hour at 80°C in an oven.

All materials used in the production of the insole, and the dimensions of the printed parts, are shown in Table 6.1.

Table 6.1 – Parts, material types, and thickness values of the fully DIW printed insole.

Part	Material type	Thickness
Base layer	5 wt% CNC-PDMS	1.5 mm (3 layers)
Interconnects	Ag520EI Silver paste (10 wt% thinner)	50 µm
Strain gauge	4wt% CB-PDMS with 10 wt% FS	400 µm (2 layers)
Bump	12.5 wt% CNC-PDMS	900 µm (3 layers)
Encapsulation layer	5 wt% CNC-PDMS	300 µm (1 layer)

6.1.2 Influence of encapsulation and cross-talk

The encapsulation layer printed on top of the insole protects the traces from any damage caused by pressure or friction from use. Since this layer modifies the shape of the bumps of the sensors, and adds additional material, we retested the static response of the piezoresistive normal sensors as per testing methodology outlined in Section 4.3.1. The responses of two sensors tested before and after encapsulation are shown in Figure 6.2.

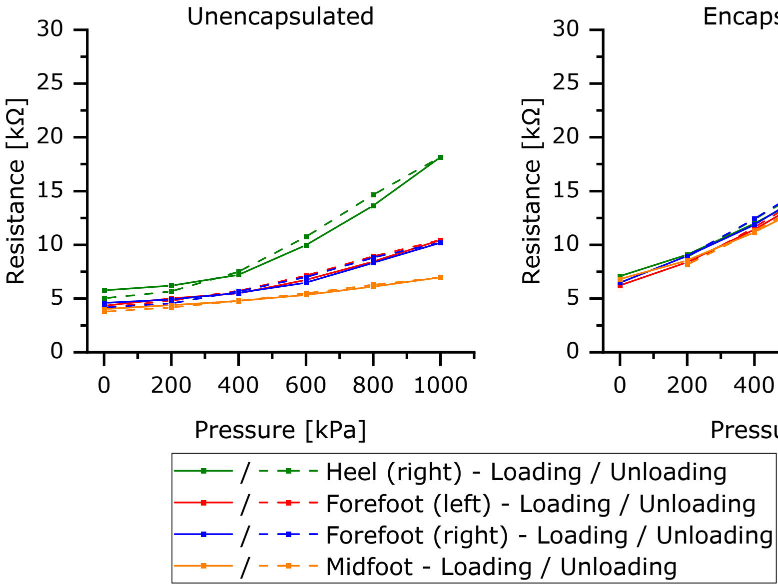

Figure 6.2 – Piezoresistive normal sensors tested on their static response before and after encapsulation with a 5 wt% CNC-PDMS layer.

The encapsulation layer adds a stiffening effect and increases the sensor response during static compression. The sensitivity increased to 16.8±1.5 Ω/kPa (0.25±0.03%/kPa) from 13.4±0.7 Ω/kPa (0.22±0.03%/kPa) before encapsulation. The sensor were slightly more responsive when encapsulated, most likely due to the stiffening effect of the additional CNC-PDMS. This effect likely results in a small compression, leading to a change in the initial resistance of the sensors from 4.7±0.7 kΩ before encapsulation to 6.7±0.3 kΩ after encapsulation.

As the encapsulation layer is monolithic, we suspected it could introduce cross-talk into the insole. Therefore, the cross-talk was evaluated by compressing one sensor repeatedly up to 1000 kPa at 20 kPa/s and reading out the response of those in its proximity (Figure 6.3 a). The resistance of the sensors in proximity shows a small increase in resistance as shown in Figure 6.3 b. The response shows a resistance change of less than 2% as shown in Figure 6.3 c, which is much smaller when compared to the actual sensor response.

6.1.3 Electronic sensor readout system and calibration

Previous sensor measurements were performed with a stationary multimeter. However, to make the insole mobile, an electronic readout system was developed by an electronics engineering intern in our lab to monitor the sensor response in real-time. The system consists of a low power Arduino compatible Feather 32u4 Bluefruit (Adafruit, NY, USA) microcontroller.

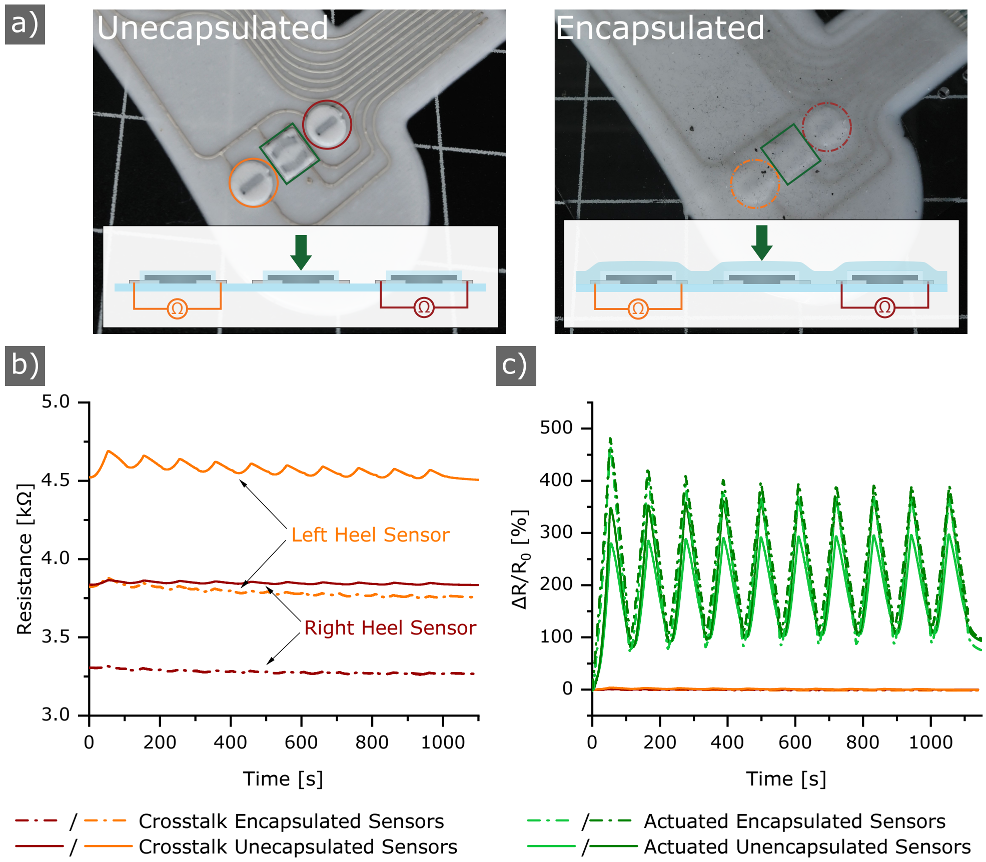

Figure 6.3 – Crosstalk tests performed on the insole. **a**) The tested sensors before and after encapsulation, with in green the actuated sensors, and in red and orange those measured. **b**) The resistance response before and after encapsulation, and the **c**) relative response versus the sensor being actuated.

This controller board has multiple pins that were connected to the piezoresistive sensors using a separate PCB with voltage dividers (Figure 6.4 a) to measure the change in resistance by the change in voltage. The microcontroller gave a digital voltage output with a bit value between 0 and 1023.

A simple C++ script was uploaded to the device by USB cable to control the readout of the pins. Using the same USB cable, voltage data was transferred to a laptop with a python script (Figure 6.4 b) that allows for the recording and display of the voltage data per sensor. The voltages were normalised by selecting load resistors (R_{load}) with respect to the range of resistance. The module also comes with bluetooth capability that would allow the information to be read out on a smartphone, but which requires a compatible app for data storage and long-term monitoring. The formula to select the reference resistor is given as

$$R_{\text{load}} = \sqrt{R_{\text{sensor},0} \cdot R_{\text{sensor,max}}} \tag{6.1}$$

where $R_{\text{sensor},0}$ and $R_{\text{sensor,max}}$ are the resistance values of the sensor at zero and maximum load, respectively.

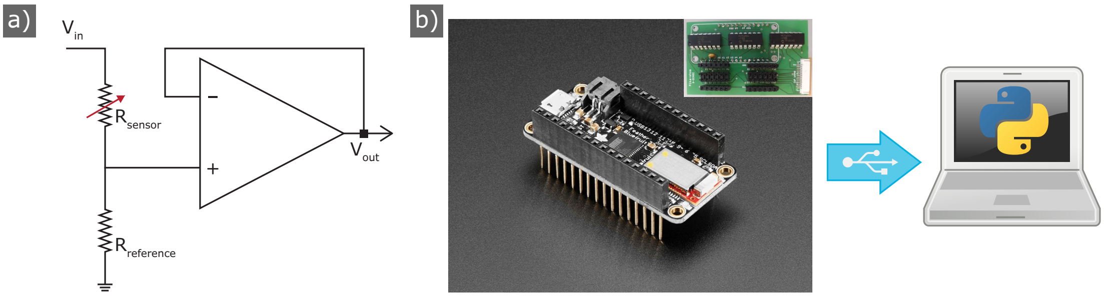

Figure 6.4 – Components of the readout system. **a**) Voltage divider PCB layout. **b**) Adafruit microcontroller with in the top right the voltage divider PCB. Voltage data is transferred from this device by USB cable to a laptop with a python script.

6.2 Sensing results of real-life gait

By connecting the insole to a prepared laptop we were able to read out the signals of each sensor and store the data. In this way we were able to record responses of free-living activities such as walking and going up and down stairs. The physical activities were carried out by a post doc to keep the gait consistent during all tests. The results are all reported in the digital voltage output of each sensor, which is a bit value between 0 and 1023, and is thus reported as an arbitrary unit (a.u).

6.2.1 Normal load distribution

The first activity performed was the testing of the sensors to see if we could detect any changes in the normal load. This was tested by letting the test subject start from a sitting down position and then stand up to see if we could detect the plantar pressure distribution. Table 6.1 shows the detected pressure distributions for a person of around 70 kg. The highest pressure distributions occurs in the rearfoot where 57.1±1.7% of the weight was located, while 42.8±2.6% of the weight was located in the forefoot. These values are in agreement with other measurements made using an external plantar pressure measurement device[205].

Table 6.2 – Sensor location and weight distribution using sensor data of a person standing on the printed insole.

Location	Foot part	Position	Weight Distribution [%]
Midfoot		S1	20.6±2.3
Forefoot Right		S2	4.1±0.5
Forefoot Distal	Forefoot	S3	3.8±0.1
Forefoot		S4+S5	10.7±0.2
Forefoot Left		S6	3.6±0.1
Heel Left		S7	16.6±0.4
Heel	Rearfoot	S8+S9	27±0.4
Heel Right		S10	13.5±1.3

A visualisation of these the normal pressures is shown in Figure 6.5.

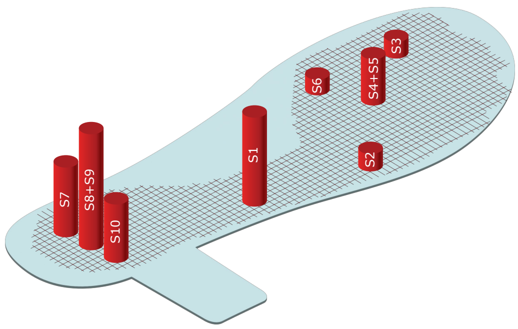

Figure 6.5 – Plantar pressure distribution over the sole determined from the sensor readout.

6.2.2 Walking on slopes

Subsequently we tested gait detection changes of the test subject walking with our insole inside of the shoe on a treadmill. As the treadmill could be adjusted to simulate the climbing of mountains, it would allows us to see how the plantar pressure distribution changes when walking on steeper slopes. To test this, the test subject was walking at a relaxed walking pace of 2 km/h for 2 minutes, before pausing for 1 minute to let the insole recover, before starting over at an incline increase of 15°. The same test was performed again at a slope of 30°. Using the shear sensors, we could see how the shear forces changed due to this slope as well. Results from these tests are shown in Figure 6.6.

The normal pressure distribution does not significantly change for the sensors that already experienced very little load. However, the sensors located at the front clearly show that, as the

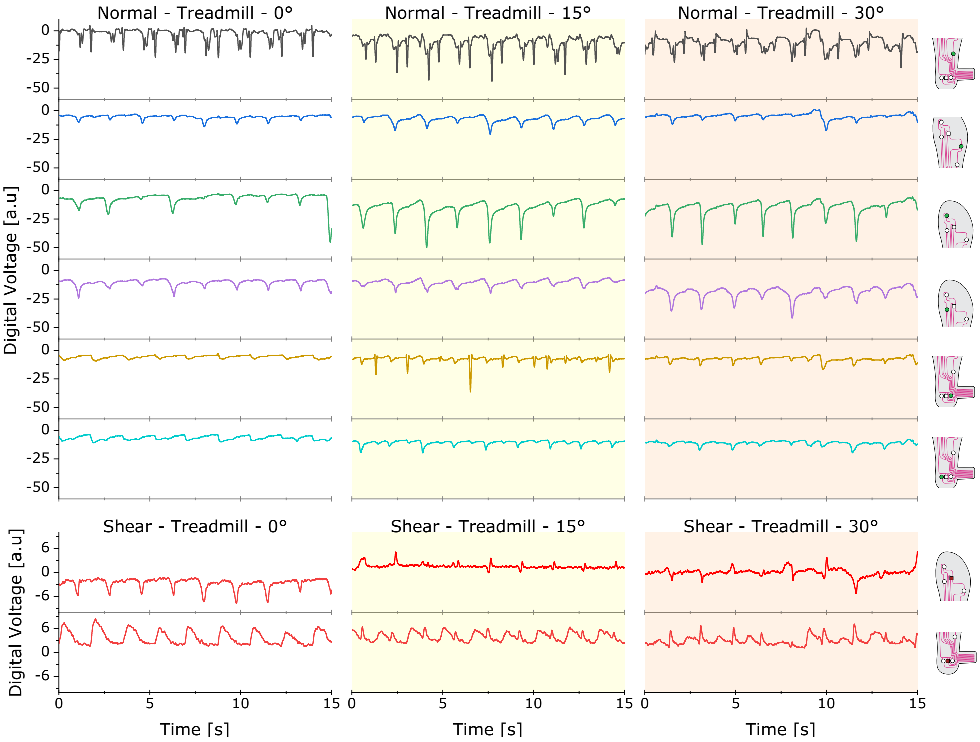

Figure 6.6 – Digital voltage plots for the data captured by the insole for a walking test at slopes with angles of 0, 15, and 30°.

slope becomes steeper, more load is being put on the front foot as the test subject compensates for the slope by changing the stance of their feet. Similar developments have been shown with external plantar pressure sensing devices on a treadmill[156].

This change in stance is especially evident from the shear forces. On a flat surface, both shear forces are of the same magnitude at around 6.3±0.9 a.u. which is in the direction of the toes for the forefoot and in the direction of heel for the rearfoot. This type of response is similar to shear force measured in an insole using optical sensors[153].

However, when the slope is increased, the shear on the forefoot becomes less unidirectional. The amplitude of shear forces detected in the heel decreases by about 18% at a 15° incline, and becomes irregular at a 30° incline. This is likely due to a perturbation in the gait due to the increase in the incline, which changes the step length and cadence[206].

These differentials were created as per Equation (4.3), with the differential (ΔR_{shear}) being determined by subtracting the signal of the "back" gauge from the "front" one, such that when a positive shear is applied the resulting differential is also positive. To calculate the differential its formula was expressed as

$$\Delta R_{\text{shear}} = \Delta R_{\text{back}} - \Delta R_{\text{front}} = (R_{\text{back}} - R_{\text{back},0}) - (R_{\text{front}} - R_{\text{front},0}), \tag{6.2}$$

6.2.3 Staircase climbing

Going up and down a staircase presents a unique type of gait motion. When either descending or ascending, almost the entire load of the body of the person is on the front of the foot causing large shear forces. We tested this hypothesis by letting the test subject walk down the staircase at a slow pace, pause at the bottom, and mount it again. The digital voltage changes of this test are shown in Figure 6.7.

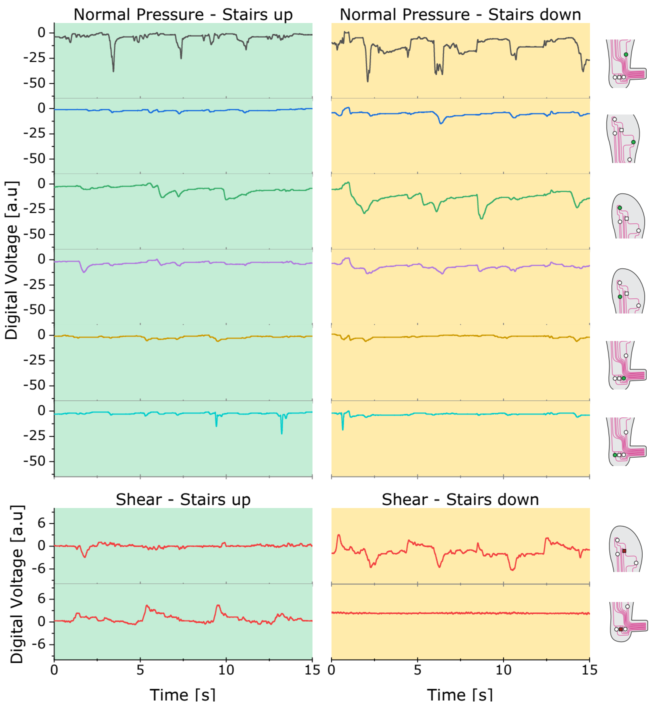

Figure 6.7 – Voltage plots for walking up and down of the stairs focusing on the front sensors.

A clear difference can be seen between normal plantar pressure distributions when going up stairs and down the stairs. When the test subject is walking up the stairs, high pressures are exerted at the front of the foot, as the whole body needs to be lifted up to place the other leg on the next stair. This does not result in intense shear forces, which in contrary, are very strongly present when the test subject is walking down the stairs. This is the result of the subject landing with their full weight on the front of the foot before stabilising, which results in a shear motion in both directions of the foot. Similar shear behaviour was seen for walking at incline angles of 30° in Section 6.2.2. In contrast, for going up the stairs, there are significant shear forces in the heel towards the back of the foot. When the heel strikes the next stair, the heel is the first part of the foot to touch the stair.

6.3 Summary and Conclusion

In this chapter the design, fabrication, and captured sensor signals of a soft fully 3D printed insole were presented. This insole had embedded piezoresistive shear and normal pressure sensors to allow for real-time sensing while inserted in a shoe. The sensor layout of the insole was adapted to the pressure map of a test subject to target skeletal areas of interest for gait monitoring. Due to the digital nature of the manufacturing process, the sensor layout could easily be adjusted either for another person or to monitor different areas of gait. Furthermore, the sensor density and even the shape of the insole could be modified to increase the data density of the gait or even enable correction of the gait. A custom made electronic wearable interface was created to be able to readout and transfer the sensor response to an external electronic device for storage and analysis.

The insole was encapsulated with a secondary layer to protect the silver interconnects from wear and tear during gait. This additional layer increased the initial resistance to 6.7±0.3 kΩ and resulted in an increased sensitivity of 16.8±1.5 Ω/kPa. Its monolithic nature was a cause of concern for cross-talk, but only resulted in the response of the unloaded sensors changing by less than 2% when a sensor in close proximity was actuated.

A test subject wore the insole to measure their plantar normal forces and shear forces during different types of static and dynamic physical activities. The normal pressure distribution over the insole due to the weight of the test subject were 57.1±1.7% and 42.8±2.6% for the rearfoot and forefoot, respectively, which are in agreement with other measurements made using external devices[205].

Using our insole, we were able to detect the normal pressure and shear force changes due to change in gait when walking on different inclines. In this test we saw a clear difference from both the pressure distribution and the shear force amplitude with the weight being shifted towards the front foot at steeper inclines. In a test with the subject descending and ascending a staircase, a clear distinction could be made in-between the two gaits. Normal pressures were quite evenly distributed when mounting the staircase, while they were more concentrated on the forefoot when going down. Furthermore, shear forces were higher in the forefoot when descending as the full weight of the test subject landed on this part.

Further tests should be performed with the insole to understand where improvements can be made. More dynamic tests such as running or jumping would allow us to tell if the sensor are able to accurately tell the difference between such activities and those with less load. Furthermore, the current data is presented in terms of digital voltage and its change from the baseline voltage. By coupling this data to a calibration step, the normal pressure and force data could be extracted.

However, these results suggest that our digitally manufactured insole could prove useful for both clinicians and sport enthusiasts. The extensive gait data that can be collected could be used to improve the health of patients with gait problems or to improve the sports performance of athletes.

7 Conclusion and Outlook

In this thesis several aspects of the state of art are advanced with respect to the 3D printing of mechanical sensors designed to monitor human motions. Advancements were presented on development of novel materials, fabrication techniques, and sensor designs. Here the conclusions of this thesis are highlighted in a summarised fashion and an outlook is provided on the remaining challenges and opportunities.

7.1 Summary and conclusion

7.1.1 Integrating highly conductive and piezoresistive features into 3D printed materials

Highly conductive flexible silver inks printed by Direct Ink Writing (DIW), which required thermal processing, were integrated into thermosensitive materials printed by Fused Deposition Modelling (FDM). The thermal mismatch between the FDM printed material, and the temperatures required to anneal the silver ink, made it not possible to use thermal curing procceses such as sintering in an oven. Therefore, an in-situ laser sintering technique was developed using a low-cost commercial laser diode which could sinter and solidify the inks straight after printing. Through a study of the laser parameters, a low resistivity value of 58.2±7.7 μΩ cm was achieved for single line features. Using the same methodology, DIW printed silver conductors were embedded within flexible FDM printed Thermoplastic Polyurethane (TPU). These films had a thickness of below 100 μm and a resistivity of 104.2±21.0 μΩ cm after sintering. This value is about a factor 100 above that of bulk silver, however, the achieved resistivity is several orders of magnitude lower than any conductive layer that can be currently created by FDM printing.

A piezoresistive silicone composite ink (CB-PDMS) was realised that could be DIW printed by giving it the necessary shear thinning properties by reinforcing it with 10 wt% fumed silica. This reinforcement allowed it to flow during printing but stabilise after deposition. The piezoresistive properties were introduced by adding carbon black (CB) microparticles into the silicone mixture. To disperse the CB particles throughout the composite a solvent was required, for which we selected pentanol. This solvent did not evaporate during printing but could be evacuated during curing of the material, resulting in a homogeneous dispersion of the CB particles in the cured composite. The network of CB inside the material ensured a pressure sensitive percolation that led to its piezoresistive properties. By tuning the CB loading of the material between 3 and 5 wt%, the resistivity could be tuned between 18.3±5.2 and 0.87±0.1 Ω m. Setting the CB loading of CB-PDMS composite further allows for the sensitivity of a strain gauges printed from this material to be tuned. For our application we chose a 4 wt% CB loading which allowed for a piezoresistive sensor with a gauge factor of 34. As this ink is silicone based, it was easily integrated with other DIW printable silicone inks we developed for structural parts of sensors. Adhesion between the materials was ensured using plasma surface activation.

7.1.2 Material and process development towards achieving three-dimensional geometries with conductive features

A thermally curable crystalline nanocellulose (CNC) reinforced Sylgard 184 silicone (PDMS) was developed in collaboration with our partners at the Complex Materials Laboratory at ETHZ and the Cellulose and Wood Materials Laboratory at EMPA. Using their methodology, a DIW printable CNC-PDMS ink was realised that exhibited ideal shear thinning properties. This allowed for the 3D printing of self-supporting multilayer three-dimensional structures that could be thermally cured after deposition. By adjusting the CNC content of the ink, mechanical properties of the cured material such as the tensile modulus, ultimate tensile strength, and surface roughness could be tuned. CNC-PDMS inks with a low CNC content (5 wt%) produced flowy, soft, and smooth materials, while those with a high content (>10 wt%) produced more rigid self supporting features. This property we exploited in the fabrication of sensors printed from these materials. Using 5 wt% CNC-PDMS, smooth surfaces were DIW printed, onto which silver paste is easily printed to achieve either flexible conductive features on top and embedded within the soft CNC-PDMS. Other more rigid structures, such as multilayer bumps to aid with force transfer, were printed using a 12.5 wt% CNC-PDMS.

A second strategy was explored by reinforcing a UV curable silicone (Silopren UV Electro 225-1) with fumed silica. By adding 5 wt% of fumed silica, a gel-like ink was created that could be DIW printed and cured within 5 minutes of UV light exposure. A Design of Experiments (DoE) analysis was performed to understand the influence of the printing pressure, speed, flow, and linespacing towards repeatably DIW printing sub 100 μm films. Through this analysis and extensive optimisation, silicone films were realised with a consistent thickness of 69.5±1.7 μm. Films were stacked on top of one another, with the printing orientation changing by 90° each layer change, and then cured in one shot to create three-dimensional 3D printed features. First printing and curing a supporting layer and then printing a pyramidical structure on top, with a reduction of 60 μm of the sides, resulted in non-planar faces with a maximum angle of 41.2±2.3°. Printing silver paste on top of these angular features allowed for slanted conductive plates with a separation of about 500 μm in-between them.

7.1.3 Development of fully 3D printed mechanical sensing devices

Using the developed CB-PDMS and CNC-PDMS formulations, piezoresistive normal sensors were created with tensile strain gauges from a 4 wt% ink and evaluated in terms of their performance. This metric is expressed by the resistance change from zero load to maximum load at 1000 kPa, and determined using a linear fit. A sensor sensitivity of 14.9±0.4 Ω/kPa (0.216±0.065 %/kPa) was achieved after application of preconditioning to reduce effects of material relaxation. Using the data from several sensors, a gauge factor of 34.0±0.1 was calculated, making it more sensitive than any other fully DIW printed normal pressure sensor reported previously. By preconditioning the sensors, the hysteresis was also reduced as the sensor response was stabilised. Lastly, we evaluated the dynamic performance of the sensor which showed repeatable behaviour over 25 minutes of testing at actuation frequencies of 0.5, 1, and 2 Hz, and pressures up to 1000 kPa which showed at most a 5% peak drift. An analysis of the dynamic response showed that the applied pressure had a significant influence on the amplitude of the signal. In contrast, the actuation speed had a negligible effect on the peak of the response but did lower the amplitude slightly. This made the developed sensor most suitable for the sensing of high dynamic force loads. However, reducing the viscoelastic behaviour of the PDMS composites could help to reduce the effects of material relaxation, to further decrease the hysteresis of the sensors.

Furthermore, a capacitive parallel plate normal pressure sensor was DIW printed from CNC-PDMS. We compared this sensor to the piezoresistive ones, to evaluate its applicability for the sensing of high normal loads and evaluate its suitability for gait sensing. The capacitive sensor had a lower but more approximately linear static response of 0.41±0.02 fF/kPa (0.052±0.007 %/kPa). This sensor did not require any preconditioning, had a lower hysteresis of 29.8±10.0%, and was able to accurately follow a dynamically changing force. Unfortunately, due to high parasitic noise, this sensor could not be easily used for human gait monitoring without a significant design revision.

Using the 4 wt% CB-PDMS formulation, two opposing piezoresistive strain gauges with chevron shapes were integrated into CNC-PDMS to create a shear force sensor. Using this design, shear forces could be distinguished in combination with a normal pressure of at least

400 kPa, and a sensitivity of the single elements was evaluated to be 2.64±0.37 %/N. A differential taken from the resistance change between the two gauges showed clear directionality of the direction of the applied force. A sensitivity of 326.3±36.2 kΩ/N up to 15 N of shear force, independent of its direction, was found. However, the magnitude of the shear force could not be reliably determined.

Both piezoresistive normal and shear force sensor were integrated into a wearable insole demonstrator to evaluate the technology for real human gait detection. Relative plantar pressure and shear force changes were measured for a set of static and dynamic activities, such as walking on inclines and ascending and descending a set of stairs. As 3D printing allows for easy sensor layout adaptation on an individual basis, this opens up a way for smart personalised wearables with embedded sensors.

Lastly, the capacitive transduction mechanism was explored further for the use of a bending sensor which was able to sense the direction of bending. A design for a sensor exploiting 3D topology, in which the capacitance increases when the plates bend towards each other, and reduces when bending away from each other, was realised. This design was modelled both analytically and through Finite Element Modelling (FEM) to validate its design. Using a prototype, these models were validated and used to design a truly fully 3D printed sensor. This completely DIW printed sensor was produced using the UV curable ink with conductive slanted plates which were encapsulated. Manual and automatic testing revealed the desired directionality and a sensitivity of 2.50±0.04 fF/° (0.11±0.00 %F/°). The sensor could be used to accurately track the bending of a limb, and its design could be adapted to track specific bending motions.

7.2 Outlook

This doctoral thesis provides a framework for the design and fabrication of fully 3D printed elastomeric sensors using piezoresistive and capacitive sensing mechanisms suited for the monitoring of a range of human motions. Materials and processes have been realised to allow for the 3D printing of these types of devices by either a single or multiple techniques. Furthermore, features with 3D topology have been realised that are either difficult or not possible to be fabricated without 3D printing technology. These 3D structures were used to developed novel methods to produce sensors as well as leading to a novel bending sensor design. However, further improvements can still be made to the material composition, processing methodology, and sensor design.

The developed laser sintering technique still warrants further investigation. At this time the actual temperatures during sintering are unknown. Improving their measurement, such as by capturing the temperature on the underside of the substrate, could yield a clearer idea of these. By developing a model of the temperature profile during sintering, linked to the laser exposure, the sintering process could be further optimised to result in less damage to the ink and substrate and lower resistivity values. While silicone is not thermally sensitive, utilising the laser sintering process for the silver ink used in our 3D printed sensors would reduce the need for thermal processing. In a printer such as the nScrypt the annealing is now a slow process due to the large thermal capacity of the heated printing bed which accommodates large prints. By utilising in-situ laser sintering of the printed inks, it could speed up the thermal processing and device fabrication speeds.

For the piezoresisitive normal pressure sensors a significant amount of hysteresis was observed. A large part of this is likely due to the viscoelastic behaviour of the silicone which introduces material relaxation[207]. Addition of carbon black already stiffens the material and reduces this effect[208], but also leads to increased conductivity which lowers their sensitivity. It would be of high interest to replace the fumed silica in the CB-PDMS composite with CNCs to reduce the effects due to material relaxation but retain printability[57]. This reinforcement could reduce the hysteresis to make the piezoresistive sensor perform better for dynamic loads. However, reinforcing polymers with natural fibers can stiffen the material[209], which warrants improvements to the shear sensor design to make it more sensitive.

One major problem in 3D printing remains the repeatability between prints which can introduce errors from one printed device to the next[166]. Improvements could be made by printing the CNC-PDMS material using the nScrypt 3D printer due to its high degree of control and precision. Using the improved CNC-PDMS formulation, a capacitive sensor with a thin dielectric could be envisioned. Furthermore, improvements could be made by creating a CNC-PDMS based on a UV curable silicone. This would reduce the processing time for the printing of PDMS, which currently takes a full hour. By printing this material using the nScrypt, both the printing quality and processing speed could be improved.

Improvements could be made for the 3D printing of conductive features on angular faces as well, as this is currently unoptimised in terms of the nozzle used for printing, the programmed printing path, and layer thickness. Through printing the UVE225-R5 ink with a higher layer thickness and the same offset, it might become possible to create even more inclined slopes. This could help with extending the bending range and improving the sensitivity of the capacitive bending sensor. By optimising its geometry, adding micro-structuring, and synthesising a new silicone based silver ink better suited for DIW printing. Conductive plates could then be printed in closer proximity, with a higher degree of accuracy and fidelity, leading to higher capacitive values and sensor sensitivities. Combining these improvements would further open up possibilities for other novel capacitive sensor designs with 3D topologies as well.

Finally, as the nScrypt is equipped with all necessary equipment to perform surface activation, laser curing, and UV curing, it makes for an ideal platform to utilise all developed fabrication techniques in a single machine. This would allow for the printing, processing, and sintering of materials, and would enable the in-situ fabrication of digitally printed sensors. These processes and their influence on both materials and sensors would need to be investigated before devices can be produced. However, if such a fabrication approach were to be developed, it would enable the realisation of personalised custom tailorable smart wearables for human motion monitoring with embedded low-power mechanical sensors.

A UV LED irradiance spectrum

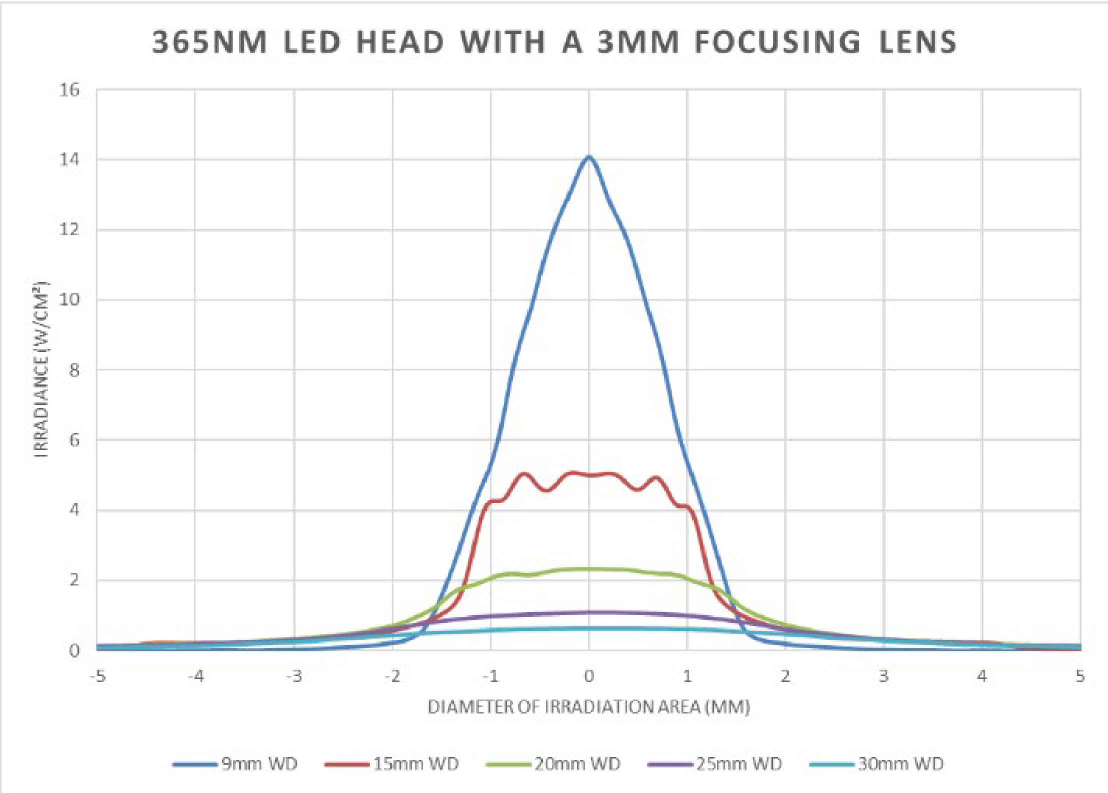

Figure A.1 – Irradiance spectrum of the 365 nm LED with 3 mm focusing lens integrated within the nScrypt 3Dn-300 printer.

Bibliography

[1] T. J. Wallin, J. Pikul, and R. F. Shepherd, "3D printing of soft robotic systems," *Nature Reviews Materials*, vol. 3, no. 6, pp. 84–100, 2018, ISSN: 2058-8437. DOI: 10.1038/s41578-018-0002-2.

[2] S. A. Tofail, E. P. Koumoulos, A. Bandyopadhyay, S. Bose, L. O'Donoghue, and C. Charitidis, "Additive manufacturing: Scientific and technological challenges, market uptake and opportunities," *Materials Today*, vol. 21, no. 1, pp. 22–37, 2017, ISSN: 1369-7021. DOI: 10.1016/j.mattod.2017.07.001.

[3] K. Salonitis, S. Ibbotson, J. G. Steingrímsson, S. Thiede, S. Heyer, and D. Chen, "Direct digital manufacturing: definition, evolution, and sustainability implications," *Journal of Cleaner Production*, vol. 107, pp. 615–625, 2015, ISSN: 0959-6526. DOI: 10.1016/j.jclepro.2015.05.009.

[4] J. I. Novak and A. R. Novak, "Is additive manufacturing improving performance in Sports? A systematic review," *Proceedings of the Institution of Mechanical Engineers, Part P: Journal of Sports Engineering and Technology*, 2020, ISSN: 1754-338X. DOI: 10.1177/1754337120971521.

[5] U. Ghosh, S. Ning, Y. Wang, and Y. L. Kong, "Addressing Unmet Clinical Needs with 3D Printing Technologies," *Advanced Healthcare Materials*, vol. 7, no. 17, pp. 1–24, 2018, ISSN: 2192-2659. DOI: 10.1002/adhm.201800417.

[6] S. Bosse, D. Lehmhus, W. Lang, and M. Busse, *Material-integrated intelligent systems: Technology and applications*. John Wiley & Sons, 2018.

[7] C. Young, M. L. Oliver, and K. D. Gordon, "Design and validation of a novel 3D-printed wearable device for monitoring knee joint kinematics," *Medical Engineering and Physics*, vol. 94, no. May, pp. 1–7, 2021, ISSN: 1873-4030. DOI: 10.1016/j.medengphy.2021.05.013.

[8] K. Xu, Y. Lu, and K. Takei, *Multifunctional Skin-Inspired Flexible Sensor Systems for Wearable Electronics*, 2019. DOI: 10.1002/admt.201800628.

[9] S. Tansaz, A. Baronetto, R. Zhang, A. Derungs, and O. Amft, "Printing Wearable Devices in 2D and 3D: An Overview on Mechanical and Electronic Digital Co-design," *IEEE Pervasive Computing*, vol. 18, no. 4, pp. 38–50, 2019, ISSN: 1558-2590. DOI: 10.1109/MPRV.2019.2948819.

[10] D. Espalin, D. W. Muse, E. MacDonald, and R. B. Wicker, "3D Printing multifunctionality: Structures with electronics," *International Journal of Advanced Manufacturing Technology*, vol. 72, no. 5-8, pp. 963–978, 2014, ISSN: 1433-3015. DOI: 10.1007/s00170-014-5717-7.

[11] E. MacDonald and R. Wicker, "Multiprocess 3D printing for increasing component functionality," *Science*, vol. 353, no. 6307, aaf2093–aaf2093, Sep. 2016, ISSN: 0036-8075. DOI: 10.1126/science.aaf2093.

[12] R. L. Truby, M. Wehner, A. K. Grosskopf, D. M. Vogt, S. G. M. Uzel, R. J. Wood, and J. A. Lewis, "Soft Somatosensitive Actuators via Embedded 3D Printing," *Advanced Materials*, p. 1 706 383, Feb. 2018, ISSN: 0935-9648. DOI: 10.1002/adma.201706383.

[13] E. MacDonald, R. Salas, D. Espalin, M. Perez, E. Aguilera, D. Muse, and R. B. Wicker, "3D printing for the rapid prototyping of structural electronics," *IEEE Access*, vol. 2, pp. 234–242, 2014, ISSN: 2169-3536. DOI: 10.1109/ACCESS.2014.2311810.

[14] T. Stuart, K. A. Kasper, I. C. Iwerunmor, D. T. McGuire, R. Peralta, J. Hanna, M. Johnson, M. Farley, T. LaMantia, P. Udorvich, and P. Gutruf, "Biosymbiotic, personalized, and digitally manufactured wireless devices for indefinite collection of high-fidelity biosignals," *Science Advances*, vol. 7, no. 41, 2021, ISSN: 2375-2548. DOI: 10.1126/sciadv.abj3269.

[15] D. J. Roach, C. M. Hamel, C. K. Dunn, M. V. Johnson, X. Kuang, and H. J. Qi, "The m4 3D printer: A multi-material multi-method additive manufacturing platform for future 3D printed structures," *Additive Manufacturing*, vol. 29, no. July, p. 100 819, 2019, ISSN: 2214-8604. DOI: 10.1016/j.addma.2019.100819.

[16] X. Zhou, K. Parida, O. Halevi, Y. Liu, J. Xiong, S. Magdassi, and P. S. Lee, "All 3D-printed stretchable piezoelectric nanogenerator with non-protruding kirigami structure," *Nano Energy*, vol. 72, p. 104 676, Jun. 2020, ISSN: 2211-2855. DOI: 10.1016/j.nanoen.2020.104676.

[17] T. Q. Trung and N. E. Lee, "Flexible and Stretchable Physical Sensor Integrated Platforms for Wearable Human-Activity Monitoringand Personal Healthcare," *Advanced Materials*, vol. 28, no. 22, pp. 4338–4372, 2016, ISSN: 1521-4095. DOI: 10.1002/adma.201504244.

[18] R. I. Haque, P.-A. Farine, and D. Briand, "3D Printed Materials Based Triboelectric Device for Energy Harvesting and Sensing," *Proceedings*, vol. 1, no. 10, p. 580, 2017. DOI: 10.3390/proceedings1040580.

[19] Y. Liu, M. Pharr, and G. A. Salvatore, “Lab-on-skin: a review of flexible and stretchable electronics for wearable health monitoring,” *ACS Nano*, vol. 11, no. 10, pp. 9614–9635, 2017, ISSN: 1936-086X. DOI: 10.1021/acsnano.7b04898.

[20] D. C. Kim, H. J. Shim, W. Lee, J. H. Koo, and D. H. Kim, “Material-Based Approaches for the Fabrication of Stretchable Electronics,” *Advanced Materials*, vol. 1902743, pp. 1–29, 2019, ISSN: 1521-4095. DOI: 10.1002/adma.201902743.

[21] Y. Liu, H. Wang, W. Zhao, M. Zhang, H. Qin, and Y. Xie, “Flexible, stretchable sensors for wearable health monitoring: Sensing mechanisms, materials, fabrication strategies and features,” *Sensors (Switzerland)*, vol. 18, no. 2, 2018, ISSN: 1424-8220. DOI: 10.3390/s18020645.

[22] G. L. Goh, H. Zhang, T. H. Chong, and W. Y. Yeong, “3D Printing of Multilayered and Multimaterial Electronics: A Review,” *Advanced Electronic Materials*, vol. 2100445, pp. 1–28, 2021, ISSN: 2199-160X. DOI: 10.1002/aelm.202100445.

[23] R. L. Truby and J. A. Lewis, “Printing soft matter in three dimensions,” *Nature*, vol. 540, no. 7633, pp. 371–378, 2016, ISSN: 1476-4687. DOI: 10.1038/nature21003.

[24] A. Cano-Vicent, M. M. Tambuwala, S. S. Hassan, D. Barh, A. A. Aljabali, M. Birkett, A. Arjunan, and Á. Serrano-Aroca, “Fused deposition modelling: Current status, methodology, applications and future prospects,” *Additive Manufacturing*, vol. 47, no. October, p. 102 378, Nov. 2021, ISSN: 2214-8604. DOI: 10.1016/j.addma.2021.102378. [Online]. Available: https://linkinghub.elsevier.com/retrieve/pii/S2214860421005327.

[25] H. Ota, S. Emaminejad, Y. Gao, A. Zhao, E. Wu, S. Challa, K. Chen, H. M. Fahad, A. K. Jha, D. Kiriya, W. Gao, H. Shiraki, K. Morioka, A. R. Ferguson, K. E. Healy, R. W. Davis, and A. Javey, “Application of 3D Printing for Smart Objects with Embedded Electronic Sensors and Systems,” *Advanced Materials Technologies*, vol. 1, no. 1, p. 1 600 013, 2016, ISSN: 2365-709X. DOI: 10.1002/admt.201600013.

[26] L. Y. W. Loh, U. Gupta, Y. Wang, C. C. Foo, J. Zhu, and W. F. Lu, “3D Printed Metamaterial Capacitive Sensing Array for Universal Jamming Gripper and Human Joint Wearables,” *Advanced Engineering Materials*, vol. 23, no. 5, p. 2 001 082, May 2021, ISSN: 1438-1656. DOI: 10.1002/adem.202001082.

[27] D. Kosmas, H.-P. van Jonbergen, M. Schouten, M. Abayazid, and G. Krijnen, “Development of a 3D Printed Gap Gauge with Embedded Force Sensor for Balancing Unicompartmental Knee Arthroplasty.,” in *2021 IEEE Sensors*, IEEE, Oct. 2021, pp. 1–4, ISBN: 978-1-7281-9501-8. DOI: 10.1109/SENSORS47087.2021.9639727. [Online]. Available: https://ieeexplore.ieee.org/document/9639727/.

[28] A. Dijkshoorn, P. Werkman, M. Welleweerd, G. Wolterink, B. Eijking, J. Delamare, R. Sanders, and G. J. M. Krijnen, "Embedded sensing: integrating sensors in 3-D printed structures," *Journal of Sensors and Sensor Systems*, vol. 7, no. 1, pp. 169–181, Apr. 2018, ISSN: 2194-878X. DOI: 10.5194/jsss-7-169-2018. [Online]. Available: https://www.j-sens-sens-syst.net/7/169/2018/.

[29] K. Kim, J. Park, J. hoon Suh, M. Kim, Y. Jeong, and I. Park, "3D printing of multiaxial force sensors using carbon nanotube (CNT)/thermoplastic polyurethane (TPU) filaments," *Sensors and Actuators, A: Physical*, vol. 263, pp. 493–500, 2017, ISSN: 0924-4247. DOI: 10.1016/j.sna.2017.07.020.

[30] N. Kumar, P. K. Jain, P. Tandon, and P. M. Pandey, "Additive manufacturing of flexible electrically conductive polymer composites via CNC-assisted fused layer modeling process," *Journal of the Brazilian Society of Mechanical Sciences and Engineering*, vol. 40, no. 4, pp. 1–13, 2018, ISSN: 1806-3691. DOI: 10.1007/s40430-018-1116-6.

[31] A. D. Valino, J. R. C. Dizon, A. H. Espera, Q. Chen, J. Messman, and R. C. Advincula, "Advances in 3D printing of thermoplastic polymer composites and nanocomposites," *Progress in Polymer Science*, vol. 98, p. 101 162, 2019, ISSN: 0079-6700. DOI: 10.1016/j.progpolymsci.2019.101162.

[32] G. Wolterink, R. Sanders, and G. Krijnen, "Thin, Flexible, Capacitive Force Sensors Based on Anisotropy in 3D-Printed Structures," *Proceedings of IEEE Sensors*, vol. 2018-Octob, pp. 18–21, 2018, ISSN: 2168-9229. DOI: 10.1109/ICSENS.2018.8589584.

[33] J. Z. Gul, M. Sajid, and K. H. Choi, "3D printed highly flexible strain sensor based on TPU-Graphene composite for feedback of high speed robotic applications," *Journal of Materials Chemistry C*, 2019, ISSN: 2050-7526. DOI: 10.1039/C8TC03423K. [Online]. Available: http://pubs.rsc.org/en/Content/ArticleLanding/2019/TC/C8TC03423K.

[34] J. F. Christ, N. Aliheidari, A. Ameli, and P. Pötschke, "3D printed highly elastic strain sensors of multiwalled carbon nanotube/thermoplastic polyurethane nanocomposites," *Materials & Design*, vol. 131, pp. 394–401, Oct. 2017, ISSN: 0264-1275. DOI: 10.1016/j.matdes.2017.06.011. [Online]. Available: https://linkinghub.elsevier.com/retrieve/pii/S0264127517305944.

[35] M. Alsharari, B. Chen, and W. Shu, "3D Printing of Highly Stretchable and Sensitive Strain Sensors Using Graphene Based Composites," *Proceedings*, vol. 2, no. 13, p. 792, 2018, ISSN: 2504-3900. DOI: 10.3390/proceedings2130792.

[36] A. Garg, A. Bhattacharya, and A. Batish, "Chemical vapor treatment of ABS parts built by FDM: Analysis of surface finish and mechanical strength," *International Journal of Advanced Manufacturing Technology*, vol. 89, no. 5-8, pp. 2175–2191, 2017, ISSN: 1433-3015. DOI: 10.1007/s00170-016-9257-1.

[37] M. Adel, O. Abdelaal, A. Gad, A. B. Nasr, and A. M. Khalil, "Polishing of fused deposition modeling products by hot air jet: Evaluation of surface roughness," *Journal of Materials Processing Technology*, vol. 251, no. July 2017, pp. 73–82, 2018, ISSN: 0924-0136. DOI: 10.1016/j.jmatprotec.2017.07.019.

[38] Y. Chai, R. W. Li, D. M. Perriman, S. Chen, Q. H. Qin, and P. N. Smith, "Laser polishing of thermoplastics fabricated using fused deposition modelling," *International Journal of Advanced Manufacturing Technology*, vol. 96, no. 9-12, pp. 4295–4302, 2018, ISSN: 1433-3015. DOI: 10.1007/s00170-018-1901-5.

[39] M. Lalegani Dezaki, M. K. A. Mohd Ariffin, and M. I. S. Ismail, "Effects of CNC Machining on Surface Roughness in Fused Deposition Modelling (FDM) Products," *Materials*, vol. 13, no. 11, p. 2608, Jun. 2020, ISSN: 1996-1944. DOI: 10.3390/ma13112608. [Online]. Available: https://www.mdpi.com/1996-1944/13/11/2608.

[40] A. Falco, M. Petrelli, E. Bezzeccheri, A. Abdelhalim, and P. Lugli, "Towards 3D-printed organic electronics: Planarization and spray-deposition of functional layers onto 3D-printed objects," *Organic Electronics: physics, materials, applications*, vol. 39, pp. 340–347, 2016, ISSN: 1566-1199. DOI: 10.1016/j.orgel.2016.10.027.

[41] F. B. Coulter, M. Schaffner, J. A. Faber, A. Rafsanjani, R. Smith, H. Appa, P. Zilla, D. Bezuidenhout, and A. R. Studart, "Bioinspired Heart Valve Prosthesis Made by Silicone Additive Manufacturing," *Matter*, vol. 1, no. 1, pp. 266–279, 2019, ISSN: 2590-2385. DOI: 10.1016/j.matt.2019.05.013.

[42] M. M. Durban, J. M. Lenhardt, A. S. Wu, W. Small, T. M. Bryson, L. Perez-Perez, D. T. Nguyen, S. Gammon, J. E. Smay, E. B. Duoss, J. P. Lewicki, T. S. Wilson, L. Perez-Perez, D. T. Nguyen, S. Gammon, J. E. Smay, E. B. Duoss, J. P. Lewicki, and T. S. Wilson, "Custom 3D Printable Silicones with Tunable Stiffness," *Macromolecular Rapid Communications*, vol. 39, no. 4, p. 1 700 563, Feb. 2018, ISSN: 1521-3927. DOI: 10.1002/marc.201700563.

[43] L.-y. Y. Zhou, Q. Gao, J.-z. Z. Fu, Q.-y. Y. Chen, J.-p. P. Zhu, Y. Sun, and Y. He, "Multi-material 3D Printing of Highly Stretchable Silicone Elastomers," *ACS Applied Materials and Interfaces*, vol. 11, no. 26, pp. 23 573–23 583, Jul. 2019, ISSN: 1944-8252. DOI: 10.1021/acsami.9b04873.

[44] J. W. Kopatz, J. Unangst, A. W. Cook, and L. N. Appelhans, "Compositional effects on cure kinetics, mechanical properties and printability of dual-cure epoxy/acrylate resins for DIW additive manufacturing," *Additive Manufacturing*, vol. 46, no. February, p. 102 159, 2021, ISSN: 2214-8604. DOI: 10.1016/j.addma.2021.102159.

[45] W. T. Nugroho, Y. Dong, A. Pramanik, J. Leng, and S. Ramakrishna, "Smart polyurethane composites for 3D or 4D printing: General-purpose use, sustainability and shape

memory effect," *Composites Part B: Engineering*, vol. 223, no. March, p. 109 104, 2021, ISSN: 1359-8368. DOI: 10.1016/j.compositesb.2021.109104.

[46] R. Tu and H. A. Sodano, "Additive manufacturing of high-performance vinyl ester resin via direct ink writing with UV-thermal dual curing," *Additive Manufacturing*, vol. 46, no. May, p. 102 180, 2021, ISSN: 2214-8604. DOI: 10.1016/j.addma.2021.102180.

[47] X. Cui, J. Li, Y. Hartanto, M. Durham, J. Tang, H. Zhang, G. Hooper, K. Lim, and T. Woodfield, "Advances in Extrusion 3D Bioprinting: A Focus on Multicomponent Hydrogel-Based Bioinks," *Advanced Healthcare Materials*, vol. 9, no. 15, p. 1 901 648, Aug. 2020, ISSN: 2192-2640. DOI: 10.1002/adhm.201901648.

[48] D. Chimene, R. Kaunas, and A. K. Gaharwar, "Hydrogel Bioink Reinforcement for Additive Manufacturing: A Focused Review of Emerging Strategies," *Advanced Materials*, vol. 32, no. 1, 2020, ISSN: 1521-4095. DOI: 10.1002/adma.201902026.

[49] M. Falahati, P. Ahmadvand, S. Safaee, Y. C. Chang, Z. Lyu, R. Chen, L. Li, and Y. Lin, "Smart polymers and nanocomposites for 3D and 4D printing," *Materials Today*, vol. 40, no. November, pp. 215–245, 2020, ISSN: 1873-4103. DOI: 10.1016/j.mattod.2020.06.001.

[50] A. Chortos, E. Hajiesmaili, J. Morales, D. R. Clarke, and J. A. Lewis, "3D Printing of Interdigitated Dielectric Elastomer Actuators," *Advanced Functional Materials*, vol. 30, no. 1, p. 1 907 375, Jan. 2020, ISSN: 1616-301X. DOI: 10.1002/adfm.201907375.

[51] J. A. Lewis, "Direct ink writing of 3D functional materials," *Advanced Functional Materials*, vol. 16, no. 17, pp. 2193–2204, 2006, ISSN: 1616-301X. DOI: 10.1002/adfm.200600434.

[52] L. Li, Q. Lin, M. Tang, A. J. Duncan, and C. Ke, "Advanced Polymer Designs for Direct-Ink-Write 3D Printing," *Chemistry - A European Journal*, vol. 25, no. 46, pp. 10 768–10 781, 2019, ISSN: 1521-3765. DOI: 10.1002/chem.201900975.

[53] S. Chen, W. S. Tan, M. A. Bin Juhari, Q. Shi, X. S. Cheng, W. L. Chan, and J. Song, "Freeform 3D printing of soft matters: recent advances in technology for biomedical engineering," *Biomedical Engineering Letters*, no. 0123456789, 2020, ISSN: 2093-985X. DOI: 10.1007/s13534-020-00171-8.

[54] *Basics of rheology - anton paar*, https://wiki.anton-paar.com/en/basics-of-rheology, Accessed: 22-12-2021.

[55] A. C. H. Tsang, J. Zhang, K. N. Hui, K. S. Hui, and H. Huang, "Recent Development and Applications of Advanced Materials via Direct Ink Writing," *Advanced Materials Technologies*, vol. 2101358, p. 2 101 358, Jan. 2022, ISSN: 2365-709X. DOI: 10.1002/admt.202101358.

[56] A. P. Almeida, J. P. Canejo, S. N. Fernandes, C. Echeverria, P. L. Almeida, and M. H. Godinho, "Cellulose-Based Biomimetics and Their Applications," *Advanced Materials*, vol. 1703655, pp. 1–31, 2018, ISSN: 1521-4095. DOI: 10.1002/adma.201703655.

[57] G. Siqueira, D. Kokkinis, R. Libanori, M. K. Hausmann, A. S. Gladman, A. Neels, P. Tingaut, T. Zimmermann, J. A. Lewis, and A. R. Studart, "Cellulose Nanocrystal Inks for 3D Printing of Textured Cellular Architectures," *Advanced Functional Materials*, vol. 27, no. 12, pp. 1–10, 2017, ISSN: 1616-3028. DOI: 10.1002/adfm.201604619.

[58] M. A. Skylar-Scott, S. Gunasekaran, and J. A. Lewis, "Laser-assisted direct ink writing of planar and 3D metal architectures," *Proceedings of the National Academy of Sciences of the United States of America*, vol. 113, no. 22, pp. 6137–6142, 2016, ISSN: 1091-6490. DOI: 10.1073/pnas.1525131113. arXiv: arXiv:1408.1149.

[59] F. Liravi and E. Toyserkani, "Additive manufacturing of silicone structures: A review and prospective," *Additive Manufacturing*, vol. 24, no. January, pp. 232–242, Dec. 2018, ISSN: 2214-8604. DOI: 10.1016/j.addma.2018.10.002.

[60] R. Su, J. Wen, Q. Su, M. S. Wiederoder, S. J. Koester, J. R. Uzarski, and M. C. McAlpine, "3D printed self-supporting elastomeric structures for multifunctional microfluidics," *Science advances*, vol. 6, no. 41, pp. 1–11, 2020, ISSN: 2375-2548. DOI: 10.1126/sciadv.abc9846.

[61] M. P. Wolf, G. B. Salieb-Beugelaar, and P. Hunziker, "PDMS with designer functionalities—Properties, modifications strategies, and applications," *Progress in Polymer Science*, vol. 83, pp. 97–134, 2018, ISSN: 0079-6700. DOI: 10.1016/j.progpolymsci.2018.06.001.

[62] A. H. Espera, J. R. C. Dizon, Q. Chen, and R. C. Advincula, *3D-printing and advanced manufacturing for electronics*, 2019. DOI: 10.1007/s40964-019-00077-7.

[63] J. Beach, S. Patterson, A. Zlatanic, J. M. Messman, and P. R. Dvornic, "New "all-in-one" silicone pastes for additive manufacturing of elastomer parts," *MRS Communications*, vol. 11, no. 2, pp. 88–93, 2021, ISSN: 2159-6867. DOI: 10.1557/s43579-020-00007-7.

[64] N. van de Werken, H. Tekinalp, P. Khanbolouki, S. Ozcan, A. Williams, and M. Tehrani, "Additively manufactured carbon fiber-reinforced composites: State of the art and perspective," *Additive Manufacturing*, vol. 31, no. July 2019, p. 100 962, Jan. 2020, ISSN: 2214-8604. DOI: 10.1016/j.addma.2019.100962.

[65] M. L. Hammock, A. Chortos, B. C. Tee, J. B. Tok, and Z. Bao, "25th anniversary article: The evolution of electronic skin (E-Skin): A brief history, design considerations, and recent progress," *Advanced Materials*, vol. 25, no. 42, pp. 5997–6038, 2013, ISSN: 0935-9648. DOI: 10.1002/adma.201302240.

[66] Z. Jiang, B. Diggle, M. L. Tan, J. Viktorova, C. W. Bennett, and L. A. Connal, "Extrusion 3D Printing of Polymeric Materials with Advanced Properties," *Advanced Science*, vol. 2001379, pp. 1–32, 2020, ISSN: 2198-3844. DOI: 10.1002/advs.202001379.

[67] J. E. Regis, A. Renteria, S. E. Hall, M. S. Hassan, C. Marquez, and Y. Lin, *Recent trends and innovation in additive manufacturing of soft functional materials*, Aug. 2021. DOI: 10.3390/ma14164521. [Online]. Available: https://www.mdpi.com/1996-1944/14/16/4521.

[68] V. Kumar, G. Lee, K. Singh, J. Choi, and D. J. Lee, "Structure-property relationship in silicone rubber nanocomposites reinforced with carbon nanomaterials for sensors and actuators," *Sensors and Actuators, A: Physical*, vol. 303, p. 111 712, 2020, ISSN: 0924-4247. DOI: 10.1016/j.sna.2019.111712.

[69] R. Venkata Krishna Rao, K. Venkata Abhinav, P. S. Karthik, S. P. Singh, V. K. R. R., V. A. K., K. P. S., and S. P. Singh, "Conductive silver inks and their applications in printed and flexible electronics," *RSC Advances*, vol. 5, no. 95, pp. 77 760–77 790, 2015, ISSN: 2046-2069. DOI: 10.1039/C5RA12013F. [Online]. Available: http://xlink.rsc.org/?DOI=C5RA12013F.

[70] J. Shintake, E. Piskarev, S. H. Jeong, and D. Floreano, "Ultrastretchable Strain Sensors Using Carbon Black-Filled Elastomer Composites and Comparison of Capacitive Versus Resistive Sensors," *Advanced Materials Technologies*, vol. 1700284, p. 1 700 284, 2017, ISSN: 2365-709X. DOI: 10.1002/admt.201700284.

[71] S. Tagliaferri, A. Panagiotopoulos, and C. Mattevi, "Direct ink writing of energy materials," *Materials Advances*, vol. 2, no. 2, pp. 540–563, 2021, ISSN: 2633-5409. DOI: 10.1039/d0ma00753f.

[72] P. Blyweert, V. Nicolas, V. Fierro, and A. Celzard, "3D printing of carbon-based materials: A review," *Carbon*, vol. 183, pp. 449–485, 2021, ISSN: 0008-6223. DOI: 10.1016/j.carbon.2021.07.036.

[73] J. T. Muth, D. M. Vogt, R. L. Truby, Y. Mengüç, D. B. Kolesky, R. J. Wood, J. A. Lewis, R. L. Truby, D. B. Kolesky, R. J. Wood, J. T. Muth, D. M. Vogt, and J. A. Lewis, "Embedded 3D Printing of Strain Sensors within Highly Stretchable Elastomers," *Advanced Materials*, vol. 26, no. 36, pp. 6307–6312, Sep. 2014, ISSN: 0935-9648. DOI: 10.1002/adma.201400334. arXiv: 1111.4970.

[74] A. Renteria, V. H. Balcorta, C. Marquez, A. A. Rodriguez, I. Renteria-Marquez, J. E. Regis, B. Wilburn, S. Patterson, D. Espalin, T.-L. Tseng, and Y. Lin, "Direct ink write multi-material printing of PDMS-BTO composites with MWCNT electrodes for flexible force sensors," *Flexible and Printed Electronics*, vol. 7, no. 1, p. 015 001, Mar. 2021, ISSN: 2058-8585. DOI: 10.1088/2058-8585/ac442e.

[75] M. Mohammed Ali, D. Maddipatla, B. B. Narakathu, A. A. Chlaihawi, S. Emamian, F. Janabi, B. J. Bazuin, and M. Z. Atashbar, "Printed strain sensor based on silver nanowire/silver flake composite on flexible and stretchable TPU substrate," *Sensors and Actuators, A: Physical*, vol. 274, pp. 109–115, 2018, ISSN: 0924-4247. DOI: 10.1016/j.sna.2018.03.003.

[76] M. S. Rahman and G. Grau, "Direct writing of stretchable metal flake conductors: improved stretchability and conductivity by combining differently sintered materials," *Flexible and Printed Electronics*, vol. 5, no. 2, p. 025 005, Jun. 2020, ISSN: 2058-8585. DOI: 10.1088/2058-8585/ab8f22.

[77] S. P. Lacour, D. Chan, S. Wagner, T. Li, and Z. Suo, "Mechanisms of reversible stretchability of thin metal films on elastomeric substrates," *Applied Physics Letters*, vol. 88, no. 20, p. 204 103, May 2006, ISSN: 0003-6951. DOI: 10.1063/1.2201874.

[78] S.-Z. Guo, K. Qiu, F. Meng, S. H. Park, and M. C. McAlpine, "3D Printed Stretchable Tactile Sensors," *Advanced Materials*, vol. 29, no. 27, p. 1 701 218, Jul. 2017, ISSN: 0935-9648. DOI: 10.1002/adma.201701218.

[79] S. Huang, Y. Liu, Y. Zhao, Z. Ren, and C. F. Guo, *Flexible Electronics: Stretchable Electrodes and Their Future*, 2019. DOI: 10.1002/adfm.201805924.

[80] H. Yang, C. Li, M. Yang, Y. Pan, Q. Yin, J. Tang, H. J. Qi, and Z. Suo, "Printing Hydrogels and Elastomers in Arbitrary Sequence with Strong Adhesion," *Advanced Functional Materials*, vol. 1901721, pp. 1–8, 2019, ISSN: 1616-3028. DOI: 10.1002/adfm.201901721.

[81] M. D. Dickey, "Stretchable and Soft Electronics using Liquid Metals," *Advanced Materials*, vol. 29, no. 27, pp. 1–19, 2017, ISSN: 1521-4095. DOI: 10.1002/adma.201606425.

[82] Y. G. Park, H. S. An, J. Y. Kim, and J. U. Park, "High-resolution, reconfigurable printing of liquid metals with three-dimensional structures," *Science Advances*, vol. 5, no. 6, pp. 1–10, 2019, ISSN: 2375-2548. DOI: 10.1126/sciadv.aaw2844.

[83] C. Votzke, U. Daalkhaijav, Y. Menguc, and M. L. Johnston, "3D-Printed Liquid Metal Interconnects for Stretchable Electronics," *IEEE Sensors Journal*, vol. XX, no. Xx, pp. 1–1, 2019, ISSN: 1530-437X. DOI: 10.1109/JSEN.2019.2894405. [Online]. Available: https://ieeexplore.ieee.org/document/8624516/.

[84] J. H. Kim, S. Kim, J. H. So, K. Kim, and H. J. Koo, "Cytotoxicity of Gallium-Indium Liquid Metal in an Aqueous Environment," *ACS Applied Materials and Interfaces*, vol. 10, no. 20, pp. 17 448–17 454, 2018, ISSN: 1944-8252. DOI: 10.1021/acsami.8b02320.

[85] P. Izak, J. Mastalska-Poplawska, J. Lis, and A. Stempkowska, "Modification of the rheological properties of screen printing ceramic paints containing gold," *Journal of Physics: Conference Series*, vol. 790, no. 1, p. 012 011, Jan. 2017, ISSN: 1742-6588. DOI: 10.1088/1742-6596/790/1/012011.

[86] J. Y. Lee, J. An, and C. K. Chua, "Fundamentals and applications of 3D printing for novel materials," *Applied Materials Today*, vol. 7, pp. 120–133, 2017, ISSN: 2352-9407. DOI: 10.1016/j.apmt.2017.02.004. arXiv: NIHMS150003.

[87] Q. Mu, C. K. Dunn, L. Wang, M. L. Dunn, H. J. Qi, and T. Wang, "Thermal cure effects on electromechanical properties of conductive wires by direct ink write for 4D printing and soft machines," *Smart Materials and Structures*, vol. 26, no. 4, p. 045 008, Apr. 2017, ISSN: 0964-1726. DOI: 10.1088/1361-665X/aa5cca. [Online]. Available: http://stacks.iop.org/0964-1726/26/i=4/a=045008?key=crossref.3dad531c59e9a395820036e58d7d44e9.

[88] G. Arias-Ferreiro, A. Ares-Pernas, A. Lasagabáster-Latorre, N. Aranburu, G. Guerrica-Echevarria, M. S. Dopico-García, and M.-J. Abad, "Printability Study of a Conductive Polyaniline/Acrylic Formulation for 3D Printing," *Polymers*, vol. 13, no. 13, p. 2068, Jun. 2021, ISSN: 2073-4360. DOI: 10.3390/polym13132068. [Online]. Available: https://www.mdpi.com/2073-4360/13/13/2068.

[89] A. Cortés, X. F. Sánchez-Romate, A. Jiménez-Suárez, M. Campo, A. Ureña, and S. G. Prolongo, "Mechanical and strain-sensing capabilities of carbon nanotube reinforced composites by digital light processing 3D printing technology," *Polymers*, vol. 12, no. 4, 2020, ISSN: 2073-4360. DOI: 10.3390/POLYM12040975.

[90] Y. He, R. Yu, X. Li, M. Zhang, Y. Zhang, X. Yang, X. Zhao, and W. Huang, "Digital Light Processing 4D Printing of Transparent, Strong, Highly Conductive Hydrogels," *ACS Applied Materials & Interfaces*, vol. 13, no. 30, pp. 36 286–36 294, Aug. 2021, ISSN: 1944-8244. DOI: 10.1021/acsami.1c08438.

[91] D. K. Patel, A. H. Sakhaei, M. Layani, B. Zhang, Q. Ge, and S. Magdassi, "Highly Stretchable and UV Curable Elastomers for Digital Light Processing Based 3D Printing," *Advanced Materials*, vol. 29, no. 15, p. 1 606 000, Apr. 2017, ISSN: 0935-9648. DOI: 10.1002/adma.201606000.

[92] V. Slesarenko and S. Rudykh, "Towards mechanical characterization of soft digital materials for multimaterial 3D-printing," *International Journal of Engineering Science*, vol. 123, pp. 62–72, 2018, ISSN: 0020-7225. DOI: 10.1016/j.ijengsci.2017.11.011. arXiv: 1710.05187.

[93] M. Smith, Y. S. Choi, C. Boughey, and S. Kar-Narayan, "Controlling and assessing the quality of aerosol jet printed features for large area and flexible electronics," *Flexible and Printed Electronics*, vol. 2, no. 1, p. 015 004, Mar. 2017, ISSN: 2058-8585. DOI: 10.1088/2058-8585/aa5af9.

[94] D. Loterie, P. Delrot, and C. Moser, "High-resolution tomographic volumetric additive manufacturing," *Nature Communications*, vol. 11, no. 1, pp. 1–6, 2020, ISSN: 2041-1723. DOI: 10.1038/s41467-020-14630-4.

[95] J. Qin, L.-j. Yin, Y.-n. Hao, S.-l. Zhong, D.-L. Zhang, K. Bi, Y.-x. Zhang, Y. Zhao, and Z.-m. Dang, "Flexible and Stretchable Capacitive Sensors with Different Microstructures," *Advanced Materials*, vol. 2008267, p. 2 008 267, Jul. 2021, ISSN: 0935-9648. DOI: 10.1002/adma.202008267.

[96] E. Davoodi, H. Fayazfar, F. Liravi, E. Jabari, and E. Toyserkani, “Drop-on-demand high-speed 3D printing of flexible milled carbon fiber/silicone composite sensors for wearable biomonitoring devices,” *Additive Manufacturing*, vol. 32, no. August 2019, p. 101 016, 2020, ISSN: 2214-8604. DOI: 10.1016/j.addma.2019.101016.

[97] H. R. Lim, H. S. Kim, R. Qazi, Y. T. Kwon, J. W. Jeong, and W. H. Yeo, “Advanced Soft Materials, Sensor Integrations, and Applications of Wearable Flexible Hybrid Electronics in Healthcare, Energy, and Environment,” *Advanced Materials*, vol. 32, no. 15, pp. 1–43, 2020, ISSN: 1521-4095. DOI: 10.1002/adma.201901924.

[98] D. F. Fernandes, C. Majidi, and M. Tavakoli, “Digitally printed stretchable electronics: A review,” *Journal of Materials Chemistry C*, vol. 7, no. 45, pp. 14 035–14 068, 2019, ISSN: 2050-7526. DOI: 10.1039/c9tc04246f.

[99] T. Dinh, T. Nguyen, H. P. Phan, T. K. Nguyen, V. T. Dau, N. T. Nguyen, and D. V. Dao, “Advances in Rational Design and Materials of High-Performance Stretchable Electromechanical Sensors,” *Small*, vol. 16, no. 14, pp. 1–25, 2020, ISSN: 1613-6829. DOI: 10.1002/smll.201905707.

[100] C. Liu, N. Huang, F. Xu, J. Tong, Z. Chen, X. Gui, Y. Fu, and C. Lao, “3D printing technologies for flexible tactile sensors toward wearable electronics and electronic skin,” *Polymers*, vol. 10, no. 6, pp. 1–31, 2018, ISSN: 2073-4360. DOI: 10.3390/polym10060629.

[101] R. Hinchet, W. Seung, and S. W. Kim, “Recent Progress on Flexible Triboelectric Nanogenerators for SelfPowered Electronics,” *ChemSusChem*, vol. 8, no. 14, pp. 2327–2344, 2015, ISSN: 1864-564X. DOI: 10.1002/cssc.201403481.

[102] Y.-F. Liu, Y.-Q. Li, P. Huang, N. Hu, and S.-Y. Fu, “On the Evaluation of the Sensitivity Coefficient of Strain Sensors,” *Advanced Electronic Materials*, vol. 4, no. 12, p. 1 800 353, Dec. 2018, ISSN: 2199-160X. DOI: 10.1002/aelm.201800353.

[103] S. Mishra, L. Unnikrishnan, S. K. Nayak, and S. Mohanty, “Advances in Piezoelectric Polymer Composites for Energy Harvesting Applications: A Systematic Review,” *Macromolecular Materials and Engineering*, vol. 304, no. 1, pp. 1–25, 2019, ISSN: 1439-2054. DOI: 10.1002/mame.201800463.

[104] M. R. Khosravani and T. Reinicke, “3D-printed sensors: Current progress and future challenges,” *Sensors and Actuators, A: Physical*, vol. 305, 2020, ISSN: 0924-4247. DOI: 10.1016/j.sna.2020.111916.

[105] H. Liu, H. Zhang, W. Han, H. Lin, R. Li, J. Zhu, and W. Huang, “3D Printed Flexible Strain Sensors: From Printing to Devices and Signals,” *Advanced Materials*, vol. 33, no. 8, pp. 1–19, 2021, ISSN: 1521-4095. DOI: 10.1002/adma.202004782.

[106] S. Mousavi, D. Howard, F. Zhang, J. Leng, and C. H. Wang, "Direct 3D Printing of Highly Anisotropic, Flexible, Constriction-Resistive Sensors for Multidirectional Proprioception in Soft Robots," *ACS Applied Materials and Interfaces*, vol. 12, no. 13, pp. 15 631–15 643, 2020, ISSN: 1944-8252. DOI: 10.1021/acsami.9b21816.

[107] G. Wolterink, R. Sanders, and G. Krijnen, "A flexible, three material, 3D-printed, shear force sensor for use on finger tips," *Proceedings of IEEE Sensors*, vol. 2019-Octob, pp. 4–7, 2019, ISSN: 2168-9229. DOI: 10.1109/SENSORS43011.2019.8956757.

[108] G. Wolterink, R. Sanders, B. J. van Beijnum, P. Veltink, and G. Krijnen, "A 3d-printed soft fingertip sensor for providing information about normal and shear components of interaction forces," *Sensors*, vol. 21, no. 13, pp. 1–13, 2021, ISSN: 1424-8220. DOI: 10.3390/s21134271.

[109] H. Wang, H. Yang, S. Zhang, L. Zhang, J. Li, and X. Zeng, "3D-Printed Flexible Tactile Sensor Mimicking the Texture and Sensitivity of Human Skin," *Advanced Materials Technologies*, vol. 4, no. 9, pp. 1–8, 2019, ISSN: 2365-709X. DOI: 10.1002/admt.201900147.

[110] M. R. Crump, A. T. Gong, D. Chai, S. L. Bidinger, F. J. Pavinatto, T. E. Reihsen, R. M. Sweet, and J. D. Mackenzie, "Monolithic 3D printing of embeddable and highly stretchable strain sensors using conductive ionogels," *Nanotechnology*, vol. 30, no. 36, 2019, ISSN: 1361-6528. DOI: 10.1088/1361-6528/ab2440.

[111] H. Yuan, M. Yadid, S.-j. Park, A. Kotikian, A. P. Nesmith, P. H. Campbell, J. J. Vlassak, J. A. Lewis, and K. K. Parker, "Instrumented cardiac microphysiological devices via multi-material 3D printing," *Nature materials*, vol. 16, no. 3, pp. 303–308, 2017. DOI: 10.1038/nmat4782.Instrumented.

[112] X. Peng, X. Kuang, D. J. Roach, Y. Wang, C. M. Hamel, C. Lu, and H. J. Qi, "Integrating digital light processing with direct ink writing for hybrid 3D printing of functional structures and devices," *Additive Manufacturing*, vol. 40, no. January, p. 101 911, Apr. 2021, ISSN: 2214-8604. DOI: 10.1016/j.addma.2021.101911.

[113] B. Shih, C. Christianson, K. Gillespie, S. Lee, J. Mayeda, Z. Huo, and M. T. Tolley, "Design considerations for 3D printed, soft, multimaterial resistive sensors for soft robotics," *Frontiers Robotics AI*, vol. 6, no. APR, pp. 1–12, 2019, ISSN: 2296-9144. DOI: 10.3389/frobt.2019.00030.

[114] Z. Wang, X. Guan, H. Huang, H. Wang, W. Lin, and Z. Peng, "Full 3D Printing of Stretchable Piezoresistive Sensor with Hierarchical Porosity and Multimodulus Architecture," *Advanced Functional Materials*, vol. 29, no. 11, pp. 1–8, 2019, ISSN: 1616-3028. DOI: 10.1002/adfm.201807569.

[115] M. O. F. Emon, F. Alkadi, D. G. Philip, D. H. Kim, K. C. Lee, and J. W. Choi, "Multi-material 3D printing of a soft pressure sensor," *Additive Manufacturing*, vol. 28, no. June, pp. 629–638, 2019, ISSN: 2214-8604. DOI: 10.1016/j.addma.2019.06.001.

[116] H. J. Kwon, S. Lee, and J.-H. Kim, "3D-printed pressure sensor with heterogeneous polymer material and annealing effect," no. March 2021, p. 10, 2021, ISSN: 1996-756X. DOI: 10.1117/12.2584838.

[117] N. M. Nair, K. Daniel, S. C. Vadali, D. Ray, and P. Swaminathan, "Direct writing of silver nanowire-based ink for flexible transparent capacitive touch pad," *Flexible and Printed Electronics*, vol. 4, no. 4, 2019, ISSN: 2058-8585. DOI: 10.1088/2058-8585/ab4b04.

[118] W. Yang, Y. Liu, W. Xu, and H. Y. Nie, "Design and Fabrication of Flexible Capacitive Sensor with Cellular Structured Dielectric Layer via 3D Printing," *IEEE Sensors Journal*, vol. 21, no. 9, pp. 10 473–10 482, 2021, ISSN: 1558-1748. DOI: 10.1109/JSEN.2021.3060281.

[119] Q. Ding, H. Chen, W. M. Zhang, and L. Shao, "All-Printed Flexible Tactile Sensors with High Sensitivity and Large Detection Range," *Proceedings of the 16th Annual IEEE International Conference on Nano/Micro Engineered and Molecular Systems, NEMS 2021*, vol. 200240, pp. 1297–1300, 2021. DOI: 10.1109/NEMS51815.2021.9451429.

[120] A. D. Valentine, T. A. Busbee, J. W. Boley, J. R. Raney, A. Chortos, A. Kotikian, J. D. Berrigan, M. F. Durstock, and J. A. Lewis, "Hybrid 3D Printing of Soft Electronics," *Advanced Materials*, vol. 29, no. 40, pp. 1–8, 2017, ISSN: 1521-4095. DOI: 10.1002/adma.201703817. arXiv: arXiv:1011.1669v3.

[121] R. I. Haque, O. Chandran, S. Lani, and D. Briand, "Self-powered triboelectric touch sensor made of 3D printed materials," *Nano Energy*, vol. 52, no. May, pp. 54–62, Oct. 2018, ISSN: 2211-2855. DOI: 10.1016/j.nanoen.2018.07.038.

[122] M. Zhu, M. Xie, X. Lu, S. Okada, and S. Kawamura, "A soft robotic finger with self-powered triboelectric curvature sensor based on multi-material 3D printing," *Nano Energy*, vol. 73, no. January, p. 104 772, 2020, ISSN: 2211-2855. DOI: 10.1016/j.nanoen.2020.104772.

[123] H. Qiao, Y. Zhang, Z. Huang, Y. Wang, D. Li, and H. Zhou, "3D printing individualized triboelectric nanogenerator with macro-pattern," *Nano Energy*, vol. 50, no. April, pp. 126–132, 2018, ISSN: 2211-2855. DOI: 10.1016/j.nanoen.2018.04.071.

[124] R. Zheng, Y. Chen, H. Chi, H. Qiu, H. Xue, and H. Bai, "3D Printing of a Polydimethylsiloxane/Polytetrafluoroethylene Composite Elastomer and its Application in a Triboelectric Nanogenerator," *ACS Applied Materials and Interfaces*, vol. 12, no. 51, pp. 57 441–57 449, 2020, ISSN: 1944-8252. DOI: 10.1021/acsami.0c18201.

[125] B. Chen, W. Tang, T. Jiang, L. Zhu, X. Chen, C. He, L. Xu, H. Guo, P. Lin, D. Li, J. Shao, and Z. L. Wang, "Three-dimensional ultraflexible triboelectric nanogenerator made by 3D printing," *Nano Energy*, vol. 45, no. December 2017, pp. 380–389, 2018, ISSN: 2211-2855. DOI: 10.1016/j.nanoen.2017.12.049.

[126] R. Lin, Y. Li, X. Mao, W. Zhou, and R. Liu, "Hybrid 3D Printing All-in-One Heterogenous Rigidity Assemblies for Soft Electronics," *Advanced Materials Technologies*, vol. 1900614, pp. 1–8, 2019, ISSN: 2365-709X. DOI: 10.1002/admt.201900614.

[127] B. Niese, P. Amend, T. Frick, S. Roth, and M. Schmidt, "Fast and flexible production of mechatronic integrated devices by means of additive manufacturing," *2016 12th International Congress Molded Interconnect Devices - Scientific Proceedings, MID 2016*, no. Mid, pp. 1–6, 2016. DOI: 10.1109/ICMID.2016.7738927.

[128] C. Shemelya, F. Cedillos, E. Aguilera, D. Espalin, D. Muse, R. Wicker, and E. Macdonald, "Encapsulated copper wire and copper mesh capacitive sensing for 3-D printing applications," *IEEE Sensors Journal*, vol. 15, no. 2, pp. 1280–1286, 2015, ISSN: 1530-437X. DOI: 10.1109/JSEN.2014.2356973.

[129] A. Wild, "Integration of functional circuits into FDM parts," *Advanced Materials Research*, vol. 1038, pp. 29–33, 2014, ISSN: 1662-8985. DOI: 10.4028/www.scientific.net/AMR.1038.29.

[130] J. Krzeminski, B. Blicharz, A. Skalski, G. Wroblewski, M. Jakubowska, and M. Sloma, "Photonic curing of silver paths on 3D printed polymer substrate," *Circuit World*, vol. 45, no. 1, pp. 9–14, 2019, ISSN: 0305-6120. DOI: 10.1108/CW-11-2018-0084.

[131] S. Agarwala, G. L. Goh, Y. L. Yap, G. D. Goh, H. Yu, W. Y. Yeong, and T. Tran, "Development of bendable strain sensor with embedded microchannels using 3D printing," *Sensors and Actuators, A: Physical*, vol. 263, pp. 593–599, 2017, ISSN: 0924-4247. DOI: 10.1016/j.sna.2017.07.025.

[132] M. Cosker, L. Lizzi, F. Ferrero, R. Staraj, and J.-m. Ribero, "3D compact antenna using liquid metal and additive technologies," in *2017 11th European Conference on Antennas and Propagation (EUCAP)*, vol. 16, IEEE, Mar. 2017, pp. 2050–2052, ISBN: 978-8-8907-0187-0. DOI: 10.23919/EuCAP.2017.7928688. [Online]. Available: http://ieeexplore.ieee.org/document/7928688/.

[133] M. Saari, B. Xia, B. Cox, P. S. Krueger, A. L. Cohen, and E. Richer, "Fabrication and Analysis of a Composite 3D Printed Capacitive Force Sensor," *3D Printing and Additive Manufacturing*, vol. 3, no. 3, pp. 136–141, Sep. 2016, ISSN: 2329-7662. DOI: 10.1089/3dp.2016.0021.

[134] C. Shemelya, F. Cedillos, E. Aguilera, E. Maestas, J. Ramos, D. Espalin, D. Muse, R. Wicker, and E. MacDonald, "3D printed capacitive sensors," in *2013 IEEE SENSORS*, IEEE, Nov. 2013, pp. 1–4, ISBN: 978-1-4673-4642-9. DOI: 10.1109/ICSENS.2013.6688247. [Online]. Available: http://ieeexplore.ieee.org/document/6688247/.

[135] T. Yamada, Y. Hayamizu, Y. Yamamoto, Y. Yomogida, A. Izadi-Najafabadi, D. N. Futaba, and K. Hata, “A stretchable carbon nanotube strain sensor for human-motion detection,” *Nature Nanotechnology*, vol. 6, no. 5, pp. 296–301, 2011, ISSN: 1748-3395. DOI: 10.1038/nnano.2011.36.

[136] U. Kalsoom, P. N. Nesterenko, and B. Paull, “Recent developments in 3D printable composite materials,” *RSC Advances*, vol. 6, no. 65, pp. 60 355–60 371, 2016, ISSN: 2046-2069. DOI: 10.1039/C6RA11334F. [Online]. Available: http://xlink.rsc.org/?DOI=C6RA11334F.

[137] K. Sim, Y. Li, J. Song, and C. Yu, “Biaxially Stretchable Ultrathin Si Enabled by Serpentine Structures on Prestrained Elastomers,” *Advanced Materials Technologies*, vol. 4, no. 1, p. 1 800 489, Jan. 2019, ISSN: 2365-709X. DOI: 10.1002/admt.201800489.

[138] S. Biswas, J. Reiprich, J. Pezoldt, T. Stauden, and H. O. Jacobs, “Metamorphic Stretchable Touchpad,” *Advanced Materials Technologies*, vol. 1800446, p. 1 800 446, Jan. 2019, ISSN: 2365-709X. DOI: 10.1002/admt.201800446.

[139] C. Didier, A. Kundu, and S. Rajaraman, “Capabilities and limitations of 3D printed microserpentines and integrated 3D electrodes for stretchable and conformable biosensor applications,” *Microsystems and Nanoengineering*, vol. 6, no. 1, 2020, ISSN: 2055-7434. DOI: 10.1038/s41378-019-0129-3.

[140] D. Qi, K. Zhang, G. Tian, B. Jiang, and Y. Huang, “Stretchable Electronics Based on PDMS Substrates,” *Advanced Materials*, vol. 33, no. 6, 2021, ISSN: 1521-4095. DOI: 10.1002/adma.202003155.

[141] J. Nakajima, K. Fayazbakhsh, and Y. Teshima, “Experimental study on tensile properties of 3D printed flexible kirigami specimens,” *Additive Manufacturing*, vol. 32, no. January, p. 101 100, 2020, ISSN: 2214-8604. DOI: 10.1016/j.addma.2020.101100.

[142] R. Zhao, S. Lin, H. Yuk, and X. Zhao, “Kirigami Enhances Film Adhesion,” *Soft Matter*, vol. 14, pp. 2515–2525, 2018, ISSN: 1744-683X. DOI: 10.1039/C7SM02338C. [Online]. Available: http://pubs.rsc.org/en/Content/ArticleLanding/2018/SM/C7SM02338C.

[143] Q. Sun, G. M. Rizvi, C. T. Bellehumeur, and P. Gu, “Effect of processing conditions on the bonding quality of FDM polymer filaments,” *Rapid Prototyping Journal*, vol. 14, no. 2, pp. 72–80, 2008, ISSN: 1355-2546. DOI: 10.1108/13552540810862028.

[144] M. N. Jahangir, J. Cleeman, H. J. Hwang, and R. Malhotra, “Towards out-of-chamber damage-free fabrication of highly conductive nanoparticle-based circuits inside 3D printed thermally sensitive polymers,” *Additive Manufacturing*, vol. 30, no. September, p. 100 886, 2019, ISSN: 2214-8604. DOI: 10.1016/j.addma.2019.100886.

[145] A. J. Lopes, I. H. Lee, E. Macdonald, R. Quintana, and R. Wicker, "Laser curing of silver-based conductive inks for in situ 3D structural electronics fabrication in stereolithography," *Journal of Materials Processing Technology*, vol. 214, no. 9, pp. 1935–1945, 2014, ISSN: 0924-0136. DOI: 10.1016/j.jmatprotec.2014.04.009.

[146] X. Wang and J. Liu, "Recent advancements in liquid metal flexible printed electronics: Properties, technologies, and applications," *Micromachines*, vol. 7, no. 12, 2016, ISSN: 2072-666X. DOI: 10.3390/mi7120206.

[147] X. Aeby, R. V. Dommelen, and D. Briand, "Fully FDM 3D Printed Flexible Capacitive and Resistive Transducers," *2019 20th International Conference on Solid-State Sensors, Actuators and Microsystems and Eurosensors XXXIII, TRANSDUCERS 2019 and EUROSENSORS XXXIII*, no. June, pp. 2440–2443, 2019. DOI: 10.1109/TRANSDUCERS.2019.8808268.

[148] R. van Dommelen, O. Chandran, S. Lani, D. Briand, R. van Dommelen, O. Chandran, S. Lani, and D. Briand, "In-Situ Laser Processing for 3D Printed Mechanical Transducers," in *2019 20th International Conference on Solid-State Sensors, Actuators and Microsystems and Eurosensors XXXIII, TRANSDUCERS 2019 and EUROSENSORS XXXIII*, IEEE, Jun. 2019, pp. 2444–2447, ISBN: 9781728120072. DOI: 10.1109/TRANSDUCERS.2019.8808510. [Online]. Available: https://ieeexplore.ieee.org/document/8808510/.

[149] J. Niittynen, R. Abbel, M. Mäntysalo, J. Perelaer, U. S. Schubert, and D. Lupo, "Alternative sintering methods compared to conventional thermal sintering for inkjet printed silver nanoparticle ink," *Thin Solid Films*, vol. 556, pp. 452–459, 2014, ISSN: 0040-6090. DOI: 10.1016/j.tsf.2014.02.001.

[150] A. Roshanghias, M. Krivec, and M. Baumgart, "Sintering strategies for inkjet printed metallic traces in 3D printed electronics Sintering strategies for inkjet printed metallic traces in 3D printed electronics," 2017.

[151] A. Rivadeneyra and J. A. López-Villanueva, "Recent advances in printed capacitive sensors," *Micromachines*, vol. 11, no. 4, 2020, ISSN: 2072-666X. DOI: 10.3390/MI11040367.

[152] S. Moscato, R. Bahr, T. Le, M. Pasian, M. Bozzi, L. Perregrini, and M. M. Tentzeris, "Infill-Dependent 3-D-Printed Material Based on NinjaFlex Filament for Antenna Applications," *IEEE Antennas and Wireless Propagation Letters*, vol. 15, pp. 1506–1509, 2016, ISSN: 1536-1225. DOI: 10.1109/LAWP.2016.2516101.

[153] C. Tavares, F. Leite, M. D. F. Domingues, T. Paixao, N. Alberto, A. Ramos, H. Silva, and P. F. D. C. Antunes, "Optically Instrumented Insole for Gait Plantar and Shear Force Monitoring," *IEEE Access*, vol. 9, pp. 132 480–132 490, 2021, ISSN: 2169-3536. DOI: 10.1109/ACCESS.2021.3115472.

[154] M. J. Hessert, M. Vyas, J. Leach, K. Hu, L. A. Lipsitz, and V. Novak, "Foot pressure distribution during walking in young and old adults," *BMC Geriatrics*, vol. 5, no. 1, p. 8, Dec. 2005, ISSN: 1471-2318. DOI: 10.1186/1471-2318-5-8.

[155] M. S. Orendurff, E. S. Rohr, A. D. Segal, J. W. Medley, J. R. Green, and N. J. Kadel, "Regional foot pressure during running, cutting, jumping, and landing," *American Journal of Sports Medicine*, vol. 36, no. 3, pp. 566–571, 2008, ISSN: 0363-5465. DOI: 10.1177/0363546507309315.

[156] I. J. Ho, Y. Y. Hou, C. H. Yang, W. L. Wu, S. K. Chen, and L. Y. Guo, "Comparison of plantar pressure distribution between different speed and incline during treadmill jogging," *Journal of Sports Science and Medicine*, vol. 9, no. 1, pp. 154–160, 2010, ISSN: 1303-2968.

[157] C. W. CHAN and A. RUDINS, "Foot Biomechanics During Walking and Running," *Mayo Clinic Proceedings*, vol. 69, no. 5, pp. 448–461, May 1994, ISSN: 0025-6196. DOI: 10.1016/S0025-6196(12)61642-5.

[158] M. Damavandi, P. C. Dixon, and D. J. Pearsall, "Ground reaction force adaptations during cross-slope walking and running," *Human Movement Science*, vol. 31, no. 1, pp. 182–189, Feb. 2012, ISSN: 0167-9457. DOI: 10.1016/j.humov.2011.06.004.

[159] A. S. Fiorillo, C. D. Critello, and A. S. Pullano, "Theory, technology and applications of piezoresistive sensors: A review," *Sensors and Actuators, A: Physical*, vol. 281, pp. 156–175, 2018, ISSN: 0924-4247. DOI: 10.1016/j.sna.2018.07.006.

[160] Y. F. Fu, F. L. Yi, J. R. Liu, Y. Q. Li, Z. Y. Wang, G. Yang, P. Huang, N. Hu, and S. Y. Fu, "Super soft but strong E-Skin based on carbon fiber/carbon black/silicone composite: Truly mimicking tactile sensing and mechanical behavior of human skin," *Composites Science and Technology*, vol. 186, no. November 2019, p. 107 910, 2020, ISSN: 0266-3538. DOI: 10.1016/j.compscitech.2019.107910.

[161] J. Berger, "Evaluation of 3d printed sensors, used to measure normal and shear plantar forces in a shoe insole," M.S. thesis, 2020.

[162] R. B. Mishra, N. El-Atab, A. M. Hussain, and M. M. Hussain, "Recent Progress on Flexible Capacitive Pressure Sensors: From Design and Materials to Applications," *Advanced Materials Technologies*, vol. 6, no. 4, pp. 1–34, 2021, ISSN: 2365-709X. DOI: 10.1002/admt.202001023.

[163] S. Rosset and H. R. Shea, "Flexible and stretchable electrodes for dielectric elastomer actuators," *Applied Physics A: Materials Science and Processing*, vol. 110, no. 2, pp. 281–307, 2013, ISSN: 0947-8396. DOI: 10.1007/s00339-012-7402-8.

[164] R. Xu, C. Wu, and H. Xu, "Particle size and zeta potential of carbon black in liquid media," *Carbon*, vol. 45, no. 14, pp. 2806–2809, Nov. 2007, ISSN: 0008-6223. DOI: 10.1016/j.carbon.2007.09.010. [Online]. Available: https://linkinghub.elsevier.com/retrieve/pii/S000862230700468X.

[165] A. Poulin, X. Aeby, G. Siqueira, and G. Nyström, "Versatile carbon-loaded shellac ink for disposable printed electronics," *Scientific Reports*, vol. 11, no. 1, pp. 1–9, 2021, ISSN: 2045-2322. DOI: 10.1038/s41598-021-03075-4.

[166] W. Oropallo and L. A. Piegl, "Ten challenges in 3D printing," *Engineering with Computers*, vol. 32, no. 1, pp. 135–148, 2016, ISSN: 1435-5663. DOI: 10.1007/s00366-015-0407-0.

[167] H. Shivashankar, R. Sangamesh, and S. M. Kulkarni, "Processing and investigation of mechanical characteristics on the polydimethylsiloxane/carbon black composites," *Materials Research Express*, vol. 6, no. 10, 2019, ISSN: 2053-1591. DOI: 10.1088/2053-1591/ab3b7e.

[168] S. Dul, A. Pegoretti, and L. Fambri, "Fused Filament Fabrication of Piezoresistive Carbon Nanotubes Nanocomposites for Strain Monitoring," *Frontiers in Materials*, vol. 7, no. February, pp. 1–13, 2020, ISSN: 2296-8016. DOI: 10.3389/fmats.2020.00012.

[169] S. BRAGE, N. WEDDERKOPP, P. W. FRANKS, L. BO ANDERSEN, and K. FROBERG, "Reexamination of Validity and Reliability of the CSA Monitor in Walking and Running," *Medicine & Science in Sports & Exercise*, vol. 35, no. 8, pp. 1447–1454, Aug. 2003, ISSN: 0195-9131. DOI: 10.1249/01.MSS.0000079078.62035.EC. [Online]. Available: http://journals.lww.com/00005768-200308000-00029.

[170] S. Gao, J. L. Chen, Y. N. Dai, R. Wang, S. B. Kang, and L. J. Xu, "Piezoelectric-Based Insole Force Sensing for Gait Analysis in the Internet of Health Things," *IEEE Consumer Electronics Magazine*, vol. 10, no. 1, pp. 39–44, 2021, ISSN: 2162-2256. DOI: 10.1109/MCE.2020.2986828.

[171] L. Y. Zhou, Q. Gao, J. Z. Fu, Q. Y. Chen, J. P. Zhu, Y. Sun, and Y. He, "Multimaterial 3D Printing of Highly Stretchable Silicone Elastomers," *ACS Applied Materials and Interfaces*, vol. 11, no. 26, pp. 23 573–23 583, 2019, ISSN: 1944-8252. DOI: 10.1021/acsami.9b04873.

[172] J. Wang, S. Yang, P. Ding, X. Cao, Y. Zhang, S. Cao, K. Zhang, S. Kong, Y. Zhou, X. Wang, D. Li, and D. Kong, "Omnidirectional Printing of Soft Elastomer for Liquid-State Stretchable Electronics," *ACS Applied Materials & Interfaces*, acsami.9b04730, 2019, ISSN: 1944-8244. DOI: 10.1021/acsami.9b04730.

[173] P. L. Fulmek, F. Wandling, W. Zdiarsky, G. Brasseur, and S. P. Cermak, "Capacitive sensor for relative angle measurement," *IEEE Transactions on Instrumentation and Measurement*, vol. 51, no. 6, pp. 1145–1148, 2002, ISSN: 0018-9456. DOI: 10.1109/TIM.2002.808052.

[174] S. Z. Homayounfar and T. L. Andrew, “Wearable Sensors for Monitoring Human Motion: A Review on Mechanisms, Materials, and Challenges,” *SLAS Technology*, vol. 25, no. 1, pp. 9–24, 2020, ISSN: 2472-6311. DOI: 10.1177/2472630319891128.

[175] P. J. Rowe, C. M. Myles, C. Walker, and R. Nutton, “Knee joint kinematics in gait and other functional activities measured using flexible electrogoniometry: How much knee motion is sufficient for normal daily life?” *Gait and Posture*, vol. 12, no. 2, pp. 143–155, 2000, ISSN: 0966-6362. DOI: 10.1016/S0966-6362(00)00060-6.

[176] F. E. Tay, X. Jun, Y. C. Liang, V. J. Logeeswaran, and Y. Yufeng, “Effects of non-parallel plates in a differential capacitive microaccelerometer,” *Journal of Micromechanics and Microengineering*, vol. 9, no. 4, pp. 283–293, 1999, ISSN: 0960-1317. DOI: 10.1088/0960-1317/9/4/301.

[177] J. F. Wu, C. Qiu, Y. Wang, R. Zhao, Z. P. Cai, X. G. Zhao, S. S. He, F. Wang, Q. Wang, and J. Q. Li, “Human limb motion detection with novel flexible capacitive angle sensor based on conductive textile,” *Electronics (Switzerland)*, vol. 7, no. 9, 2018, ISSN: 2079-9292. DOI: 10.3390/electronics7090192.

[178] R. Nur, N. Matsuhisa, Z. Jiang, M. O. G. Nayeem, T. Yokota, and T. Someya, “A Highly Sensitive Capacitive-type Strain Sensor Using Wrinkled Ultrathin Gold Films,” *Nano Letters*, vol. 18, no. 9, pp. 5610–5617, 2018, ISSN: 1530-6992. DOI: 10.1021/acs.nanolett.8b02088.

[179] R. A. Serway and J. W. Jewett, *Physics for scientists and engineers*. Cengage learning, 2018.

[180] *Electric field from voltage*, http://hyperphysics.phy-astr.gsu.edu/hbase/electric/efromv.html, Accessed: 11/03/2022.

[181] J. M. Bueno-Barrachina, C. S. Cañas-Peñuelas, and S. Catalan-Izquierdo, “Capacitance Evaluation on Non-parallel Thick-Plate Capacitors by Means of Finite Element Analysis,” *Journal of Energy and Power Engineering*, vol. 5, pp. 373–378, 2011.

[182] M. Cen-Puc, A. Schander, M. G. Vargasgleason, and W. Lang, “An assessment of surface treatments for adhesion of polyimide thin films,” *Polymers*, vol. 13, no. 12, 2021, ISSN: 2073-4360. DOI: 10.3390/polym13121955.

[183] C. Mendes-Felipe, J. Oliveira, I. Etxebarria, J. L. Vilas-Vilela, and S. Lanceros-Mendez, *State-of-the-Art and Future Challenges of UV Curable Polymer-Based Smart Materials for Printing Technologies*, 2019. DOI: 10.1002/admt.201800618.

[184] B. Burkett, J. Smeathers, and T. Barker, “Walking and running inter-limb asymmetry for paralympic trans-femoral amputees, a biomechanical analysis,” *Prosthetics and Orthotics International*, vol. 27, no. 1, pp. 36–47, 2003, ISSN: 0309-3646. DOI: 10.3109/03093640309167975.

[185] A. S. Sanca, J. C. Rocha, K. J. Eugenio, L. B. Nascimento, and P. J. Alsina, "Characterization of resistive flex sensor applied to joint angular displacement estimation," *Proceedings - 15th Latin American Robotics Symposium, 6th Brazilian Robotics Symposium and 9th Workshop on Robotics in Education, LARS/SBR/WRE 2018*, pp. 39–44, 2018. DOI: 10.1109/LARS/SBR/WRE.2018.00016.

[186] L. Ricci, F. Taffoni, and D. Formica, "On the orientation error of IMU: Investigating static and dynamic accuracy targeting human motion," *PLoS ONE*, vol. 11, no. 9, pp. 1–15, 2016, ISSN: 1932-6203. DOI: 10.1371/journal.pone.0161940.

[187] M. Ha, S. Lim, and H. Ko, "Wearable and flexible sensors for user-interactive health-monitoring devices," *Journal of Materials Chemistry B*, vol. 6, no. 24, pp. 4043–4064, 2018, ISSN: 2050-750X. DOI: 10.1039/c8tb01063c.

[188] S. Majumder, T. Mondal, and M. J. Deen, "Wearable sensors for remote health monitoring," *Sensors (Switzerland)*, vol. 17, no. 1, 2017, ISSN: 1424-8220. DOI: 10.3390/s17010130.

[189] D. V. Dimitrov, "Medical Internet of Things and Big Data in Healthcare," *Healthcare Informatics Research*, vol. 22, no. 3, p. 156, Jan. 2016, ISSN: 2093-3681. DOI: 10.4258/hir.2016.22.3.156. [Online]. Available: http://jama.jamanetwork.com/article.aspx?doi=10.1001/jama.2010.1923%20http://e-hir.org/journal/view.php?id=10.4258/hir.2016.22.3.156.

[190] G. Lopez, S. Abe, K. Hashimoto, and A. Yokokubo, "On-Site Personal Sport Skill Improvement Support Using only a Smartwatch," *2019 IEEE International Conference on Pervasive Computing and Communications Workshops, PerCom Workshops 2019*, pp. 158–164, 2019. DOI: 10.1109/PERCOMW.2019.8730681.

[191] Y. Ling, T. An, L. W. Yap, B. Zhu, S. Gong, and W. Cheng, "Disruptive, Soft, Wearable Sensors," *Advanced Materials*, vol. 32, no. 18, pp. 1–13, 2020, ISSN: 1521-4095. DOI: 10.1002/adma.201904664.

[192] A. Drăgulinescu, A.-M. Drăgulinescu, G. Zincă, D. Bucur, V. Feieș, and D.-M. Neagu, "Smart Socks and In-Shoe Systems: State-of-the-Art for Two Popular Technologies for Foot Motion Analysis, Sports, and Medical Applications," *Sensors*, vol. 20, no. 15, p. 4316, Aug. 2020, ISSN: 1424-8220. DOI: 10.3390/s20154316. [Online]. Available: https://www.mdpi.com/1424-8220/20/15/4316.

[193] A. Middleton, S. L. Fritz, and M. Lusardi, "Walking speed: The functional vital sign," *Journal of Aging and Physical Activity*, vol. 23, no. 2, pp. 314–322, 2015, ISSN: 1543-267X. DOI: 10.1123/japa.2013-0236.

[194] D. K. White, T. Neogi, M. C. Nevitt, C. E. Peloquin, Y. Zhu, R. M. Boudreau, J. A. Cauley, L. Ferrucci, T. B. Harris, S. M. Satterfield, E. M. Simonsick, E. S. Strotmeyer, and Y. Zhang, "Trajectories of gait speed predict mortality in well-functioning older adults: The health, aging and body composition study," *Journals of Gerontology - Series A Biological Sciences and Medical Sciences*, vol. 68, no. 4, pp. 456–464, 2013, ISSN: 1079-5006. DOI: 10.1093/gerona/gls197.

[195] G. V. Ostir, I. M. Berges, K. J. Ottenbacher, S. R. Fisher, E. Barr, J. R. Hebel, and J. M. Guralnik, "Gait Speed and Dismobility in Older Adults," *Archives of Physical Medicine and Rehabilitation*, vol. 96, no. 9, pp. 1641–1645, Sep. 2015, ISSN: 0003-9993. DOI: 10.1016/j.apmr.2015.05.017. [Online]. Available: https://linkinghub.elsevier.com/retrieve/pii/S0003999315004499.

[196] A. F. DeJong and J. Hertel, *Gait-training devices in the treatment of lower extremity injuries in sports medicine: current status and future prospects*, Dec. 2018. DOI: 10.1080/17434440.2018.1551130.

[197] M. Menolotto, D. S. Komaris, S. Tedesco, B. O'flynn, and M. Walsh, "Motion capture technology in industrial applications: A systematic review," *Sensors (Switzerland)*, vol. 20, no. 19, pp. 1–25, 2020, ISSN: 1424-8220. DOI: 10.3390/s20195687.

[198] J. Tao, M. Dong, L. Li, C. Wang, J. Li, Y. Liu, R. Bao, and C. Pan, "Real-time pressure mapping smart insole system based on a controllable vertical pore dielectric layer," *Microsystems and Nanoengineering*, vol. 6, no. 1, p. 62, Dec. 2020, ISSN: 2055-7434. DOI: 10.1038/s41378-020-0171-1. [Online]. Available: http://www.nature.com/articles/s41378-020-0171-1.

[199] K.-c. Jung, J.-h. Son, and S.-h. Chang, "Self-Powered Smart Shoes with Tension-Type Ribbon Harvesters and Sensors," *Advanced Materials Technologies*, vol. 6, no. 2, p. 2 000 872, Feb. 2021, ISSN: 2365-709X. DOI: 10.1002/admt.202000872.

[200] Z. Zhang, K. Du, X. Chen, C. Xue, and K. Wang, "An air-cushion triboelectric nanogenerator integrated with stretchable electrode for human-motion energy harvesting and monitoring," *Nano Energy*, vol. 53, no. June, pp. 108–115, 2018, ISSN: 2211-2855. DOI: 10.1016/j.nanoen.2018.08.011.

[201] Z. Zhang, T. He, M. Zhu, Z. Sun, Q. Shi, J. Zhu, B. Dong, M. R. Yuce, and C. Lee, "Deep learning-enabled triboelectric smart socks for IoT-based gait analysis and VR applications," *npj Flexible Electronics*, vol. 4, no. 1, pp. 1–12, 2020, ISSN: 2397-4621. DOI: 10.1038/s41528-020-00092-7.

[202] F. Alaimo, A. Sadeqi, H. Rezaei Nejad, Y. Jiang, W. Wang, D. Demarchi, and S. Sonkusale, "Reel-to-reel fabrication of strain sensing threads and realization of smart insole," *Sensors and Actuators A: Physical*, vol. 301, p. 111 741, 2020, ISSN: 0924-4247. DOI: 10.1016/j.sna.2019.111741.

[203] D. Sengupta and A. G. Prakash Kottapalli, "Ultralight Weight Piezoresistive Spongy Graphene Sensors for Human Gait Monitoring Applications," *15th IEEE International Conference on Nano/Micro Engineered and Molecular System, NEMS 2020*, vol. 2020, pp. 120–123, 2020. DOI: 10.1109/NEMS50311.2020.9265580.

[204] A. F. Carvalho, A. J. Fernandes, R. Martins, E. Fortunato, and F. M. Costa, "Laser-Induced Graphene Piezoresistive Sensors Synthesized Directly on Cork Insoles for Gait Analysis," *Advanced Materials Technologies*, vol. 5, no. 12, pp. 1–8, 2020, ISSN: 2365-709X. DOI: 10.1002/admt.202000630.

[205] M. Birtane and H. Tuna, "The evaluation of plantar pressure distribution in obese and non-obese adults," *Clinical Biomechanics*, vol. 19, no. 10, pp. 1055–1059, 2004, ISSN: 0268-0033. DOI: 10.1016/j.clinbiomech.2004.07.008.

[206] A. S. McIntosh, K. T. Beatty, L. N. Dwan, and D. R. Vickers, "Gait dynamics on an inclined walkway," *Journal of Biomechanics*, vol. 39, no. 13, pp. 2491–2502, 2006, ISSN: 0021-9290. DOI: 10.1016/j.jbiomech.2005.07.025.

[207] M. Hossain and Z. Liao, "An additively manufactured silicone polymer: Thermo-viscoelastic experimental study and computational modelling," *Additive Manufacturing*, vol. 35, no. June, p. 101 395, 2020, ISSN: 2214-8604. DOI: 10.1016/j.addma.2020.101395.

[208] V. Kumar, M. N. Alam, A. Manikkavel, M. Song, D. J. Lee, and S. S. Park, "Silicone rubber composites reinforced by carbon nanofillers and their hybrids for various applications: A review," *Polymers*, vol. 13, no. 14, 2021, ISSN: 2073-4360. DOI: 10.3390/polym13142322.

[209] K. Pickering, *Properties and performance of natural-fibre composites*. Elsevier, 2008.

Ryan van Dommelen

Additive Manufacturing and Microsystems Engineer

Rue des Sablons 12
Neuchâtel
Switzerland
26 July 1989 - The Netherlands
+41786830217
ryanmvd@gmail.com
ryanmvd
Work Permit B

I am a mechanical engineer driven by innovation and with an interest in research and development. For the last four years, I have been researching additive manufacturing techniques towards the development of micro-systems for human motion monitoring and healthcare solutions. My aim is to develop technologies that can improve health and wellbeing.

Work Experience

03-2018 to 05-2022 — **Research Assistant**, *EPFL - Microcity*, Neuchâtel, Switzerland
Development of fully 3D printed sensors for the monitoring of human motions
- Design and fabrication of soft mechanical sensors for human gait analysis
- 3D printing of soft silicone systems with highly conductive interconnects
- Development of 3D printable materials and 3D printing based fabrication methodologies

01-2012 to 07-2012 — **Engineering Intern**, *Hörchner & Hammersma B.V.*, Pijnacker, The Netherlands
Mechanical design of an electromechanical drivetrain prototype
- Full development of a drivetrain design for a tractor with a variable wheel track
- 3D CAD design of various parts (SolidEdge) and general engineering consultancy

Education

03-2018 to 05-2022 — **Doctoral Program in Microsystems and Microelectronics**, *École Polytechnique Fédérale de Lausanne (EPFL)*, Neuchâtel (CH)
Thesis: 3D printing of elastomeric mechanical sensors designed for human motion monitoring

01-2015 to 08-2017 — **Master Precision and Microsystems Engineering (PME)**, *Delft University of Technology (TU Delft)*, Delft, The Netherlands
Masters program on precision mechanics, mechatronics, and microsystems engineering with a specialisation towards biomedical applications
Master thesis subject: Self-Assembled Colloidal Crystals for the use in Pattern Replication by Hot Embossing

09-2013 to 01-2015 — **Pre-master program (HBO to MSc)**, *Delft University of Technology (TU Delft)*, Delft, The Netherlands
Bridging program for applied science graduates for admission to a master program

09-2008 to 09-2012 — **HBO Mechanical Engineering (B.Eng.)**, *The Hague University of Applied Sciences*, Delft, The Netherlands
Applied university degree in mechanical engineering

Skills and Experience

Computational	Python 3, Matlab, COMSOL Multiphysics, OriginLab	■■■■□
	FEMAP, Ansys, ImageJ	■■□□□
CAD	Inventor, Autodesk Fusion 360, SolidEdge, SolidWorks	■■■■■
	AutoCad, Catia	■■■□□
Graphics	Adobe Photoshop & Illustrator	■■■■■
	Adobe After Effects	■■■□□

Technical and Lab

Design of Experiments (DoE), ANOVA, Scanning Electron Microscopy (SEM), Atomic Force Microscopy (AFM), Four Point Probing (4PP), Fast Fourier Transformation (FFT), Thin Film Deposition, Spincoating

Languages

Dutch Native
English C2
French B2-C1
German A2
Spanish A2

Soft Skills

Project management

Supervised 3 semester projects and co-supervised a master student with their thesis including being part of their thesis jury.

Team work and collaboration

Collaborated with scientific staff from ETH Zurich and EMPA and led several research activities for a project within the Strategic Focus Area (SFA) Advanced Manufacturing framework on the 3D printing of personalisable soft smart wearables.

Presentation and communication

Passionate about science communication in part due to my background in amateur theater (5+ years), allowing me to feel at ease with crowds and public speaking. During my PhD work I had the opportunity to present my work in the form of two talks and two poster presentations at international conferences.

Interests and Hobbies

Outdoor Sports, Photography, Hiking, Graphic Design, Cooking